CONFERENCE PROCEEDINGS

Mechanical, Manufacturing, Materials and Biomedical Engineering Conference

showcasing postgraduate research at local universities

Endorsed by the
SOUTH AFRICAN INSTITUTION OF MECHANICAL ENGINEERING
(Western Cape Branch)

SAIMechE

7 November 2025
Belmont Conference Centre, Rondebosch
University of Cape Town

Stellenbosch UNIVERSITY IYUNIVESITHI UNIVERSITEIT

University of Cape Town · iYunivesithi yaseKapa · Universiteit van Kaapstad

Cape Peninsula University of Technology
creating futures

Preface

This volume contains the extended abstracts for the research presented at SAIMechE WC Postgraduate Conference on Mechanical, Manufacturing, Materials and Biomedical Engineering held on Friday, November 7, 2025 at Belmont Square Conference Centre.

There were 55 submissions of extended abstracts from postgraduate students. All abstracts have been reviewed by the program committee. The review process was managed and proceedings were created using EasyChair (www.easychair.org).

SAIMechE Western Cape, in association with local engineering faculties at the Cape Peninsula University of Technology, Stellenbosch University and the University of Cape Town has presented this conference annually since 2012. The conference is aimed at providing an opportunity for our local postgraduate students to showcase their current research and interesting technological developments in topics related to the broad field of mechanical engineering.

The conference was initially funded by a donation from the Cape Initiative in Materials and Manufacturing (CIMM). It is only through continued sponsorship that it is possible to continue to offer this vibrant event. In 2025, the SAIMechE WC Postgraduate Conference was graciously sponsored by AAT Composites, Aluminium Federation of South Africa, John Thompson, MECAD and the Department of Mechanical and Mechatronic Engineering at Stellenbosch University.

We would like to thank all supervisors and students for their participation and efforts in making this, once more, a successful opportunity to showcase excellence in engineering research in the Western Cape, South Africa.

Special thanks are extended to Carmelita Jonker and Denise Botha for their immense administrative assistance.

November 7, 2025
Cape Town

SAIMechE WC PG Conference 2025,
Organising Committee

Organising Committee

Carl Tshamala	Stellenbosch University
Graeme John Oliver	Cape Peninsula University of Technology
Melody Neaves	Stellenbosch University
Sa-aadat Parker	University of Cape Town
Steeve Chung Kim Yuen	University of Cape Town

Scientific Committee

Arnold Pretorius	University of Cape Town
Boitumelo Ramatsetse	Stellenbosch University
Brendon Nickerson	Stellenbosch University
Cletus Magoda	Cape Peninsula University of Technology
Clint Steed	Stellenbosch University
Colin du Sart	University of Cape Town
Efe Orumwense	Cape Peninsula University of Technology
Francois Rozon	Stellenbosch University
Martin Venter	Stellenbosch University
Nicole Taylor	Stellenbosch University
Rashid Haffejee	Stellenbosch University
Sherlyn Gabriel	University of Cape Town
Thorsten Becker	University of Cape Town
Vinay Shekhar	Stellenbosch University
Wei Hua Ho	University of Cape Town

Keynote Speaker: Prof Trevor J. Cloete - University of Cape Town

Multi-Strain Rate Testing of Bone - a 20 Year Retrospective

This year we were honored to receive a keynote talk from Dr Trevor Cloete. Dr Cloete obtained his B.Ing and M.Ing (Meganies) from Stellenbosch University. Thereafter he completed his PhD in the field of Structural Impact under the supervision of Prof G. N. Nurick at the University of Cape Town (UCT). He is currently a Senior Lecturer in the Department of Mechanical Engineering at UCT with research interests in the field of Impact Mechanics, with a particular focus on Structural Response and Dynamic Material Characterization.

The mechanical properties of bone have been a topic of study at the Blast Impact and Survivability Research Unit (BISRU) at UCT for the last 20 years. This work has focused on the macroscopic strength and stiffness of cortical and trabecular bone, typically obtained from femurs or humerii of large terrestrial vertebrates. Of particular interest has been the effect of strain rate, with tests being conducted from speeds of 0.001/s to 1000/s. Indeed, a large part of the work has been devoted to developing new testing techniques for specific strain rate regimes. A summary of the techniques developed and significant results obtained was presented.

Best Presentation Award

The best presentation as voted by the conference attendees was awarded to Mr. Mpilonhle Nxasana who is currently a master's student at the Department of Mechanical Engineering at the University of Cape Town. Mpilonhle provided an enthusiastic presentation on his topic entitled "Control Design of a Coaxial Tiltrotor Quadcopter for Mixed Flight Regimes". This study proposed a design and implementation of a control system for a coaxial tiltrotor quadcopter involving an overactuated configuration that allows for independent translational and rotational motion control.

Mpilonhle is also part of the dynamic MechatronicSystems.Group (MS.G) and is supervised by Dr Arnold Pretorius.

Best Abstract Award

The Best Abstract Award was presented to Mr. Timothy Reddy, who is completing his master's degree in the Department of Mechanical Engineering at the University of Cape Town. His extended abstract, titled "AQUA: The Adaptive Quality Upscaling Architecture," investigates the integration of additive manufacturing, subtractive machining, and optical metrology within a unified system to enable faster, less wasteful, and dimensionally verifiable components.

Timothy has a strong interest in the entrepreneurial potential of advanced manufacturing technologies, and his current research focuses on the development of hybrid processes for metal. He is supervised by Prof. Lukas du Plessis at the Advanced Manufacturing Laboratory.

Sponsored Prizes

- **Best use of Siemens software (sponsored by Aerotherm):** Jaco Mostert – "Commercial Electric Vehicle Thermal Management System Modelling and Testing"
- **Best aluminium-related project (sponsored by AFSA):** Abdul Benjamin – "Fracture Prediction of Realistic Intermetallic Particles in a Plasticity Model of Wrought Aluminium"
- **Best composites-related project (sponsored by AAT Composites):** Mpho Ntloane – "Determining the Flexural Response of Basalt Fibre Reinforcement Composite with a Bio Polymer Matrix as a Sustainable, High-performance Material"
- **Most impactful research project (sponsored by SU Mechanical and Mechatronic Engineering Department):** Dylan Opperman – "Operationalising Predictive Maintenance through a Digital Twin System for Bulk Water Pumping Systems"
- **Best solar thermal research project (sponsored by STERG):** Connal Winter – "A Method of Deflectometry Based on Photogrammetry for Heliostat Optical Quality Assessment"

MECAD Sponsored Prizes

- **Best Use of CAD in Design:** Braden Nicholson – "Induction Heating in an Extreme-temperature Fracture Toughness Testing Apparatus"
- **Best Application of Finite Element Methods (FEM):** Musimwa Valery Mukengere – "Design and Simulation of an Assistive Lower Limb Exoskeleton"
- **Best Application of Computational Fluid Dynamics (CFD):** Maxwell Bischof – "A numerical investigation into cryogenic fuel storage tanks under violent sloshing excitation"
- **Best Experimental Methodology / Analysis:** Tumelo Selialia – "Effects of Varying Cuboid Charges Aspect Ratio on the Blast Wave Propagation in Free Air"
- **Best in Advanced Manufacturing / Materials Processing:** Ingrid Botha – "Characterisation Method of PLA/CB Shape Memory Behaviour via Custom FDM Tool Path Planning"
- **Best in Biomedical Engineering:** Karl Zapke – "Articulating Drop Foot Orthosis Testing Device"
- **Best in Thermal-Fluid Sciences / Energy Systems:** Nicola Cilliers – "Development of a Transient 1D Finite Volume Thermofluid Network Modelling Methodology for the Human Cardiovascular System"
- **Best in Mechatronics / Robotics / Control:** Mpilonhle Nxasana – "Control Design of a Coaxial Tiltrotor Quadcopter for Mixed Flight Regimes"
- **Best in Structural Integrity / Dynamics:** Refiloe Selai – "Mathematical Modelling of Wind-induced Vibrations in Transmission Line Conductors"
- **Best in System Modelling / Data Analytics:** Reece Liebenberg – "Development of a Data Model for Hospital Waste Streams"

Table of Contents

CHARACTERISATION METHOD OF PLA/CB SHAPE MEMORY BEHAVIOUR VIA CUSTOM FDM TOOL PATH PLANNING

Ingrid Retha Botha[a] & Glen Bright[a]

[a] Mechatronics and Robotics Research Group, Discipline of Mechanical Engineering, University of KwaZulu-Natal, Durban, South Africa

Shape Memory Polymers (SMP) define thermoplastic or thermoset polymer geometries capable of assuming a secondary shape. The elastic potential energy between molecular chains results in the geometry returning to the original state upon applying an external stimulus. The study employs joule-heating as the stimulus, where the heat generated by electrical resistance in response to current flow activates the SMP response. Interest in SMP research has resurged in the past decade due to the complex architectures made possible by additive manufacturing techniques. However, the popular Fused Deposition Modelling (FDM) technique has shown limited adoption compared to alternative techniques due to the anisotropic qualities introduced by printing parameters. This results in different thermal, mechanical, and electrical properties depending on the measurement direction. Printing parameters in this context refer to the height, width, layer, orientation, and direction of the deposited filament. The authors propose a different perspective on anisotropy – viewing it as a design opportunity. The study aims to create a variable SMP response within a single printed geometry through the control of printing parameters. This paper proposes a methodological framework for characterising and designing programmable SMP architectures using FDM technology.

Background:

The adoption of SMP structures in actuator and sensor design has been limited due to the capabilities of traditional polymer manufacturing technologies. The introduction of commercially available additive manufacturing technologies resulted in a resurgence in SMP application research – defined as 4D printing by Skylar Tibbits in 2013 [1]. In order to expand the potential for FDM production of SMP designs, refined control of printing parameters is necessary, allowing responses to be programmed into sections of the geometry. The printing parameters are controlled using tool path planning and G-code. Commercial printers utilise slicer software to generate G-code from imported models. However, slicer-generated G-code prioritises print speed, dimensional accuracy, and surface finish. Parametric design software such as Grasshopper (Rhinoceros, USA) provides a platform to generate custom G-code for variable parameter control. The material selected to validate the methodology is a Poly(Lactic) Acid (PLA) matrix with conductive Carbon Black (CB) filler nanoparticles (ProtoPasta, USA). The PLA matrix exhibits SMP properties under thermal stimulus, reverting to the original structure when heated above the glass transition temperature of approximately 60°C[2]. The CB acts as a conductive network within the matrix to allow for joule-heating upon the application of an electrical current.

The printing parameters of interest are the layer height, width, and raster angle, Figure 1. Raster angle refers to the direction of the extruded filament, with the reference axis in this scenario being the direction of current flow. To program a nonhomogeneous response in the printed structure, the proposed methodology implements raster angle to establish high and low resistance areas and variable cross-sectional areas to control current flow direction.

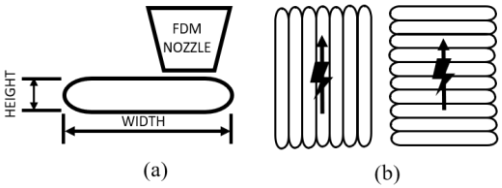

Figure 1: Control printing parameters (a) extruded height and width, (b) raster angle relative to applied current direction

However, the abovementioned printing parameters are not isolated during FDM operation and affect the extrusion speed, thermal inertia, nanoparticle distribution, electrical percolation threshold, and interlayer adhesion. This introduces multiple regressor variables into the study. Therefore, the proposed methodology implements inferential statistical analysis to assess and categorise the strength of the relationship between the multiple regressors and the response variables. The regressors demonstrating a strong correlation with the response variables are incorporated into a predictive model.

This study focused on developing a methodological framework to characterise the response to variable print parameters. The quantitative and qualitative results analysis is outside the scope of the presented work.

Proposed Methodology:

The primary relationships are divided into three subdivisions based on the scale of the investigated structures: the microstructure, mesostructure, and macrostructure, Figure 2. Mesostructure is an intermediate scale and refers to the layout and orientation of extruded layers that comprise the larger structure.

[a] bothai@ukzn.ac.za

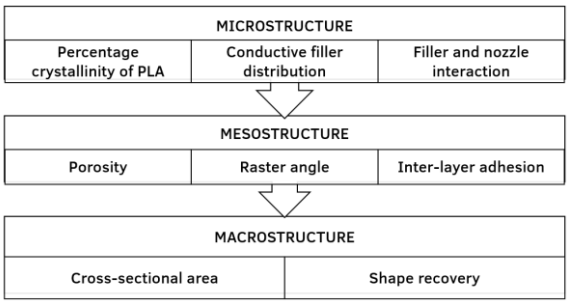

Figure 2: Variables under study to be assessed against thermal, electrical, and mechanical performance

The characteristics of each structural level are analysed using two geometries. The first is an extrusion of a single layer and no adjacent paths, further referred to as the extrudate. The second geometry is a plate consisting of an equal number of adjacent paths and layers. A collection of paths and layers will exhibit two significant differences from a single extrudate: porosity at contact sites and conductive heat transfer through adjacent layers. The above two geometries consist of nine combinations of layer height and width, with the plate sample including an additional variation of raster angle, Table 1. All toolpaths are generated using the Grasshopper parametric design software (Rhinoceros, USA). Ensuring control over all variables involved in FDM manufacturing.

Table 1: Extrusion parameters of each sample set

Sample	Width (mm)	Height (mm)	Cross-sectional area (mm^2)
0104	0.4	0.1	0.04
0106	0.6	0.1	0.06
0108	0.8	0.1	0.08
0204	0.4	0.2	0.07
0206	0.6	0.2	0.11
0208	0.8	0.2	0.15
0304	0.4	0.3	0.10
0306	0.6	0.6	0.16
0308	0.8	0.8	0.22

The experimental methodology is represented in Figure 3. The flow chart presents the two sample categories, which are further divided into the sample sets defined in Table 1. Row three of the flowchart indicates the measurement procedure. Acronyms at this level refer to Differential Scanning Calorimetry (DSC), Stereomicroscope (SM), Scanning Electron Microscope (SEM), Digital Multimeter (DMM), and Infra-red (IR) camera. Thereafter, the variable of interest of each characterisation procedure is listed, followed by the logical progression based on statistical analysis of results. The primary statistical analysis techniques used in this study include regression testing and Analysis of Variance (ANOVA).

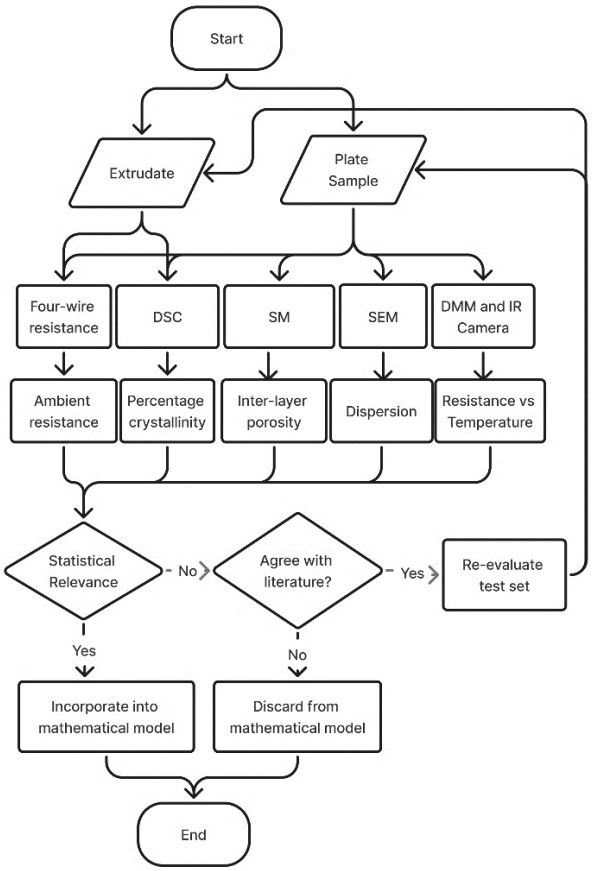

Figure 3: Flow chart of methodology

Conclusion:

The study proposes an advanced technique of variable layer thickness toolpath planning to print programmable structures using FDM technology and a conductive SMP material. Such structures contain heating paths defined by custom tool path planning, resulting in constrained shape recovery once the material is heated above the glass transition temperature via joule-heating. The focus of this methodological framework is the characterisation and contextualisation of the thermal and electrical responses to changing printing parameters. Printing parameters of interest are layer height, layer width, and raster angle. Understanding these relationships and their statistical significance provides the tools to develop a mathematical model defining the resistive response and mechanism of heat generation.

References:

[1] S. Tibbits, "4D Printing: Multi-Material Shape Change," *Architectural Design*, vol. 84, no. 1, pp. 116-121, 2014

[2] D. Rahmatabadi *et al.*, "Advancing sustainable shape memory polymers through 4D printing of polylactic acid-polybutylene adipate terephthalate blends," *European Polymer Journal*, vol. 216, p. 113289, 2024

RELIABILITY ASSESSMENT AND DEVELOPMENT OF A STEREOVISION SYSTEM FOR MEASURING BONE FRACTURE MOTION

CV Mwenecho[a], K Schreve[b] & N Ferreira[c]

[a] Institute for Biomedical Engineering, Stellenbosch University, South Africa
[b] Department of Mechanical and Mechatronic Engineering, Stellenbosch University, South Africa
[c] Division of Orthopaedic Surgery, Department of Surgical Sciences, Stellenbosch University, South Africa.

Introduction: Controlled interfragmentary movement (IFM) at bone fracture sites is vital for successful healing[1]. Stereo vision (SV) systems have increasingly been used to evaluate IFM in both in vitro[2] and in vivo[3] settings. However, in vitro tests involve manual loading of the specimen, whereas the reported in vivo studies do not assess all IFM modalities. Therefore, the specific type and extent of IFM occurring during key clinical procedures remain unknown.

Objectives: This paper aims to address this gap by evaluating the capabilities of three different camera-based systems for measuring six degrees of freedom (DOF) micromotions, similar in magnitude to IFM. It also demonstrates the development of an SV system for in vivo measurement of IFM.

Method: A pilot study was performed to evaluate the capabilities of the Vicon and SV systems in measuring micromotions in 0.05 mm increments. A microstage device provided ground-truth data across a full 1 mm range. For the Vicon system, displacement was applied vertically, while cameras recorded the positions of four reflective markers attached to the microstage. To examine the impact of camera-to-marker distance, a second session was conducted with two of the ten Vicon cameras moved to within 3000 mm of the microstage. The SV experiment employed a pair of Canon cameras (EOS 600D and EOS 4000D) and a pair of Alvium 1800 U-158 mono CS-Mount. For the Canon cameras, displacement was applied laterally (parallel to the image plane), and axially (towards the camera pair). To evaluate the influence of marker size, the experiment was conducted using big (⌀22 mm), medium (⌀14 mm), and small (⌀9 mm) markers. For Alvium cameras, displacements were applied laterally and only big markers were used. Marker images from both SV systems were extracted as ellipses using an ellipse fitting algorithm (OpenCV). Through triangulation, the 3D coordinates of each marker were identified. For each system, error analysis was performed by calculating the mean difference between the ground truth and the measured data. A theoretical approach was employed to assess the rotational capability of SV systems. This was done by applying the law of propagation of uncertainty for uncorrelated quantities using the following formula:

$$s_c^2(y) = \sum_{i=1}^{N} \left(\frac{\partial f}{\partial x_i}\right)^2 s^2(\bar{x}_i) \qquad (1)$$

where $s_c^2(y)$ denotes the uncertainty of each Euler angle, $s^2(\bar{x}_i)$ represents the standard variance of the coordinates and f denotes the relationship between the Euler angles and the coordinates. The uncertainty of total displacement (the difference between the regression line and 95% prediction interval) was used to calculate the uncertainty of the coordinates. Based on the results of the pilot study, an SV system for IFM measurement was developed (Figure 2). The system was tested in a trial run to evaluate its effectiveness in tracking marker clusters attached to the limb. Markers were attached to the lateral aspect of the shank using cable ties, with the subject moving across the cameras. The captured grayscale frames were processed using ellipse fitting to identify the 2D coordinates of the markers' centroid. Along with the calibration data, these coordinates will be vital in the reconstruction of the 3D coordinates of the markers.

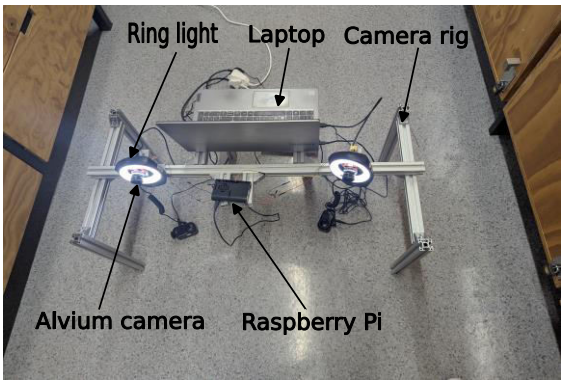

Figure 2: The developed SV system

Re*sults:* Figure 3 shows the displacement results from the Vicon, Alvium, and Canon systems. The Vicon system exhibited error values of 13.7±24.12 μm and 14.80±9.78 μm for the first and second sessions, respectively. Table 1 presents the error values for the Canon SV system across the tested marker sizes. Notably, medium markers exhibited lower error values, particularly for lateral displacements. Additionally, lateral displacements were more accurate than axial displacements, especially for medium and big markers. For the tested optical systems, Alvium cameras showed relatively low error values of 6.2±3.7 μm and 2.92±2.05 μm in the first and second sessions, respectively. Rotational uncertainties for the different Euler angles were calculated from the maximum displacement uncertainty using equation 1, and the results are shown in Table 2. Figure 4 displays

[a]28431235@sun.ac.za

a grayscale image with ellipse fitting from a trial run of the developed SV system.

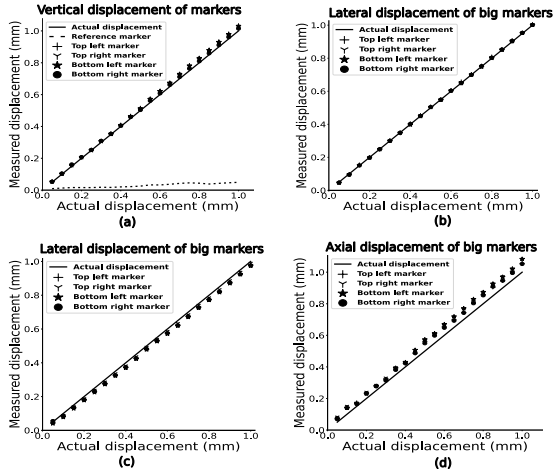

Figure 3: Measured vs total actual displacement. (a): Vicon cameras; (b): Alvium cameras; (c) and (d): Canon cameras.

Table 1: Displacement errors (mean±SD) for the canon SV system. L.disp and A.disp represent lateral and axial displacements, respectively.

	L.disp (μm)	A.disp (μm)
Big markers	20.07 ± 4.63	47.94 ± 16.76
Medium markers	6.99 ± 3.49	21.23 ± 10.79
Small markers	23.11 ± 6.16	19.72 ± 9.88

Table 2: Maximum rotational uncertainties.

	Roll (°)	Pitch (°)	Yaw (°)
Canon	0.059	0.044	0.046
Alvium	0.021	0.016	0.016
Vicon	0.026	0.019	0.019

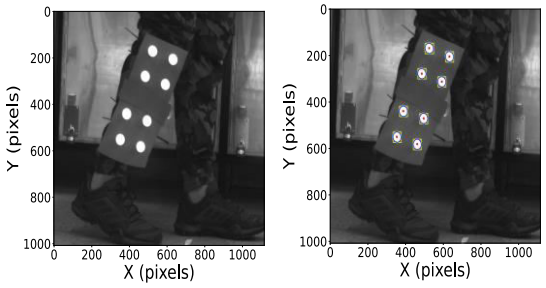

(a) Raw image **(b) Ellipse fitting**

Figure 4: Grayscale raw image with ellipse fitting

Discussion: Observations of the Vicon system revealed that the far camera setup yielded less accurate results compared to the close camera setup. Moving two of the furthest cameras within a distance of 3000 mm significantly improved the results. For the SV system, marker size and the direction of motion had a considerable effect on measurement accuracy. Medium markers exhibited more accurate results than the other tested markers. Thus, it can be deduced that there is a limit to marker size for improved measurement accuracy, with 14 mm diameter markers being the most effective among those tested. This is justifiable since large markers, despite being associated with a higher pixel count, are more prone to optical blurring and distortions. Regarding displacement direction, lateral movements yielded more accurate results than axial movements. This is quite understandable as SV systems exhibit larger depth errors than lateral errors. Since controlled lateral displacements were applied in the study, marker depth remained constant, resulting in higher lateral accuracy. However, in clinical settings, lateral movements are often accompanied by depth changes, which can reduce the measurement accuracy. Moreover, since the half pins are inserted in the medial aspect of the tibia, it is practically impossible to track the markers as the person moves across the cameras. In this way, the subject would have to move toward the cameras within a volume that falls in the field of view of both cameras. Alvium cameras have demonstrated the ability to provide more precise measurements with relatively small mean errors and uncertainty values. This supports the idea of developing the SV system for measuring IFM using these cameras. With the help of ring lights, the cameras can detect the displacement of markers. The results of ellipse fitting (Figure 4) are promising, and with proper calibration, accurate positional coordinates can be obtained through triangulation.

Conclusion: Alvium cameras demonstrated superior performance over Canon cameras in measuring micromotion in 0.05 mm increments. Furthermore, ⌀14 mm markers provided greater accuracy than ⌀22 mm and ⌀9 mm markers. Thus, an SV system using Alvium cameras and ⌀14 mm markers can effectively quantify interfragmentary movements at fracture sites.

References:

1. Claes LE, Heigele CA, Neidlinger-Wilke C, Kaspar D, Seidl W, Margevicius KJ, et al. Effects of Mechanical Factors on the Fracture Healing Process. Clinical Orthopaedics and Related Research (1976-2007). 1998 Oct;355:S132.

2. Saeidi M, Barnes SC, Berthaume MA, Holthof SR, Milandri GS, Bull AMJ, et al. Low-cost locally manufacturable unilateral imperial external fixator for low- and middle-income countries. Front Med Technol [Internet]. 2022 Nov 28 [cited 2025 Mar 27];4.

3. Duda GN, Sporrer S, Sollmann M, Hoffmann JE, Kassi JP, Khodadadyan C, et al. Interfragmentary movements in the early phase of healing in distraction and correction osteotomies stabilized with ring fixators. Langenbeck's Archives of Surgery. 2003;387:433–40.

A Numerical Study of Technical Viability of Pico-Scale Vertical-Axis Wind Turbines for Rural Electrification in Southern Africa

Temilola John Busayo [1], Tiyamike Ngonda [2,*] and Olukayode Ayodele [1]

Department of Mechanical and Mechatronic Engineering, Cape Peninsula University of Technology, Bellville, South Africa.

Abstract

This research investigates the possibility of using a pico-scale Darrieus vertical-axis wind turbine—typically featuring rotor diameters of 0.3–0.6 m and power outputs under 100 W—for electrifying the rural areas of Southern Africa through numerical simulations. The simulations are carried out using transient six degrees of freedom (6DOF) ANSYS Fluent Computational Fluid Dynamics (CFD) at wind speeds of 2–10 m/s and angles of attack (AoA) from 0° to 25°. The results indicate that at 10° AoA, the maximum power output is 34.75 W at wind speeds of 5–8 m/s, which is more than enough to meet the lighting needs in high-wind areas through power-hungry appliances. However, drag limits the overall gain.

Introduction

The continuous and uninterrupted supply of electricity is a necessity for the sustainable development of society. However, a total of 675 million people, mainly located in the rural areas of sub-Saharan Africa and South Asia, do not have access to energy, which causes a halt in the development of the regions in stagnant. In the eastern part of South Africa, approximately 15% of rural households in Eastern Cape and KwaZulu-Natal are without electricity due to the high cost of extending the electricity grid[2]. Pico-scale vertical axis wind turbines (VAWTs) with power outputs less than 100 watts (<100 W) can meet off-grid power requirements for LED lighting and charging batteries during low wind periods (3-7 m/s). They can provide an economical and compact alternative to solar photovoltaic (PV) and horizontal axis wind turbines (HAWTs) in Southern Africa's various terrains[4–6].

The strong and consistent winds of 6-8 m/s from the oceanic fronts blowing across the Coastal Western/Eastern Cape areas favor the installation of VAWTs, as opposed to the turbulent winds with a speed of 2-4 m/s experienced in inland Limpopo/Botswana, which are caused by diurnal cycles and further aggravated by dust and salt on plateaus[4,7]. VAWT's ability to capture wind from all directions gives it a distinct advantage in the location of installation.

This computational fluid dynamics (CFD) study (using ANSYS Fluent, 6DOF) examines pico-Darrieus at wind speeds of 2–10 m/s and angles of attack (AoA) of 5°–10°. 34.75 W peaks obtained for rural loads—advancing SDG 7 through site-specific hybrids, pending validation[10].

Materials and Methods Summary

The examination conducted in this paper uses quantitative methods to evaluate the potential of pico-scale wind turbines for the electrification of rural areas through the application of computational fluid dynamics (CFD) simulations in ANSYS Fluent, verifying the performance of the turbines under different wind speeds (2–10 m/s) at certain locations. The option of numerical methods rather than experiments was taken due to the great savings in costs and time[1], and this was one of the reasons why Hashem (2018), who worked on airfoil Cp for Darrieus H-rotors[2], and Liang (2017), who worked on hybrid Savonius-Darrieus KD ratios using realizable k-ε for steady/unsteady Navier-Stokes, were able to get such good results. The process utilizes a transient 6DOF for the purposes of self-stalling and torque generation.

Blade Geometry: From the various options, the NACA 2414 airfoil was picked because of its excellent L/D ratio, moderate stall, and 14% thickness-to-chord ratio which consequently enhances structural integrity during cyclic loading[3].

The blade geometry is arranged as shown in Figure 1.

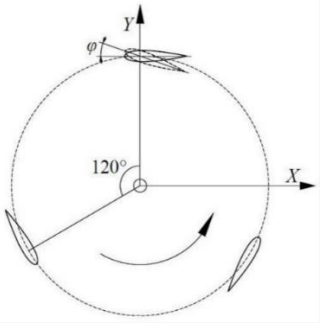

Figure 1: Three-bladed rotor configuration of a vertical axis wind turbine (VAWT) with 120° angular spacing between blades.

Computational Domain: An outer stationary rectangular domain (6 m × 0.5 m × 3 m) surrounds a rotating cylindrical inner domain (r=0.3 m) which is located at a distance of 3 m from the inlet. The inlet and outlet are provided to ensure that the flow is developed properly; the interfaces allow for the sliding of the mesh.

Setup and Solution: A transient pressure-based solver utilizing an absolute velocity and realizable k-ε turbulence model with low-Re enhanced wall treatment for air (ρ=1.225 kg/m³, μ=1.7894×10⁻⁵ Pa·s)

[a] Place the corresponding author's email address here as a "footer" in 8-point font size

was thereby setup. The following boundary conditions were used: velocity inlet (2–10 m/s, 1% turbulence, 1 m scale), pressure outlet, and no-slip moving walls for blades. The dynamic 6DOF (blade mass 0.1 kg, I=mr²) allowed for unrestrained movement[12].

Numerical Scheme: The combination of the SIMPLE algorithm with second-order implicit transient (Δt=0.05 s, 60 iterations per step, 600 total) and hybrid initialization guaranteed convergence even for unsteady flows.

Result

The performance of the pico-scale Darrieus VAWT was evaluated under different flow conditions (wind speeds of 2–10 m/s) and allowed to rotate freely to be able to capture self-starting and aerodynamics using CFD simulations with a 6DOF dynamic mesh in ANSYS Fluent. The measurements used to determine performance included torque, angular velocity (ω), power (P = Tω for single blade, 3Tω total), Cp = P_{turbine} / (0.5 ρ A V3), lift, and drag that indicated the best conditions at moderate AoA (5°–10°).

The wind speed increased the angular velocity (e.g., from 3.33 rad/s at 2 m/s 0° AoA to 24 rad/s at 10 m/s 10° AoA), and the apex was at 10° AoA before the stall that occurred at >15° dropped it (e.g., at 25°, rad/s was 19). Torque increased from very small values at wind speeds less than 4 m/s (0.0101–0.0111 Nm at 2 m/s) to the maximum at 8 m/s (0.5536 Nm at 10° AoA), with moderate AoA providing good balance between lift and drag; however, power performance reduced at higher wind speeds, peaking at 38.3 W at 9 m/s before dropping by 9.3% (3.55 W) to 34.75 W at 10 m/s—achieving only 45% of the theoretically expected 77.2 W based on cubic velocity scaling from 5 m/s—due to dominant drag effects.

Following the power output, it was 34.75 W at 10° AoA which is enough for rural low-loads. The maximum value of Cp was 0.419 (6 m/s, 10° AoA) and then it decreased more than 10° because of the separation. Drag went up with AoA/speed, while lift was at the maximum at 5°–10°.

Conclusion

The pico-scale Darrieus VAWTs CFD research implies that the South African rural areas' electrification plan can be aerodynamically feasible, with the angle of attack and wind speed of 10° and 6 to 8 m/s respectively, producing 38.29 W peaks—very suitable to load such as LED lighting (5 W) and mobile charging (5–10 W). The torque (0.5536 Nm at 8m/s) gives the VAWT the power to self-start at 3-4 m/s, which translates to a daily usage of 15.5 hours in the coastal areas, but only 4.1 hours in the plains where low wind conditions (<4 m/s) produce less than 5 W. The coastal sites in the Western and Eastern Cape are perfect for the independent operation of VAWTs; while in other regions, hybrids with PV/batteries are necessary to maintain over 80% reliability. The simulation limitations (e.g., unmodeled turbulence/friction leading to 10–20% output drops) make field validation a requirement. This study brings to light the issue of low-Re VAWTs in SSA, thus contributing towards the achievement of SDG 7 by creating solutions tailored to specific sites.

Reference

1. Ferreira et al., 2007 – Investigated the use of fine mesh elements in CFD simulations to improve resolution across sliding interfaces and turbine blade regions.
2. Meyer, E. L., & Overen, O. K. (2021). Towards a sustainable rural electrification scheme in South Africa: Analysis of the status quo. *Energy Reports*, 7, 4273-4287.
3. Omole, F. O., Olajiga, O. K., & Olatunde, T. M. (2024). Challenges and successes in rural electrification: A review of global policies and case studies. *Engineering Science & Technology Journal*, 5(3), 1031-1046.
4. Hassan, Q., Algburi, S., Sameen, A. Z., Salman, H. M., & Jaszczur, M. (2023). A review of hybrid renewable energy systems: Solar and wind-powered solutions: Challenges, opportunities, and policy implications. *Results in Engineering*, 20, 101621.
5. Hashem, I. and Mohamed, M.H., 2018. Aerodynamic performance enhancements of H-rotor Darrieus wind turbine. *Energy*, *142*, pp.531-545.
6. Tahzib et al., 2022 – Described the computational domain setup for accurate modeling of aerodynamic performance in wind turbines.
7. Al-Rawajfeh, M. A., & Gomaa, M. R. (2023). Comparison between horizontal and vertical axis wind turbine. *International Journal of Applied Power Engineering*, 12(1), 13-23.
8. Mohamed, M. H. (2016). While studies have explored AoA adjustments and hybrid Savonius-Darrieus designs for larger turbines.
9. Wasiati, S. W., Augusta, F. A., Purwanto, V. R. P., Wulandari, P., & Syahrirar, A. (2020, April). Darrieus type vertical axis wind turbine (VAWT) design. *Journal of Physics: Conference Series*, 1517(1), 012064.
10. Zou, J., Li, J., & Chen, J. (2021). Performance evaluation of a hybrid Darrieus–Savonius vertical axis wind turbine under dynamic stall conditions. *Renewable Energy*, 163, 1947-1960.
11. Nour Khlaifat et al., 2020 – Performed grid sensitivity analysis, showing convergence trends in CFD results based on mesh density.
12. Ighodaro, O., & Akhihiero, D. (2021). Modeling and performance analysis of a small horizontal axis wind turbine. *Journal of Energy Resources Technology*, 143(3), 031301.
13. Liang, X., Xu, C. and Li, T. (2017) 'A computational study of the effects of the radius ratio and attachment angle on the performance of a Darrieus-Savonius combined wind turbine', Renewable Energy, 113, pp. 329–334. doi:10.1016/j.renene.2017.05.089.

A FINITE ELEMENT APPROACH TO OPTIMISING DIGITAL IMAGE CORRELATION SPECKLE PATTERNS

N Phukubye[a], Prof. G Venter[a] & Dr. M Neaves[a]

[a] Department of Mechanical and Mechatronic Engineering, Stellenbosch University, Joubert street, Stellenbosch 7602, South Africa

This research focuses on evaluating and improving the accuracy of digital image correlation (DIC) by optimising speckle patterns. It is well established that speckle pattern morphology can significantly affect DIC measurement accuracy. In the present work, digital speckle patterns are generated and evaluated using quality assessment metrics. The patterns are deformed using a combination of pixel remapping and a smooth displacement field obtained from a finite element (FE) simulation. The undeformed and deformed image pairs are subsequently analysed using an in-house, subset-based DIC tool called SUN-DIC. The displacement field also serves as ground truth against which the DIC measurements are evaluated. Metamodels are optimised using a gradient-based algorithm to determine the optimum pattern input parameters that minimise measurement error.

Introduction: Digital image correlation (DIC) is a non-contact optical tool for full-field deformation and strain measurement, widely used in fields such as experimental mechanics, automotive design, and aerospace. The tool determines the changes on a surface by comparing images of that surface taken before and after deformation. The images are divided into subsets and corresponding subsets are found through the minimisation of grey level differences. A key aspect of DIC's accuracy is the quality of speckle patterns applied to specimen surfaces. These high-contrast, randomised patterns enable the tracking of displacements, and their quality has a direct impact on the reliability of DIC measurements [1].

Generating and evaluating digital speckle patterns: Digital speckle patterns, with dimensions of 2000 by 500 pixels, were generated using the *speckle_pattern* and *noise* libraries in Python. The image aspect ratio was selected to match that of the images from the DIC Challenge 2.0 dataset [2], which served as references during the development of the workflow pipeline. The *speckle_pattern* library was used to generate traditional speckle pattern and checkerboard images. The *noise* library was used to generate images using Perlin noise. The addition of texture functions enabled more variety, and the two libraries were used to create six classes of patterns which were further extended to 12 through application of repeated blurring and sharpening with the aim of making the existing patterns look like Turing patterns. There were 600 images per class totalling about 7200 speckle patterns. The patterns were evaluated using several pattern quality metrics: the mean intensity gradient (MIG), the E_f metric [3], the sum of square of subset intensity gradients (SSSIG), Shannon entropy, autocorrelation peak radius, the mean intensity of the second derivative (MIOSD), and the area under the power spectrum of the images. A representative image from each of the 12 pattern classes is presented in Figure 1.

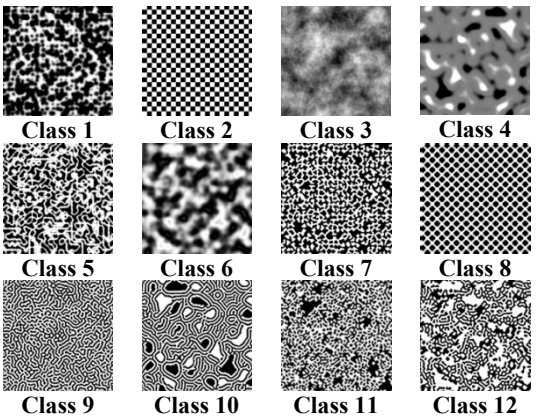

Figure 1: Different classes of digital speckle patterns were generated, analysed and deformed for the present work.

FE-based deformation: An FE simulation of a 2D plate that had the same aspect ratio as the images was created in MSC Apex. The plate was simply supported on one edge and had a load applied towards the positive x-direction on the opposite side, simulating a constant strain deformation in one direction. The locations of the nodes and their deformations were imported into a Python environment and were subsequently interpolated using radial basis functions to generate a smooth field. The field was used to remap the underlying pixels through SciPy's *map_coordinates.* Figure 2 illustrates the concept described above.

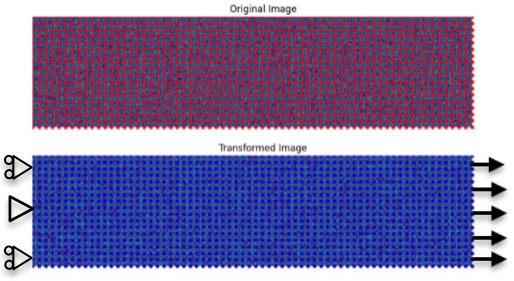

Figure 2: A discrete FE mesh was used to deform patterns.

DIC analysis: Following the image deformation process, the reference and deformed image pairs were evaluated using SUN-DIC, a subset-based DIC tool

[a] Email: 23710276@sun.ac.za

that was developed at Stellenbosch University [4]. The chosen DIC parameters are listed in Table 1

Table 1: The settings used during the DIC analysis

Parameter	Value
Subset size	33
Step size	11
Shape function	Affine
Correlation criterion	ZNSSD
Optimisation algorithm	IC-GN

Error analysis and optimisation: The DIC process yields a grid of measured subset displacements. An error analysis was conducted by interpolating the FE mesh, which contained the simulated displacements, onto the DIC grid. The resulting errors, which were also on the DIC coordinate frame, were reduced to single bias error and root mean squared error (RMSE) values corresponding to each image pair. The RMSE and bias error, along with pattern quality values that were evaluated prior to the DIC process, were used as objectives for optimisation. Support vector regression was used to generate the necessary metamodels from the data, and the metamodels were optimised using the SLSQP optimiser from SciPy. This resulted in a batch of patterns that were optimised for the different objectives across the 12 classes. Of these, the six patterns with the lowest RMSE values were selected and are listed in Table 2, including the class and objective for which they were optimised.

Table 2: The six top-ranked patterns from the optimisation process, including their classes and objectives.

Rank	Pattern class	Objective	RMSE value [pixels]
First	1	SSSIG	3.37e-4
Second	4	Bias error	3.65e-4
Third	6	RMSE	4.19e-4
Fourth	4	RMSE	4.21e-4
Fifth	1	MIG	4.42e-4
Sixth	6	Bias error	4.88e-4

The subsets for the top patterns are shown in Figure 4 with their rankings indicated underneath.

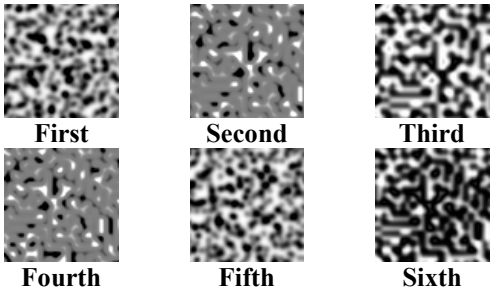

Figure 4: The top six patterns resulting from the optimisation process, ranked by RMSE

Their associated histograms are presented in Figure 5 as kernel density estimates.

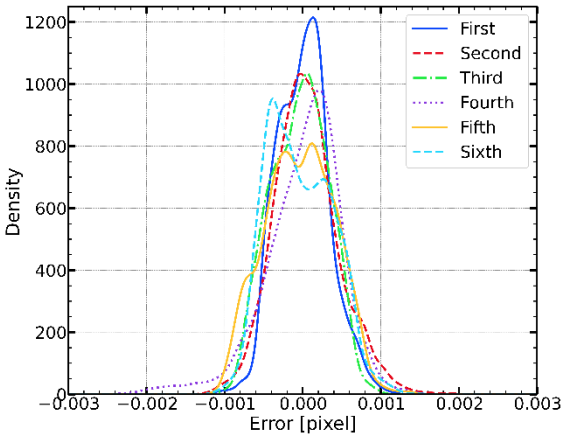

Figure 6: Kernel density estimates for the patterns with the six lowest RMSE values, from the optimised batch

Concluding remarks: Optimising patterns towards maximising gradient-based metrics produced results that were similar to the ones achieved when optimisation was specifically towards minimising the RMSE. This may be an indication that gradient-based metrics may be reliable indicators for a good speckle pattern. The top-performing patterns across different classes exhibited spatial features of similar size, suggesting a common structural characteristic associated with optimal DIC performance

References:

1. Crammond, G., Boyd, S., and Dulieu-Barton, J. Speckle pattern quality assessment for digital image correlation. Optics and Lasers in Engineering, Vol. 51, No. 12, 2013, pp. 1368–1378.

2. Reu, P. L., Blaysat, B., Andò, E., Bhattacharya, K., Couture, C., Couty, V., Deb, D., Fayad, S. S., Iadicola, M. A., Jaminion, S., and Klein, M. DIC challenge 2.0: developing images and guidelines for evaluating accuracy and resolution of 2D analyses: focus on the metrological efficiency indicator. Experimental Mechanics, Vol. 62, No. 4, 2022, pp. 639–654.

3. Hu, X., Xie, Z., and Liu, F. Assessment of speckle pattern quality in digital image correlation from the perspective of mean bias error. Measurement, Vol. 173, 2021, p. 108618.

4. Venter, G. SUN-DIC. GitHub, 2024. Available at: https://github.com/gventer/SUN-DIC [Accessed: 21 September 2025].

DEVELOPMENT AND VALIDATION OF HOMOGENISED 2D VORONOI LATTICES

IJH Howlett & M Venter & J van der Merwe

Department of Mechanical and Mechatronic Engineering, Stellenbosch University, Stellenbosch, South Africa

***Aim & Objectives**:* The aim of this study is to develop a computational framework for homogenizing two-dimensional (2D) Voronoi lattices. This forms the foundation for future three-dimensional (3D) lattice homogenization, supporting the design of functionally graded synthetic bone implants. See Figure 1 for the outline of the steps to develop the computational framework.

The objectives of this study are to:

- Review and evaluate existing numerical homogenization techniques for lattice structures.
- Generate 2D Voronoi lattices as a learning exercise in preparation for the provided 3D generation algorithm.
- Develop and implement a homogenization methodology specifically for 2D Voronoi lattices.
- Validate the methodology through finite element simulations on 2D pilot models.
- Compute the effective material properties of 2D Voronoi lattices using the validated framework

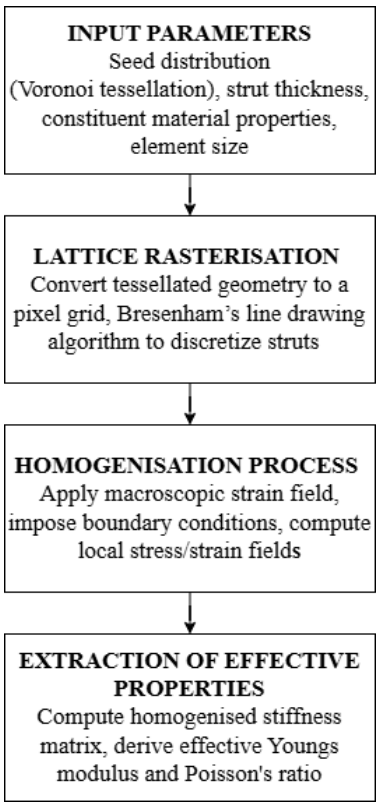

Figure 1 Flowchart outlining the steps to develop the computational framework

***Introduction**:* Many South African orthopaedic patients suffer from critically sized bone defects (CSBDs) due to trauma, infection, or malignancy[1]. These defects, typically >1–2 cm or >50% of the bone circumference[2] exceeding the bone's regenerative capacity and can lead to infection, disability, or amputation[3].

Current treatments include autograft, allograft and synthetic implants[4]. Synthetic implants, particularly additively manufactured (AM) porous lattices, offer tuneable material properties to replicate surrounding bone properties. Significant research has been done which focuses on improved osseointegration, bone regrowth and reduced stress shielding.

Advances in AM has enabled the fabrication of highly complex structures, enhancing the biomimicry of synthetic implant architectures and improving implant design[5]. These lattices are often designed to replicate the surrounding bone's material characteristics. For example, matching the stiffness of the cancellous and trabecular bone, of 0.1-4.5 GPa and 10-40 GPa respectively[6]. To achieve this, design parameters such as the lattice architecture, porosity, and structure are adjusted[7]. Current methods for generating Voronoi lattices typically adjust the strut thickness and the seed distribution as the input parameters, followed by validating their effective material characteristics using homogenisation algorithms, experimental characterisation, or numerical simulations. Homogenised material characteristics are the effective material properties of a heterogeneous structure, such as a lattice, where the macroscale equivalent properties describe the overall behaviour. These properties are essential for characterising lattices and for meaningful comparison to bone scaffolds.

To better replicate the varying mechanical properties of bone, functional grading can be introduced by either layered or continuous gradient design[7]. Layered gradient design involves changing the lattice parameters in a step wise manner between layers[7]. However, with non-stochastic lattices, such as body-centred cubic, diamond or other polyhedron structures, this can lead to stress concentrations at the strut connections[8]. Continuous gradient designs avoid these problems by gradually changing the properties, and Voronoi lattices are particularly well suited as the density is controlled by the seeding distribution.

23675985@sun.ac.za

Functionally graded Voronoi lattices have successfully replicated cortical bone properties across varying porosities[9] and improved stability and stress shielding compared to uniform lattices[10]. Therefore, Voronoi lattices will be the primary architecture investigated in this project.

Although a few studies have fitted homogenized lattice behaviour to design curves that guide parameter selection for specific mechanical targets, a research gap remains for Voronoi lattices [11]. This research addresses this gap by proposing a computational and experimental framework for developing and validating homogenisation algorithms for 2D Voronoi lattices.

Description of methodology and experimental techniques: The 2D homogenisation code will be developed as a pilot study for the 3D homogenisation framework, which will be explored in a later study. To achieve this, the numerical homogenisation calculations outlined in Cook (2002)[12] and Andreassen & Andreassen (2014)[13] will be implemented to determine the effective material properties and the representative volume element (RVE) of porous plates and lattices. The framework will then be validated through finite element simulations (FEM) of the same samples under identical boundary conditions, conducted using MSC Apex and ANSYS Mechanical. The homogenisation code will first be tested on simpler structures to ensure reliability and to build confidence for its application to more complex architectures. Validation will include low-porosity plates (10% porosity), as well as RVEs of these plates, including four-hole samples as defined in Cook (2002)[12]. A comparison between the FEA results and the homogenisation code predictions will determine whether the code can accurately homogenise porous structures and calculate effective material properties. Once validated, the approach will be extended to more complex structures such as Voronoi lattices, to ensure the frameworks robustness and generalizability.

Expected Results: This study is expected to validate 2D homogenisation code for calculating the effective material properties of porous plates and lattices. Additionally, it will serve as a learning exercise for Voronoi lattice generation. The validated 2D framework will form the foundation for homogenising 3D Voronoi lattices, using a provide Voronoi generation algorithm. This framework will aid the design of patient-specific implants with improved biomechanical compatibility.

Conclusion: This study aims to develop a computationally homogenised framework for 2D Voronoi lattices and porous plates. This research will serve as the basis for further research in the homogenisation of 3D Voronoi lattices.

References:

1. Song X, Xu L, Zhang W. Biomimetic synthesis and optimization of extracellular vesicles for bone regeneration. Journal of Controlled Release. 2023;355:18-41.
2. Schemitsch EH. Size Matters: Defining Critical in Bone Defect Size! Journal of Orthopaedic Trauma. 2017;31:S20-S2.
3. Verrier S, Alini M, Alsberg E, Buchman SR, Kelly D, Laschke MW, et al. Tissue engineering and regenerative approaches to improving the healing of large bone defects. European Cells & Materials. 2016;32:87-110.
4. Vidal L, Kampleitner C, Brennan MA, Hoornaert A, Layrolle P. Reconstruction of Large Skeletal Defects: Current Clinical Therapeutic Strategies and Future Directions Using 3D Printing. Frontiers in Bioengineering and Biotechnology. 2020;8:61.
5. du Plessis A, Broeckhoven C, Yadroitsava I, Yadroitsev I, Hands CH, Kunju R, et al. Beautiful and Functional: A Review of Biomimetic Design in Additive Manufacturing. Additive Manufacturing. 2019;27:408-27.
6. Wu C, Luo J, Zhong J, Xu Y, Wan B, Huang W, et al. Topology optimisation for design and additive manufacturing of functionally graded lattice structures using derivative-aware machine learning algorithms. Additive Manufacturing. 2023;78.
7. Chen H, Han Q, Wang C, Liu Y, Chen B, Wang J. Porous Scaffold Design for Additive Manufacturing in Orthopedics: A Review. Frontiers in Bioengineering and Biotechnology. 2020;8:609.
8. Mirzaali MJ, Nava AH, Gunashekar D, Nouri-Goushki M, Doubrovski EL, Zadpoor AA. Fracture Behavior of Bio-Inspired Functionally Graded Soft-Hard Composites Made by Multi-Material 3D Printing: The Case of Colinear Cracks. Materials (Basel). 2019;12(17).
9. Wang G, Shen L, Zhao J, Liang H, Xie D, Tian Z, et al. Design and Compressive Behavior of Controllable Irregular Porous Scaffolds: Based on Voronoi-Tessellation and for Additive Manufacturing. ACS Biomater Sci Eng. 2018;4(2):719-27.
10. Zhao H, Han Y, Pan C, Yang D, Wang H, Wang T, et al. Design and Mechanical Properties Verification of Gradient Voronoi Scaffold for Bone Tissue Engineering. Micromachines (Basel). 2021;12(6).
11. Barba D, Alabort E, Reed RC. Synthetic bone: Design by additive manufacturing. Acta Biomater. 2019;97:637-56.
12. Cook RD. Concepts and applications of finite element analysis. 4th ed. New York, N.Y: Wiley; 2002.
13. Andreassen E, Andreasen CS. How to determine composite material properties using numerical homogenization. Computational Materials Science. 2014;83:488-95.

23675985@sun.ac.za

One-Dimensional Model of an Electric Commercial Vehicle Drivetrain for a Specified Service Route

Tiaan Bezuidenhout, Prof. Gerhard Venter & Prof. Rong-Jie Wang

Department of Engineering, Stellenbosch University, Stellenbosch, South Africa

Introduction: The electric automotive sector has been steadily increasing in size. Due, in part, to environmental concerns stemming from internal combustion greenhouse gas emissions. This trend has also been observed in the commercial vehicle industry. System-level modelling with service route integration can aid in the design and component selection process for electric commercial vehicles.

The purpose of this work is the documentation of the development process of a 1-D electric vehicle modelling or simulation protocol. This method utilises Simcenter AMESim software to model the behaviour of a vehicle on a specified service route. Part of this analysis is a simplified method for estimating the efficiency-capability curve of a permanent magnet synchronous motor (PMSM) drivetrain as well as a method for estimating the slope at various points along the service route. Prospects for this project include drivetrain parameter optimisation, which can aid in component selection and design. Some sections of the project are still ongoing and have yet to be completed. These are mentioned where applicable.

Background: The observation of negative environmental effects caused by greenhouse gas emissions[1] have made electric vehicles a preferable alternative to internal combustion powered vehicles. This change is also slated to take place in the road freight industry[2], which is a significant contributor to greenhouse gas emissions[3].

Some simulation methods are present in literature[4,5,6]. However, many do not include route parameter measurement and implementation, particularly slope measurement. Thus, this work has an emphasis on the modelling of environmental conditions.

Simulation Method: Proposed software to be used is Simcenter AMESim, due to the multi-domain capabilities of the software and the readily available libraries that allow for component modelling. This software uses bond graph modelling to simplify simulation using energy flow[7]. In this method, each major component is modelled individually, with the simulation calculating energy flow between elements. The major components are the battery, motor, gearbox and an inertia model of the vehicle.

Route Parameter Estimation: A requirement for the simulation protocol is a method for determining the slope of the road surface, as this influences the power consumption of the vehicle. The derivative of vehicle altitude, with respect to the distance travelled, along service routes can be used to estimate the road slope at various points.

An alternative to this method is presented, where the road slope is obtained by determining the directional gradient from a Digital Elevation Model (DEM). Initial comparisons between these measurements were conducted. An example of a tested route from the validation dataset is shown in Figure 1.

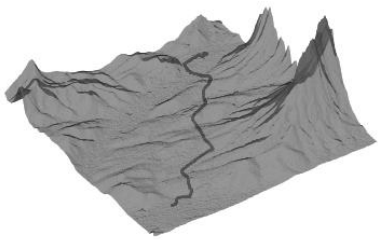

Figure 1: Example of route from validation dataset

Electric Motor modelling: The goal of the motor model is to determine the efficiency of the motor at various points on the motor capability curve, representing the motor load throughout the driving cycle. A popular method for determining the efficiency-capability curve is the use of finite-element (FE) analysis with software packages, such as Ansys MotorCAD. However, detailed information about the motor construction and operation is required to conduct this analysis.

Other efficiency estimation methods, which require relatively fewer input parameters, are also considered[8]. These make use of no-load, open-circuit and short-circuit tests. These methods have shown to be less accurate than FE analysis.

Sufficient information has been obtained to create an FE model of the electric motor used in the validation dataset and, thus, determine the motor efficiency directly. Using measured equivalent circuit parameters, the rotor and stator geometry can be optimised for the simulated parameters to match the physical measurements. This will allow for the comparison of FE simulation with other estimation methods.

Battery Modelling: The following sections have been partially completed or are planned to be completed later.

24814555@sun.ac.za

The behaviour of the battery under charging and discharging cycles is to be described in the simulation protocol. The method currently under consideration is the Tremblay battery model[9], shown in Figure 2. This represents an equivalent-circuit battery model and was modified from the Shepherd model, to supress algebraic loops in closed-loop simulations. Other methods such as Kalman-Filter estimation are also under consideration.

These are used in parallel with provided discharge curves and battery nameplate information, to simulate the battery behaviour.

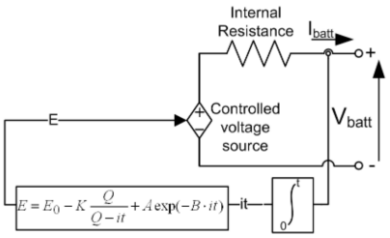

Figure 2: Tremblay battery model

Here, Q is the nominal battery capacity in Ah and K, A and B are constants used to fit the estimated discharge curve to discharge test data. These can be obtained by testing or are provided by the battery manufacturer.

Vehicle Inertia Modelling: The proposed modelling method for the vehicle is an inertia model. This model simulates the behaviour of the vehicle, approximated to a mass. The following forces influence the motion of the vehicle, following the provided equations:

- Wind resistance: $\frac{1}{2}\rho A_f C_d V^2$
- Rolling resistance: $C_{RR} mg\cos\alpha$
- Road slope : $mg\sin\alpha$

Where C_d, and C_{RR} are wind and rolling resistance coefficients. A_f, V and m are vehicle frontal area, velocity and mass respectively. α is the road slope.

Validation dataset: To determine the validity of the simulation model, it will be compared against physical measurement of an electric vehicle running along a service route. Measurements that were taken from a retrofitted electric minibus are planned to be used for this purpose.

Implementation: Upon completing the model validation phase of the project, the method is then applied to one or more other vehicles. This is to gauge the value and applicability of the simulation in variable circumstances.

Larger commercial vehicles and especially ones with ancillary systems, are slated to be used in the final application. These consume additional power from the battery for traction and accessory mechanisms. These can be additional motors or hydraulic pumps.

Optimisation: After implementing the model on different vehicles, a possible use case would be to optimise some vehicle parameters. The objective of this optimisation would be to maximise the efficiency or performance of the vehicle. This can include the optimisation battery pack architecture and chemistry to best suit the operational requirements. These relate to the service route requirements and duties of ancillary systems. These optimisations are planned to be conducted, and their effects are to be reported on to assess their viability in their application.

Acknowledgements: I would like to thank the Stellenbosch Engineering Media Lab for providing the test data of the retrofitted electric minibus.

References

1. Martins, F; Felgueiras, C; Smitkova, M; Caetano, 1. N. *Analysis of Fossil Fuel Energy Consumption and Environmental Impacts in European Countries*. Energies, Vol. 12, No. 6, 2019, pp. 964.

2. European Commission. *Regulation (eu) 2024/1610 of the European parliament an of the council*. Official journal of the European union. Series L. 2024.

3. Ntuli, M.N. Andrew, C. Eloka-Eboka, Festus Maina Mwangi, D.R.E.E. and Dioha, M.O. *Energy sustainability and carbon dioxide emissions mitigation options for South Africa's road transport sector*. Nature Materials, vol. 48. 2024.

4. Miri, I., Fotouhi, A. and Ewin, N. *Electric vehicle energy consumption modelling and estimation—a case study*. International Journal of Energy Research, vol. 45, no. 1, 2021 , pp. 501–520.

5. Bramerdorfer, G., Marth, E. *Computationally Efficient System-Level Evaluation of Battery Electric Vehicles.* IEEE Workshop on Electrical Machines Design, Control and Diagnosis, 2021, pp 311-317.

6. Husain, I., Islam, M. S., *Design, Modelling and Simulation of an Electric Vehicle System.* SAE Transactions, vol.108, sec. 6, 1999, pp 2168-2176.

7. Broenink, J.F. *Introduction to physical systems modelling with bond graphs*. SiE whitebook on simulation methodologies, vol. 31, no. 2. 1999.

8. Kahourzade, S. et al. *Estimation of PM Machine Efficiency Maps from Limited Data*. IEEE Transactions on Industry Applications, 56(3), 2020, pp. 2612-2621.

9. Tremblay, O., Dessaint, L.A. and Dekkiche, A.I. *A generic battery model for the dynamic simulation of hybrid electric vehicles*. IEEE Vehicle Power and Propulsion Conference, 2007, pp. 284–289.

24814555@sun.ac.za

FINITE ELEMENT MODELLING OF TEMPERATURE FIELD DURING SOLIDIFICATION OF HYPER-PERITECTIC STEEL ALLOYS USING ADAPTIVE MESH REFINEMENT

B. M. S. Obanda, M. P. Venter, N. Mahomed
Department of Mechanical and Mechatronic Engineering, Stellenbosch University, Stellenbosch, South Africa

Abstract

This research aims to develop a finite element computational model to simulate the temperature field in the mushy zone during equiaxed solidification of hyper-peritectic steel alloys. The governing equation is a quasi-steady-state heat transfer equation, defined over a two-dimensional mould-cavity geometry, that accounts for heat conduction and temperature-and composition-dependent latent heat of fusion during solidification. The model is coupled to a micro-segregation model to account for the evolution of phase volume fractions during the solidification process. The three-stage micro-segregation model incorporates the alloy-specific peritectic reaction constant to solve the extent of phase transformations during the isothermal peritectic reaction stage, assuming complete mixing of solute in the liquid phase The Galerkin Method is used to formulate the finite element discretisation problem, and the resulting nonlinear algebraic system is solved using Newton–Raphson iteration. To resolve steep thermal gradients in the mushy zone, adaptive mesh refinement is incorporated into the computational framework. The simulations are implemented in a Python environment and validated against experimental data

Introduction and Aim

Solidification of metals is a primary method employed in the foundry industry to produce high-quality castings with complex geometries[1]. Peritectic steel alloys, renowned for their exceptional material properties, including high strength, excellent toughness, and superior weldability, are widely utilised in the manufacture of critical components across industries such as aerospace, automotive, and heavy machinery, where structural integrity and performance under extreme conditions are essential .[2,3,4]

Moreover, hyper-peritectic steel alloys are of interest in sandcasting due to their lower volumetric shrinkage, which results from inter-dendritic feeding that persists below the peritectic temperature.[5]

Hence, understanding the solidification behaviour of hyper-peritectic steel is important for optimising manufacturing processes, reducing defects, improving quality, and developing new steel alloys with tailored properties for specific applications.[6] To this end, an accurate model of the temperature field can enhance the design of casting processes for hyper-peritectic steel products. Currently, there is no computational model in the literature that adequately captures the isothermal reaction for hyper-peritectic steel alloys.

This research therefore aims to solve the temperature field in the mushy zone during equiaxed solidification of hyper-peritectic steel alloys, using a modified three-stage micro-segregation model to capture the isothermal reaction and to account for the alloy-specific peritectic reaction.

Methodology

The model is based on the quasi-steady state of the heat transfer equation within the domain Ω consisting of the subdomains: mould, solid, mushy zone, and liquid. The governing equation incorporates temperature-dependent material properties. A suitable micro-segregation model was developed to capture the isothermal peritectic reaction based on a modified Lever Rule that accounts for the peritectic reaction constant. The weak formulation of the partial differential equation is constructed in the Sobolev space $H^1(\Omega)$, and the Galerkin approximation is derived using finite-dimensional subspaces to construct a discrete nonlinear system. The analysis of the existence and uniqueness of a weak solution was examined along with the convergence of the approximation solution. The full code for solving the weak form of the quasi-steady heat transfer equation is implemented in a Python environment, where the geometry and meshing are generated with the Gmsh Python Application Programming Interface and the mesh data are read through meshio. The temperature field is discretised using bilinear four-node isoparametric quadrilateral elements with 2×2 Gauss quadrature and is advanced in pseudo-time by a fully implicit Backward Euler scheme ($\theta = 1$). The nonlinear finite element system is solved with the Newton-Raphson method, and all numerical calculations are performed in NumPy. The global matrices are assembled in LIL and converted to CSR for the linear solve; for current sizes we use SciPy

(spsolve), while for larger systems it is planned to switch to SciPy GMRES with pyamg AMG. The boundary conditions include Dirichlet and radiation. The Zienkiewicz-Zhu error estimator is used to refine the Gmsh (background mesh) size field to capture high temperature gradients in the mushy zone. The resulting numerical solution is tested against experimental data.

Results

The results of the research are ongoing; it is expected that the theoretical understanding of solidification in peritectic steel alloy systems will provide practical tools and insights for producing high-quality steel alloys. It allows for the investigation of various 'what-if' scenarios in alloy solidification without the need for extensive experimental setups.

References

1.Eshraghi M. *Numerical Simulation of Solidification Processes.* Metals, vol.13, no.7, 2023, pp.1-2.

2.Luo S et al. *In Situ Observation and Phase-Field Modelling of Peritectic Solidification of Low-Carbon Steel.* Metallurgical and Materials Transactions A, vol.51, no.2, 2020, pp.767-777.

3.Ai et al. *Effect Mechanism of α-Ferrite Sustained Precipitation on High-Temperature Properties in Continuous Casting for Peritectic Steel*. Metals , vol. 14, no. 3, 2024, pp.1-14.

4.Karma A. *Model of Banding in Diffusive and Convective Regimes during Directional Solidification of Peritectic Systems.* Metallurgical and Materials Transactions A, vol. 29, 1998, pp. 1457-1570.

5.Mahomed N. et al. *A numerical time integration procedure for secondary dendrite arm spacing in hyper-peritectic steel alloys*. International Journal of Metalcasting, 2024, pp.1-17.

6.Azizi G. et al. *Review of Peritectic Solidification Mechanisms and Effects in Steel Casting.* Metallurgical and Materials Transactions B, vol.51, no.5, 2020, pp.1875-1903.

AERODYNAMIC OPTIMIZATION OF AN ELECTRIC VEHICLE FOR ENERGY EFFICIENCY

L. Mushavhanamadi[a] & A. Rugbani[b]

[a] Department of Mechanical Engineering, Cape Peninsula University of Technology, Pretoria, South Africa
[b] Department of Mechanical Engineering, Cape Peninsula University of Technology, Cape Town, South Africa

Abstract: Electric vehicles (EVs) offer a significant contribution toward the advancement of sustainable transportation as they are widely recognised for reducing the emission of Greenhouse gases (GHGs). However, their efficiency is heavily determined by aerodynamic performance. This study focuses on aerodynamic optimization of EV body design to reduce drag and enhance energy efficiency. Current literature has limited research on the whole EV body Computational Fluid Design (CFD) simulation and has focused on isolation rather than as a system level approach. Meanwhile, without the link of the underbody airflow, where drag still matters but behaves differently, the areas of high pressure and separation, it is uncertain as to which area of the vehicle requires prioritisation in shape refinement. Iterations on the EV geometry refinement using CFD simulations will be conducted to determine an admissible coefficient of drag (Cd) under a variety of operating conditions. The EV body shape to be optimized aims to achieve a drag reduction compared to the previous experimental results from literature, which will result in significant improvements in range and performance. The expected outcomes include validated CFD models, quantified improvements in aerodynamic performance, and practical design recommendations for future EV development with longer range and lower energy consumption.

Keywords: electric vehicle, energy efficiency, coefficient of drag, aerodynamics optimization, computational fluid dynamics

Introduction: The modern automotive technologies have demonstrated a gradual shift from the Internal Combustion Engine (ICE) to EV as zero emission alternatives driven by regulations like the Paris Agreement, which mandates a 43% decline in GHG by 2030[1]. This transition has placed EVs at the forefront of sustainable transportation, maximizing the driving range for EVs. A key factor for consumer adoption, aerodynamic drag, which accounts for 60% of total resistance, and the current limitations of battery technology make EVs susceptible to energy loss[2].

The aerodynamic efficiency (L/D ratio) remains a considerable factor in determining overall EV performance, as the EV's shape is significantly affected by pressure drag at speeds of more than 80 km/h[3]. This research deals with the main causes of EV aerodynamic drag, leveraging the underbody attachments, wheel housing, and recommendations to minimize the impacts of flow separation, enhance the energy efficiency for improved range benchmarking from CFD simulation based on current literature.

Model development: The aerodynamically optimized EV geometry will be developed. The external aerodynamic CFD simulation and optimization will be achieved as illustrated in Figure 1, a CAD model imported into ANSYS for the CFD simulation, solving the Navier-Stokes equations. The turbulence model choice will be the viscous realizable k-ε model with enhanced wall treatment[3].

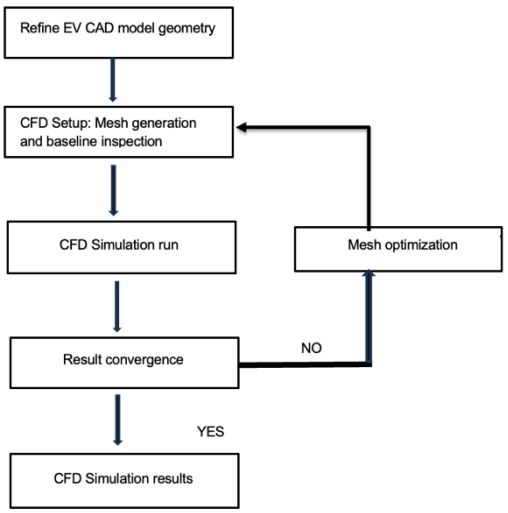

Figure 1: Graphical representation of the CFD simulation analysis process.

Model Validation: The quantitative results (Cd, Cl, and drag force) will be analysed using MATLAB. Statistical comparison and trend identification of numerical outputs will be arranged graphically to determine the most efficient drag performance of EVs, including the underbody design.

Results: In the absence of actual prototypes, ANSYS software is chosen to run CFD simulations. The selection was based on the software's ability during pre-processing, simulation capabilities, which rely on the Navier-Stokes and continuity equations, and the ability to set up multi-region complex problems[3]. Table 1 Simulation parameter setting of different aerodynamic theories validated from published studies to evaluate the EV aerodynamic performance.

[a] 214005372@mycput.ac.za

Table 1: CFD Simulation parameters[4]

Configuration	Drag Coefficient
Base	0.158
5^0	0.151
7^0	0.154
9^0	0.155
11^0	0.155
13^0	0.156

Conclusion: This research addresses the current EV adoption limitations, which focus on the aerodynamic potential. Although advancements in current design have been made, it's adoption has also been hindered across the world by challenges related to energy efficiency, contributing to the charging infrastructure gaps, battery regenerative charging systems, and range constraints. The methodological strategy focuses on reducing aerodynamic drag using CFD simulation, which often upholds the crash safety regulations, employs a multi-region optimization that could contribute to measurable performance improvements.

References:

1. IEA, Africa Energy Outlook 2023,» International Energy Agency, 2019.
Available: http://www.iea.org/reports/africa-energy-outlook-2023.
Accessed [23 September 2025].
2. Xia, Z. and Huang, M., 2024. Optimizing the Aerodynamic Efficiency of Electric Vehicles via Streamlined Design: A Computational Fluid Dynamics Approach. *International Journal of Heat & Technology*, *42*(3).http://dx.doi.org/10.18280/ijht.420315.
3. Tran, J., Fukami, K., Inada, K., Umehara, D., Ono, Y., Ogawa, K. and Taira, K., 2024. Aerodynamics-guided machine learning for design optimization of electric vehicles. *Communications Engineering*, *3*(1), p.174.Available at: https://doi.org/10.1038/s44172-024-00322-0.
4. Piratla, S., 2023. Evaluating the aerodynamics of different passenger vehicle configurations. *Authorea Preprints*., doi: 10.36227/techrxiv.24139254.

EFFECTS OF VARYING CUBOID CHARGES ASPECT RATIO ON THE BLAST WAVE PROPAGATION IN FREE AIR

T. Selialia, S. Chung Kim Yuen & S. Gabriel

Blast Impact and Survivability Research Unit (BISRU), Department of Mechanical Engineering, University of Cape Town, Rondebosch, South Africa

Blast wave propagation of cuboid-shaped explosive charges with varying aspect ratios remains underexplored, unlike blast wave propagation of spherical and cylindrical-shaped explosive charges. This paper presents the results of an experimental study investigating blast wave propagation of cuboid-shaped charges of 10 g plastic explosive (PE4) with varying aspect ratios (L:W:H) of 1:1:1, 2:1:1, and 3:1:1 detonated in free air. The blast wave pressure-time histories were measured at four scaled distances (Z) of 1.5 m/kg$^{1/3}$, 1.8 m/kg$^{1/3}$, 2.5 m/kg$^{1/3}$ and 3.0 m/kg$^{1/3}$ in the directions normal to the faces of the charges. The results showed the effect of aspect ratio on the peak overpressure of the blast wave.

Introduction: Explosions, whether accidental or intentional, frequently occur worldwide and result in severe consequences, including significant damage to infrastructure[1]. The response of the infrastructure (or objects) to explosions can be estimated if blast wave parameters such as arrival time, peak overpressure, impulse, and duration are known[2]. The study of explosions has been conducted using explosive charges with different shapes[3]. Whilst there is significant literature on studies conducted using spherical[1] and cylindrical[3] charges, the same cannot be stated for cuboid-shaped explosive charges[4]. Cuboid charges are increasingly becoming relevant in scenarios involving improvised explosive devices (IEDs), where charges are arranged or packed in containers such as briefcases, suitcases or boxes[5]. It is therefore crucial to understand the propagation of blast waves from cuboid-shaped explosive charges to support the development of predictive tools and help mitigate the severe consequences associated with explosions. This paper presents an experimental study of 10 g PE4 cuboid charges to determine the effects of varying aspect ratio on the propagating blast wave in free air.

Methodology: Shaped in 3D printed moulds, 10 g PE4 cuboid explosive charges with aspect ratios (AR) of length:width:height = 1:1:1, 2:1:1, and 3:1:1 were centrally detonated to create the blast wave. Piezoelectric flush-mount pressure gauges with varying operating pressures ranging from 344.7 kPa to 1379 kPa were used to measure the pressure-time histories of the blast wave at different scaled distances. The pressure gauges were positioned at radial distances of 343 mm, 412 mm, 572 mm, and 687 mm from the detonation point as shown in Figure 1. The corresponding scaled distances (Z) of 1.5 m/kg$^{1/3}$, 1.8 m/kg$^{1/3}$, 2.5 m/kg$^{1/3}$, and 3.0 m/kg$^{1/3}$ were determined using Equation 1 where R represents the radial distance in metres and W represents the trinitrotoluene (TNT) equivalent weight of PE4 in kilogram.

$$Z = \frac{R}{\sqrt[3]{W}} \tag{1}$$

The pressure gauges were mounted inside hollow steel rods that were screwed onto a steel plate measuring 1100 mm x 1100 mm x 12 mm. The diaphragms of the pressure gauges were at a height of 343 mm, measured from the steel plate to match the height of burst of the explosive charge as shown in Figure 2.

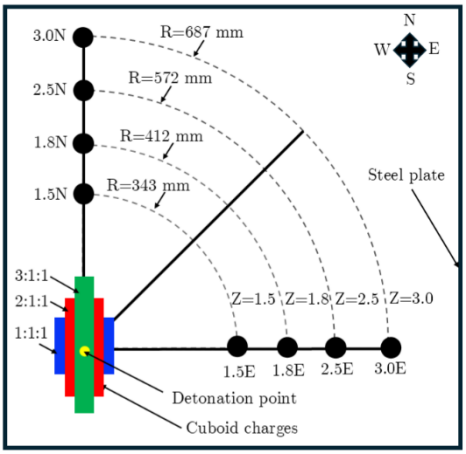

Figure 1: Photograph of the experiment setup

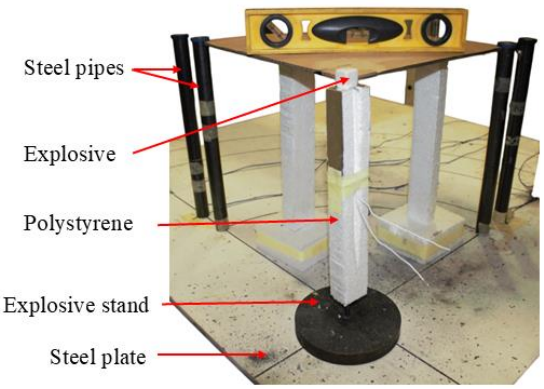

Figure 2: Experiment setup pressure gauges locations

Results: Figure 3 shows the typical pressure-time histories of the blast wave in the East and North direction at scaled distances of Z = 1.5 m/kg$^{1/3}$ and 2.5 m/kg$^{1/3}$. Generally, a typical Friedlander pressure

SLLTUM001@myuct.ac.za

waveform[6] was observed, whereby at the arrival time of the blast wave, the pressure instantaneously rose (overpressure) before decaying exponentially. At closer scaled distances to the detonation point (Z = 1.5 m/kg$^{1/3}$), multiple peak overpressures were observed, compared to a smoother pressure rise at farther scaled distances (Z = 2.5 m/kg$^{1/3}$). The peak overpressure obtained from the experimental pressure-time histories are summarised in Table 1. In each direction normal to the surface of the cuboid charge (East and North), the peak overpressure decreased with increasing scaled distance in free air as expected.

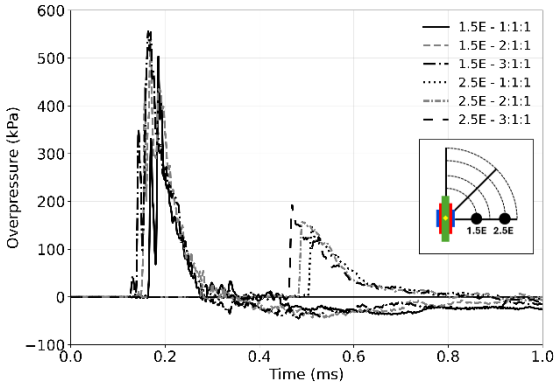

(a)

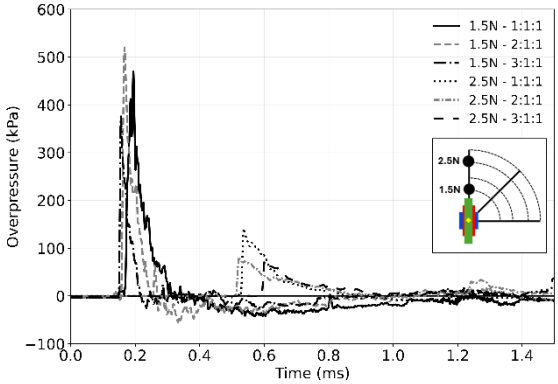

(b)

Figure 3: Pressure-time histories in the (a) East and (b) North directions

Table 1: Peak overpressure (kPa) in the East and North directions

		Z (m/kg$^{1/3}$)			
Direction	**AR**	**1.5**	**1.8**	**2.5**	**2.5**
East(E)	1:1:1	590	392	147	88
	2:1:1	548	487	159	107
	3:1:1	648	481	197	126
North(N)	1:1:1	559	366	135	86
	2:1:1	514	288	79	55
	3:1:1	392	212	74	59

Discussion: When the mass (10 g) and square cross-section (W = H) of the charges were kept constant and the aspect ratio was increased (Length, L increased), the cuboid charges contracted along the East direction and elongated along the North direction. As the aspect ratio increased, the surface areas normal to the East direction also increased, and the peak overpressure generally increased. In contrast, as the aspect ratio increased, the surface area normal to the North direction decreased, and the peak overpressure also reduced. The increase and decrease in peak overpressure in the East and North directions were likely associated with the directional energy released by the explosive charges due to the smaller and larger surface area of the charge in that direction, as observed by Shi et al. [7].

Conclusion: Small-scale explosion experiments were conducted in free air with cuboid charges of varying aspect ratios. The shape of the cuboid charge (aspect ratio) was found to influence the peak overpressure of the blast waves produced from the surface (normal to East direction) and end (normal to North direction) of the charges.

References:

1. E. M. Mendham, S. E. Rigby, D. G. Farrimond, A. Tyas, and G. Pezzola, "Far field blast parameters from cuboidal charges," *The 4th International Conference on Structural Safety Under Fire & Blast Loading (CONFAB 2024)*, September 2024.
2. A. Filice, M. Mynarz, and R. Zinno, "Experimental and empirical study for prediction of blast loads," *Applied Sciences*, vol. 12, no. 5, 2022.
3. Y. Shi, N. Wang, J. Cui, C. Li, and X. Zhang, "Experimental and numerical investigation of charge shape effect on blast load induced by near-field explosions," *Process Safety and Environmental Protection*, vol. 165, pp. 266-277, 2022.
4. L. Gan, Z. Zong, Z. Chen, T. Wu, J. Lin, and M. Li, "Differences in responses of square steel plates exposed to blast loads generated by cubic and spherical explosives," *Thin-Walled Structures*, vol. 182, p. 110332, 2023.
5. E. Seyhan, "The forensic imaging techniques of portable x-ray units used in render safe operations of improvised explosive devices (IEDs)," *The Egyptian Journal of Radiology and Nuclear Medicine*, vol. 44, no. 4, pp. 845–851, 2013.
6. P. Shirbhate and M. Goel, "A critical review of blast wave parameters and approaches for blast load mitigation," *Archives of Computational Methods in Engineering*, vol. 28, 2020.
7. G. Shi, Z. Huang, X. Jia, and X. Zu, "The effect of cuboid explosive shape on the dimension of damaged area in masonry walls subjected to contact explosions," *International Journal of Protective Structures*, vol. 0, no. 0, 2024.

COMMERCIAL ELECTRIC VEHICLE THERMAL MANAGEMENT SYSTEM MODELLING AND TESTING

JC Mostert[a] & MTF Owen[b] & G Venter[c]

[a] Department of Mechanical Engineering, Stellenbosch University, Stellenbosch, South Africa
[b] Department of Mechanical Engineering, Thermofluids Research Group, Stellenbosch, South Africa
[c] Department of Mechanical Engineering, Material, Optimization and Design Research Group, Stellenbosch, South Africa

Introduction: Climate change remains an urgent global challenge, driving efforts to reduce greenhouse gas emissions. In 2017, the global warming temperature reached approximately 1˚C above pre-industrial levels and has been increasing at a rate of about 0.2˚C per decade. The Paris Agreement aims to limit the increase in global average temperature to 1.5˚C above pre-industrial levels by 2030[1]. Within this context, the transport sector is the fourth largest emitter, with road transport contributing the largest share[2]. Electrification of transport is a key mitigation strategy. Battery electric vehicles (EV) offer zero tailpipe emissions and significantly higher Tank-to-Wheel efficiencies (50–80%) compared to internal combustion engine vehicles (14–42%)[3]. However, EVs and commercial EVs continue to face challenges in driving range and battery life. Auxiliary loads, such as lighting, onboard electronics, and especially cabin heating, consume significant power from the battery, reducing the energy available for driving. Unlike internal combustion vehicles, which can reuse waste heat, EVs require dedicated heating systems that draw directly from the battery. This limitation motivates the present work, which investigates alternative heating methods to improve the efficiency and practicality of commercial EVs.

Commercial EV thermal management systems currently rely on two primary heating technologies. Positive temperature coefficient (PTC) heaters provide fast and reliable heating but consume substantial electrical power, directly limiting driving range[4]. In contrast, heat pump (HP) systems, operating on the vapor compression cycle, offers higher efficiency by recovering ambient or component waste heat and amplifying the thermal energy through the compression process[4]. However, HP performance decreases at very low ambient temperatures, often requiring hybrid configurations that combine HPs with PTC heaters. Research efforts to improve HP architectures have explored suction line heat exchangers, vapor injection compressors, and reversible designs for combined heating and cooling[5,6,7,8]. Additional enhancements include integrating alternative heat sources, such as air recirculation systems and thermal energy storage units. Performance is also highly dependent on working fluid selection: while R134a has been widely used, low global warming potential refrigerants such as R1234yf, R290, and R744 (CO_2) are increasingly studied, with CO_2-based systems showing promising performance in sub-zero conditions despite more complex system designs[8,9,10].

The aim of this project is to conceptually design and evaluate an efficient heat recovery system for application in a commercial electric vehicle. To achieve this, the first objective was the development and validation of a heat pump system simulation model. This model was then extended into a simplified thermal management framework for controlled testing. The testing phase examined: (i) the use of alternative refrigerants within the heat pump cycle, (ii) the influence of orifice diameter variation, and (iii) the impact of incorporating an internal heat exchanger into the system.

Methodology: The HP system model was developed in Simcenter Amesim using a dataset of an existing HP, provided by an industry partner, containing performance values and fluid state measurements across the cycle. The data were extrapolated using simple thermodynamic and heat transfer theory. The working fluids in the system were R134a as refrigerant and a 50% ethylene-glycol/water coolant mixture. Compressor performance was characterized from provided efficiency curves, defined as functions of the compressor speed and the pressure ratio across the compressor. These data were expanded into a full efficiency map using a second-order spline interpolation and densifying the number of data points.

Component geometries, such as the orifice diameter and the heat exchanger equivalent lengths, were unknown; to address these uncertainties, a component-wise design and optimization process was conducted. Figure 1 illustrates how the optimization loop was wrapped around the simulation model script to iteratively solve for the unknowns until alignment with the experimental data was achieved. The completed HP system simulation model, shown in Figure 2, was validated against the test data by allowing the system to converge to a steady-state compressor speed consistent with the measured energy balance in test data. Figure 3 shows this validation and compares the simulation model to the test data in terms of compressor power and COP, demonstrating strong agreement to within 10% tolerance.

[a] Email address: 22605215@sun.ac.za

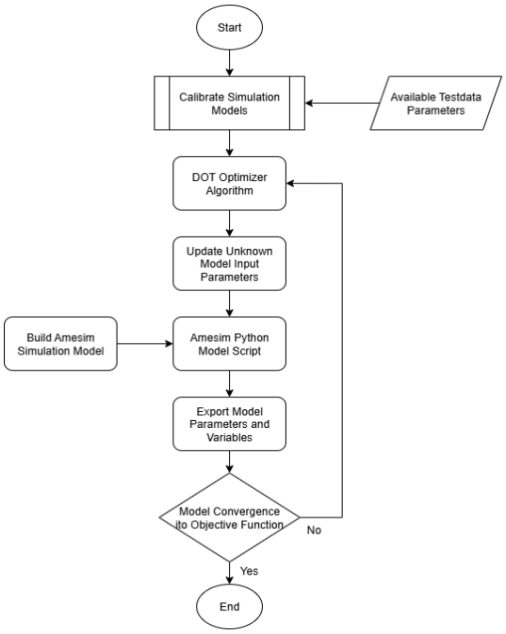

Figure 1: Graphical representation of optimization studies process

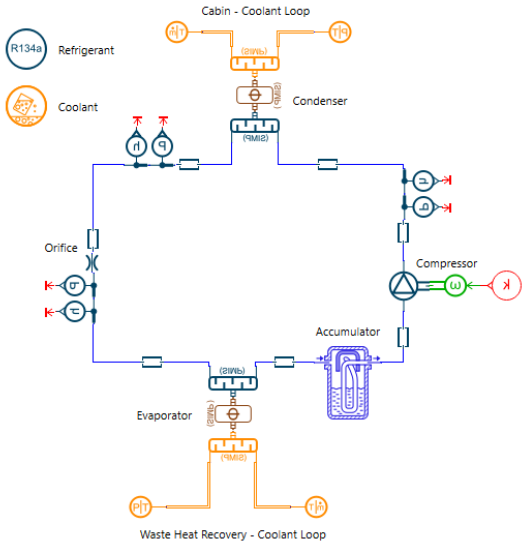

Figure 2: Heat pump simulation model

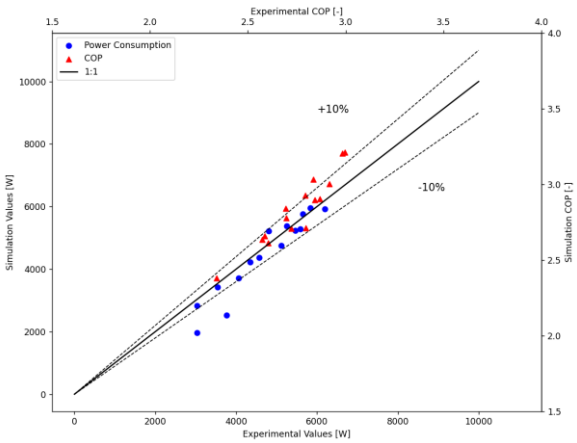

Figure 3: Simulation model validation against test data

Results and findings: At this stage, the testing phase of the simplified thermal management model is ongoing. Preliminary simulations have demonstrated stable operation of the heat pump system and confirmed the model's ability to resolve different heating configurations. Early trends indicate sensitivity to refrigerant choice, and expansion valve operation, though full parametric analyses are still in progress. Further testing will provide a comprehensive assessment of system performance under varying operating conditions.

References:

1. UNFCCC (2018). The Paris Agreement. T.I.A.S. No. 16-1104. Available at: https://unfccc.int/documents/184656
2. IPCC, 2023: Sections. In: Climate Change 2023: Synthesis Report. Contribution of Working Groups I, II and III to the Sixth Assessment Report of the Intergovernmental Panel on Climate Change [Core Writing Team, H. Lee and J. Romero (eds.)]. IPCC, Geneva, Switzerland, pp. 35-115, doi: 10.59327/IPCC/AR6-9789291691647
3. Albatayneh, A. et al. (2020) Comparison of the overall energy efficiency for internal combustion engine vehicles and electric vehicles, Environmental and Climate Technologies, vol. 24, pp. 669–680. doi:10.2478/rtuect-2020-0041.
4. Dan, D. et al. (2023) Review of Thermal Management Technology for Electric Vehicles, Energies, 16(12), p. 4693. doi:10.3390/en16124693.
5. Preissner, M. et al. (2000) Suction line heat exchanger for r134a automotive air-conditioning system, Purdue e-Pubs. In: International Refrigeration and Air Conditioning Conference. Available at: http://docs.lib.purdue.edu/iracc/494.
6. Barbosa Jr., J.R. and Hermes, C.J.L. (2014). Suction Line Heat Exchangers. HEDH Multimedia. doi:10.1615/hedhme.a.000402
7. Tahiragaoglu, B. et al. (2022) The investigation on the heating performance of the heat pump system with waste heat recovery for the Electric Vehicle, 2022 International Symposium on Multidisciplinary Studies and Innovative Technologies (ISMSIT), pp. 947–951. doi:10.1109/ismsit56059.2022.9932859.
8. Lee, S. et al. (2022) Experimental study on an electric vehicle heat pump system with multi-level waste heat recovery using a vapor injection technique at low ambient temperatures, Energy Conversion and Management, vol. 267. doi:10.1016/j.enconman.2022.115935.
9. Junqi, D. et al. (2021) Experimental study of R744 heat pump system for Electric Vehicle Application, Applied Thermal Engineering, 183, pp. 116–191. doi:10.1016/j.applthermaleng.2020.116191.
10. Kwon, S. et al. (2024) Performance comparison of a direct heat pump using R1234YF and indirect heat pumps using R1234YF and R290 designed for cabin heating of Electric Vehicles, Energy, vol. 297. doi:10.1016/j.energy.2024.131311.

Development of a 3D-Printed, High-Temperature Peristaltic Pump Using Stereolithography

D. Ebrahim[a] , V. Fester [b], O. Nemroaui[c], L. Meyer[d]

[a,c,d] Department of Mechanical and Mechatronic Engineering, Cape Peninsula University of Technology, Cape Town, South Africa

[b] Department of Chemical Engineering, Cape Peninsula University of Technology, Cape Town, South Africa

This study presents the design and characterization of a 3D-printed, high-temperature peristaltic pump using stereolithography (SLA) for solar heat transfer applications. The pump, fabricated with heat-resistant resin and minimal parts, handles nanofluids and viscous media with a power consumption below 3 watts. Analytical models for volumetric flow rate and efficiency were validated experimentally, achieving average volumetric efficiencies of 84% at 20°C and 90% at 95°C, and overall efficiencies of 19% at 20°C and 11% for 95°C water.

Introduction

During an investigation into heat transfer improvement mechanisms for parabolic trough systems, a need emerged for pumping nanofluids as working fluids. Nanofluids are base fluid with suspended particles within the fluid. These fluids exhibit improved heat transfer properties because of the suspended particles within the base fluid (Khamlich et al., 2023). But these fluids typically have a negative impact on erosive wear, higher viscosity and agglomeration (Okello, 2025).

Bilal Ahmed highlighted the preferred choice of pump to be utilised to address these challenges which is a peristatic pump (Ahmed et al., 2024). Yet, commercial peristaltic pumps are bulky and not known for high heat tolerances mainly due to normally have plastic parts which melt well below boiling point (Ferretti et al., 2023).

Problem Statement

Current peristaltic pumps are not designed to operate reliably under the high temperatures generated in parabolic trough systems, limiting the ability of experimenting with nanofluids at high temperatures.

Objective

Considering the recommendation made by Ching, who proposes a 3D-printed customizable alternative manufacture method for these pumps (Ching et al., 2021). Therefore, the study's main objective is to design a 3D-printed peristatic pump which enables high heat testing of nanofluid. This objective can be broken up into three steps: 1. Investigate analytical approach and designs of peristatic pump; 2. Design and manufacture of pump prototype and 3. Experimental investigation of pump prototype.

Investigation

The 3-roller peristaltic pump operates by sequentially compressing a flexible tube with three evenly spaced rollers. As the rollers rotate along the curved track, they pinch the tube shut and propel the trapped fluid from inlet to outlet (Ching et al., 2021). D. Cruz-Moreira and M. Behrens highlight the advantage of the 3 roller's precision in pumping (Cruz-Moreira et al., 2021). Hence, the design will be focused on 3 roller peristaltic pump.

The analytical approach will focus on this design by considering the trapped liquid internal area, A_{int} and the length of the tube with trapped liquid, L_{zone}. Eq. (1) utilises the geometrical `properties mentioned to calculate the trapped fluids total volume, V_{zone} (Gasoto et al., 2022). The theoretical volumetric rate of the fluid, Q_{th}, can be determined from the trapped volume, V_{zone} , the rotor's angular velocity, ω_{rotor}, using Eq. (2) (Carotenuto et al., 2025).

$$V_{zone} = A_{int}.L_{zone} \quad \text{Eq. (1)}$$

$$Q_{th} = 3.\omega_{rotor}.V_{zone} \quad \text{Eq. (2)}$$

Furthermore, the theoretical volumetric rate can be validated against the actual/measured volumetric rate (Ferretti et al., 2023). The overall efficiency of the pump, η_{eff}, can be determined by theoretical pressure drop across system, ΔP, and volumetric flowrate, Q_{th} with the power input. The power input being the voltage drop across motor, V, and current flowing through motor, I (Lin et al., 2025).

$$\eta_{eff} = \frac{\Delta P.Q_{th}}{V.I} \quad \text{Eq. (3)}$$

Therefore, the two parameters the study will use to evaluate the performance of the peristatic pump will be the volumetric efficiency and overall efficiency.

Design and manufacture of experimental set up

The peristaltic pump consists of four 3D-printed parts in figure 2 (a) below: (1) protective cover, ensuring rollers and tube follow a curved path during rotation; (2–3) roller holders, driven by the motor; (4) flexible tube holder, securing the tube in place. The Creality R6 resin Desktop printer in combination with SunLu High Temperature Resin – grey was used. The parts depicted below had less than 5% shrinkage from geometrical design.

The test setup consists of four core components depicted below in Figure 2 (b): (1&5) measurement beakers for fluid storage and transfer. (2) Adjustable height for varying pressure drops, Bernoulli utilised to calculate pressure drop. (3) Pulse width modulator to

[a] Place the corresponding author's email address here as a "footer" in 8-point font size

control the rotating speed of rollers/Impeller. (4) Resin 3D-printed peristaltic pump.

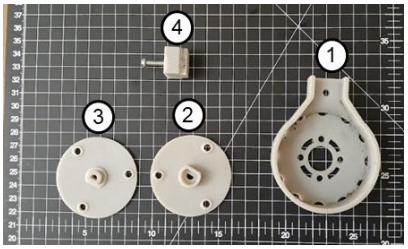

(a)

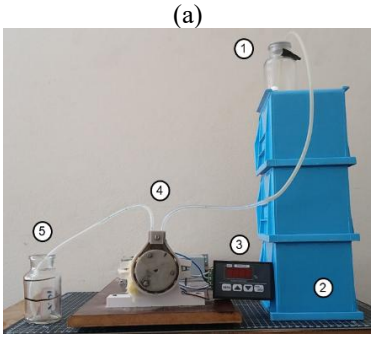

(b)

Figure 1: (a) 3D Printed Peristatic Pump and (b) Experimental Test Set-up

Experimental results

The two result being looked a comparison between theoretical and actual volumetric rate and Eq. (3), volumetric efficiency and overall efficiency. Firstly for Eq. (2), the ω_{rotor} is measured via a tachometer in test setup and actual volumetric rate is taken from timed filling of measurement beakers. For Eq. (3), the voltage is controlled with the pulse width modulator and current measured with multi-meter. The two results (a) Volumetric efficiency and (b) overall efficiency given below in Figure 4.

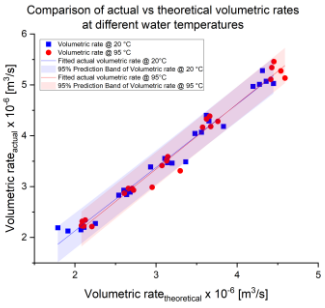

(a)

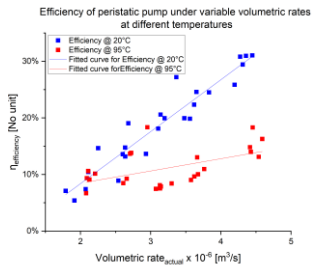

(b)

Figure 2: Volumetric rate comparison

Discussion and Conclusion

The study successfully designed and tested a 3D resin-printed, high-temperature peristaltic pump, utilising less than 3 Watts. The pumps analytical approach was validated experienced difference of +-8%. The efficiencies of 19% at 20°C and 11% for 95°C. Efficiency should be further investigated.

References:

Ahmed, B., Liu, D., Zhang, Y. & Hussien, M.A. 2024. Peristaltic pumping of convective nanofluid with magnetic field and thermal radiation in a porous channel. *Case Studies in Thermal Engineering*, 53.

Carotenuto, C., Ferrari, F., Salerno, S., Bernabei, F., Lababidi, W., Montorsi, L. & Milani, M. 2025. Lumped parameter modeling and experimental characterization of pressure effects in a roller-type peristaltic pump with neoprene tubing for dialysis machines. *International Journal of Thermofluids*, 26.

Ching, T., Vasudevan, J., Tan, H.Y., Lim, C.T., Fernandez, J., Toh, Y.C. & Hashimoto, M. 2021. Highly-customizable 3D-printed peristaltic pump kit. *HardwareX*, 10.

Cruz-Moreira, D., Visone, R., Vasques-Nóvoa, F., S. Barros, A., Leite-Moreira, A., Redaelli, A., Moretti, M. & Rasponi, M. 2021. Assessing the influence of perfusion on cardiac microtissue maturation: A heart-on-chip platform embedding peristaltic pump capabilities. *Biotechnology and Bioengineering*, 118(8): 3128–3137.

Ferretti, P., Pagliari, C., Montalti, A. & Liverani, A. 2023. Design and development of a peristaltic pump for constant flow applications. *Frontiers in Mechanical Engineering*, 9.

Gasoto, S.C., Schneider, B. & Setti, J.A.P. 2022. Study of the Pulse of Peristaltic Pumps for Use in 3D Extrusion Bioprinting. *ACS Omega*, 7(28): 24091–24101.

Khamlich, S., Jakobi, J., Khamliche, T., Ismail, F., Nemraoui, O., Rehbock, C., Fester, V. & Barcikowski, S. 2023. Enhanced heat transfer of laser-fabricated copper nanofluid at ultra-low concentration driven by the nanoparticle surface area. *Journal of Molecular Liquids*, 383: 122104.

Lin, L., Duan, Y., Aziz, T., Shami, A., Al-Asmari, F., Mohamed, R.A.E.H. & Cui, H. 2025. Design of a peristaltic pump-based feeding device for achieving continuous production in food 3D printing. *Innovative Food Science and Emerging Technologies*, 100.

Okello, J.A. 2025. A Review of Applications and Challenges Facing Use of Nanofluids. *Journal of Engineering Research and Reports*, 27(9): 244–254. https://www.journaljerr.com/index.php/JERR/article/view/1638.

DAMAGE EVOLUTION AND FLEXURAL RESIDUAL PROPERTIES OF GFRP LAMINATES CLAMPED ON TWO SIDES AND SUBJECTED TO AIRBLAST

S Mashau[a] , CJ von Klemperer[b] , S Chung Kim Yuen[a] & GS Langdon[a]

[a] BISRU, Department of Mechanical Engineering, University of Cape Town, Cape Town, South Africa
[b] Department of Mechanical Engineering, University of Cape Town, Cape Town, South Africa

Abstract:
This paper examines changes to the flexural properties of Glass Fibre Reinforced Polymer (GFRP) laminates when impulsively loaded by the detonation of an explosive charge. Different masses of explosive were detonated to generate a range of uniform blast loads causing different responses in the laminates. Four-point flexural tests were performed to quantify the residual flexural strength and stiffness of the "damaged" laminates. When dynamically loaded with relatively low impulses, the laminate experienced comparatively little damage, and consequently the flexural properties remained unchanged. Increasing the shock wave pressure beyond a threshold value caused notable damage, resulting in an appreciable loss of residual flexural strength and stiffness.

Introduction:
Fibre-reinforced polymer (FRP) composites have been extensively preferred as a replacement to metals due to their excellent mechanical properties[1,2]. This choice allows for the design of structures with desirable strength to weight properties. When subjected to explosive loading (either accidental or intentional), composites can exhibit unpredictable damage patterns, such as fibre breakage or matrix fragmentation, which can compromise the overall structural integrity of the material[2]. One of the primary challenges with composites is the difficulty in detecting damage, especially internal defects. Depending on the load intensity, composites can experience internal delamination damage which is not always visible[2]. To ensure the safety and reliability of composite materials, it is important to understand how they fail and their residual properties after being exposed to damage. This paper thus reports on the residual flexural strength of GFRP laminates that were subjected to uniform blast loads.

Material Manufacturing and Characterisation:
The GFRP laminate was made from WOVITEX 400P E-glass fibres and Prime-27 epoxy polymer together with an appropriate slow hardener. The continuous glass fibre used in the laminate were of a 0°/90° plain weave with an areal density of 200 g/m^2. The fibres were vacuum infused with the epoxy to produces 5.6 mm thick laminates consisting of 18 layers. The laminates were post cured according to manufacturer specifications[2] before being CNC-routed or cut by water jet to produce the required samples for the mechanical tests. Four point-bend flexural tests and tensile tests were performed according to the relevant ASTM standards[3,4] for polymer matrix composite materials to confirm manufacturing repeatability. The properties of the manufactured GFRP material are presented in Table 1. A span to thickness ratio of 20:1 was used for the flexural tests. The flexural test data was the baseline data for assessing post blast flexural properties later. Complex stress states occur in composite materials during flexural tests due to tensile, compressive and shear stresses being set up simultaneously[5]. Flexural tests are relevant for assessing residual properties as various structures are typically loaded in bending and not in compression, which is traditionally used to assess residual properties[5].

Table 1: Flexural and Tensile Properties.

PROPERTY	MEAN	STD DEV
Flexural Strength	327 MPa	3 MPa
Flexural Modulus	32.1 GPa	0.8 GPa
Tensile Strength	362 MPa	17 MPa
Tensile Modulus	28.4 GPa	1.3 GPa

Blast Testing:
The blast test panels of size 200 x 300 mm^2 were clamped between a square blast tube and a clamp frame on two opposite short sides to present an exposed area of 200 x 200 mm^2. The bolts were torqued equally to ensure uniform clamping pressure along the clamped region. The blast tube assembly shown in Figure 1 was attached to a horizontal pendulum, used to determine the impulse imparted onto the panels. The panels were blast loaded by detonating cylindrical discs of Plastic Explosive 4 (PE4). A 22 mm diameter was used for charge masses less than 8 g and a diameter of 28 mm for charge masses larger than 8 g. Different diameters were chosen to optimize the impulse imparted to the panel and ensure complete detonation[6]. The PE4 cylinder was attached to a polystyrene pad that was placed at the end of the blast tube and detonated at a stand-off distance of 300 mm to generate a uniform blast load.

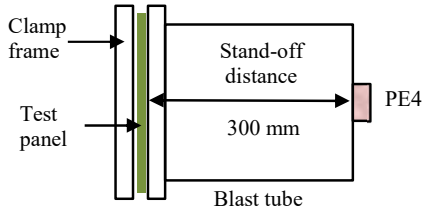

Figure 1: Blast tube assembly.

The response of the panels was captured using high speed cameras and analysed using Digital Image Correlation (DIC). The blast loaded panels were cut by

[a] Shivasi.mashau@uct.ac.za

waterjet into smaller rectangular specimens of 220x15 mm^2 for four-point flexural tests to determine of the residual flexural properties of the material.

Results:

The blasted tested panels were visually inspected to establish the evolution of damage in the panels with increasing load. The following damage was noted, listed in order of occurrence: clamp boundary damage (CBD), matrix damage along the centre (MDC) and bolt hole damage (BHD), delamination (D) and in-plane cracking, and through thickness cracking (TTC) along the clamp boundary. The damage visible on the face of the panel is shown in Figure 2.

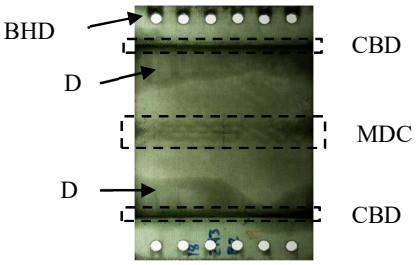

Figure 2: Panel damage at 47.8 Ns.

The panels were photographed on a backlit lightbox to help quantify panel delamination after the blast tests. The delamination damage visualised by this technique included the superposition of all the delamination damage through all the layers and interfaces in the panel. Delamination was visible as the darker regions, cannot be easily identified by layer. The delaminated regions were traced, and their projected areas calculated, to determine the delamination area as a percentage of the exposed area. The evolution of the delamination and other damage is presented in Table 2.

Table 2: Damage progression with increasing impulse.

Impulse (Ns)	28.8	39.7	47.8
CBD	Yes	Yes	Yes
MDC & BHD	No	Yes	Yes
Delamination	0%	35%	41%
TTC	No	Yes	Yes

Four-point flexural test specimens were waterjet cut from these impacted panels to determine residual properties of the damaged material. The specimens were assigned an image-based brightness value related to the degree of delamination. Delamination makes the specimen less translucent resulting in lower brightness values from the photographs. The results for the residual properties of specimens against specimen brightness are shown in Figure 3. This may provide an easy method of quantifying the damage in a part.

The DIC data provided the transient response of the panels during the blast. The initial displacement of the panels confirm that they were uniformly loaded by the blast. The maximum displacement of centre of the panels increased with an increase of impulse, the panels rebounded and oscillated at lower impulses but tended to slip between the clamp frame and blast tube at higher impulses resulting in crushing at the bolt holes. The panels did not no rebound when slippage occurred.

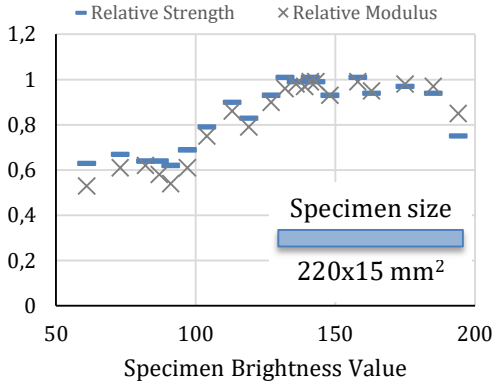

Figure 3: Residual properties (normalised by flexural strength and modulus) vs specimen brightness value.

Conclusions:

The damage progression for panels clamped on two opposite sides and subjected to increasing blast impulses was evaluated. A correlation was found between an image-based damage evaluation and residual properties; this has the potential of being implemented in image processing techniques for rapid damage assessment for translucent materials. The transient response of the panels was assessed using DIC showed that the displacement of the centre of the panels was directly proportional to the applied impulse.

References:

1. S. A. Tekaur, K Shivakumar, A Shukla, *"Mechanical behavior and damage evolution in E-glass vinyl ester and carbon composites subjected to static and blast load"* https://doi.org/10.1016/j.compositesb.2007.02.020

2. A. P. Mouritz, *"Advances in understanding the response of fibre-based polymer composites to shock waves and explosive blasts"* https://doi.org/10.1016/j.compositesa.2019.105502

2. Gurit, Gurit Resins, https://gurit-resins.com/prime-infusion-systems/

3. ASTM International, *"D3039/D3039M17 Standard Test Method for Tensile Properties of Polymer Matrix Composite Materials"*

4. ASTM International, *"D7264/D7264M-15 Standard Test Method for Flexural Properties of Polymer Matrix Composite Materials"*

5. H Ullah, A. R. Harland, V. V. Silbersschmidt, *"Characterisation of mechanical behaviour and damage analysis of 2D woven composites under bending"* https://doi.org/10.1016/j.compositesb.2015.01.036

6. S. A. Davids, G. S. Langdon and G. N. Nurick, "*The influence of charge geometry on the response of partially confined right circular stainless-steel cylinders subjected to blast loading*" https://doi.org/10.1016/j.ijimpeng.2017.02.015

Hybrid solar-hydro pneumatic power system for improved load management

MT Madavha[a], E Orumwense[b] & MT Kahn[c]

[a] Department of Mechanical and Mechatronic engineering, Cape Peninsula University of Technology, Cape Town, South Africa

[b-c] Department of Mechanical and Mechatronic engineering, Cape Peninsula University of Technology, Cape Town, South Africa

Introduction

As the need for clean and reliable energy sources grows, it becomes increasingly important to integrate renewable technologies with advanced energy storage solutions in order to achieve a sustainable energy environment and future. [1]. One promising method involves using solar photovoltaic (PV) technology to power compressors in a pneumatic system based on Adiabatic Compressed Air Energy Storage (A-CAES) principles, which is then integrated into a Closed-Loop Pumped Hydro Energy Storage (PHES) system.

In 2021, pumped hydroelectric storage capacity worldwide reached 165 GW and 4298 TWh of electricity generated from hydropower, making it the most frequently utilized storage technique [2]. This technology is critical for expediting the energy transition while complementing and capitalizing on the intermittent nature of renewable energy, with other renewable energy storage systems like CAES and solar PV being researched in this study. These storage power plants may readily replace natural gas-based technologies as backup systems for power systems and are currently the most nature-friendly, efficient, and long-term storage technology developed on a big scale [3].

In this combined energy storage model, solar PV panels produce electricity that powers compressors using A-CAES technology. A-CAES works by adiabatically compressing air and storing it in an underground cavern or high-pressure vessel, where it can be later released and expanded to generate electricity [4]. The integration of this CAES technology with a Closed-Loop PHES system, which involves circulating water between reservoirs for energy storage and release, creates a synergistic storage solution [5]. Bazdar [6] and Yang [7] explored hybrid solar–CAES–hydro systems, showing their potential to stabilize renewable energy supply but also identifying limitations such as incomplete optimization of control strategies and unclear performance under varying demand conditions. Utilizing solar PV-powered compressors in the A-CAES system provides several significant advantages. Solar PV offers a renewable and sustainable energy source, which reduces dependence on fossil fuels and cuts greenhouse gas emissions [8]. The adiabatic compression process stores energy efficiently with minimal heat loss, and the closed-loop PHES system facilitates effective water management and continuous energy output [9]. Together, these technologies improve the efficiency, stability, and flexibility of the energy storage system.

This study aims to examine the design, implementation, and performance of a solar PV-powered A-CAES system within a Closed-Loop PHES framework. The research will explore how this hybrid system can enhance energy storage capabilities, optimize resource utilization, and contribute to a more sustainable energy infrastructure. By assessing the operational dynamics and benefits of this integrated approach, the research intends to provide valuable insights into the future of renewable energy storage and generation.

Problem statement

Conventional hybrid solar–hydropower systems, particularly run-of-river PHES plants, face significant efficiency and reliability challenges. Without dedicated pumping systems, these facilities lose water to the environment, limiting storage capacity during dry periods and reducing overall energy delivery to the grid. This dependency often requires fossil-fuel backup plants, undermining sustainability goals. Addressing these limitations requires innovative hybrid solutions that can recycle water, store surplus renewable energy, and provide consistent generation capacity.

Methodology

The system design components comprises of solar PV arrays, compressors, high-pressure storage tanks, water reservoirs, and hydraulic turbines. The PV subsystem generates direct current power for the compressors, which store energy by adiabatically compressing air. During discharge, the compressed air displaces water into the PHES upper reservoir, generating electricity via turbines. MATLAB/Simulink is employed for energy flow and system modelling, while EPANET is applied to simulate hydraulic performance. Analytical models are used for sizing PV arrays, compressor power, storage tanks, and turbines. Evaluation metrics include round-trip efficiency, solar utilization, water consumption, and system performance under peak and off-peak scenarios.

Proposed system model/design

Figure 1 illustrates the conceptual hybrid design. A PV array powers a compressor that pressurizes ambient air into dual high-pressure tanks. The compressed air is

[a] Place the corresponding author's email address here as a "footer" in 8-point font size

then fed into air–water chambers, displacing water under pressure. The displaced water flows through a hydraulic turbine to generate electricity, while returning to the reservoir for recycling. Automated controllers coordinate the pneumatic and hydraulic subsystems to maintain pressure stability and continuous operation. This closed-loop design reduces water dependency, enables flat-terrain deployment, and supports both off-grid and grid-connected application.

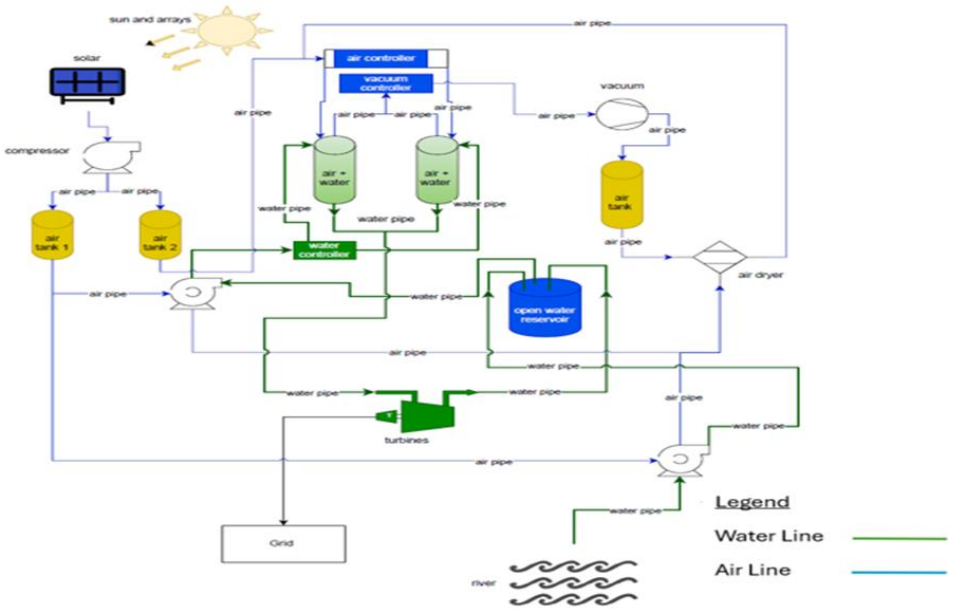

Figure 1: hybrid solar-pneumatic-hydro power generation system

Findings

Based on established performance trends in prior studies and the theoretical configuration of the proposed model, it is strongly expected that the solar-powered hybrid A-CAES–PHES system will achieve higher efficiency, improved operational stability, and reduced water consumption compared with standalone systems. For example, integrating A-CAES enables effective heat recovery and flexible site selection, while PHES provides proven long-duration storage capacity. By decoupling storage from strict natural elevation requirements and utilizing abundant solar energy to drive compressors, the system design is expected to offer tangible advantages for deployment in water-stressed and energy-scarce regions.

Conclusion

Integrating solar PV with A-CAES and closed-loop PHES creates a synergistic storage solution that leverages the strengths of each technology. The outcomes of this study are expected to advance knowledge on hybrid storage systems, providing insights into sustainable design, resource optimization, and performance improvement. Ultimately, this approach contributes to resilient, low-carbon energy infrastructure aligned with global renewable energy transition goals.

References:

[1] International Energy Agency, “International Energy Agency (IEA) World Energy Outlook 2022,” *Int. Inf. Adm.*, p. 524, 2022.

[2] IHA, “Hydropower Status Report,” *Int. Hydropower Assoc.*, p. 52, 2022.

[3] N. Naval, J. M. Yusta, R. Sánchez, and F. Sebastián, “Optimal scheduling and management of pumped hydro storage integrated with grid-connected renewable power plants,” *J. Energy Storage*, vol. 73, no. June, 2023, doi: 10.1016/j.est.2023.108993.

[4] D. L. Pottie *et al.*, “Adiabatic Compressed Air Energy Storage system performance with application-oriented designed axial-flow compressor,” *Energy Convers. Manag.*, vol. 304, no. February, p. 118233, 2024, doi: 10.1016/j.enconman.2024.118233.

[5] K. Forrest, B. Shaffer, A. Blakers, M. Stocks, B. Lu, and C. Cheng, “Progress in Energy A review of pumped hydro energy storage,” 2020.

[6] E. Bazdar, M. Sameti, F. Nasiri, and F. Haghighat, “Compressed air energy storage in integrated energy systems: A review,” *Renew. Sustain. Energy Rev.*, vol. 167, no. May, p. 112701, 2022, doi: 10.1016/j.rser.2022.112701.

[7] B. Yang *et al.*, “Review of innovative design and application of hydraulic compressed air energy storage technology,” *J. Energy Storage*, vol. 98, no. PA, p. 113031, 2024, doi: 10.1016/j.est.2024.113031.

[8] T. M. Y. Khan and E. Jassim, “Solar Thermal Systems , and the Dawn of Energy,” pp. 1–30, 2023.

[9] IRENA, “World energy transitions outlook 2023: 1.5°C Pathway,” *World Energy Transitions*, pp. 1–258, 2023.

A Method of Deflectometry based on Photogrammetry for heliostat optical quality assessment

C.D. Winter[a] & Dr. W.J. Smit[b]

[a] Department of Mechanical and Mechatronic Engineering, Stellenbosch University, Stellenbosch, South Africa

A novel method for deflectometry using the photogrammetry has been designed and tested. The system is designed to measure the optical quality of heliostats in both laboratory and outdoor environments. The method operates by attaching a target to an EOS Mark II camera lens. Using photogrammetry-based pose estimation, the position and orientation of both the camera and its attached target can then be determined. Using reflective laws allows for the calculation of the normal. By taking multiple photos of the specular surface under test and with the reflection of the target seen over the mirror surface. Multiple images of multiple reflection points are stitched together to create a slope map across the entire surface of the specular surface. The system can produce slope maps to an accuracy of 0.5mrad under repeated tests.

Introduction: Research done at the University of Stellenbosch in the STERG (Solar Thermal Energy Research Group) division is concerned with the manufacturing of heliostats. Heliostats represent a significant cost portion to the construction of a CSP (Concentrating Solar Power) station their role is as a solar collector, their surface is highly reflective, and their dimensions are optimized to concentrate light onto a receiver, however, there is no existing system to measure the slope of manufactured heliostats currently in use at the department. Knowing the slope is important in the quality assessment and research into heliostat technologies.

Deflectometry is an optical measurement method used to inspect and measure the 3D shape and defects of specular (mirror-like) reflective surfaces by analysing the deformation of a known, structured light pattern reflected off the surface. Deflectometry is defined mainly by the principle of surface acquisition using a controlled and organised environment[1].

Although accurate measurement systems for manufactured heliostats exist, they require components such as lasers, mounting frames or projectors, which can be costly and timely to setup. This research aimed at designing a simple and modular system using minimal equipment and expertise to provide high accuracy slope data for manufactured heliostats, with the addition of being used on mounted heliostats without the need for heliostats to be removed from their operational position and could lead to an infield heliostat slope measurement system for maintaining heliostats.

Key differences between existing method and the designed method:

- **Robustness:** Designed method can operate reliably in challenging environments.
- **Efficiency:** Measurements are taken rapidly, with all processing managed in software.
- **Calibration:** No physical calibration is required.
- **Scaling:** Only one physical scaling measurement is needed.

Methodology: The objective of the method is to calculate the normal of a reflective surface at a specified point given by:

$$\frac{\vec{n}}{|\vec{n}|} = \frac{\vec{r} - \vec{\imath}}{|\vec{r} - \vec{\imath}|}$$

Where $\vec{n}$ is the calculated normal, $\vec{r}$ and $\vec{\imath}$ are the reflected and incident rays respectively. For two rays in 3D space, we require three known points. We accomplish this by using a camera and mounted target. Therefore, the incident and reflected rays are determined using the position of the camera centre modelled as a pinhole camera, reflection point on the reflective surface and target points around the camera to determine the normal vectors of the reflective surface.

The camera centre is calculated from photogrammetry in a Meshroom[2] pipeline using the features in the environment to estimate pose of the camera relative to structures seen in the images. The target is a set of LEDS fitted onto an MDF board and bound to the lens of an EOS mark II camera. The camera and target translate and rotate together through space allowing for the target to be oriented according to the cameras pose in space.

Figure: 1 shows the laboratory test setup and test procedure with the target and camera being seen inside the reflective surface. The reflective surface is mounted onto a board and surrounded by CCtags[3], a type of fiducial marker used in computer vision, are placed around the test surface and define the plane of the specular surface to extract the reflection points. CCtags are additionally used to mask features detected inside the mirror surface, which decreases accuracy of the camera pose estimation, as well as used for scaling of photogrammetry

[a] Connal Daniel Winter 22901299@sun.ac.za

Multiple images of the surface are captured, where the reflected target appears at different, overlapping positions. For each image a pose estimation is performed and for relative pose between the reflective surface and camera. For each reflection point on the plane the normal calculation is performed allowing for the relative slope across the surface to estimated.

Figure 1: Test procedure and laboratory setup

Experimentation and discussion: A manufactured test heliostat with a designed focal length of 45m is used. The slope is displayed in mrad as the angle between each normal on the surface and a reference normal chosen. Figure: 2 depicts the point cloud slope measurement in mrad for the test heliostat with the reference normal set at the surface centre. The red box depicts the bounds of the heliostat facet. Each point represents a target point on the surface.

Figure: 3 shows a smoothed slope map by fitting the slope data with a cubic smoothing spline to visualize the slope variation across the surface. A heliostat is expected to concentrate light onto a fixed point at a specified distance, and therefore exhibits a parabolic shape based on the focal distance. The map shown in figure: 3 shows a central point of near zero slope with slope increasing towards the outer edges of the heliostat surface.

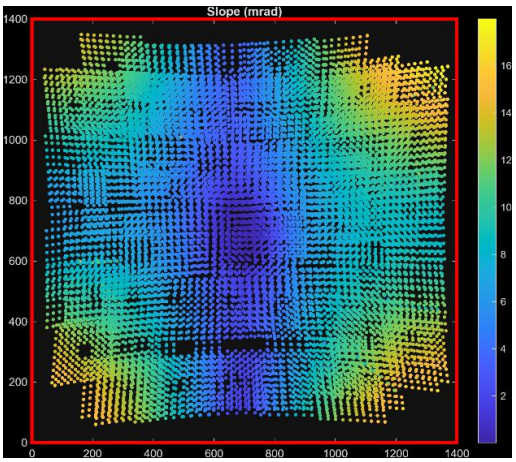

Figure 2: Point cloud slope map of heliostat

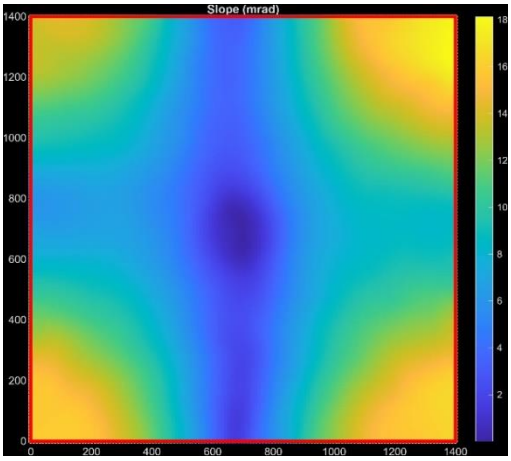

Figure 3: Smoothed slope map of heliostat

A robust ground truth for the slope could not be established, as no reliable method for slope validation was available however a laser scanning is used to validate the shape and slope range. System accuracy was evaluated through repeated experiments conducted under varying environmental conditions, camera settings, and target distances. The results exhibited correspondence within 0.5 mrad on the same specular surface, confirming the validity of the derived slope measurements. Additionally, the method effectively distinguished between concave and convex surface profiles, indicating its robustness in detecting minor changes in slope orientation.

References:

1. Burke J, Pak A, Höfer S, Ziebarth M, Roschani M and Beyerer J (2023) *Deflectometry for specular surfaces: an overview.* Adv. Opt. Technol. 12:1237687. doi: 10.3389/aot.2023.1237687

2. Carsten Griwodz, Simone Gasparini, Lilian Calvet, Pierre Gurdjos, Fabien Castan, Benoit Maujean, Gregoire De Lillo, & Yann Lanthony (2021). AliceVision Meshroom: *An open-source 3D reconstruction pipeline*. In Proceedings of the 12th ACM Multimedia Systems Conference - MMSys '21. ACM Press.

3. Lilian Calvet, Pierre Gurdjos, Carsten Griwodz, and Simone Gasparini. Detection and Accurate Localization of Circular Fiducials under Highly Challenging Conditions. In *Proceedings of the 2016 IEEE Conference on Computer Vision and Pattern Recognition (CVPR)*, 562 – 570. Las Vegas, United States, June 2016. URL: https://hal.archives-ouvertes.fr/hal-01420665/document, doi:10.1109/CVPR.2016.67.

DEVELOPMENT OF AN OPTICAL TRACKING SYSTEM FOR REAL-TIME ROBOTIC APPLICATIONS

S. Pitman[a] & A. Pretorius

MechatronicSystems.Group, Department of Mechanical Engineering, University of Cape Town, South Africa

Determining the position and orientation (pose) of a moving object is essential in robotics for tasks such as avoiding obstacles, tracking trajectories, and analysing motion. Optical motion capture (MoCap) provides this pose data by calculating an object's pose relative to a fixed reference, without requiring onboard sensors. Such systems are indispensable when testing control algorithms indoors. However, existing MoCap solutions are expensive, rely on proprietary software, and are often inaccessible to research groups and small enterprises in research-constrained environments. Furthermore, these cameras are often arranged without systematic optimisation, which can reduce accuracy and robustness.

This project addresses these challenges in two ways. First a camera placement optimiser that uses a Guided Genetic Algorithm (GGA) to determine the minimum number and best arrangement of cameras was developed. The optimisation ensures well-conditioned triangulation while reducing the effects of resolution degradation and dynamic occlusion, culminating in a more robust improved pose estimate. Second, this project presents a scalable, real-time multi-camera algorithm that estimates the full six degree-of-freedom pose of a rigid-body robot using an Extended Kalman Filter (EKF) to fuse noisy measurements with the system's dynamic model. The final deliverable is a modular, open-source MoCap system that makes advanced motion tracking more affordable and accessible, particularly for robotics research in the Global South.

Introduction: Optical MoCap uses a network of cameras to track the markers on the object to infer its position and orientation. As opposed to other motion tracking systems, optical is most ubiquitous as it imposes no weight or movement restrictions on the platform being studied.

Commercial systems are prohibitively expensive, often costing hundreds of thousands of Rands, placing them out of reach for many research institutions. Even when cost is not the primary obstacle, these systems rely on proprietary software that restricts customisation. This limits their flexibility for laboratories that may desire a system that scales well to their choice of cameras, their capture volume, and which is easily portable.

At the University of Cape Town, an open-source, low-cost, MoCap system using an asynchronous EKF multi-camera set-up was developed [1]. While this work laid valuable foundations, it had several limitations: a MATLAB licence was required, the testing room had to be blacked-out, there was no real-time feedback between the system and the subject, and there was no investigation into how camera placement affected tracking performance.

The above-mentioned constraints to existing systems highlight the need for an affordable, scalable MoCap solution that delivers reliable, real-time full pose estimation.

Methodology: A simulation environment was developed in Simulink to model an Unmanned Aerial Vehicle (UAV) flying inside the MechatronicSystems.Group flight space. Initially, cameras were placed on the walls of the simulated room and used to track the four markers positioned on the motors of the UAV using the proposed EKF algorithm. This simulated setup serves to safely and rapidly validate the software implementation before experimental deployment.

The EKF is implemented from first principles, rather than relying on pre-built Simulink blocks. This approach was chosen to enable later porting to faster, open-source languages such as Python or C++.

A Kalman Filter integrates noisy sensor measurements with a model of the system dynamics to produce a refined state estimate. In this scenario, the measurements are the detected centroids of optical markers on the UAV, while the predicted states are the UAV's position, orientation, and their respective derivatives. The EKF extends this principle to nonlinear systems, which is necessary as the system model is nonlinear both in state transition (due to quaternion dynamics) and measurement function (due to projecting coordinates from a 3D world frame to a 2D-image plane).

The next stage investigated how the number and placement of cameras affect tracking accuracy. A quality metric was designed to assess the three largest contributors to MoCap degradation, namely, resolution, triangulation, and occlusion. Following the approach in [2], an ellipsoid error volume was modelled to evaluate pixel-level uncertainty. Each detected marker may lie within a square uncertainty region centred on the detected point in the image

[a] ptmsha001@myuct.ac.za

plane. Projective pyramids were formed from the edges of this region through the camera centre and intersected with pyramids from other cameras. An ellipsoid was conservatively overfitted to the resulting intersection region, with its volume representing the uncertainty caused by resolution limits. As described in [3], cameras must maintain a convergence angle between their view vectors that is sufficiently non-parallel (40°-140°), to avoid poorly conditioned triangulation. The concept in [4] was further adopted to encourage observed redundancy by grouping camera orientations into regions of equivalent visibility, thereby probabilistically reducing dynamic occlusion.

These quality metrics were used as the fitness function in a Guided Genetic Algorithm (GGA). Unlike a standard genetic algorithm that starts from a purely random population, the GGA is seeded with a baseline configuration known to produce reasonable results and to incite a faster performing convergence to a global solution. Each configuration (set of camera poses) was treated as an individual in the population, with crossover and mutation generating new arrangements that should improve performance on the tasks defined by the quality metric. The fitness scores were then used to select and evolve the best-performing configurations.

Preliminary Results:

Early simulations showed that in a two-camera parallel stereo configuration, the largest positional error occurred along the depth axis (aligned with the camera's view vectors). When the cameras were arranged perpendicularly, triangulation became better conditioned, substantially improving accuracy and confirming the findings in [3].

The influence of camera resolution was also examined, given that high-resolution cameras are expensive and may limit system scalability. Results from the initial setup showed that positional uncertainty increases as the object moves farther from the cameras, with the degradation being more pronounced in parallel configurations than in converging cameras –see Figure 1 and 2. These findings suggest the importance of optimising camera placement to maintain accuracy without excessive hardware costs.

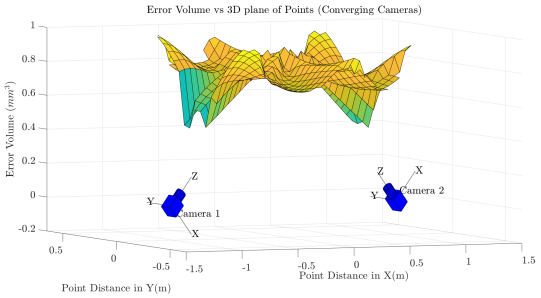

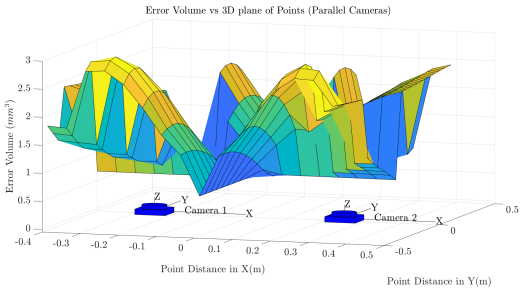

Figure 1 and 2: Surface plots showing the error volume caused by image quantisation for a plane of points at Z=1m observed by a (left) converging camera and (right) parallel stereo pair.

Future Work:

The next phase of this research involves implementing a guided genetic algorithm to place a minimum number of cameras that sufficiently mitigate tracking degradation from suboptimal arrangements. Once the optimal positions and orientations are obtained, they will be integrated into the simulation, where the EKF will be refined to enhance tracking precision.

A data processing framework will then be developed to handle the multi-camera input, either through Precision Time Protocol (PTP) synchronisation or the asynchronous approach such as in Meyer [1]. After validation in simulation, experimental trials using low-cost cameras will be conducted to evaluate tracking performance, real-time capabilities and verify the benefits of the optimised placement. Finally, if time permits, a Graphical User Interface (GUI) will be designed to streamline calibration and tracking, improving usability and enabling deployment in research and commercial applications.

References:

[1] Z. Meyer and A. Pretorius, “Design of a low-cost optical motion capture system using a multi-camera configuration and an asynchronous extended Kalman filter,” *MATEC Web Conf.*, vol. 406, p. 04010, 2024, doi: 10.1051/matecconf/202440604010.

[2] R. Sharma, “Analysis of uncertainty bounds due to quantization for three-dimensional position estimation using multiple cameras,” *Opt. Eng.*, vol. 37, no. 1, p. 280, Jan. 1998, doi: 10.1117/1.601615.

[3] G. Olague and R. Mohr, “Optimal camera placement for accurate reconstruction,” *Pattern Recognit.*, vol. 35, no. 4, pp. 927–944, Apr. 2002, doi: 10.1016/s0031-3203(01)00076-0.

[4] P. Rahimian and J. K. Kearney, “Optimal Camera Placement for Motion Capture Systems,” *IEEE Trans. Vis. Comput. Graph.*, vol. 23, no. 3, pp. 1209–1221, Mar. 2017, doi: 10.1109/TVCG.2016.2637334.

Embedded Systems Design of a Low-Cost Flight Controller for use in UAV Platforms

Daniel Fraser[a*], Arnold Pretorius[a], James Hepworth[a], Natasha Botha[b]

[a]MechatronicSystems.Group, Mechanical Engineering Department, University of Cape Town, Cape Town, SA
[b]Centre for Robotics and Future Production, Council for Scientific and Industrial Research, Pretoria, SA

Serving as a critical interface between high-level software and low-level electronic systems, flight controllers are essential for aerial robotic applications. However, their significant cost poses a barrier to widespread adoption. While affordable, off-the-shelf flight controllers exist, they generally do not support the firmware required for research- and industry-level implementation, such as PX4. This work presents an embedded system designs for low-cost flight controllers that are PX4 compliant. The research delves into examining the necessary components, existing open-source firmware/software, and appropriate hardware solutions. The presented designs are based on open standards and capable of operating with various platforms, applications, and components. The final design is shown to be low in cost while also demonstrating substantial potential for integration with existing applications. The flight controllers were verified with a range of tests, including the implementation of a control system that was responsible for governing the roll angle of a quadcopter. The overall flight controller performance is shown to be comparable with the performance and functionality of commercial solutions.

Introduction: Unmanned Aerial Vehicles (UAVs) have become a popular area of research in robotics over the past decade. However, the significant cost and knowledge barrier of UAV hardware remains a challenge for research and commercial entities in developing regions, such as Southern Africa. To address the high cost and to grow in-house knowledge, the Aerial Robotics Capability (ARC) Project, led by the MechatronicSystem.Group in partnership with the CSIR, aims to develop a low-cost quadcopter platform that can be used for a wide range of research and industry applications. One aspect of Project ARC is designing a low-cost extendible flight controller for use on multiple research platforms. The flight controller aims to be both robust and convenient to use, whilst also affordable at scale.

Background of Flight Controllers: The flight controller is an embedded system responsible for the reliable operation of a UAV. The system's primary objectives are to collect signals from internal/external devices, convert them into meaningful data, and output signals for communication and control. Flight controllers need many components to operate reliably. These typically include: sensors, such as accelerometers, gyroscopes, magnetometers, and storage devices and interfacing components [1]. Additionally, flight controllers typically support wireless communication through Wi-Fi/Bluetooth via a System on Chip or external radio modules. The flight controller components are mounted and connected using a Printed Circuit Board (PCB). The PCB design electrically connects various components together to allow for communication. A crucial aspect of the flight controller is the firmware, which serves as the bridge between software and low-level electronic signals. PX4-Autopilot was selected for its superior software compatibility and lack of affordable options. Current PX4-based open-source options are further evaluated.

Bitcraze: is a Swedish company that focuses on open-sourced, small-scale, low-cost UAV quadcopter products. They provide schematics and details of components for their flagship product, the Crazyflie 2.1+. The open-sourced ideology gives developers access to their community developed firmware and applications [2]. Bitcraze developers have allowed for partial PX4-firmware compatibility.

Pixhawk: is an independent open-hardware project delivering accessible, cost-effective, and high-quality autopilot hardware design standards. It also serves as the reference hardware platform for the PX4-Autopilot firmware [3]. Within the Pixhawk standards, various pinouts and block diagrams serve as guidelines for developing Pixhawk-compliant flight controllers. A key advantage of following these standards is seamless integration with the PX4 ecosystem, granting access to numerous applications and components. However, the lack of open-source hardware designs and schematics increases development complexity.

Methodology: Two flight controllers were developed in line with open-source platforms. These models were then tested with commercial platforms to verify the performance and compatibility.

PW Module: The Please Work (PW) Module (shown in Figure 1.) is a 50x50 mm flight controller based on the Crazyflie bolt 1.1 schematics. The board has similar components; with further extendibility and pins for direct interfacing. The board has the ability to run limited PX4 firmware. The solution was a successful experience gain, however, on verification, challenges emerged from firmware conflicts leading to some inconvenient use conditions

SWAN Module: The Should Work Approximately Now (SWAN) Module (shown in Figure 1.), with a 35x35 mm footprint, was subsequently developed based on the FMU-v6c Pixhawk standard. The board

[a] FRSDAN004@myuct.ac.za

was confirmed to have increased PX4 compatibility when compared to the PW module, enabling access to external components and applications.

Figure 1: PW (left) and SWAN (right) flight controller solutions.

SWAN Results: As a result of the satisfactory performance of the SWAN module and to assess the performance and limitations of the prototype, an additional test was designed. The test involved a control system built in Simulink, which targeted roll angles of: 0°, 10°,, and -10° at various time points. The control system was deployed to both a commercial flight controller (Holybro Kakute H7 [4]) and the PW prototype. The flight controllers were stacked together and roll angle measurements collected (shown here).

Figure 2 illustrates the roll angle measured from both flight controllers, revealing a strong similarity between the transient response from the commercial and custom-built systems. The Root Mean Square Error (RMSE) for the roll angle was calculated to be 0.799°, indicating a relatively low difference as a typical IMU (in this case, a BMI088 [5]) has orientation errors of approximately 0.5°. In addition to this error, there existed significant alignment offsets for each controller in the stacked configuration. Despite the minor offset, the transient response of the SWAN prototype demonstrated significant alignment to the commercial alternative.

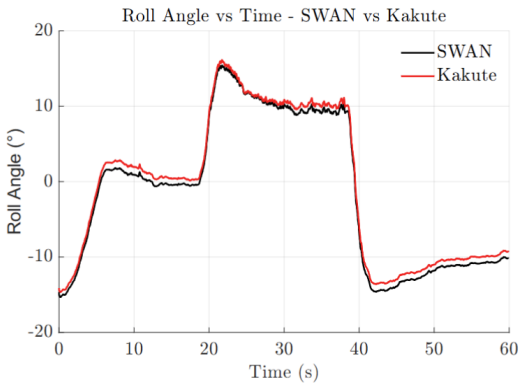

Figure 2: Graph showing roll angle (◦) vs time (s) for the dynamic test of the Kakute (red) and SWAN (black) controllers.

Cost Comparison: Table 1 highlights the potential of a custom solution to achieve significant cost savings compared to their open-source commercial platform (Crazyflie Bolt 1.1 & Pixhawk 6C respectively). The PW and SWAN prototypes can be manufactured at only 11.6% and 10.74% of the cost of the commercial platform, when producing 25 units. This substantial reduction in cost aims to support the widespread access of the project by enhancing accessibility to affordable UAV research platforms. Notably, there are significant overheads associated with providing commercially compliant systems which the custom-built controller avoids. The shown reductions therefore aim to highlight the cost advantage of customisable hardware for in-house research purposes and not for providing a completely commercially compliant system.

Table 1: Cost comparison between PW & SWAN Prototype and their commercial alternative.

	PW	SWAN
Cost for 5 boards ($)	242.45	232.42
Cost per board ($)	48.49	46.48
% Cost for 5 boards	23.65	32.97
% Cost for 25 boards	11.60	10.74

Conclusion: This research successfully met its objectives by reviewing flight controller fundamentals, evaluating existing designs, and analysing open-source firmware to guide development decisions. By selecting an appropriate open hardware standard, two prototypes were developed: the first provided practical insights into PX4-Autopilot architecture, while the second demonstrated a fully customised, adaptable flight controller capable of accommodating specific use cases, physical constraints, connector standards, and sensor configurations. In particular, the PW prototype achieved significant cost savings compared with commercial alternatives without compromising on performance or compatibility. Together, the prototypes illustrate the feasibility, robustness, and scalability of custom UAV systems, highlighting their potential to support accessible innovation and serve as a foundation for future research and development in UAV technologies.

References:

1.Amuthesh, Flight Controller Wiring for Drones [online].Available from: https://www.linkedin.com/pulse/flight-controller-wiring-drones-amuthesh-m-ychpc/ [2025].

2.Bitcraze. Crazyflie 2.1+ [online]. Available from: https://www.bitcraze.io/products/crazyflie-2-1-plus/ [2025].

3.Pixhawk. Pixhawk Standards [online]. Available from: https://github.com/pixhawk/Pixhawk-Standards [2025].

4.Holybro, Kakute H7 v1.3 (MPU6000), [online]. Available from: https://holybro.com/products/kakute-h7 [2025]

5.Bosch Sensortec, Inertial measurement unit BMI088[online] Availbe from: https://www.bosch-sensortec.com/products/motion-sensors/imus/bmi088/ [2025]

ANALYSIS OF BIOMETRY DATA FROM MAJOR POPULATION GROUPS ON THE ANTERIOR CHAMBER OF THE HUMAN EYE AND ITS IMPLICATION ON GLAUCOMA

V.T. Muzhambi[a], I Karangwa[b], N Basson[c], S Williams[d] Y.L Mgwebi[e] & W.H Ho[a,f]

[a] Department of Mechanical Engineering, University of Cape Town, Cape Town, South Africa
[b] Department of Statistical Science, University of Cape Town, Cape Town, South Africa
[c] Department of Thermal and Fluids Engineering, University of Twente, Netherlands
[d] Department of Ophthalmology, University of the Witwatersrand, South Africa
[e]Department of Medicinne, University of Cape Town, Cape Town, South Africa
[f]Centre for Research in Computational and Applied Mechanics, University of Cape Town, South Africa

This study investigates ethnic variations in anterior chamber biometry and their influence on glaucoma risk. A meta-analysis of 48 studies (1997–2024) comprising 57,139 eyes from Sub-Saharan African (SSA), East Asian (EA), Middle Eastern (ME), and European descendant (ED) populations was conducted. Significant differences were observed across key parameters including anterior chamber depth, lens thickness, and central corneal thickness. Sub-Saharan African eyes exhibited shallower chambers, thicker lenses, and thinner corneas, indicating higher susceptibility to primary angle-closure glaucoma (PACG). In contrast, East Asian populations showed longer axial lengths, correlating with elevated myopia-related risk. These findings highlight the importance of ethnicity-specific screening and diagnostic thresholds for glaucoma, reinforcing the need for inclusive biometric data in clinical practice.

Introduction: Glaucoma is a leading cause of irreversible blindness worldwide, disproportionately affecting specific ethnic populations[1]. Anatomical variations in anterior chamber biometry such as anterior chamber depth (ACD), anterior chamber angle (ACA), axial length (AL), lens thickness (LT), central corneal thickness (CCT), white-to-white (WTW) corneal diameter, and pupil diameter (PD) are key determinants of glaucoma risk[2]. While previous studies have provided valuable insights, most have focused on single populations, leading to fragmented knowledge[3]. This study consolidates biometric data from multiple populations to investigate ethnic differences and their implications for glaucoma risk, with a view to supporting tailored diagnostic and treatment approaches.

Methodology: A meta-analysis of 48 peer-reviewed studies published between 1997 and 2024 was conducted, encompassing biometric data from 57,139 eyes across four major ethnic groups: SSA[1,4], EA[1,3,5], ME[2,3], and ED[1,2,6]. Relevant studies were identified through comprehensive searches in PubMed, Scopus, and Google Scholar using combinations of keywords such as ocular biometry, glaucoma, and ethnic differences. Inclusion criteria required adult participants (>18 years), clearly defined ethnicity, and the use of standardized anterior segment measurement techniques such as Optical Coherence Tomography (OCT), Scheimpflug imaging, Ultrasound Biomicroscopy (UBM), or corneal topography. Studies with pediatric cohorts, duplicate data, or non-peer-reviewed sources were excluded. Where results were disaggregated by sex or age, weighted averages were computed. Cohen's d was used to quantify effect sizes and assess the magnitude and clinical relevance of biometric variations between populations. The updated Cohen's d thresholds of 0.15 (small), 0.40 (medium), and 0.75 (large) were applied to interpret effect sizes[7].

Results: Distinct biometric variations emerged between groups. ACD was highest in EA (3.00 ± 0.16 mm) and lowest in SSA (2.76 ± 0.30 mm), indicating elevated PACG risk in SSA[4]. AL was longest in EA (23.55 ± 1.19 mm), correlating with high myopia prevalence. CCT was thinnest in SSA (~533 µm) vs EA (~560 µm), potentially leading to underestimation of intraocular pressure and delayed diagnosis[5]. LT was thickest in SSA, contributing to angle crowding and PACG susceptibility. WTW was largest in ED (~12.01 mm), smallest in EA (~11.67 mm), influencing intraocular lens (IOL) sizing. ACA was widest in ME (~38.8°), narrowest in ED (~32.4°). PD differences were minor but remain clinically relevant. Cohen's d analysis revealed moderate-to-large effect sizes for ACD, CCT and LT showed d values approaching or exceeding 0.75 in several group comparisons, indicating large, practically significant differences that influence ACD and angle configuration. CCT differences reflected medium-to-large effects, suggesting measurable variation in corneal thickness sufficient to affect intraocular pressure estimation and screening precision. Collectively, these effect sizes demonstrate that the observed biometric disparities are substantial enough to inform ethnicity-specific diagnostic thresholds and enhance glaucoma detection accuracy.

Conclusion: This meta-analysis confirms that meaningful biometric variations exist among major ethnic groups, with effect sizes indicating clinically significant differences in parameters such as ACD, LT, and CCT. The use of Cohen's d reinforced that these variations are not only statistically detectable but also diagnostically relevant. Such disparities influence anterior chamber configuration and intraocular pressure estimation, thereby shaping glaucoma risk profiles. These findings underscore the necessity of incorporating ethnicity-specific biometric baselines into diagnostic frameworks and screening algorithms.

Thersiamuzhambi@gmail.com or MZHVHU001@myuct.ac.za

Table 1: Average Measurements per Parameter per Ethnicity

	E.A	E.D	M.E	S.S.A
ACA (°)	38.24 ± 16.20	33.25 ± 7.40	38.78 ± 5.25	36.61 ± 6.43
ACD (mm)	3.00 ± 0.16	2.96 ± 0.25	2.79 ± 0.17	2.76 ± 0.30
AL (mm)	23.55 ± 1.19	23.65 ± 0.84	23.31 ± 0.50	23.06 ± 0.92
CCT (µm)	559.83 ± 34.82		557.50 ± 34.21	509.89 ± 33.61
LT (mm)			4.18 ± 0.10	3.93 ± 0.57
WTW (mm)	11.67 ± 0.33	12.01 ± 1.25	11.72 ± 0.48	11.72 ± 0.52
PD (mm)	4.50 ± 0.84	4.22 ± 0.90		

Table 2: Pairwise Cohen's d Effect Sizes and Sample Sizes (N) for Biometric Parameters Across Ethnic Groups

		S.A vs M.E	S.A vs E.D	S.A vs E.A	M.E vs E.D	M.E vs E.A	E.D vs E.A
ACA	N	5313	9131	8126	4222	3217	7035
	D	0.322	0.507	0.150	0.758	0.035	0.446
ACD	N	13690	7872	22939	14918	25341	24167
	D	1.956	0.395	1.224	1.852	0.349	0.145
AL	N	3313	8042	5467	8895	6320	11049
	D	0.386	0.344	0.438	0.219	0.249	0.061
WTW	N	3472	3217	29558	3411	29752	28491
	D	0.002	0.341	0.217	0.359	0.222	0.658
CCT	N	5782	-	5233	-	1695	-
	D	1.314	-	1.368	-	0.068	-
LT	N	7262	-	-	-	-	-
	D	1.542	-	-	-	-	-
PD	N	-	-	-	-	-	1492
	D	-	-	-	-	-	0.315

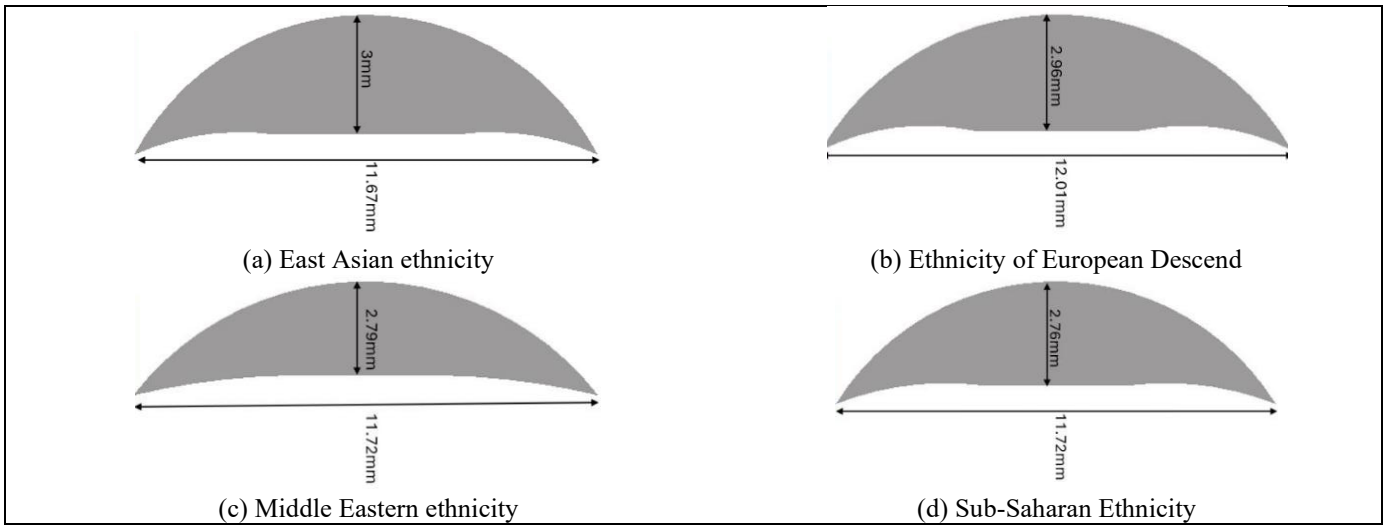

(a) East Asian ethnicity (b) Ethnicity of European Descend

(c) Middle Eastern ethnicity (d) Sub-Saharan Ethnicity

Figure 1: Average Shape of Eye Per Ethnicity

References:

1. Congdon NG, Youlin Q, Quigley H, et al. Biometry and Primary Angle-closure Glaucoma among Chinese, White, and Black Populations. *Ophthalmology*. 1997;104(9):1489-1495. doi:10.1016/S0161-6420(97)30112-2

2. Marchini G. Biometric data and pathogenesis of angle closure glaucoma. *Acta Ophthalmol Scand*. 2002;80(s236):13-14. doi:10.1034/j.1600-0420.80.s236.3.x

3. Ang M, Chong W, Tay WT, et al. Anterior Segment Optical Coherence Tomography Study of the Cornea and Anterior Segment in Adult Ethnic South Asian Indian Eyes. *Investig Opthalmology Vis Sci*. 2012;53(1):120. doi:10.1167/iovs.11-8386

4. Mashige KP, Oduntan OA. Axial length, anterior chamber depth and lens thickness: Their intercorrelations in black South Africans. *Afr Vis Eye Health*. 2017;76(1):7 pages. doi:10.4102/aveh.v76i1.362

5. Mercieca K, Odogu V, Fiebai B, Arowolo O, Chukwuka F. Comparing Central Corneal Thickness in a Sub-Saharan Cohort to African Americans and Afro-Caribbeans. *Cornea*. 2007;26(5):557-560. doi:10.1097/ICO.0b013e3180415d90

6. Rufer F, Schroder A, Erb C. White-to-White Corneal Diameter: Normal Values in Healthy Humans Obtained With the Orbscan II Topography System. *Cornea*. 2005;24(3):259-261. doi:10.1097/01.ico.0000148312.01805.53

7. Loth E, Ahmad J, Chatham C, et al. The meaning of significant mean group differences for biomarker discovery. Ouellette F, ed. *PLOS Comput Biol*. 2021;17(11):e1009477. doi:10.1371/journal.pcbi.1009477

INDUCTION HEATING IN AN EXTREME-TEMPERATURE FRACTURE TOUGHNESS TESTING APPARATUS

Braden Nicholson[a], Thorsten Becker[b]

[a,b]Centre for Materials Engineering, Department of Mechanical Engineering, University of Cape Town, Rondebosch, Cape Town, South Africa

A fracture toughness testing apparatus was designed for a Gleeble 3800 machine to perform induction-heated tests at up to 1000 °C. This involved consideration of the mechanisms of induction heating and heat transfer. The apparatus was designed with several features, including unloaded heat shields and cooling channels, to prevent critical components from reaching dangerous temperatures. Manufacturing is almost complete, with testing planned shortly.

Introduction: The mechanism of material failure via fatigue crack propagation and subsequent brittle fracture has been empirically studied since the early- to mid-19th century—it has long been known that flaws in materials reduce their observed strength in service. During the 20th century, the field became known as "fracture mechanics", and in modern times fracture is a major consideration in design. The Centre for Materials Engineering (CME) at the University of Cape Town (UCT) conducts research into fatigue and fracture of various engineering metals, including nickel and titanium alloys, at high temperatures. At present, this testing is done with a furnace mounted to a hydraulic ESH fatigue machine. This is disadvantageous as 1) it takes hours to heat up and cool down; 2) it causes oxidation in the fixtures as the environment is also heated; 3) it does not allow for optical methods such as DIC; and 4) it cannot reach above 600 °C. The CME also houses a Gleeble 3800,[1] a thermomechanical simulation machine with an attached induction heating system capable of performing tests at temperatures exceeding 1000 °C in a vacuum chamber. However, it does not contain a fracture toughness testing module. Adding this capability to the machine would improve the testing abilities of the lab by making testing more efficient and by broadening the range of possible measurement techniques—it would address each of the four listed issues. The aim of this project is to design, manufacture, and validate a fracture toughness testing apparatus for the Gleeble 3800, capable of operating at sample temperatures up to 1000 °C, which complies with relevant ASTM standards.

Background literature: For fracture toughness testing, sample geometry and testing fixture guidelines are governed by ASTM E1820.[2] The CME primarily uses compact tension (CT) samples, which are loaded via a system of clevises and clearance pins to allow for slight rotation. Clevises are machined from a metal (almost ubiquitously a steel) with strength and stiffness sufficient to withstand the necessary loading with minimal strain. The design challenge in this project is presented by the degrading properties of metals at high temperatures. Any material feasible for this application does not have sufficient strength at 1000 °C to withstand the potential loading—even nickel-based alloys are weak at this temperature.[3] Therefore, to achieve the aim, the clevises would need to be kept below the sample temperature. To do this, the heating method must be considered. Induction heating works through a high-frequency AC current, which induces an oscillating magnetic field. This magnetic field induces eddy currents in the workpiece, thus dissipating power and heating it.[4] One feature of induction heating is its "skin depth" (δ) which describes the exponential decay of the magnetic field below the surface of a material. At a depth of δ, the induced current density has decayed to 37% of its initial value, and at a depth of 4δ, it has decayed to virtually zero. Since for most induction heated metals $\delta < 0.3$ mm, power dissipation essentially all happens in the outermost 1.2 mm of material.[5] Also important for design is the effect of geometry on heat transfer. Heat flows via conduction from the sample to the other components and then via convection into the coolant. The design goals are to maximise the temperature difference between sample and other components and to minimise it between the components and the coolant. According to Fourier's law of conduction and Newton's law of cooling, this can be achieved by reducing area of contact between system components and by maximising it in the cooling channels. Increased coolant velocity and channel length also serve to reduce clevis temperature.[6]

Design: Figure 1 shows part of the current design.

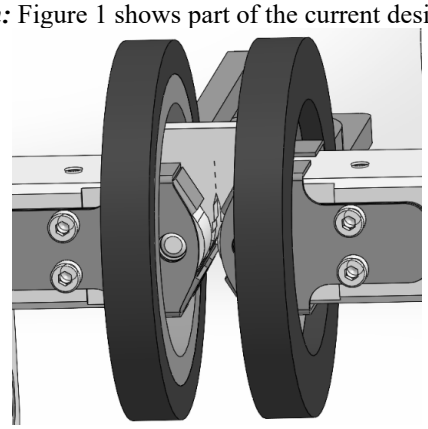

Figure 1: CAD design of the clevises inside the heating coils, with a CT sample mounted.

[a] NCHBRA002@myuct.ac.za

Many design features were intended to ensure the maximum possible temperature difference between sample and clevis such that the clevis has a low risk of failure. These include the following:

1. Tungsten carbide (94WC-6Co) pins were bought for use with the apparatus. They have extremely high strength (≈1790 MPa) and resist strength degradation at high temperature.[7] Additionally, their lower thermal conductivity reduces heat transfer between sample and clevis.
2. The clevises were designed with variable wall thickness to minimise area of contact with the sample, reducing heat transfer.
3. The clevises contained cooling channels that could be integrated with the internal Gleeble cooling system. These are shown in Figure 2.
4. Unloaded heat shields were placed over the clevises, which only contact them in a location not directly heated. This blocks the magnetic field and allows for heat to be transferred backwards and not into critical sections of the clevis.
5. The clevises were designed for the smallest and thinnest sample geometry in conformance with ASTM E1820. This is beneficial for heating uniformity and lowers the stress on the apparatus.

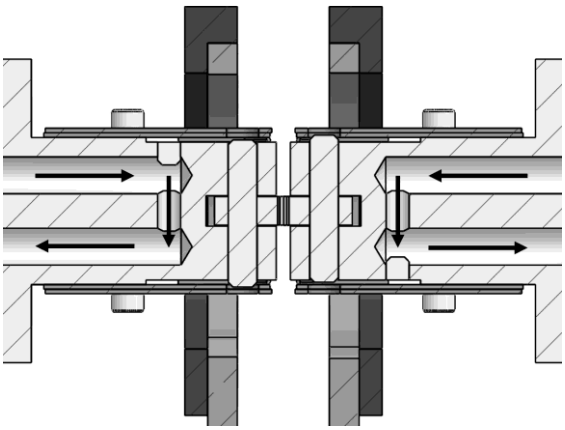

Figure 2: A section view of the cooling channels with coolant flow indicated by arrows.

Outcomes: A low-temperature (max. 500 °C) version of the apparatus was manufactured. Clevises were machined from AISI H13 tool steel and heat treated to 56 HRC. Figure 3 shows the apparatus being tested for assembly and fitment. The design fits to the machine as expected without interference with other functions. Assembly is straightforward and does not require the operator to lift excessive weight or to reach difficult places. Additionally, the clevis alignment process using the pictured bracket was proven sufficient for sample orientation.

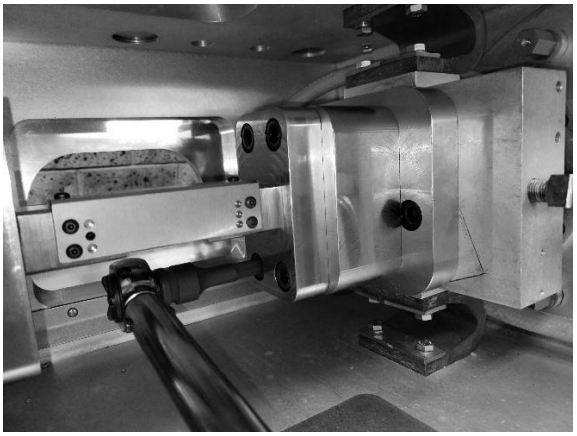

Figure 3: Part of the apparatus mounted to the machine, with an alignment bracket attached and a torque wrench fitted to a cap screw head.

Work outstanding: While the bulk of the low-temperature apparatus has been manufactured, the heat shields have not, and tests have not yet been performed. One of the most important characteristics is the distribution of temperature in the rig; this will be quantified by taking data from several thermocouples in differing locations on the sample and on critical apparatus components. After cooling efficiency is determined, a high-temperature clevis will be designed which will support sample temperatures of 1000 °C. These will then be tested, after which results will be consolidated and the entire apparatus put into use. Should time allow, the design will be scaled for different sample geometries.

References:

1. "Gleeble 3800-GTC." Dynamic Systems Inc, 2024. Accessed: Dec. 04, 2024. [Online]. Available: https://gleeble.com/products/gleeble-systems/gleeble-3800.html
2. *Standard test method for measurement of fracture toughness*, E1820-24, 2024. doi: 10.1520/E1820-24.
3. *ASM Handbook: Properties and Selection: Nonferrous Alloys and Special-Purpose Materials*, 10th ed., vol. 2. ASM International, 1990.
4. E. M. Purcell and D. J. Morin, *Electricity and Magnetism*, 3rd ed. 2013.
5. E. J. Davies, *Conduction and Induction Heating*. Peter Perigrinus Ltd., 1990.
6. J. P. Holman, *Heat Transfer*, 9th ed. McGraw Hill, 2002.
7. W. Acchar, U. U. Gomes, W. A. Kaysser, and J. Goring, "Strength Degradation of a Tungsten Carbide-Cobalt Composite at Elevated Temperatures," *Mater. Charact.*, vol. 43, no. 1, pp. 27–32, July 1999.

Development of a virtual test facility for large diameter axial flow cooling fans

JA Steenkamp[a], SJ van der Spuy[a] & HCR Reuter[b]

[a] Department of Mechanical and Mechatronic Engineering, University of Stellenbosch, Stellenbosch, South Africa

[b] Industrial Water Cooling (IWC), a NEXT Cooling Group, Stellenbosch, South Africa

The objective of this work is to develop a virtual test facility for large diameter axial flow fans using computational fluid dynamics (CFD). A periodic three-dimensional CFD model (P3DM) based on an ISO 5801[1] type A fan test facility is developed, automated and adapted for a range of fan geometries using ANSYS® Fluent and PyFluent scripting. The output of the P3DM is validated against experimental data as well as supplementary analytical models based on the Euler turbomachinery equation and blade element momentum theory. Results agree well with the experimental data of various fans and does so at a relatively low computational cost.

Introduction: Large diameter axial flow fans are critical components in mechanical draft air-cooled condensers and air-cooled heat exchangers. Highly efficient fans limit parasitic power losses and improve the overall performance of the plants where they are utilised. Fan performance testing is traditionally done by testing physical scale models, which can be time consuming and expensive. Recent advances in computational hardware and software presents CFD as a potentially useful tool to mitigate this, but setting up a simulation that yields accurate results requires a good understanding of the underlying fluid mechanics and CFD principles, and familiarity with CFD software. This work attempts to address these challenges by developing a virtual test facility that allows a user to model the performance of an axial flow fan in a reasonable time with limited inputs. Analytical models based on the Euler turbomachinery equation and blade element theory, referred to as the blade element model (BEM) are initially developed as a foundation. A periodic three-dimensional CFD model based on an ISO 5801 type A fan test facility is then developed, validated and verified for a known fan. The setup of the model is automated using PyFluent scripts and it is adapted to accept a range of fan geometries with minimal changes.

Analytical models: The initial analytical model assumes two-dimensional, axisymmetric flow with no total pressure loss. Relations are found between duty point, hub-tip ratio and downstream velocity distribution to find preliminary estimates of ideal fan static pressure and fan static efficiency.

The analytical model is expanded to consider blade geometry. Spanwise lift and drag forces from two-dimensional blade elements are linked to the spanwise distribution of axial and tangential velocity, from which fan static pressure and fan static efficiency is calculated using the Euler turbomachinery equation. The lift and drag coefficients are obtained using XFOIL[2].

Numerical model: A P3DM based on the same used in previous studies[3] is set up with the commercial CFD code ANSYS® Fluent. The Reynolds averaged Navier-Stokes (RANS) equations are solved in a reference frame rotating with the fan rotor to simulate steady conditions. The generalised k-ω (GEKO)[4] model is used to model turbulence. The baseline mesh consists of ~1.9×10^6 cells. Verification and validation are carried out using the M-fan designed by Wilkinson[5]. The model is adapted and the setup automated for fans that differ from the M-fan in terms of blade shape, number of blades, hub-tip ratio, hub shape, solidity, tip gap and duty point. Figure 1 shows the computational domain and boundary conditions for the numerical model.

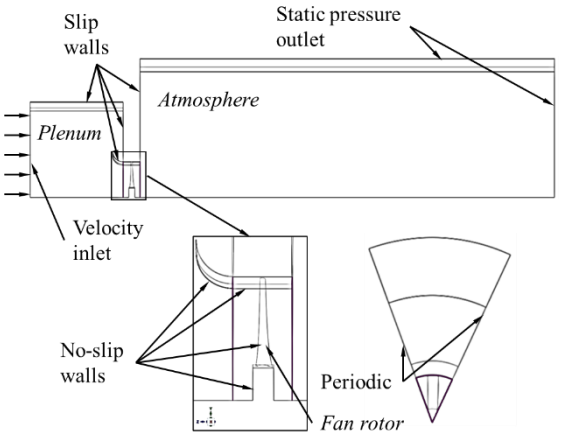

Figure 1: Numerical model computational domain and boundary conditions

Results: Exemplary performance prediction results for the M-fan are shown in Figures 2, 3 and 4 where "tc" is tip clearance. Exemplary results for the B2a fan[6] are shown in Figures 5, 6 and 7.

The BEM correlates well with the zero tip-gap P3DM results, especially at higher flow rates. The P3DM with a tip gap shows fair correlation with experimental results, though the fan static efficiency tends to be sensitive to relatively small overprediction of pressure and underprediction of shaft power, more prevalent for the B2a-fan results.

[a] 23553022@sun.ac.za

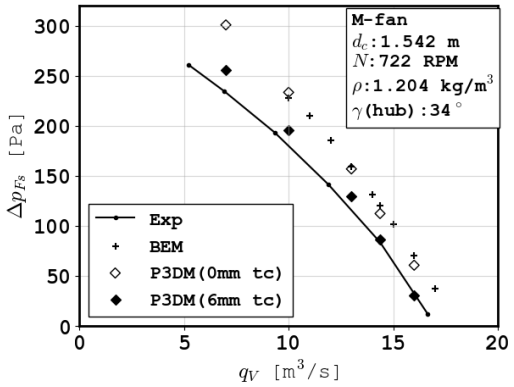

Figure 2: M-fan static pressure results

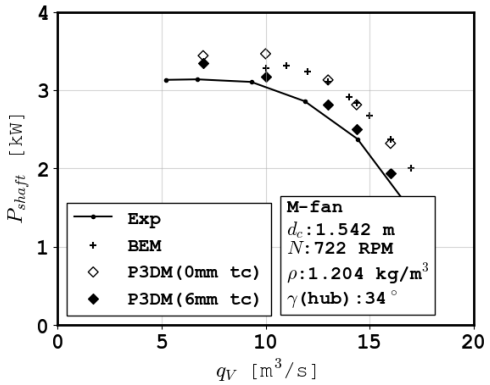

Figure 3: M-fan shaft power results

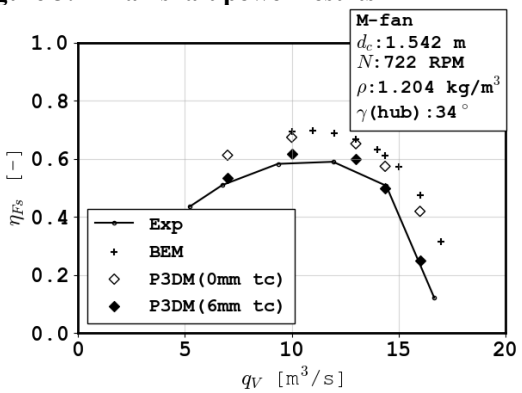

Figure 4: M-fan static efficiency results

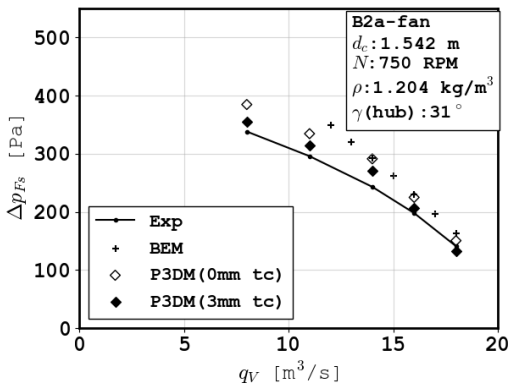

Figure 5: B2a-fan static pressure results

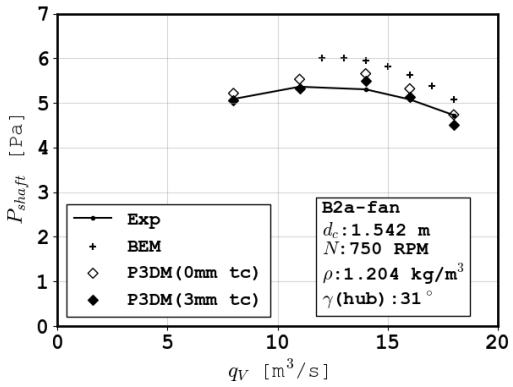

Figure 6: B2a-fan shaft power results

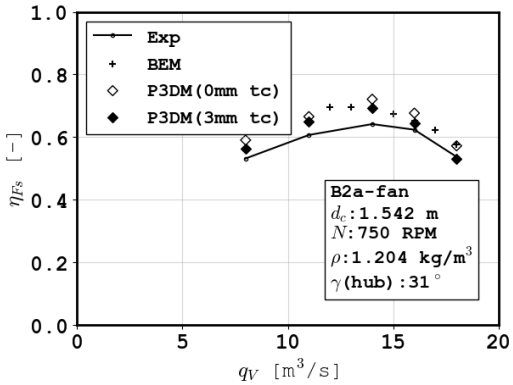

Figure 7: B2a-fan static efficiency results

References:

1. ISO, *Industrial fans – Performance testing using standardized airways.*2007.
2. Drela, M. *XFOIL: An analysis and design system for low Reynolds number airfoils*. 1989. Springer.
3. Louw, F.G., *Investigation of the flow field in the vicinity of an axial flow fan during low flow rates*, in Department of Mechanical and Mechatronic Engineering. 2015, University of Stellenbosch.
4. Menter, F.R., R. Lechner, and A. Matyushenko, *Best Practice: Generalised k-ω (GEKO) Two-Equation Turbulence Modeling in Ansys CFD*. 2021.
5. Wilkinson, M.B., *The Design of an Axial Flow Fan for Air-Cooled Heat Exchanger Applications*, in Department of Mechanical and Mechatronic Engineering. 2017, University of Stellenbosch.
6. Louw, F.G., *The Design of an Axial Flow Fan for Application in Large Air-Cooled Heat Exchangers*, 2012, presented at the ASME Turbo Expo GT2012.

DYNAMIC PROCESS MODEL INVESTIGATION INTO A BIOMASS-FIRED BOILER USING FLOWNEX® SE

David Sserwanja [a], Leon Malan [a] and Wim Fuls [a]

[a] ATProM Research Unit, University of Cape Town

Introduction

Biomass fired boilers are in operation in South Africa and globally to produce process heat and electricity. Apart from using material that may otherwise go to waste, biomass can also be considered as a sustainable fuel source. In comparison to other boiler fuels like coal and heavy furnace oil, the fuel composition of biomass can vary greatly. The moisture content, for example, can change as much as 20%. This variation, combined with the relatively small size of these furnaces and different operational requirements pose a significant challenge in boiler operation. In this project, a dynamic model of a biomass-fired boiler is developed in the Flownex simulation environment (Flownex® SE) for a boiler with no existing dynamic model. The model is first verified for steady state operation, whereafter several transient events are modelled. Perspectives on the boiler dynamic response and control are provided.

Case study boiler

The boiler is a subcritical water-tube unit co-firing coal and sugarcane bagasse in Southern Africa. It generates 105 t/h of superheated steam at 32 bar and 400 °C for sugar mill process heating and electricity production, with excess power sent to the grid. The system includes a moving-grate stoker, furnace, two bare-tube superheaters (SH1 and SH2), a spray-type attemperator (ATT), evaporator tube bank (EV), air heater (AH) and extended-surface economiser (EC) as shown in Fig 1.

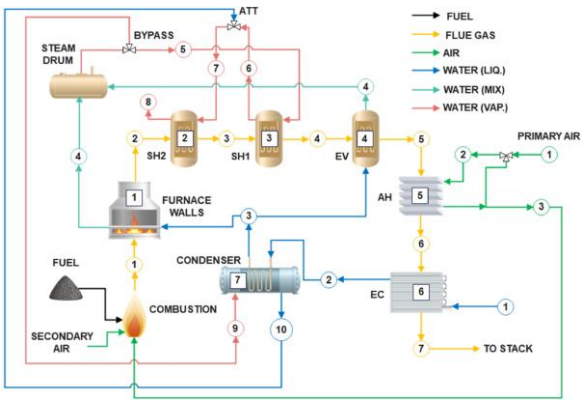

Fig 1: Process flow diagram of the integrated model[1].

Fuel is fed at the rear onto the moving grate and burns with the combustion air as it advances, with ash removed at the discharge zone. The flue gas released from the fuel combustion rises through the furnace and passes through SH2, SH1, EV, AH and EC before exiting through the stack.

Feedwater from the deaerator is preheated in the EC, further heated in a condenser, then sent through the EV and water walls surrounding the furnace. Steam/water mixture enters the steam drum, where only steam is separated, part of it is used for attemperation and the rest is superheated in SH1 and SH2.

Methodology

An integrated one-dimensional (1D) steady state model of the boiler is developed in Flownex® SE and verified against results from a Python model, which were validated with site data. This is then followed by setting up a 1D transient model in Flownex® SE. This steady state model consists of individual components, such as the combustion model, the furnace model, and models for each of the heat exchangers (SH1, SH2, EV, AH and EC).

In the fuel combustion model, the composition of the flue gas released, and the adiabatic flame temperature (AFT) of the fuel are determined. The flue gas composition is determined from the combustion molar balance equation and the AFT is determined from the combustion energy balance equation.

The furnace is modelled using zero-dimensional (0-D) semi-empirical furnace model known as the direct method (Hottel) [2] where the furnace exit temperature of the flue gas (FET) and the radiative-convective heat to the water walls around the furnace are determined.

For modelling SH1, SH2, EV, and EC, an in-house ATProM Flownex® SE library component known as the Evaporator, Convective Heater with Direct Radiation (ECRD) is used. This component is designed to be calibrated at a design-base performance condition (100% loading), from which an overall heat exchanger UA value is calculated.

It uses the design-base conditions to determine the overall heat transfer coefficient (UA) and pressure drop coefficients and then scales the UA for off-design operation using convection correlations and radiation effects. Heat transfer is calculated using the ε–NTU method for parallel, counterflow, or crossflow configurations. If steam is partially in the saturation region, single-stream evaporator equations are applied. During initialization, inlet and outlet steam conditions are evaluated to adapt the models to account for phase change. The design heat duty and effective specific heats for the gas and steam sides are calculated to determine heater effectiveness. An iterative loop computes the design overall UA, separating convective (UA_c) and radiative (UA_r) contributions. Radiation is represented as an equivalent UA using Stefan–Boltzmann relations [3].

At off-design conditions, only convection varies, while radiation remains constant. Gas-side convection is scaled using Reynolds, Prandtl, and property ratios as shown in Equation (1).

[a] davidsserwanja14@gmail.com

$$UA = UA_D \left(\frac{\dot{m}}{\dot{m}_D}\right)^a \left(\frac{k}{k_D}\right)^{\frac{2}{3}} \left(\frac{\mu}{\mu_D}\right)^{\frac{1}{3}-a} \left(\frac{cp}{cp_D}\right)^{\frac{1}{3}} \quad (1)$$

In Equation (1), the subscript *D* refers to the design condition. All fluid properties and mass flows apply to the gas side only and are calculated at the inlet temperature and pressure. The parameter *a* depends on tube spacing and other geometric factors; a value of 0.6 suits many geometries.

The combined off-design UA is calculated from the fouled, convective, and radiative components. Heat transfer is iterated until convergence using updated specific heats.

Since the working fluid in the AH is air rather than water, the same methodology is applied, with air used as the working fluid.

For calibration, an existing steady-state Python model of the same case study boiler is used with the inputs as shown in Table 1. The calibrated component can then be applied to other load cases, such as the 65% and 35% conditions used in this study. After developing individual models for the boiler components, they are integrated into a single complete model, as shown in Fig 1.

Table 1: Site measured data (model inputs) for 100% load case for the boiler [1].

Parameter	Values	Units
Fuel		
HHV of fuel	8894	kJ/kg
Unburnt carbon	0.007	Kg/kg
Furnace radiation loss	0.00514	W/W
Air		
Ambient air temperature	298	K
Ambient air pressure	101,325	Pa
Relative humidity	95	%
Excess air ratio	1.24	-
AH outlet air temperature	493	K
Water		
Inlet water temperature	371	K
Spray water temperature	487	K
Final steam pressure	2773	kPa(a)
Desired final steam temperature	675	K
Final steam flow rate	28.8	kg/s

Steady state verification.

Table 2: Comparison of Flownex and Python results.

100 % load case				
Steam side				
Parameter	**Units**	**Flownex**	**Python**	**Error (%)**
SH1 outlet temperature	K	648.85	649.6	0.116
ATT outlet temperature	K	576.4	577	0.104
Spray water temperature	K	487	487	-
SH2 outlet pressure	kPa(a)	2773	2773	-
SH2 outlet temperature	K	674.2	674.4	0.030
Final steam flow rate	kg/s	28.8	28.8	-
Steam drum pressure	kPa(a)	3115.2	3115.2	-
EC inlet water temperature	K	371.2	371.2	-
EC outlet water temperature	K	466.7	464.9	0.387
Flue Gas Side				
EV outlet temperature	K	725.3	723.1	0.304
AH outlet temperature	K	650.1	648.2	0.293
EC outlet temperature	K	477.5	476.6	0.189
Air side				
AH inlet temperature	K	298.5	298.5	-
AH outlet temperature	K	479.2	479.2	0

Some of the results from the Flownex® SE steady state model validation with the Python model are presented in Table 2. The Flownex® SE steady state model shows a very good agreement with the results from the steady state model, with an error less than 0.5 % for all the compared parameters between the two models.

Current Work

The Flownex® SE transient model of the boiler is being developed by incorporating the thermal inertia of the fluids. Control systems, such as steam drum water level control, will be developed next. Finally, the transient behaviour of the boiler under varying fuel moisture content will be investigated.

References

[1] P. Rousseau, R. Laubscher, and B. T. Rawlins, "Heat Transfer Analysis Using Thermofluid Network Models for Industrial Biomass and Utility Scale Coal-Fired Boilers," *Energies (Basel)*, vol. 16, no. 4, p. 1741, Feb. 2023, doi: 10.3390/en16041741.

[2] Y. Zhang, Q. Li, and H. Zhou, "Heat Transfer Calculation in Furnaces," in *Theory and Calculation of Heat Transfer in Furnaces*, Elsevier, 2016, pp. 131–172. doi: 10.1016/B978-0-12-800966-6.00005-3.

[3] A. / Prof and W. Fuls, "Rankine Cycle Components."

[a] davidsserwanja14@gmail.com

DESIGN, SIMULATION, AND TESTING OF A SPRAY WASHING DRONE FOR CLOSE-RANGE CLEANING

Z. Bisschoff[a] & W.J. Smit[b]

Department of Mechanical and Mechatronic Engineering, Stellenbosch University, Stellenbosch, South Africa

Spray washing drones can clean hard-to-reach surfaces that typically require risky manual labour. These drones make use of high-pressure water to clean surfaces like high-rise building windows, rooftop solar panels, and heliostats. Spray-washing drones are exposed to various external forces during operation, which must be actively counteracted to maintain a stable position while washing. The spray reaction force is the most significant disturbance, making it challenging for the drone to maintain a fixed position during washing and potentially causing a collision with the surface when washing is abruptly stopped. In this research, several different drone configurations were designed, simulated, and tested to identify the one that best maintains the drone in a fixed position during washing and minimises forward drift after washing. The integration of a pressure switch system performed the best, enabling the drone to maintain stability during washing and reducing forward drift by 45%.

Introduction: Spray washing drones provide an effective solution for cleaning surfaces that are difficult to reach manually. Hard-to-reach surfaces like high-rise building windows and rooftop-mounted solar panels typically require cleaners to use special equipment like rappel gear or scaffolding to work at dangerous heights. The hazardous working conditions frequently result in fall incidents where workers are injured or killed[1]. Spray washing drones can also be used to wash heliostats on concentrated solar power (CSP) plants. Conventional heliostat cleaning methods involve using large, specialised trucks with pressure washing nozzles fitted to a hydraulic arm to clean the heliostats. The combination of oversized trucks and human error often results in damage to heliostats. A spray washing drone can operate in confined spaces and use sensors to maintain a safe distance from heliostats, thereby reducing the risk of damage.

Engineering Problem: A spray washing drone is continually subjected to external forces during operation. Figure 1 illustrates a free-body diagram of all the external forces acting on a spray-washing drone. High-pressure water is supplied by a ground-based pressure washer, which is connected to the drone through a high-pressure hose. High-pressure water exiting the nozzle produces a significant spray reaction force (F_{wash}) that pushes the drone away from the washing surface. For safe and efficient cleaning, the drone must maintain a constant distance from the washing surface. Specifically for cleaning heliostats, the spray nozzle must be close to the heliostat surface for effective cleaning. To remain stable during washing, the drone must counteract F_{wash} as well as additional forces such as the weight of the suspended hose (F_{hose}) and the hose bend force (F_{bend}).

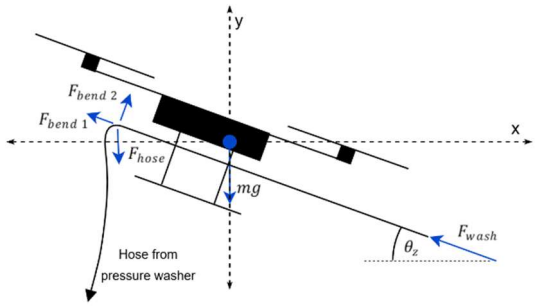

Figure 1: Free-body diagram of high-pressure spray washing drone.

The spray washing drone typically holds its position by pitching forward to create a thrust component that counteracts the spray reaction force. The drone's position controller automatically reacts to external disturbances and adjusts the drone's attitude to counteract the disturbances. A problem arises when the drone pitches forward to counteract the spray reaction force. If the reaction force is suddenly removed due to water supply problems, the drone drifts forward toward the washing surface, risking a crash or potential damage to the washing surface. When the reaction force is removed, the drone starts drifting forward because of the initial pitch angle. The controller responds only after detecting a position error; it then commands the drone to pitch backwards to stop the forward motion. At this stage, the drone already has forward momentum, which results in significant forward drift before the drone returns to its original position.

Methodology: The research methodology focuses on the design, simulation, and testing of a spray-washing drone that is capable of safely performing close-range cleaning operations. Different drone configurations were simulated to determine which configuration would be best for keeping the drone stable and minimising forward drift during the washing operation. The final drone build was based on the configuration that performed best in the simulations. Washing flight tests were conducted with the drone to validate the results of the simulations.

Drone Design and Simulation: The drone was designed specifically to be used as a spray washing

[a] 28862538@sun.ac.za

drone that cleans surfaces up to a height of 15m at a working pressure of 200 Bar and flow rate of 10 l/min, based on the washing conditions required for heliostats[2]. A general X-frame quadcopter design was used as a base for all the simulated configurations. The component selection of the standard quadcopter configuration was primarily guided by achieving a thrust-to-weight ratio of at least 3, as this is recommended for payload-carrying drones[3]. A flight controller that supports open-source ArduPilot flight control software was selected to allow for flight code modifications.

Simulations were conducted in MATLAB Simulink. The simulated flight controller was based on the ArduPilot control structure. The control systems and dynamics of the following drone configurations were modeled:

- **Standard quadcopter**: Uses position control and pitches forward to counteract the spray reaction force and maintain a constant distance from the washing surface.
- **Quadcopter with pressure switch**: Standard quadcopter with a pressure switch installed on the hose at the outlet of the pressure washer that triggers a rapid pitch-back manoeuvre when the pressure supply of water is abruptly removed. A normally open pressure switch was selected, as it can be easily attached to a small-diameter hose, is inexpensive, and can detect any type of water supply failure within the system.
- **Quadcopter with auxiliary motors**: Two additional counter-rotating motors and propellers in-line with the spray lance that directly counteract the spray reaction force.
- **Quadcopter with auxiliary motors plus pressure switch**: Same as above, with a pressure switch to instantly deactivate the extra motors when washing stops.

The standard quadcopter served as the control. A simulated spray reaction force was applied during washing and then abruptly removed, after which the forward drift (displacement in the x-axis) was measured. The 30 N spray reaction force was calculated from the nozzle dimensions and the washing conditions required for heliostat cleaning. The standard quadcopter controller gains were used for horizontal and vertical position control in all configurations, with the exception of the auxiliary motors configuration, which used a custom controller for the horizontal position control. This custom controller's gains were tuned to minimise the forward drift for this configuration in order to fairly compare it to the other configurations.

Experimental Flight Validation: The simulation results guided the final drone build, which was tested using a pressure washer under the same conditions as the simulations. In the experiments, the spray reaction force was applied and then abruptly removed once the drone stabilised. A video camera captured the subsequent forward drift, and Tracker software was used to measure the drone's x-axis displacement.

Results and Discussion: The simulations revealed that the quadcopter with pressure sensor configuration was the best practical solution. All configurations maintained steady flight under washing conditions, but the quadcopter with a pressure sensor and the quadcopter with extra motors plus a pressure sensor showed the greatest reduction in forward drift. The quadcopter with a pressure sensor configuration reduced forward drift by almost 60%; it only drifted forward by 0.34m compared to 0.8m from the standard quadcopter. Since both configurations performed similarly, the quadcopter with a pressure sensor configuration was selected for the final build due to its simpler and more efficient design.

The experimental flight validation yielded similar results to the simulation. Figure 2 shows the results of the experimental flight validation, measuring forward drift from the moment washing stopped. The quadcopter with a pressure sensor configuration reduced forward drift by 45%. The forward drift experienced by the standard quadcopter was 0.97m compared to only 0.53m experienced by the pressure switch configuration. The significant reduction in forward drift is a direct result of the faster response triggered by the pressure switch system compared to the response from only the position controller.

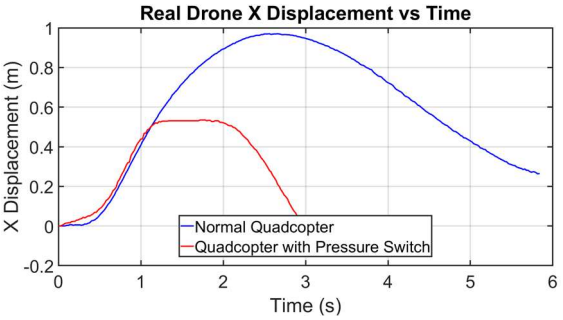

Figure 2: Experimental flight validation results.

References:

1. Hussein, F., Hisham El, S. & Alaa, K. Robotic Façade Cleaning System for High-Rise Building. International Conference on Computer Engineering and Systems, 2019.

2. Fernández-García, A., Álvarez-Rodrigo, L., Martínez-Arcos, L., Aguiar, R. & Márquez-Payés, J. M. Study of Different Cleaning Methods for Solar Reflectors Used in CSP Plants. Energy Procedia 49, 80-89, 2014.

3. Biczyski, M., Sehab, R., Whidborne, J., Krebs, G. & Luk, P. Multirotor Sizing Methodology with Flight Time Estimation. Journal of Advanced Transportation, 2020.

DESIGN AND SIMULATION OF AN ASSISTIVE LOWER LIMB EXOSKELETON

Mukengere MV & Petersen M

Department of Mechanical Engineering, Cape Peninsula University of Technology, Cape Town, South Africa

Lower limb impairments are increasingly affecting the elderly, and this is expected to become a serious problem by 2050, as this demographic is projected to reach 2.1 billion. A lower limb exoskeleton (LLE) offers a potential solution to this challenge. In this study, a size-adaptable 3D model of an assistive LLE was developed using SolidWorks, followed by a Finite Element Analysis (FEA) in ANSYS to assess the structural integrity of the robot frame. Additionally, a gait controller for the robot was designed using MATLAB to mimic human walking based on the kinematic and dynamic model of the LLE.

Introduction: According to the United Nations, the elderly population was 962 million in 2017, and this is expected to reach 2.1 billion by 2050[1]. Recently, exoskeletons have become a key technology for assisting individuals with limb disabilities, sparking interest due to their potential profitability, where the industry is projected to reach R32.4 billion by 2025[2]. To enable the use of the LLE without crutches, Atalante incorporated six degrees of freedom related to the lower limb into its design[3]. In contrast, the Vanderbilt LLE design mainly focuses on the sagittal plane, with the hip and knee pitch joints actuated to support locomotion within this system[4]

Problem statement: Despite advancements in LLEs, many walking robots remain heavy for everyday use[5], causing higher metabolic costs and reducing comfort[6]. The size and weight of LLEs depend on the materials and components, such as motors, harmonic drives, and batteries[7]. This research aims to create a lightweight, stable LLE that retains structural integrity.

Objectives: The primary aim of this research is to design a lightweight 3R walking LLE constrained in the sagittal plane, supported by several sub-objectives that serve as tools to achieve the main goal. First, develop an analytical kinematic and dynamic model of the LLE. Then, create a 3D size-adaptable LLE and perform FEA. Next, simulate a walking gait, then design a conceptual control system. Finally, build a prototype for experiments.

Stress analysis: After gathering the necessary information on existing LLE designs, the LLE related to this research was modelled in SolidWorks. Figure 1 shows the 3D model of the LLE on the right, alongside a Linear Inverted Pendulum Model (LIPM), which supports in achieving the LLE's walking gait cycle, as discussed later. Following the 3D modelling, an FEA of the leg segments was conducted using ANSYS.

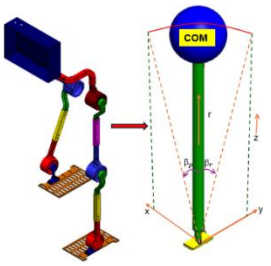

Figure 1: 3D Model of the LLE and its LIPM

In this mini-paper, only a section of the thigh is discussed in Figure 2 below, in the Results section. The simulation focused on specific parts to evaluate whether the selected components of the walking robot could withstand the axial loads in one scenario or the transverse loads in the other.

The materials used were aluminium 6082-T6 and 6061-T6 due to their strong strength-to-weight ratio; aluminium is generally known for this characteristic[8]. Low-carbon steel was used for fasteners because of its superior yield strength.

The results of the FEA of the sampled segment, specifically the thigh depicted in Figure 2 below, demonstrate the segment's capacity to withstand applied axial and transverse loads. In both scenarios, the maximum Von Mises stresses remained below the yield strength of aluminium and low-carbon steel, thereby preventing permanent deformation. Based on the structural analysis outcomes, it was concluded that this frame can support a user weight of up to 81 kg.

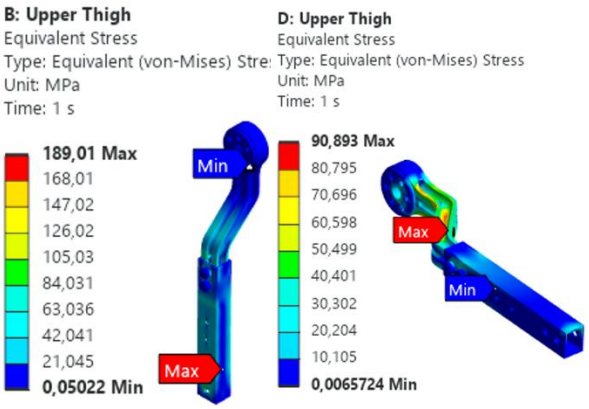

Figure 2: FEA simulation of the thigh

Walking simulation: After completing and validating the FEA simulation, the CAD file was imported into Simulink to design the walking gait, based on the principles of the LIPM, as shown in Figure 1, where the centre of mass (COM) is confined to move only within the horizontal plane, with the constraint plane represented by the normal vector (kx, ky, -1) and the z-

valerymmuk@gmail.com

axis intersection, zc, as defined by kajita[9] in the associated equation 1 below.

$$z = k_x x + k_y y + z_c \quad \textbf{1}$$

Using Equations 2 and 3 below, developed by Kajita[9], the motion of the walking robot was described with equation 2, and the LIPM orbital energy (E), representing the LLE, was defined in the second equation.

$$\ddot{y} = \frac{g}{z_{com}} y \quad \textbf{2}$$

$$E = \frac{1}{2}\dot{y}^2 - \frac{g}{2z_{com}} y^2 \quad \textbf{3}$$

The pose and orientation of the foot's end-effector were determined using the analytical method of forward and inverse kinematics. The existing relationship between the kinematics is shown below in Figure 3.

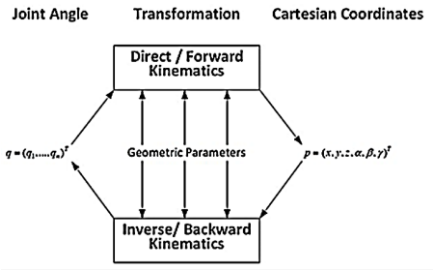

Figure 3: Kinematics of a mechanism[10]

Inverse dynamics were used to determine the exact torques required by the hip, knee, and ankle joints of the walking robot, utilising the equations of motion in relation to the Euler-Lagrange equation. The resulting torques were used to select the appropriate actuators for each joint. The equation of motion, provided below as equation 4, includes the mass matrix. $M(\theta)$, Coriolis terms$C(\theta, \dot{\theta})$, gravity vector $G(\theta)$, and the torque τ.

$$M(\theta)\ddot{\theta} + C(\theta, \dot{\theta})\dot{\theta} + G(\theta) = \tau \quad \textbf{4}$$

The simulation result of the walking gait cycle of the robot in MATLAB, as shown in Figure 4, demonstrates that the walking robot can walk 5.65 m in 10 seconds, under the influence of the defined forward and inverse kinematics, LIPM, and inverse dynamics.

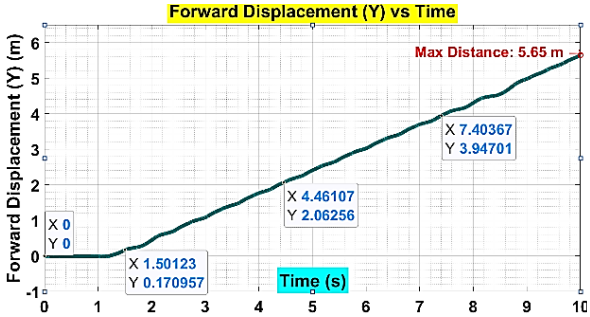

Figure 4: Travelled distance

Figure 5 illustrates the graphs related to the torque and angle of the hip joint, showing the maximum flexion and extension torques and angles.

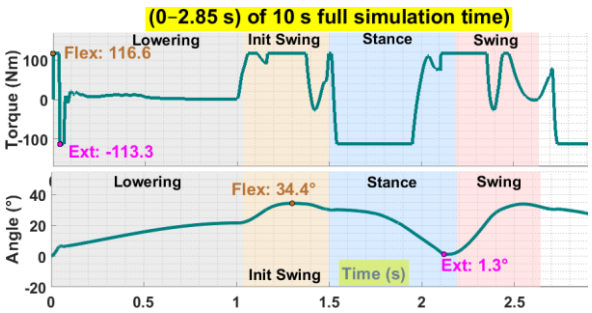

Figure 5: Torque and angle of the hip joint

Conclusion: The simulation results confirm that the walking robot can support the user's weight and effectively walk in the sagittal plane by using the specified joint torques to position its segments accurately.

References:

1. Department of Economic and Social Affairs. *World Population Prospects 2019: Data Booklet*. *United Nations* (2019).
2. Golabchi, A., Chao, A. & Tavakoli, M. A Systematic Review of Industrial Exoskeletons for Injury Prevention: Efficacy Evaluation Metrics, Target Tasks, and Supported Body Postures. *Sensors* **22**, (2022).
3. Kerdraon, J. *et al.* Evaluation of safety and performance of the self balancing walking system Atalante in patients with complete motor spinal cord injury. *Spinal Cord Ser Cases* **7**, (2021).
4. Farris, R. J., Quintero, H. A. & Goldfarb, M. Performance evaluation of a lower limb exoskeleton for stair ascent and descent with Paraplegia. in *Proceedings of the Annual International Conference of the IEEE Engineering in Medicine and Biology Society, EMBS* 1908–1911 (2012).
5. Fosch-Villaronga, E. & Özcan, B. The Progressive Intertwinement Between Design, Human Needs and the Regulation of Care Technology: The Case of Lower-Limb Exoskeletons. *Int J Soc Robot* **12**, 959–972 (2020).
6. Zhang, L., Liu, Y., Wang, R., Smith, C. & Gutierrez-Farewik, E. M. Modeling and Simulation of a Human Knee Exoskeleton's Assistive Strategies and Interaction. *Front Neurorobot* **15**, (2021).
7. Rodríguez-Fernández, A., Lobo-Prat, J. & Font-Llagunes, J. M. Systematic review on wearable lower-limb exoskeletons for gait training in neuromuscular impairments. *J Neuroeng Rehabil* **18**, 1–21 (2021).
8. Sharma, N., Saini, G. S., Singh, G., Goyal, S. & Sharma, P. A comprehensive study on aluminium alloy series-a review. *Recent Advances in Mechanical Engineering* **1**, 11–27 (2017).
9. Kajita, S. *et al.* Biped walking pattern generation by using preview control of zero-moment point. in *Proceedings - IEEE International Conference on Robotics and Automation* vol. 2 1620–1626 (2003).
10. Iris Dynamics Ltd. Kinematics relation. https://irisdynamics.com/articles/forward-and-inverse-kinematics (2023).

valerymmuk@gmail.com

EXTENDING A DIGITAL IMAGE CORRELATION ALGORITHM TO DEAL WITH DISCONTINUOUS DISPLACEMENT FIELDS

Samir Harris[a] & Thorsten H. Becker[abc]

[a] Centre for Materials Engineering, Department of Mechanical Engineering, University of Cape Town, Cape Town, South Africa
[b] Department of Mechanical and Mechatronic Engineering, Stellenbosch University, Stellenbosch, Country B
[c] eNtsa, Nelson Mandela University, Gqeberha, South Africa

This study aims to develop an extension of the state-of-the-art digital image correlation (DIC) algorithm, ADIC. Existing methods for addressing discontinuities, such as cracks, voids, or shear bands, are employed to enhance ADIC's capability to handle these issues. An outline of these methods illustrates how they can be combined and applied with ADIC to develop the extension.

Background: Digital Image Correlation (DIC) algorithms typically involve capturing a series of digital images of speckled material surfaces and partitioning the initial image into regions called subsets. An initial continuous function, known as the shape function, is used to project each subset from the reference image to the subsequent deformed image, as depicted in Figure 1.

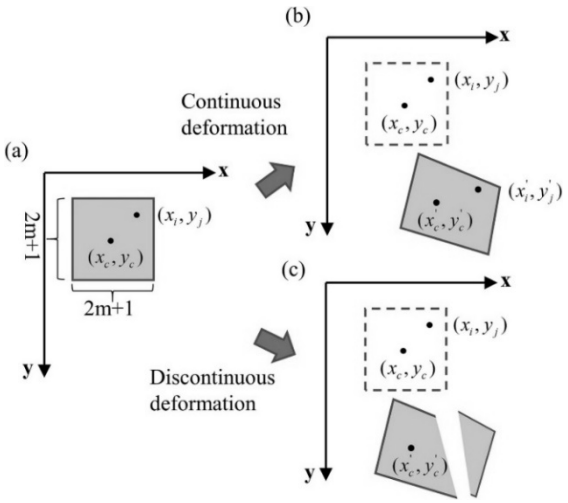

Figure 1: A subset before and after deformation. (a) Reference subset. (b) Continuous deformed subset. (c) Discontinuous deformed subset.[1]

The reference subsets are then compared to the deformed subsets using a correlation criterion that quantifies the effectiveness of the shape function. Discontinuities pose significant challenges to DIC methodologies. They disrupt the foundational assumption that a continuous shape function can accurately map a reference subset to its deformed counterpart. Consequently, DIC algorithms may struggle to successfully correlate or require extended computational efforts to identify optimal shape functions that accurately represent the subset matching. The aim is to extend ADIC[2] to effectively deal with discontinuous displacement fields by incorporating state-of-the-art discontinuity dealing methods from the body of DIC work.

Methods: The ADIC algorithm employs subset-based DIC methodologies, integrating state-of-the-art techniques to accommodate arbitrary subset shapes and arrangements. The single-camera ADIC2D[2] is being extended because it is simpler to expand the 2D case and then apply it to the 3D case than to extend ADIC3D first.

Contemporary methodologies, such as Smart DIC, Random Sample Consensus (RANSAC), and subset splitting, effectively address discontinuities within the ADIC framework. These approaches require an initial DIC analysis to identify regions requiring further refinement.

The Smart DIC algorithm dynamically adjusts both the subset size and the order of the shape function to minimise the total mean absolute error for each subset[3]. By imposing appropriate bounds on subset dimensions (typically 11 to 101 pixels), Smart DIC ensures the exclusion of impractical values, thereby enhancing measurement accuracy.

RANSAC is a robust linear fitting technique that iteratively samples data to identify dominant inlier populations. It effectively mitigates the influence of poorly matched subsets. In the context of DIC, RANSAC isolates subsets with significant mismatches and performs iterative analyses on randomly selected pixel samples[4], thereby enhancing the reliability of the correlation process.

Subset splitting addresses poorly matched subsets by partitioning them along a delineated curve, typically a line, to split regions exhibiting discontinuous behaviour. Both segments undergo separate correlation analysis and contribute to the overall correlation criterion. The larger segment is kept to represent the subset and the smaller segment is discarded[1,5,6]. This iterative approach facilitates the accurate characterisation of discontinuities within the material under investigation.

[a] HRRSAM007@myuct.ac.za

Subset splitting can utilize RANSAC for delineation of the splitting curve, due to RANSAC being a robust linear fitting technique[4]. It can expose the underlying discontinuity as a curve for subset splitting.

Plots in Figure 2 shows the desired result. Subset splitting addressed an induced discontinuous displacement in a synthetic image, against poorly performing standard DIC.[1]

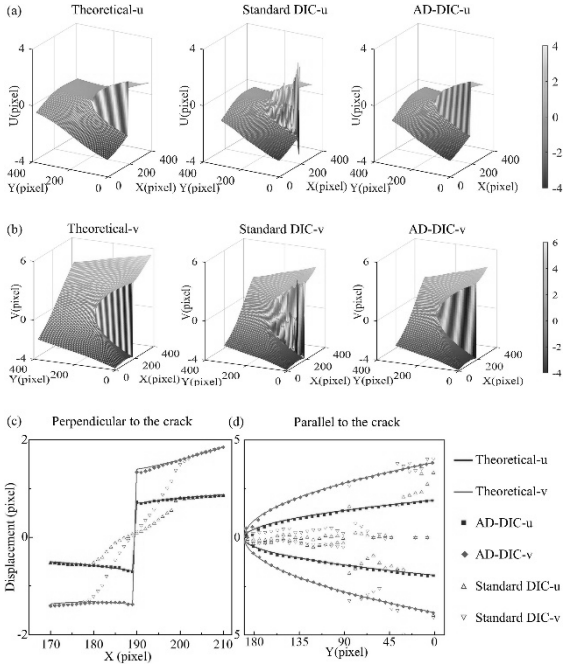

Figure 2: Theoretical vs Standard DIC vs AD-DIC-type subset splitting. Using synthetic speckle images on a mixed-mode I/II crack (a) x displacements, (b) y displacements, (c) displacement perpendicular to the crack, and (d) displacement parallel to the crack.[1]

Displacements perpendicular and parallel to the crack in Figure 2 (c) and (d) from subset splitting track closely to the theoretical displacement, demonstrating its efficacy over standard DIC. While Figure 2 only showcases this for subset splitting, it is desired that similar improvements can be realised with the RANSAC and Smart DIC methods.

Planned Activities: Implementation of the discontinuity dealing methods and integration with ADIC2D as the correlation engine is required. Testing to demonstrate the methods implementations dealing with discontinuities will use synthetic images and existing image sets. Results will be examined to illustrate whether improvements were realised by the implementations of the Smart DIC, RANSAC, and subset splitting methods.

Conclusion: The integration of these methodologies within the ADIC algorithm will enhance its ability to adaptively manage discontinuities. Smart DIC's adaptive sizing reduces the impact of discontinuities on subsets, while RANSAC and subset splitting directly tackle these irregularities. RANSAC's effectiveness in linear fitting complements subset splitting by accurately determining line parameters, even in the presence of non-dominant pixel populations, thereby improving the robustness and precision of DIC analyses.

References:

1. Yuzhe, T. Cheng, Z. Jinquan, X. Jialun, N. and Yuan Q. *A new digital image correlation method for discontinuous measurement in fracture analysis*. Theoretical and Applied Fracture Mechanics, vol. 130, p. 104299, 2024. doi: 10.1016/j.tafmec.2024.104299.
2. Atkinson, D. and Becker, T. *A 117 Line 2D Digital Image Correlation Code Written in MATLAB*. Remote Sensing, vol. 12, no. 18, p. 2906, 2020. doi: 10.3390/rs12182906.
3. Jianhui, Z. and Bing, P. *Smart DIC: User-independent, accurate and precise DIC measurement with self-adaptively selected optimal calculation parameters*. Mechanical Systems and Signal Processing, vol. 222, p. 111792, 2024. doi: 10.1016/j.ymssp.2024.111792.
4. Baldi, A. *Robust Algorithms for Digital Image Correlation in the Presence of Displacement Discontinuities*. Optics and Lasers in Engineering, vol. 133, p. 106113, 2020. doi: 10.1016/j.optlaseng.2020.106113.
5. Poissant, J. and Barthelat, F. *A Novel "Subset Splitting" Procedure for Digital Image Correlation on Discontinuous Displacement Fields.* Experimental Mechanics, vol. 50, no. 3, pp. 353-364, 2009. doi: 10.1007/s11340-009-9220-2.
6. Han, J. and Pan, B. *A novel method for measuring discontinuous deformation in digital image correlation based on partition and dividing strategy*. Engineering Fracture Mechanics, vol. 204, pp. 185-197, 2018. doi: 10.1016/j.engfracmech.2018.09.036.

DEVELOPMENT OF A TRANSIENT 1D FINITE VOLUME THERMOFLUID NETWORK MODELLING METHODOLOGY FOR THE HUMAN CARDIOVASCULAR SYSTEM

N Cilliers[a], R Laubscher and P Rousseau[b]

[a] Department of Mechanical & Mechatronic Engineering, University of Stellenbosch, Stellenbosch, South Africa
[b] Department of Mechanical & Mechatronic Engineering, University of Stellenbosch, Stellenbosch, South Africa

Introduction: It is well-documented that cardiovascular disease (CVD) is the world's leading cause of death. The ability to simulate CVD progression has valuable diagnostic and prognostic potential in the field of cardiovascular health. Simulations could be used to detect and accurately describe the pressure differences experienced in the main arteries of the body, as well as variations in arterial structure caused by CVD pathologies, such as atherosclerosis or stenosis. Modelling blood flow in large systemic arteries requires the simultaneous solution of the dynamic one-dimensional mass and momentum balance equations for incompressible flow in compliant tapered tubes, together with an equation of state that describes the influence of the fluid pressure on the stretching of the vessel wall.

The conventional approach is to apply the mass balance and momentum balance to a single control volume that represents a finite increment along the blood flow path. The transient ODEs of the balance equations are then integrated via a fully explicit second-order accurate two-step Lax-Wendroff finite difference scheme, as shown in Olufsen et al. [1] and Diem and Bressloff [2]. A difficulty encountered in this approach is that special boundary values are required at arterial bifurcations, which is significant due to the extensive branching of vessels in the cardiovascular system. Consequently, simple static pressure continuity is often assumed, or alternatively, a Bernoulli approach, which is valid for steady flow in rigid pipes and not strictly applicable to pulsatile, elastic arterial flow.

This paper presents a dynamic one-dimensional finite-volume thermofluid network methodology that eliminates difficulties associated with the convective terms and the need to expressly determine the velocities in the nodes for the solution of the momentum balance equation.

1D Network formulation: The flow path is discretised via a node and element structure as shown in Figure 1, where elements represent finite increments of the arteries, and nodes represent the connecting points between these increments. The nodes are indicated by squares, while the elements are indicated by circles. Each element is connected to only two nodes, at the inlet and outlet, while a node can be connected to multiple elements. The mass balance is solved on the nodes, while the momentum balance is solved on the elements. Furthermore, the momentum balance equation is written in terms of stagnation properties at the nodes, rather than static properties. This enables the use of zero-dimensional junctions and bifurcations in the flow network with no need for special boundary values.

The component characteristic of the nodes is volume, which can be computed using the half volumes of the elements connected to the node. For example, in the case of the discretised straight artery shown in Figure 1, the volume of Node 2 is calculated as:

$$V_{Node\ 2} = \frac{1}{2}(\sum_i A_e L + \sum_e A_i L),$$

by taking the sum of all the incoming half-element volumes ($A_{e,1}L_1$) and all the outgoing half-element volumes ($A_{i,2}L_2$). This allows the total fluid volume to be evenly distributed across the network. Since the ends of the elements connected to each node all have the same static pressure that is equal to the static pressure in the node, the volume of each node may be written in terms of the static pressure in the node, using the pressure-area relationship:

$$A(p) = A_{\text{ref}} + \frac{3}{4}A_{\text{ref}}\frac{D_{\text{ref}}}{E_w}(p - p_{\text{ref}}),$$

where A_{ref} and D_{ref} are the reference area and diameter of the half elements connected to the node, E_w is the effective wall stiffness, and p_{ref} is the reference pressure. The cross-sectional area of each element is dynamically updated based on the local static pressure, also using this pressure-area relationship. Specifically, the area at the inlet and outlet of each element, i.e., at the half-elements, is computed using this relationship. The average area of the element is then taken as the mean of its inlet (A_i) and outlet (A_e) areas. This pressure-area coupling captures the compliant behaviour of the vessel walls, allowing the model to simulate physiologically realistic flow dynamics.

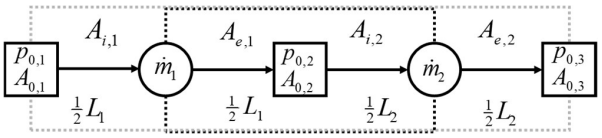

Figure 1: Straight, single artery network discretisation diagram with 3 nodes and 2 elements

The resulting ODEs are solved via Euler temporal integration, which may be approached in a coupled or segregated manner. The backward Euler (fully-

[a] 23799277@sun.ac.za

implicit) and semi-implicit approaches are compared for a benchmark case study in terms of applicability, stability, speed, and accuracy compared to the conventional Lax-Wendroff approach.

The case study for a single, elastic artery segment from VamPy [2] is replicated to validate the solutions produced by the network solver presented in this paper. The radius of the arterial segment at rest tapers exponentially. The Olufsen material model [1], with a Young's modulus that depends on the vessel radius, r_0, at zero transmural pressure, is used to describe the elastic behaviour of the deformable vessel wall. An inlet mass flow rate of pulsatile nature is prescribed as the inlet boundary condition, and physiologically realistic pressure is prescribed at the outlet boundary. This study, therefore, captures the key hemodynamic variables, such as pressure, velocity, and cross-sectional area variations, over time. In VamPy, the Lax-Wendroff method is used, which directly discretises the partial differential equations on a uniform grid in space and time.

The network method, however, is a finite volume-based solver, which enforces mass balance and momentum conservation across discrete network nodes and elements, and not uniform grid points as seen in the Lax-Wendroff technique. Each element represents a physical vessel segment or control volume and enforces momentum conservation. Mass balance is enforced across the nodes. The network method makes use of simple Euler integration, allowing for fully- and semi-implicit solving, which are first and second-order accurate, respectively. In the network solver, larger time steps can be taken when solving since the time step is limited by the local stiffness of the problem, rather than the strict CFL condition as in the case of VamPy.

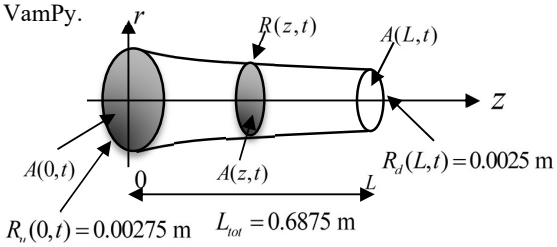

Figure 2: Schematics and geometry of the case study

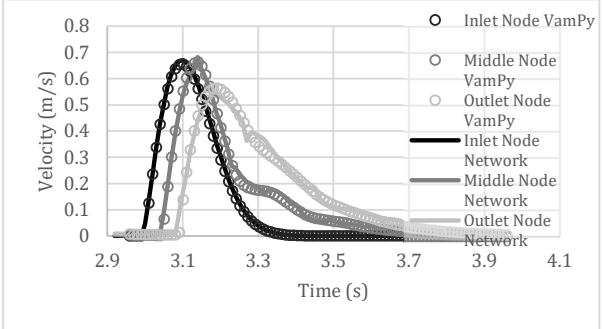

Figure 3: Node Velocities (m/s) vs Time (s) for the last cardiac cycle

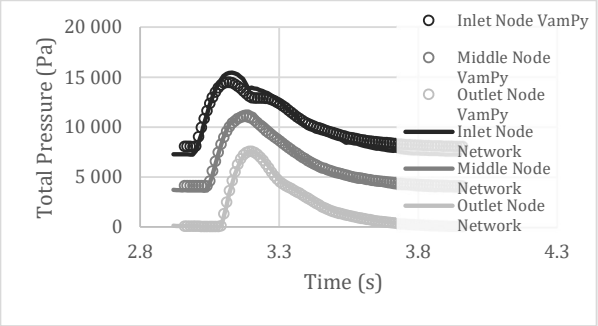

Figure 4: Total Pressures (Pa) vs Time (s) for the last cardiac cycle

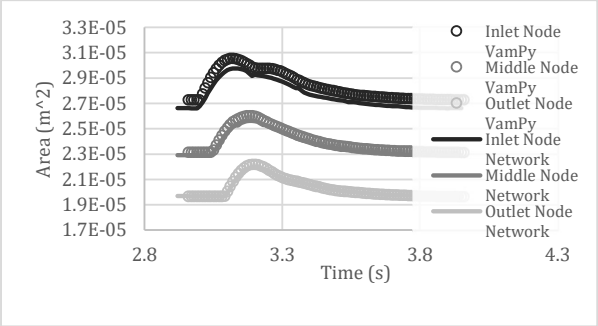

Figure 5: Areas (m^2) vs Time (s) for the last cardiac cycle

In Figures 2-5, the semi-implicit thermofluid network solver is compared to the results obtained by the Lax–Wendroff (VamPy) formulation to evaluate its accuracy when simulating transient, pulsatile blood flow problems, which ran for four cardiac cycles. Using a larger timestep ($\Delta t = 1\times10^{-4}$ s) and a first-order Euler integration scheme ($\alpha = 0.6$), the network method successfully reproduced the characteristic haemodynamic response observed in Vampy ($\Delta t = 1\times10^{-5}$ s). Both models captured the sharp systolic rise and gradual diastolic decay in total pressure, area and velocity across the inlet, middle, and outlet nodes. Slight discrepancies and sharper "peaks" were observed in the network solution, attributed to the lower-order discretisation and damping inherent to the semi-implicit formulation. However, despite these discrepancies, the pressure, velocity and area RMS difference from VamPy remained within an average <12% range of the VamPy predictions. Overall, the thermofluid network approach achieved comparable accuracy at significantly reduced computational cost, demonstrating its suitability for large-scale transient vascular flow simulations.

References:

1. Olufsen, M.S., et al., *Numerical Simulation and Experimental Validation of Blood Flow in Arteries with Structured-Tree Outflow Conditions.* Annals of Biomedical Engineering, 2000. **28**(11): p. 1281-1299.
2. Diem, A.K. and N.W. Bressloff, *VaMpy: A Python Package to Solve 1D Blood Flow Problems.* Journal of Open Research Software, 2017.

MATHEMATICAL MODELLING OF WIND-INDUCED VIBRATIONS IN TRANSMISSION LINE CONDUCTORS

R Selai[a] & E Orumwense[a]

[a] Department of Mechanical & Mechatronics Engineering, Cape Peninsula University of Technology, Bellville, South Africa

Aim & Objectives: This study aims to mathematically model wind-induced vibrations in transmission line conductors with improved accuracy by defining realistic boundary conditions that reflect true structural behavior. The specific objectives are to:

- Review and compare existing mathematical models used in cable vibration analysis.
- Derive equations of motion using both the Euler–Bernoulli beam theory and the Energy Balance Method (EBM)
- Model the conductor as both a beam in tension and a taut string under various end conditions (hinged and clamped).
- Validate the theoretical models against experimental data from literature.
- Define and standardize realistic boundary conditions for enhanced correlation between theoretical and field behavior

Introduction: Transmission line conductors serve as the primary medium for electrical power transmission. Due to cost advantages, overhead lines are preferred, yet they are vulnerable to environmental conditions, mainly wind. Wind-induced vibrations (WIV) manifest in three main forms- galloping, aeolian vibration, and sub-span oscillation depending on wind speed, cable configuration, and ice accretion conditions. These vibrations subject the slender, flexible cables to cyclic loading, often leading to fatigue damage, reduced lifespan, and costly power interruptions in South Africa (Malwande et al., 2022), as illustrated in Fig. 1.

Several researchers have modelled the dynamic behavior of conductors under wind loading. While Dutkiewicz & Machado, (2019) achieved strong agreement between experimental and numerical results under hinged boundary conditions, they did not consider the clamp stiffness. This limitation motivates the current study's focus on realistic boundary conditions. Similarly, Ojo, (2019) used the same boundary conditions when developing his analytical model which was validated experimentally. This motivated the authors of the current study to modify this model by changing the boundary conditions to investigate the effect of boundary conditions in modelling.

Yoon et al., (2023) compared the taut-string and beam models under hinged-end assumptions and concluded that the Euler–Bernoulli beam model most accurately represents real conductor behavior. This comparison ignited an interest in comparing boundary conditions of different cable models under the same conditions. On the other hand, the conclusion drawn by Huang et al., (2023) stressing that cables behave as strings when free and as beams when pre-tensioned and constrained, show limitations in boundary conditions guidelines of which this study will address.

Zhao et al., (2020) and Foti et al., (2024) differ in their treatment of boundary conditions with the afore mentioned studies as they assumed fixed boundary conditions when Zhao et al., (2020) applied Lagrange's method to develop an aeolian vibration-based health monitoring system, noting that natural frequency shifts can indicate physical anomalies such as icing or strand breakage, had modelled the cable as a beam. Meanwhile Foti et al., (2024) used the energy balance method to propose a probabilistic approach for predicting aeolian vibrations and modelled the conductor as a taut string. This promotes the aim of this study to bring consistency in the assumption of boundary conditions. Furthermore, authors that assumed the boundary conditions are hinged did not justify their assumptions the same as those who stated the boundary conditions are fixed. The authors of this study believe it is these limitations that bring uncertainties to the current mathematical models and hence aims to close this gap by defining and standardizing the boundary conditions for improved theoretical-experimental correlation.

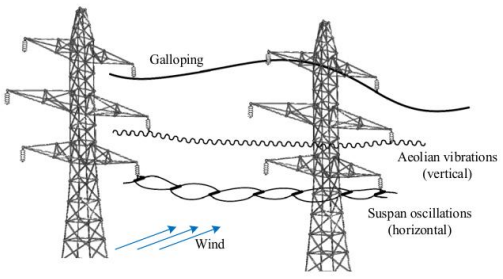

Figure 1: Overhead lines under wind loads *(Zanelli et al., 2022)*

Description of Methodology: The study employs two modelling approaches i.e., the Euler–Bernoulli beam theory and the Energy Balance Method, to derive equations of motion for conductors subjected to wind-induced vibrations. The summary of the procedure is illustrated in Fig. 2 below.

The corresponding author's email address: OrumwenseE@cput.ac.za

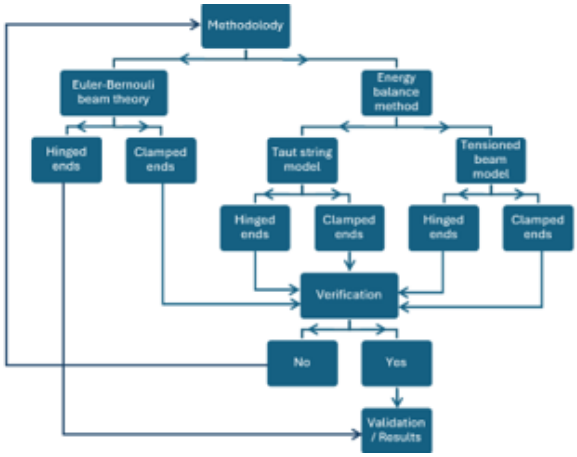

Figure 2: Flow chart of the proposed methodology

1. Euler–Bernoulli Beam Theory: Model the conductor as a beam under tension with hinged, then clamped boundary conditions. The governing equation of motion for transverse vibration is

$$EI\frac{d^4y(x,t)}{dx^4} + T\frac{d^2y(x,t)}{dx^2} + \rho A\frac{d^2y(x,t)}{dt^2} = 0 \qquad 1$$

Where E- Young's modulus, I- the second moment of area, T-the axial tension, ρ- the mass density, and A- the cross-sectional area. The boundary conditions determine the natural frequencies. This model accounts for bending stiffness and axial tension simultaneously, providing realistic predictions of natural frequencies for conductors that are tensioned and clamps supported.

2. Energy Balance Method: Model the conductor as both a taut string and a beam under different boundary conditions (hinged and clamped). The EBM method equates the time-averaged energy input from wind to the structural damping energy dissipated by the conductor. The energy per vibration cycle is expressed as:

$$E_{in} = E_{diss} \qquad 2$$

Where $E_{in} = 0$ and E_{diss} is calculated using the power law model. From this relation, the equivalent natural frequency f_n is obtained by balancing aerodynamic energy with structural response energy. This method captures nonlinear effects of wind flow and is effective in estimating amplitudes in the field.

Both the analytical results will be compared against experimental and in situ data from literature (Ojo, (2019) & Dutkiewicz & Machado, (2019)) to validate their accuracy and assess how boundary conditions influence natural frequency.

Expected Results: The results of this study are expected to give the following: 9.

- It is anticipated that the clamped ends model will yield higher natural frequencies than the hinged ends model.
- The correlation between experimental and theoretical frequencies is expected to improve when realistic boundary conditions are incorporated.

These results will enhance the accuracy of engineering models and provide valuable insights for design, monitoring, and failure prevention in high-voltage transmission systems.

Conclusion: The outcomes of this study are expected to inform practical guidelines for selecting appropriate boundary condition representations in design codes, strengthening the relationship between analytical models and real-world condition. Which in turn improves predictive maintenance and structural safety of transmission networks.

References:

1. Dutkiewicz, M. & Machado, M.R. 2019. Measurements in situ and spectral analysis of wind flow effects on overhead transmission lines. *Sound and Vibration*, 53(4): 161–175.
2. Foti, F., Denoël, V., Martinelli, L. & Perotti, F. 2024. A probabilistic approach to the Poffenberger-Swart bending stress of conductors subject to aeolian vibrations. In *Journal of Physics: Conference Series*. Institute of Physics.
3. Huang, X., Lu, X., Zhao, L. & Feng, G. 2023. Modal parameter calculation and vibration characteristic analysis of transmission line conductor. *IET Generation, Transmission and Distribution*, 17(11): 2483–2496.
4. Malwande, S., Ngonda, T. & Kaunda, M. 2022. Experimental investigation of self-damping characteristics of the ACSR Beresford and TERN transmission line conductors using log-decrement and quality factor methods. *Materials Today: Proceedings*, 56: 1653–1658.
5. Ojo, E.E. 2019. The Developed Analytical Model Used to Evaluate the Dynamic Behaviour of Power Line Conductors. In *2019 IEEE PES/IAS Power Africa*. IEEE: 611–616.
6. Tian, B., Cai, M., Zhou, L., Huang, H., Ding, S., Liang, J. & Hu, M. 2022. Numerical Simulation of Galloping Characteristics of Multi-Span Iced Eight-Bundle Conductors Tower Line System. *Buildings*, 12(11).
7. Yoon, R., Gulbahce, E. & Barry, O. 2023. Free Vibration Modeling of Power Line Conductors. In *IFAC-Papers Online*. Elsevier B.V.: 409–414.
8. Zhao, L., Huang, X., Zhang, Y., Zhu, Y., Jia, J. & Zhu, C. 2020. Aeolian vibration-based structural health monitoring system for transmission line conductors. *Structural Control and Health Monitoring*, 27(6).

WHEEL STRESS INDUCED BY RAILWAY SINGULAR DEFECTS

M Noordien[a], B Nickerson[a] & N Dhansay[a]

[a] Department of Mechanical and Mechatronic Engineering, Stellenbosch University, Stellenbosch, South Africa

This research is tied in with Gibela's agreement with Passenger Rail Agency of South Africa (PRASA) to provide maintenance for South Africa's passenger railways. The focus of this research is to investigate the wheel-rail interaction under transient loading conditions caused by rail singular defects and its contribution to fatigue damage. A finite element model was developed in MSC Apex to simulate the wheel stress induced by the nominal contact load. A detailed description of the planned experimental setup for model validation is presented. Preliminary Finite Element Analysis (FEA) results show strong correlation with Hertzian contact theory and provide an accurate approximation of the contact load. The discovered linear relationship between radial strain and lateral contact patch offset suggests a practical means of compensating wheelset lateral misalignment during testing. These findings form the basis for further experimental verification and introduction of transient loads to the model.

Problem statement: The key to maintaining railway infrastructure lies in understanding the interaction between the wheel and rail under various loading conditions. Long-term rolling contact may result in several types of fatigue damage such as cracks, wear, and material loss[1]. Transient contact loads from singular rail defects create stress concentrations which may promote crack initiation and propagation in the wheel. The wide range of key parameters such as defect geometries, sizes, and train speeds makes real-world testing impractical and costly. A numerical model is therefore preferred, enabling comprehensive parametric studies and full stress-field evaluation to better identify potential failure zones.
Experimentally determining the wheel–rail contact load is typically performed by instrumenting sensors on the rail. However, this approach provides data only at a single location. The present research investigates the feasibility of wheel-mounted measurements for continuous monitoring of wheel–rail contact loads along the travel path.

Aim and Objectives: The aim of this research is to develop a FEA model that simulates the wheel stress induced by various types of singular defects and determine its contribution to fatigue damage. The objectives for this this study are:

1. Develop a FEA model of the wheel-rail contact
2. Validate FEA model through an experimental setup measuring wheel-rail interactions for comparison with simulation results.
3. Perform a parametric study to evaluate the level of influence parameters such as defect size, defect type and train speed has on the wheel stress profile.
4. Analyse simulated stress concentration zones to identify potential crack initiation sites.
5. Compile results and propose practical recommendations for defect tolerance thresholds and key features to incorporate in maintenance strategies.

Finite element modelling: The wheel's stress state is governed by a nominal contact load represented by static (pseudo-dynamic) Hertzian theory, transitioning to a dynamic, non-linear Hertzian formulation when the wheel encounters a singular defect[2]. Table 1 outlines the mesh sizes and model settings used in the static FEA model developed in MSC Apex. The nominal contact force is applied over an elliptical Hertzian contact patch. The contact patch is calculated based on wheel and rail geometry, material properties, and applied force. This model makes use of a varying mesh that decreases in size towards the regions of interest such as the contact patch and strain gauge locations. The mesh size has been refined in a mesh convergence study until the FEA average normal stress plateaued at the approximate Hertzian average normal stress.

Table 1: FEA model configuration

Model settings			
Element type	**No. of elements**	**Contact force**	**Contact patch axis dim.**
TET10	385339	5.125 kN	Major: 5.3 mm Minor: 4.1 mm
Mesh sizes [mm]			
Contact patch	**SG location**	**General**	
0.5, 1, 2, 7	2,5	15	

Planned experimental setup: A decommissioned train wheelset and rail section will be instrumented with strain gauges to measure radial strains, from which the wheel–rail contact forces are derived as depicted in Figure 1. The strain signals will be transmitted via a wireless telemetry module mounted on the wheelset and processed by a data acquisition system. Mounting the sensors directly on the wheel will enable continuous measurement along the travel path. Strain gauges will be installed on either the outer or inner face of both wheels. The experimental setup will aim to determine the nominal contact and excitation force due to the collision with the singular defect.

[a] 23900075@sun.ac.za

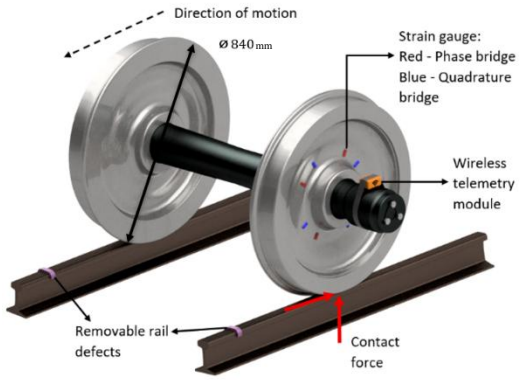

Figure 1: Experimental setup

Preliminary FEA model results: As the wheel rotates, the angular position of the strain gauge varies with time relative to the contact point. This produces harmonic strain signals. To extract the contact load from the measured strains, demodulation is required to eliminate the effects of wheel rotation. The harmonic elimination variant used in this research isolates the first harmonic[3]. Therefore, it is important that the first harmonic be dominant in the signal for an accurate result. Radial strain data were simulated at radial positions across the wheel web, incremented by the length of one LY41-6-350 strain gauge, during wheel rotation as shown in Figure 2.

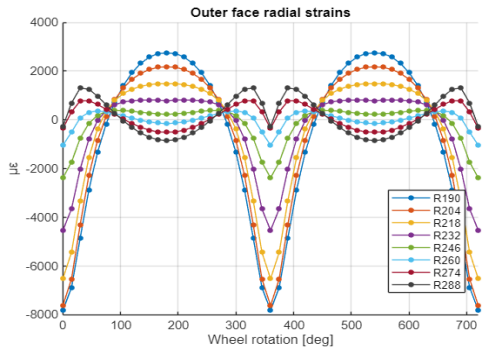

Figure 2: Radial strains across varied wheel radii

A Fast Fourier Transform (FFT) was applied to decompose the time-domain signals into their frequency components and identify the dominant harmonic. The harmonic decomposition is shown in Figure 3 and aligns with previous studies[3].

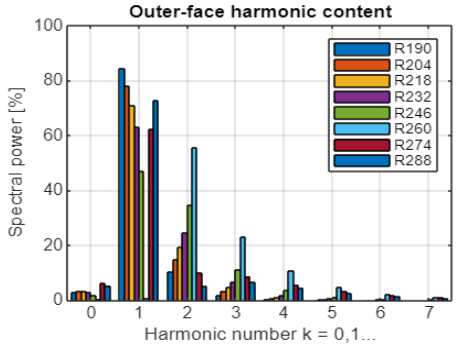

Figure 3: Harmonic decomposition at varied wheel radii

Figure 3 indicates that a radial distance of R190 mm has the most dominant first harmonic out of all the radii and is therefore the optimal position for the placement of strain gauges. Demodulating the harmonic phase- and quadrature-bridge signals at R190 mm results in an approximate steady-state strain[3], as seen in Figure 4.

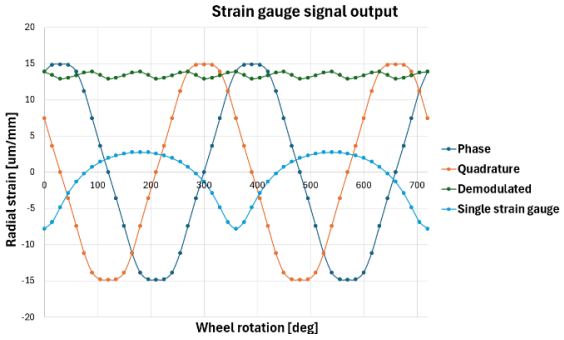

Figure 4: Strain output signals

The contact force calculated using the steady state radial strain differs from the input FEA contact force by no more than 2.6%.

To account for lateral wheelset misalignment, an additional FEA study was conducted where the contact patch position was laterally offset along the wheel tread from the centre location. The simulated radial strain response showed a linear trend with increasing offset. This indicates that, in the experimental setup, if strain gauges are mounted on both outer wheel faces, the average of the two measured strain signals will represent the equivalent strain of a nominally aligned wheelset. Averaging the opposing strain signals therefore compensates for any lateral misalignment of the wheel–rail contact during testing. The preliminary FEA results are subject to validation pending the results of the planned experiments.

Conclusion: The optimal radius for strain gauges was determined to be R190 mm due its dominant first harmonic. Preliminary FEA results indicate that the model predicts contact load within a 2.6% error and converges to the expected Hertzian stress when measuring at the optimal radius. The radial strain's harmonic content matches prior studies[3], and the linear relation between strain and contact patch offset enables correction for lateral wheelset misalignment. These findings support upcoming experimental validation and model extension for transient defect-induced loads.

References:

1. Liu, J., Yang, W. & Wang, Z. *Fatigue Crack Propagation Analysis of Rail Surface Under Mixed Initial Crack Patterns*, 2024.
2. Kosarchuk, V., Tverdomed, V. & Bambura, O. *Calculation Schemes for Determining Contact Stresses in Railway Rails*, 2025.
3. Gomez, E., Giménez. *Method for the reduction of measurement errors associated to the wheel rotation in railway dynamometric wheelsets,* 2011

PROCESS LEVEL INVESTIGATION OF FLUE GAS LATENT HEAT RECOVERY USING A CONDENSING HEAT EXCHANGER IN A BIOMASS BOILER

Z Abrahams & L Malan

ATProM Research Unit, Department of Mechanical Engineering, University of Cape Town, South Africa

Introduction: Biomass fuels offer an alternative to traditional fossil fuels. The relatively high moisture content of biomass fuels results in the flue gas containing a large amount of water vapour following the combustion process within the biomass-fired boiler. During the vaporisation of water, a considerable amount of latent heat is absorbed. Unused latent heat in the water vapour decreases the overall boiler efficiency. One way to recover a portion of this latent heat is to condense the moisture out of the flue gas stream.

The condensation process is a complex combined heat and mass transfer process. The flue gas can be considered a mixture of water vapour and non-condensable (NC) gases. The presence of NC gases has proven to inhibit the condensation heat and mass transfer rate[1]. Additionally, the mass transfer results in a decrease in the partial pressure and saturation temperature of the flue gas due to the decrease in the water vapour content. This results in variations in the water vapour volume, mass flow rate, and enthalpy of the flue gas along the flow path[2].

The primary objective of this research is to develop a process level, steady-state numerical model of a flue gas condensing heat exchanger using Python. The proposed condensing heat exchanger model can be placed within an integrated boiler model to analyse the effect on various boiler process parameters such as the flue gas latent heat recovery, moisture extraction and the overall boiler efficiency. The numerical model can also be used to provide insight into the technical feasibility and design of the heat exchanger for prototype development and cost-benefit analysis.

Modelling Methodology: The numerical model is based on a shell-and-tube countercurrent cross-flow heat exchanger with an in-line arrangement of horizontally aligned U-bend tubes. Cooling water flows inside the tubes and hot flue gas flows across the exposed tube bank which allows for heat transfer between the two fluid streams.

As flue gas enters the heat exchanger at a relatively high temperature, the heat exchanger model is divided into an Economiser and a Condenser section as shown in Figure 1. Both sections are discretised into control volumes where one control volume represents a single pass of a tube row.

In the Economiser section, no condensation takes place, and only sensible heat is transferred from the hot flue gas to the working fluid. The heat transfer in each control volume is analysed using the effectiveness-NTU method[3].

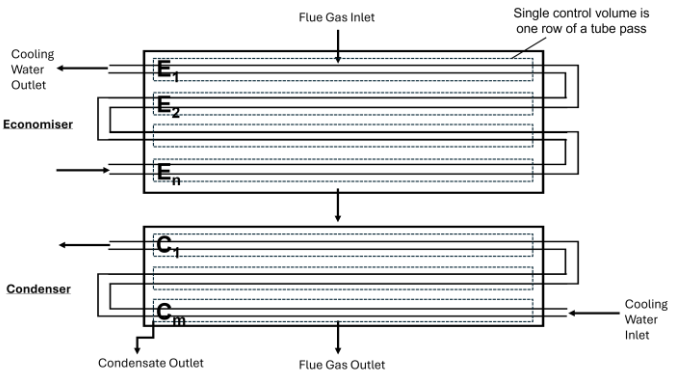

Figure 1: Schematic of the heat exchanger discretised into control volumes. There is an Economiser section made up of *n* many tube passes and a Condenser section made up of *m* many tube passes.

The dewpoint temperature is the saturation temperature of water at the partial pressure of the water vapour present in the flue gas. The objective of the Economiser is to extract all sensible heat up to the point where the flue gas temperature drops below the dewpoint temperature and condensation commences. This is then defined as the start of the Condenser section.

Many researchers have implemented the Colburn-Hougen method[4] to theoretically model the condensation of a vapour mixture in the presence of NC gases. The Colburn-Hougen method can be extended to include the combined effect of mass and heat transfer by introducing a correction factor, commonly referred to as the Ackermann correction factor, E_T. The Ackermann correction factor has shown to improve results when compared to experimental studies[5].

The total heat transfer to the cooling water is the sum of the sensible heat transfer and the latent heat transfer through the gas boundary layer. This means that heat transfer is therefore governed by simultaneous temperature and concentration gradients.

The respective heat fluxes can be written as,

$$q'_{total} = q'_{sensible} + q'_{latent,} \quad (1)$$

$$q'_{total} = \alpha'(T_i - T_c), \quad (2)$$

[a] abrzai005@myuct.ac.za

$$q'_{sensible} = \alpha_{fg} \cdot E_T \cdot (T_{fg} - T_i), \quad (3)$$

and

$$q'_{latent} = \beta_m \cdot (y_{h2o} - y_i) \cdot \Delta h_v\,, \quad (4)$$

where q' indicates the heat transfer flux [W/m^2] and the subscript indicates the heat transfer type. α' is the heat transfer coefficient [W/K·m^2] from the interface of the condensate film to the cooling water and α_{fg} is the heat transfer coefficient of the flue gas. T_i, T_c and T_{fg} are the temperatures [K] of the interface of the condensate film, cooling water and flue gas respectively. β_m is the mass transfer coefficient [kg/m^2·s] and Δh_v is the latent heat of vaporisation of water [J/kg]. y_{h2o} and y_i are the mole fractions of water vapour at T_{fg} and T_i, respectively.

This indicates that the sensible heat transfer is the product of the heat transfer coefficient and the temperature difference with the inclusion of the Ackermann correction factor to account for the simultaneous heat and mass transfer. The latent heat transfer is analogous to this as it is the product of the mass transfer coefficient, the mole fraction difference and the latent heat of vaporisation. The sum of the sensible and latent heat transfer computes the total heat lost by the flue gas and gained by the cooling water.

Results: In a study by Terhan and Comakli[6], a numerical model is used to analyse a condensing heat exchanger for a 60 MW natural gas fired heating system. Using our modelling methodology, the resulting heat exchanger temperature profiles for the Economiser and Condenser sections are respectively shown in Figures 2 and 3. This is plotted against the results of Terhan and Comakli. The temperature profiles for the two fluid streams are plotted relative to the flue gas inlet (due to the counter-flow heat exchanger design, this will be the cooling water outlet).

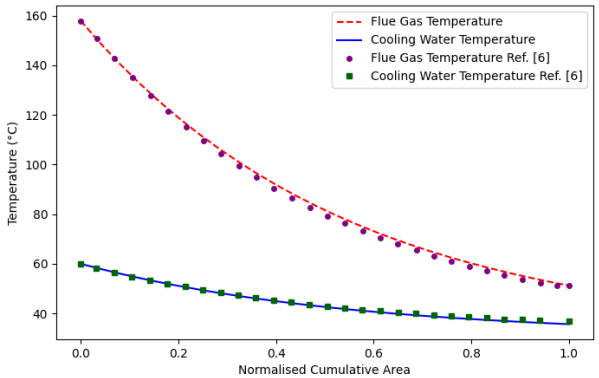

Figure 2: Temperature profile of Economiser section

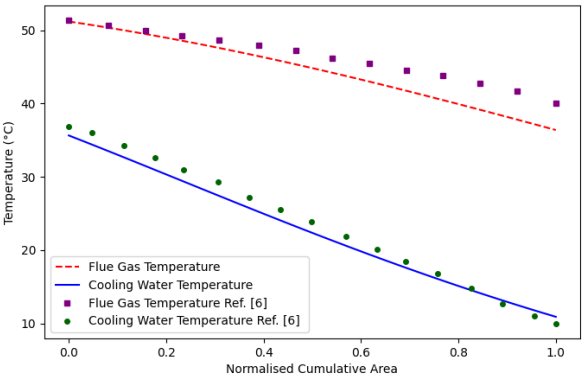

Figure 3: Temperature profile of Condenser section

The temperature profiles are in good agreement with the literature. The heat transfer area calculated in our modelling methodology requires 3.75 passes more than Terhan and Comakli's model.

Conclusion: A total of 33.75 passes (25 passes in the Economiser section and 8.75 passes in the Condenser section) are needed to cool the flue gas from 158°C to approximately 40°C. By condensing the moisture out of the flue gas, 240 kW of latent heat are recovered. The improvement in heat recovery can improve the efficiency of the boiler system. Next steps in this research include conducting a parametric analysis and placement study of the condensing heat exchanger.

References:

1. Alshehri, A., Andalib, S. and Kavehpour HP. *Numerical modeling of vapor condensation over a wide range of non-condensable gas concentrations.* International Journal of Heat and Mass Transfer, Vol. 151.

2. Yang, K., Yang, J., Da, Y., Han, L., Deng, L. and Che, D. *A numerical study on convective condensation of flue gas in tubular heat exchangers.* Applied Thermal Engineering, Vol. 243.

3. Incropera, FP. and DeWitt, DP. *Fundamentals of heat and mass transfer.* John Wiley & Sons, New York, 1996.

4. Colburn, AP. and Hougen, OA. *Design of cooler condensers for mixtures of vapors with noncondensing gases.* Industrial and Engineering Chemistry, Vol. 26, No. 11.

5. Rączka, P. and Wójs, K. *Methods of thermal calculations for a condensing waste-heat exchanger.* Chemical and Process Engineering, Vol. 35, No. 4, pp. 447-461.

6. Terhan, M. and Comakli, K. *Design and economic analysis of a flue gas condenser to recover latent heat from exhaust flue gas*. Applied Thermal Engineering, Vol. 100, pp. 1007-1015.

AQUA: The Adaptive Quality Upscaling Architecture.

Timothy Reddy[a] & Lukas du Plessis[b]

[a, b] Department of Mechanical Engineering, University of Cape Town, Cape Town, South Africa.

Ensuring consistent and verifiable quality in advanced manufacturing remains a persistent challenge, particularly as production methods evolve toward greater complexity and automation. The Adaptive Quality Upscaling Architecture (AQUA) is a hybrid manufacturing platform that integrates additive, subtractive and vision-based processes within a single system to enable fast and precise fabrication. This Master's project focuses on the research and development of AQUA's Vision subsystem, which incorporates a multiscale laser-triangulation 3D-scanner for in-process monitoring and dimensional verification.[1,2] The system employs both macro and micro scanning modes to balance coverage, precision and efficiency, with the aim of achieving feature resolution down to 20 µm using low-cost, locally available hardware. AQUA is built on a modified polar-coordinate architecture controlled through Klipper-based software. Current work is directed toward establishing a closed-loop feedback framework that will allow the platform to scan, analyse, and compare part geometry against digital models to support adaptive correction and enable full hybrid operation in future models.

Introduction: Quality assurance remains one of the main barriers to the broader industrial adoption of additive manufacturing. As printing complexity increases, so too does the need for reliable, real-time monitoring capable of detecting deviations as they occur.[1] Vision-based systems are particularly well suited for this purpose, offering detailed observation of layer deposition, surface features, and emerging defects during fabrication.

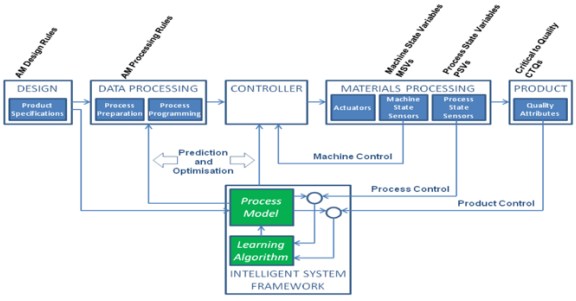

Figure 1: A closed-loop quality control strategy.[2]

Recent research has emphasised Zero-Defect AM, which relies on integrated sensors, intelligent feedback control and prediction-optimisation frameworks to maintain product quality. Such closed-loop approaches form the basis for future self-correcting manufacturing architectures, as is shown in *Figure 1* above. [2]

The Adaptive Quality Upscaling Architecture (AQUA) addresses this challenge by combining additive, subtractive, and vision-based technologies into a single, integrated platform. Its core workflow follows a repeatable sequence: rapid large-nozzle printing, geometric scanning and comparison to the CAD model, subtractive refinement, re-scanning, and targeted repair or deposition until the part meets specification. This hybrid, scan–compare–correct process provides the foundation for adaptive quality control and closed-loop manufacturing.

The aim of this research is to develop and integrate a low-cost, high-accuracy multiscale scanning system for in-process monitoring and dimensional verification as a foundational step toward a closed-loop hybrid manufacturing platform.

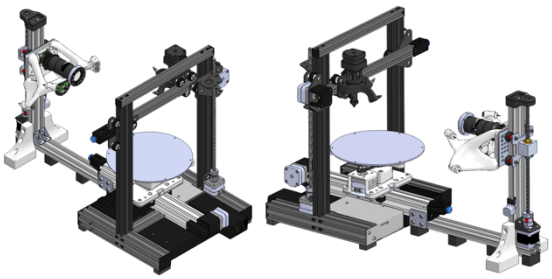

Figure 2: CAD model of modified printer.

Methodology: The prototype system is based on a modified Creality Ender 3 V2 printer, converted from Cartesian to polar motion. A custom rotary build table was designed and integrated into the frame, driven by a stepper motor through a GT2 timing-belt reduction and supported on precision bearings to minimise run-out. The extruder remains on the gantry to provide radial and vertical motion, while dedicated Z_{cam} and Bed_{cam} axes position the camera-laser scanning module for focus tuning. A full CAD model, as shown above in *Figure 2* aligns the cameras, lasers and lighting, ensuring adjustable baselines for both macro and micro scanning configurations. Structural rigidity and bed flatness were verified through mechanical testing, and path-planning limits were introduced to control acceleration near the bed centre.

The system is operated through Klipper firmware on a dual-MCU configuration, with a Python-based interface managing synchronised motion, lighting, focus control, and data capture.

[a] *RDDTIM002@myuct.ac.za*

The Vision subsystem uses laser triangulation, projecting a laser line onto the part's surface while a camera observes its deformation; whereby local height ($\cong \Delta D \cdot tan\theta$) is computed from the laser–camera baseline and measured angle.[3] Two scanning modes are implemented: (1) macro scanning with autofocus for full-part evaluation, and (2) micro scanning with a microscope lens for 10–20 µm feature analysis.

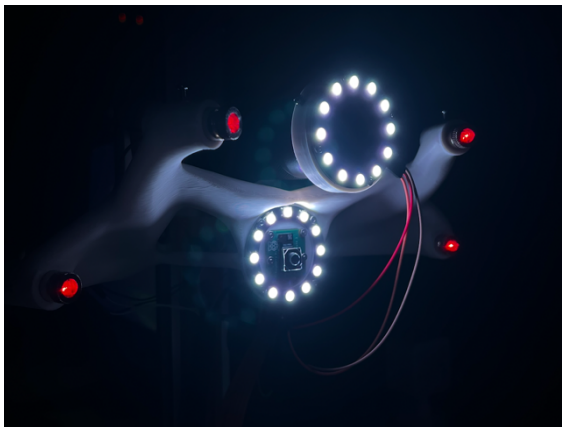

Figure 3: Fully assembled multiscale 3D-Scanner.

Calibration follows standard OpenCV procedures to determine camera intrinsics and distortion, this was done using various checkerboard patterns at various angles. The laser plane is aligned using a reference target at known offsets, and the rotary axis is planned to be further verified by scanning a calibrated cylinder through 360°, establishing an accurate transform chain for 3D reconstruction.[4]

Klipper manages time-critical motion, while Python routines coordinate laser activation, focus changes, and lighting control. Peripheral endoscopic cameras monitor extrusion in real time, and the system can automatically pause and log anomalies such as under-extrusion or layer misalignment. The same control pathways will later drive adaptive corrections using scan data, forming the basis of the closed-loop feedback system.

Results and Findings: The mechanical and electrical subsystems of the AQUA prototype have been designed, manufactured and validated. The modified polar printer architecture, additional motion axes and control electronics function reliably under coordinated operation. Integrating new motors, drivers and peripherals presented challenges in synchronisation, which were addressed through firmware configuration and modular macros that automate homing, lighting, laser control and image capture at defined angular increments.

In parallel, a multiscale scanning algorithm is being developed to process images, shown in *Figure 4* below, and generate 3D point clouds from both macro and micro modes. The current setup successfully produces usable macro-level point clouds suitable for whole-part inspection, while optimisation continues the micro scanner, which is more sensitive to vibration and calibration drift. The scanning routine, calibration process and camera synchronisation are being refined to increase accuracy and reduce computation time, ensuring that the system operates efficiently in a production environment.

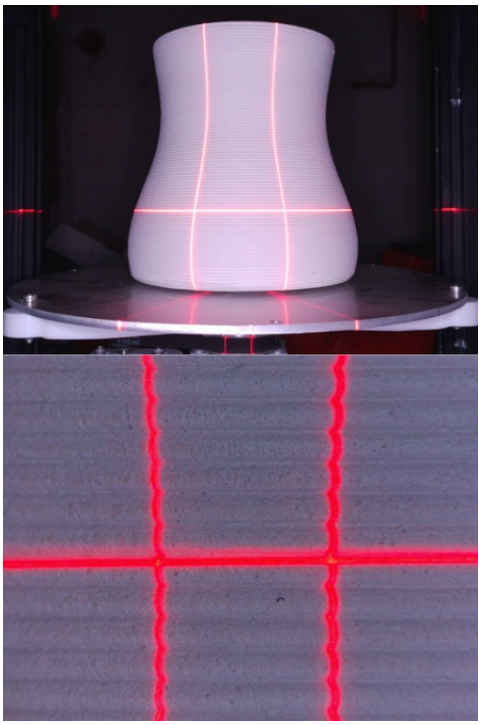

Figure 4: Macro Image (Top), Micro Image (Bottom)

Conclusion: AQUA demonstrates a practical framework for adaptive quality upscaling by merging additive, subtractive, and vision processes into a single machine. This Master's project delivers a calibrated multiscale vision system and establishes the mechanical, electrical, and software foundation for closed-loop hybrid manufacturing. The current results confirm functional integration of the modified architecture and scanning system, while optimisation of calibration, algorithms, and closed-loop feedback remains ongoing. Future work will finalise the feedback control loop, integrate subtractive tooling, and advance AQUA toward a fully autonomous, self-correcting manufacturing platform.

References:

1. R. G. Kim et al., *A Survey of Image-Based Fault Monitoring in Additive Manufacturing*, Sensors, 2023.
2. M. Faes et al., *Process Monitoring of Extrusion-Based 3D Printing Laser Scanning*, KU Leuven, 2020.
3. R. A. Wagh et al., *Laser Triangulation for Object Height Measurement*, IJREST, 2015.
4. OpenCV Docs, *Camera Calibration*, 2024.

[a] *RDDTIM002@myuct.ac.za*

DEVELOPMENT OF AN ENEGY-EFFICIENT DIRECT LIQUID COOLING FOR SERVERS IN DATA CENTRES

A. Dlokovana & E. Orumwense

Department of Mechanical & Mechatronics Engineering, Cape Peninsula University of Technology, Cape Town, South Africa

Aim & Objectives: This study aims to develop and validate a digital twin of a single-phase immersion cooling system and use ANSYS Fluent CFD together with MATLAB system models to optimise tank and server designs, minimising pumping and heat-rejection power and improving data-centre Power Usage Effectiveness (PUE).

The objectives of this study are as follows:

- Conduct a systematic review of SPIC literature on papers published in the last 5 years to extract benchmark metrics and identify key design gaps.
- Simulate and evaluate SPIC thermal behavior across loads, coolant types, and flow rates using ANSYS Fluent and MATLAB, and demonstrate model accuracy within ≈5% or within compared to published data.
- Quantify SPIC's impact on PUE and cooling energy and optimise tank and server designs to maximise heat transfer while minimising pumping and heat-rejection power, aiming to achieve a PUE of ≤ 1.1.
- Deliver a validated digital twin and practical design guidelines via a full thesis benchmarked against published data, assessing scalability and feasibility.

Introduction: The rapid growth of artificial intelligence (AI) has driven a sharp increase in demand for computational power and the global expansion of data centres. Despite technological advances, most facilities still rely on traditional air cooling, which is increasingly inadequate because air's low thermal conductivity and heat capacity limit its ability to remove high localized heat loads[1]. Modern CPUs can exceed 300 W, and GPUs may reach 1,000 W, further stretching air-cooling limits[2]. Thermal management systems commonly account for around 40% of a data centre's total electricity consumption. **Figure *1***[3] presents a typical data-centre energy breakdown indicating that nearly 40% of facility energy is consumed by cooling, underscoring the need to improve cooling efficiency to reduce overall energy use and PUE.

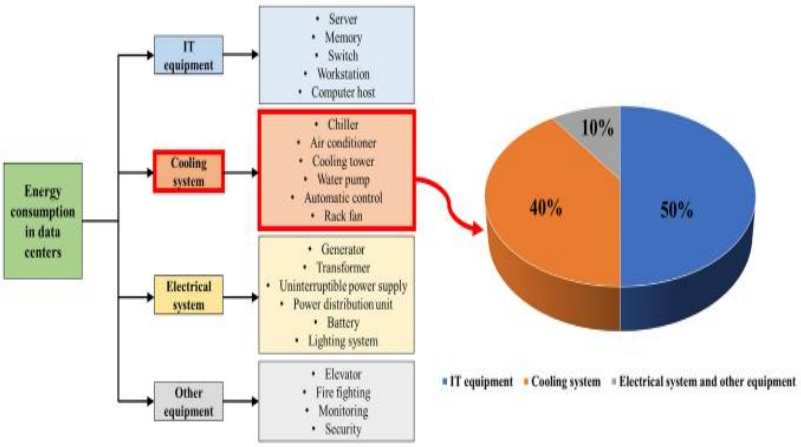

Figure 1: Energy Consumption in Data Centers[3]

Adopting Direct Liquid Cooling, specifically Single-Phase Immersion Cooling (SPIC), the work will develop a validated digital twin that couples three-dimensional CFD models in ANSYS Fluent with one-dimensional system models in MATLAB. A structured simulation campaign based on design-of-experiments, global sensitivity analysis and response-surface optimisation will quantify thermal performance, pressure loss and energy use across representative server loads and facility conditions. Results will be used to identify configurations that minimise pumping and heat-rejection power and therefore improve data-centre PUE.

The literature positions SPIC as a practical middle ground between cold plates and two-phase immersion. SPIC combines simpler server plumbing with near-complete heat capture and easier maintenance, and pilot and system-level studies report reduced auxiliary equipment requirements and higher coolant outlet temperatures that open opportunities for waste-heat reuse[4]. Work by Milnes[5] highlights that fluid selection and flow management strongly govern component temperatures in SPIC deployments.

230003702@mycput.ac.za

Key limitations identified in recent reviews are the lower intrinsic heat-transfer capacity of common dielectric fluids compared with water and a strong sensitivity to internal flow distribution, which makes co-design of tanks, manifolds and heatsinks essential. Nonetheless, several surveys conclude that SPIC offers a balanced pathway for many operators by lowering system complexity relative to two-phase immersion and avoiding the intensive plumbing of cold-plate solutions, while still delivering meaningful PUE reductions and heat-reuse potential[6].

Methodology: A validated digital twin of a single-phase immersion cooling system will be built by coupling 3-D CFD models in ANSYS Fluent with a 1-D system model in MATLAB to represent the server, tank, CDU and secondary loop. Temperature-dependent fluid properties and conjugate heat transfer will be solved with appropriate turbulence closures, refined boundary-layer meshing and grid-independence testing. Design of experiments will explore key variables (tank/manifold layout, flowrate, heatsink geometry, coolant choice and inlet temperature), followed by global sensitivity analysis to rank influences. Response-surface modelling will be used together with multi-objective trade-off analysis to identify design solutions that balance peak CPU temperature, pressure loss and pumping/heat-rejection energy. Model outputs will be benchmarked against published experimental cases and uncertainty quantified to produce conservative performance bounds. Final deliverables include the validated ANSYS+MATLAB digital twin, Pareto-optimal design sets, concise heatsink/manifold guidance and archived scripts and reduced datasets for reproducibility.

Expected Results: A SPIC and demonstrable reductions in cooling energy and PUE, with lower peak CPU temperatures and improved temperature uniformity. Global sensitivity and multi-objective optimisation will identify the few dominant design variables and feasible parameter envelopes that balance thermal performance against pressure loss and pump energy. The 3-D CFD model will provide high-fidelity flow and temperature fields to generate Pareto fronts, probabilistic PUE estimates, and practical heatsink/manifold design guidance for deployment.

Conclusion: This study develops and validates a digital twin of a SPIC system to investigate and optimise server and tank design for improved thermal and energy performance. The results will identify practical design choices and operating ranges that reduce cooling energy and improve data-centre PUE. Findings will be shared through peer-reviewed publication and concise guidance aimed at engineers and researchers considering immersion cooling deployments.

References:

1. Kandasamy, R., Ho, J.Y., Liu, P., Wong, T.N., Toh, K.C. & Chua, S.J. 2022. Two-phase spray cooling for high ambient temperature data centers: Evaluation of system performance. Applied Energy, 305.
2. Deng, Z., Zhang, S., Ma, K., Jia, C.B., Sun, Y., Chen, X., Luo, Y., Li, B. & Li, T. 2023. Numerical and experimental study on cooling high power chips of data centers using double-side cooling module based on mini-channel heat sink. Applied Thermal Engineering, 227.
3. Cai, S. & Gou, Z. 2024. Towards energy-efficient data centers: A comprehensive review of passive and active cooling strategies. Energy and Built Environment.
4. Hnayno, M., Chehade, A., Klaba, H., Polidori, G. & Maalouf, C. 2023. Experimental investigation of a data-centre cooling system using a new single-phase immersion/liquid technique. Case Studies in Thermal Engineering, 45.
5. David, M.P., Nagrani, P., Yuksel, A. & Hu, Y. 2024. Simulation Study of Single-phase Immersion Cooling of a Single Server and a Cluster of Servers in a Tank. In InterSociety Conference on Thermal and Thermomechanical Phenomena in Electronic Systems, ITHERM. IEEE Computer Society.
6. Azarifar, M., Arik, M. & Chang, J.Y. 2024. Liquid cooling of data centers: A necessity facing challenges. Applied Thermal Engineering, 247.

230003702@mycput.ac.za

OPERATIONALISING PREDICTIVE MAINTENANCE THROUGH A DIGITAL TWIN SYSTEM FOR BULK WATER PUMPING SYSTEMS

D Opperman[a], C Steed[a] & Prof AH Basson[a]

[a] Department of Mechanical and Mechatronic Engineering, Stellenbosch University, Stellenbosch, South Africa

Bulk water pumping systems are critical to municipal and industrial water distribution networks, yet maintenance remains largely reactive, resulting in unplanned downtime. This research aims to develop and evaluate a Digital Twin (DT) system that operationalises Predictive Maintenance (PdM) through the integration of Machine Learning Operations (MLOps).

A preliminary scoping review of DT and PdM research in water and mechanical systems revealed a lack of deployable frameworks that manage the full lifecycle of Machine Learning (ML) models. This gap motivates the development of a modular DT framework capable of adaptive model deployment, feedback integration, and real-time decision support to initiate and optimise maintenance actions.

The DT mirrors pump operation through sensor data, simulation, and analytics to predict degradation and Remaining Useful Life (RUL), while MLOps ensures continuous training, deployment and monitoring of PdM models.

Preliminary work includes defining functional and non-functional requirements, designing a scalable DT architecture with embedded MLOps functions, and implementing a Minimum Viable Product (MVP) for data ingestion, anomaly detection, and model validation. The initial MVP leverages pre-trained or benchmarked PdM models identified from existing literature, focusing on integrating them within an auditable, operator-centric workflow rather than creating new model architectures.

The scoping of related work suggests that vibration-based features, such as spectral peaks and RMS, are an effective indicator of bearing degradation. The outcomes of this research are expected to provide an adaptive, auditable, and deployable framework that advances PdM implementation for water infrastructure management.

Background

Bulk water pumping systems form the backbone of municipal and industrial water distribution networks. Their operational reliability depends on centrifugal pumps, yet maintenance practices remain largely reactive, often relying on manual inspections or fixed service intervals. These approaches rarely detect early-stage degradation, leading to unplanned downtime and high costs.

Predictive Maintenance (PdM) and Digital Twin (DT) technology offer a pathway toward condition-based and data-driven asset maintenance. A DT creates a virtual representation of the physical asset, enabling real-time monitoring and performance simulation [1], while PdM employs Machine Learning (ML) models to detect anomalies and predict Remaining Useful Life (RUL) [3]. However, despite significant progress in both domains, the operationalisation of PdM, the process of training model outputs into actionable maintenance procedures, remains underdeveloped in industrial settings [2,3].

Early work suggests that successful operationalisation depends on integrating two perspectives: an operator-centric view, where human expertise and decision authority remain central, and a model-centric view, supported by Machine Learning Operations (MLOps) for the continuous deployment and governance of PdM models [4]. This research explores how these perspectives can be reconciled within a DT framework to enable practical, sustainable maintenance automation.

Purpose/Aim

The purpose of this study is to investigate the requirements and mechanisms for operationalising PdM through a DT system that bridges operator-centric decision-making and model-centric automation. The work identifies gaps in how machine-initiated maintenance procedures are currently implemented and proposes an architecture that embeds human feedback, lifecycle management, and transparent decision support.

Research Question

How can an operator-centric approach to MLOps enable the practical operationalisation of PdM in bulk water pumping systems?

Methodology:

A scoping review of literature on PdM, MLOps, and DT applications in water and mechanical systems [1-4] was conducted to identify existing limitations in operationalising PdM. The review revealed a lack of lifecycle management, feedback integration, and verification mechanisms for PdM model outputs.

Building on these findings, the study adopts the System Engineering Body of Knowledge methodology [SEBok v2.x, 2024], comprising:

1. Problem definition and stakeholder analysis to contextualise maintenance challenges.
2. Requirement specification, aligning with ISO 25010 standards [ISO 25010].
3. Architecture design, incorporating MLOps-driven model lifecycle management.
4. Prototype (MVP) development to implement data pipelines, PdM workflows, and dashboards.
5.

[a] 29624134@sun.ac.za

6. Validation and evaluation using representative case studies.

System Architecture:

The proposed architecture enables continuous model operation and integration between machine-centric and operator-centric processes. Data from IoT sensors and SCADA systems flow into a feature store for preprocessing and versioning. The DT framework integrates existing, validated PdM models from literature rather than developing new ones. These include conventional feature-based methods such as Random Forests (RF) and Support Vector Machines (SVMs), as well as deep learning approaches like Convolutional Neural Networks (CNNs), which have been widely applied in vibration-based fault diagnosis [3]. MLOps components manage the ML model lifecycle, encompassing version control, deployment, performance monitoring, and automated retraining, while operator interfaces provide real-time maintenance recommendations.

To minimise false positives, the DT incorporates root-cause analyses (RCA) by cross-referencing anomalies with contextual process variables before issuing alerts. Confirmed events trigger feedback updates and, when appropriate, initiate maintenance actions through predefined workflows.

This closed loop ensures that PdM insights evolve with operational reality, maintaining both trust and traceability.

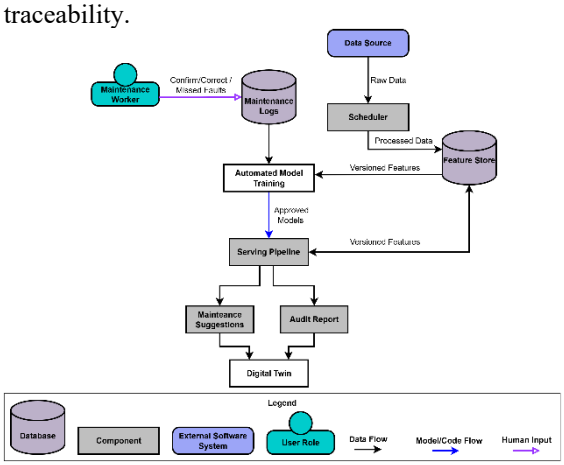

Figure 1 Proposed MLOps-enabled Digital Twin architecture illustrating automated model training, deployment, and operator feedback integration.

Results and Findings

Preliminary work defined a comprehensive set of functional and non-functional requirements for operationalising PdM, highlighting the need for interoperability, auditability, and human-in-the-loop governance [4]. The scoping review confirmed that PdM research is primarily operator-centric, relying on domain expertise for interpretation [2,3], whereas MLOps is model-centric, focusing on automation and scalability [4]. Bringing these paradigms through hybrid feedback loops is essential for real-world adoption.

An MVP prototype is being developed to demonstrate data ingestion, preprocessing, anomaly detection, and dashboard visualisation. Initial tests using vibration-based datasets indicate that root-mean-square (RMS) and spectral-peak features are effective early indicators of bearing degradation [2,3], supporting the feasibility of ML-based PdM integration within the DT framework.

Implications/Value

This research contributes a structured, operator-integrated framework for operationalising PdM in critical water infrastructure. By embedding MLOps into a DT environment, the system enables:

- Continuous model management with transparent decision tracking
- Reduction of false positives through RSA and operator validation.
- Adaptive maintenance scheduling informed by real-time analytics,
- A deployable foundation for scaling PdM across multiple pumping stations.

From a broader perspective, this work advances understanding of how DT and MLOPs technologies can be combined to move PdM from theoretical promise to operational reality.

References:

1. Redelinghuys A.J.H., Basson A.H., & Kruger K. *A six-layer architecture for digital twins with aggregation. J. Intelligent Manufacturing,* 31 (6), 1383–1402 (2020).
2. Olesen J.F. & Shaker H.R. *Predictive maintenance for pump systems and thermal power plants: State-of-the-art review. Sensors,* 20 (8), 2425 (2020).
3. Carvalho T.P. et al. *A systematic literature review of machine-learning methods applied to predictive maintenance. Computers & Industrial Engineering,* 137, 106024 (2019).
4. Human C., Basson A.H., & Kruger K. *A design framework for a system of digital twins and services. Computers in Industry,* 144,

DETERMINING THE FLEXURAL RESPONSE OF BASALT FIBRE REINFORCEMENT COMPOSITE WITH A BIO POLYMER MATRIX AS A SUSTAINABLE, HIGH-PERFORMANCE MATERIAL

M.P. Ntloane[a], S. Gabriel[a, b], J. Dicks[a], and S. Chung Kim Yuen[b]

[a] Centre for Materials Engineering (CME), Department of Mechanical Engineering, University of Cape Town
[b] Blast Impact & Survivability Research Unit (BISRU), Department of Mechanical Engineering University of Cape Town

Abstract: The development of fibre reinforced polymer matrix composites that are both sustainably derived and capable of achieving acceptable mechanical properties for high-performance applications remains lacking. Herein, the use of basalt fibre reinforcement was investigated with Prime 37 epoxy (35% bio content) polymer matrix to assess its flexural strength compared to glass, Kevlar® and basalt/flax fibres of similar g/m^2. Using 4-point bending flexural test, the highest flexural strength and elastic modulus was measured for basalt in both the 90° and 45° orientations. Between the two orientations basalt exhibited the highest strength and modulus of 354 MPa and 42 GPa respectively at 90°. Through investigating the flexural properties of basalt against glass, Kevlar® and basalt/flax fibres, it was established that basalt fibre reinforcement within a bio-based epoxy polymer matrix presented an industrially relevant and sustainable material suitable for high-performance applications.

Introduction: Fibre reinforced polymer (FRP) composites are important materials that can achieve excellent specific mechanical properties suited for high-performance applications. FRP composites are progressively being incorporated into high-performance applications, e.g., automotive, marine, and aerospace [1]. High-performance applications in the industries mentioned require a balance between high specific strength while maintaining low density. Common reinforcing synthetic fibres used are glass and Kevlar®. However, these fibres are derived from non-renewable resources and require energy-intensive processes, imposing a shortfall in their environmental sustainability [2,3]. Research on plant-based renewable fibres such as hemp, jute, and flax stand as a sustainable alternative. Although these fibres have excellent tribological qualities [4] and serve as abundant, renewable feedstocks, their poor mechanical and hygroscopic properties limit their use in high performance applications. To improve these properties, surface treatments or hybridization with synthetic fibres [56] are employed, which diminish their overall sustainability [7].The development of basalt fibre now presents a balance between sustainability and meritorious mechanical properties. Basalt is a naturally occurring mineral, composed of a combination of oxides, with major constituents including SiO_2, Al_2O_3, Fe_2O_3, Na_2O, and CaO [8]. It is abundant and does not release harmful by-products during processing [9]. Aside from this, the presence of inorganic oxides in the chemical structure of basalt fibre further facilitates improved mechanical properties in harsh environments that are commonly lacking in the other natural fibres. The vast majority of examples demonstrating the mechanical properties of basalt fibres within FRP composites have relied on petroleum-derived epoxy resins [10,11]. It is therefore relevant to also consider using polymer matrices derived from renewable resources for improved sustainability.

The overarching goal of this research was to establish the mechanical properties of basalt fibres compared to glass, Kevlar® or basalt/flax fibres within a bio-based epoxy polymer matrix. The aim of this paper is to establish an understanding of the flexural performance of basalt fibre reinforced with Prime 37 bio-based epoxy matrix resin to assess the strength and stiffness of basalt fibre while also capturing the effects of fibre orientation.

Materials and methods

Materials and specimen manufacturing*:* The materials tested were plain weave basalt (110 g/m^2), glass (106 g/m^2), Kevlar® (110 g/m^2), and basalt/flax (95 g/m^2) fibres. Gurit Bio-Prime 37 epoxy resin was used as the matrix. Composite panels were manufactured using the vacuum infusion technique, followed by slow overnight curing. Composite panels were manufactured and the specimens were cut from the panels using a waterjet. Additionally, the cut specimens were post cured in a vacuum oven at a temperature of 50°C for 16 hours.

Mechanical testing: 4-point bending quasistatic flexural testing was performed at 4 mm/min crosshead speed. 90° and 45° fibre orientations were tested.

Results and discussion:

4-point bend flexural testing: As shown in **Figure 1** and **Figure 2**, the 90° fibre orientation exhibited higher flexural strength and modulus compared to the 45° orientation. Among the investigated fibres, basalt

ntlmph008@myuct.ac.za

exhibited the highest flexural strength in both orientations.

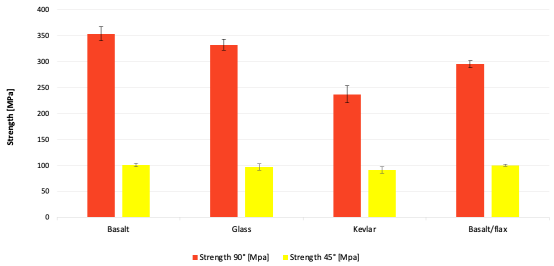

Figure 1: *Flexural strength of fibres at 90° and 45° orientations*

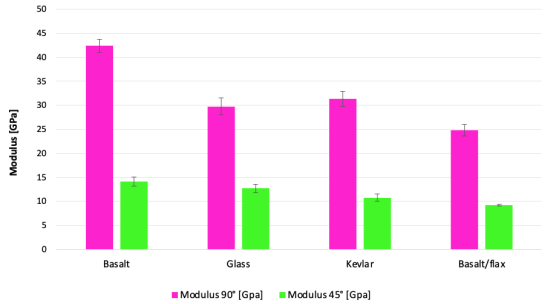

Figure 2: *Flexural modulus of fibres at 90° and 45° orientations*

Basalt/flax composites exhibited brittle behaviour in the 90° orientation but demonstrated flexural strength that is 58 MPa higher than Kevlar®. The low values for Kevlar are attributed to its failure under compression as well as slippage during testing. The flexural strength of glass and basalt fibres was comparable, with basalt showing slightly higher values than glass. However, the flexural modulus of basalt fibre was significantly higher than that of glass as a result of the complex chemical composition of basalt fibre. Additionally, the variation of basalt, glass and Kevlar® fibres in the 45° orientation is due to mixed load-sharing between fibres and matrix.

Conclusion: With the current impetus to develop materials that can both achieve adequate mechanical properties as well as satisfy sustainability goals, basalt fibres present themselves as a promising candidate. The initial results show that the use of basalt fibre reinforcement within a bio-based epoxy polymer matrix could be used as an industrially viable alternative to using traditional fibres such as glass or polyaramids.

References:

1. Rajak, D. K., Pagar, D. D., Menezes, P. L. & Linul, E. Fiber-reinforced polymer composites: Manufacturing, properties, and applications. *Polymers* vol. 11 Preprint at https://doi.org/10.3390/polym11101667 (2019).
2. Aguilera, R. F., Eggert, R. G., Lagos, G. & Tilton, J. E. *Depletion and the Future Availability of Petroleum Resources*.
3. Gonzalez, V., Lou, X. & Chi, T. Evaluating Environmental Impact of Natural and Synthetic Fibers: A Life Cycle Assessment Approach. *Sustainability (Switzerland)* **15**, (2023).
4. Olodu, D. D., Okagbare, G. O. & Ikri, S. O. A Review on the Industrial Applications and Properties of Fiber-Reinforced and Other Polymeric Composites. *NIPES - Journal of Science and Technology Research* **4**, 144–162 (2022).
5. Salman, S. D. Partial replacement of synthetic fibres by natural fibres in hybrid composites and its effect on monotonic properties. *Journal of Industrial Textiles* **51**, 258–276 (2021).
6. Nurazzi, N. M. *et al.* A review on mechanical performance of hybrid natural fiber polymer composites for structural applications. *Polymers* vol. 13 Preprint at https://doi.org/10.3390/polym13132170 (2021).
7. Madueke, C. I., Mbah, O. M. & Umunakwe, R. A review on the limitations of natural fibres and natural fibre composites with emphasis on tensile strength using coir as a case study. *Polymer Bulletin* vol. 80 3489–3506 Preprint at https://doi.org/10.1007/s00289-022-04241-y (2023).
8. Ralph, C., Lemoine, P., Summerscales, J., Archer, E. & McIlhagger, A. Relationships among the chemical, mechanical and geometrical properties of basalt fibers. *Textile Research Journal* **89**, 3056–3066 (2019).
9. Jamshaid, H. & Mishra, R. A green material from rock: basalt fiber – a review. *Journal of the Textile Institute* vol. 107 923–937 Preprint at https://doi.org/10.1080/00405000.2015.1071940 (2016).
10. Chowdhury, I. R., Pemberton, R. & Summerscales, J. Developments and Industrial Applications of Basalt Fibre Reinforced Composite Materials. *Journal of Composites Science* vol. 6 Preprint at https://doi.org/10.3390/jcs6120367 (2022).
11. Karvanis, K., Rusnáková, S., Krejčí, O. & Žaludek, M. Preparation, thermal analysis, and mechanical properties of basalt fiber/epoxy composites. *Polymers (Basel)* **12**, (2020).

LiDAR TO INFER RAILWAY INFRASTRUCTURE MEASUREMENTS

MS Suleiman[a], A Bekker & NC Taylor

[a] Department of Mechanical & Mechatronic Engineering, Stellenbosch University, Stellenbosch, South Africa

Abstract: The condition of railway infrastructure has a direct effect on the operation and condition of trains. Light Detection and Ranging (LiDAR) technology enables the automated assessment of railway infrastructure, which is a critical need for modern railway maintenance systems. This extended abstract presents preliminary work towards developing a Cyber-Physical System (CPS) for the automatic determination of the track gauge. The development of the CPS is guided by a set of functional and non-functional requirements that were formulated through a systems engineering approach. The CPS comprises a physical measurement system to be installed on the train, which feeds information to the software components for processing. Preliminary tests show that reflectance and intensity information in point cloud scans can prove valuable in calculating the track gauge.

Introduction: Railway transport contributes greatly to a country's ability to move passengers to their desired destinations. South Africa depends on passenger trains to transport thousands of commuters to and from their workplaces daily. To ensure the smooth operation of South Africa's railway network, railway assets need to be in good condition since the reliability of the entire rail network is a function of the reliability of the various infrastructure subsystems[1].

Current condition monitoring practices include visual inspection and data analysis from asset condition monitoring devices[1]. These methods are both time-consuming and cost intensive. The extensive amount of rail infrastructure, such as over 2000 kilometres of commuter railway track, puts pressure on maintenance teams doing manual inspection due to scheduling and budget constraints[2]. Human error can also be introduced during visual inspections, which may lead to defects being missed[2].

Light Detection and Ranging (LiDAR) is a non-destructive testing method that can produce detailed point clouds of the physical geometry of railway infrastructure features, which can aid in infrastructure condition monitoring[3]. This is because information about the geometry of the infrastructure components in question can be captured, processed, and saved automatically, leading to more efficient decision-making and eliminating the need for tedious and labour-intensive inspections by humans. A Cyber-Physical System (CPS) is a system that integrates cyber components, such as software architectures and programs, and physical components, such as infrastructure, using modern sensor, network, and computing technologies[4].

Track condition will influence dynamic wheel-rail interaction[5]. Thus, an active train-borne railway infrastructure monitoring CPS can contribute to the health of both the train and the railway infrastructure it interacts with.

Objectives: The objective of this study is to develop and evaluate a proof-of-concept CPS that utilizes LiDAR technology to map railway infrastructure geometry and detect railway infrastructure defects, with a particular interest in the automatic determination of incorrect track gauge. The development will include the design and implementation of a digital representation of the railway infrastructure within a South African context. The CPS will process LiDAR data collected to extract track geometry from other environmental features and determine anomalies in the track gauge. The results will be visualized and reported through a dashboard to support infrastructure condition monitoring and informed maintenance decision-making.

Requirements analysis: The railway environment comprises two main infrastructure components, namely the track, which consists of the rails, sleepers, and ballast, and the Overhead Traction Equipment (OHTE), which consists of the masts, catenary wires, ground wires, and the contact wire. The track is a crucial component of the railway infrastructure that interacts directly with the train. It has an impact on the condition of the train, the vehicle dynamics, and ride quality. This study focuses on the track gauge. The track gauge is defined as the smallest distance between the points P1 and P2 on the two rails in Figure 1 and is measured parallel to the top tangent of the rail heads.

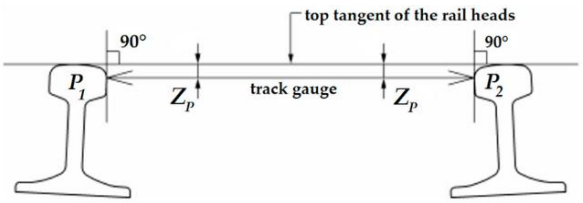

Figure 1: Track gauge measurement definition[6].

South African railway tracks have a nominal gauge of 1065 mm for straight tracks[7]. It was determined that the CPS should be able to automatically detect the track gauge and provide an automated report with alerts to the necessary personnel for track sections that do not fall within the permissible limits[7] for the track gauge. The CPS requirements are divided into functional and non-functional requirements that were developed through a systems engineering approach. The functional requirements are presented in Table 1.

[a] 23843500@sun.ac.za

Table 1: CPS functional requirements

FR ID	Description
FR1	Record LiDAR point cloud data of the railway environment suitable for determining the track gauge.
FR2	Identify the position of the defective gauge using a GPS.
FR3	Process the LiDAR point cloud data automatically to determine the track gauge and identify deviations.
FR4	Present information about the railway infrastructure state.
FR5	Create an automated track condition report that notifies maintenance personnel of track gauge faults.

The non-functional requirements are a measure of the quality of the CPS and are derived from the ISO 25010-2023 standards. **Co-existence** ensures that the measurement component of the CPS can be installed on the train and share its environment without impacting the train itself via permanent modifications. **Operability** means that the CPS user interface should be easy and intuitive for the maintenance team to use. **Reliability** specifies that the measurement system should be able to capture data while the train is operational without any failure or loss of data. **Security** means that the CPS should only be accessible to the designated persons of the maintenance team. **Installability** dictates that the measurement component of the CPS should be designed in a modular way so that it can be successfully moved from train to train. Finally, **Safety** requires the measurement component of the CPS not to interfere with the train driver or passengers in any way that may harm them.

Preliminary LiDAR point cloud results: Preliminary LiDAR point cloud scans of the railway environment were captured at the Gibela Paarden Eiland Depot in reflectance mode and intensity mode. Reflectance refers to how much light reflects off a surface and is a property of the material itself. Intensity refers to the power of the reflected laser pulse as recorded by the LiDAR and is dependent on the material type, distance, and angle of incidence of the target object. Figure 2 shows the point cloud of the railway environment in reflectance mode, while Figure 3 shows the railway environment in intensity mode. Points with higher reflectance and intensity are indicated in red. The reflectance and intensity values measured are relative to one another and can be used to compare points in the same recording. These modes can be used to distinguish features and can be used in processing to calculate the track gauge. The material properties of rails result in the lasers emitted by the LiDAR to not reflect back to the sensor, causing them to appear as invisible bands in Figure 2. In intensity mode, the rails appear as lower intensity bands in relation to the environment around them. These distinct features can be useful for developing algorithms for extracting the rails from the surrounding environment. Once the rails are extracted, the rail gauge can be determined by performing distance computations between the extracted rail points from the point cloud.

Conclusion: This extended abstract presented the system requirements for a CPS that incorporates LiDAR technology to determine deviations in the track gauge. Initial railway environment point cloud scans have shown that various features of the data, such as reflectance and intensity, can aid in the calculation of track gauge. Ongoing work focuses on developing the software components of the CPS.

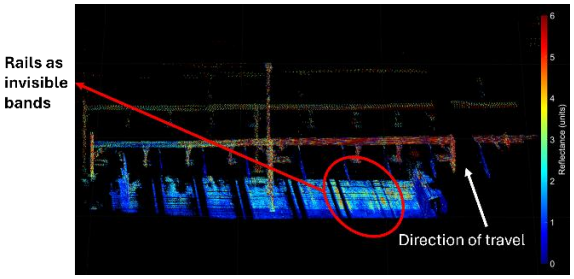

Figure 2: Railway environment in reflectance mode.

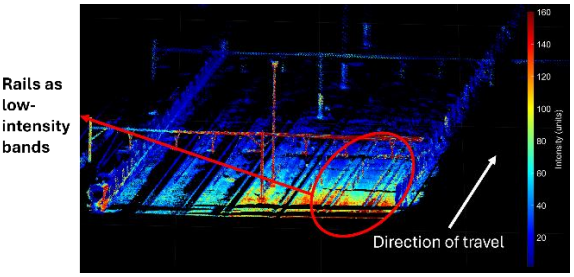

Figure 3: Railway environment in intensity mode.

References:

1. Railway Safety Regulator. *Research Report: Investigating the State of Railway Infrastructure in South Africa*. 2024.
2. Lidén, T. *Railway Infrastructure Maintenance - A Survey of Planning Problems and Conducted Research*. Transportation Research Procedia, Vol 10, 2015, pp. 574-583.
3. Kaartinen, E., Dunphy, K. & Sadhu, A. *LiDAR-Based Structural Health Monitoring: Applications in Civil Infrastructure Systems*. Sensors (Basel), Vol. 22, Issue 12, 2022.
4. Alguliyev, R., Imamverdiyev, Y. & Sukhostat, L. 2018. *Cyber-physical systems and their security issues. Computers in Industry*, Vol. 100, 2018, pp. 212-223.
5. Taylor, M.A.P. *Chapter 8 - Rail transportation systems*. Climate Change Adaptation for Transportation Systems, Elsevier, 2021, pp. 237-275.
6. Fischer, S., Németh, D. & Horváth, H. *Investigation of the Track Gauge in Curved Sections, Considering Hungarian Railway Lines*. Infrastructures, Vol. 8, Issue 4, 2021.
7. Transnet. *Manual for Track Maintenance.* 2012.

A MODULAR DIGITAL TWIN SYSTEM FOR A SMART AUTOMATION AND LEARNING FACTORY LABORATORY

M. Beyer[a] & N. Taylor[b]

Mechatronic Automation and Design Research Group, Department of Mechanical & Mechatronic Engineering, University of Stellenbosch, South Africa

The rapid evolution of Industry 4.0 (I4.0) and Industry 5.0 (I5.0) has transformed manufacturing and learning factory environments, emphasising the need for flexible, human-centric, and sustainable systems. This research proposes the development of a modular and extendable Digital Twin (DT) system for the Stellenbosch Automation and Learning Factory (SALF) Lab. The system aims to support laboratory operations by enabling real-time monitoring, decision-making, and integration of human and machine interactions.

Introduction: I5.0 aims to advance manufacturing contexts and laboratories beyond automation towards human-machine collaboration, adaptability, and sustainability. This shift is centred in DT systems, which is described as a virtual representation of a physical system, enabling real-time monitoring, simulation, and optimisation[1].

Despite growing interest in DT technologies, most existing architectures were designed for fixed industrial setups, making them ill-suited for dynamic, human-centric laboratory environments. These settings are characterised by continuously changing user interactions, variable workflows, and the need to integrate diverse equipment types. As a result, many current DT systems lack the scalability, interoperability, and adaptability required for smart learning factories[2].

This research therefore aims to develop a proof-of-concept modular DT system for the SALF Lab. The proposed framework emphasises modularity, scalability, and human-centricity, enabling real-time monitoring and adaptive decision support within an educational and experimental environment. Leveraging a systems engineering approach guided by Systems Engineering Body of Knowledge (SEBoK)[3], the research follows an iterative development process through a minimum viable product (MVP) and case study evaluation in the SALF Lab. The outcome will demonstrate how the development of a modular DT system can improve efficiency, adaptability, and sustainability in smart manufacturing and learning factory environments aligned with I5.0 principles[4].

System requirements analysis: The system requirements analysis defines the operational context of the SALF Lab, identifying existing limitations and stakeholder needs to inform the design of the DT system. The SALF Lab is a complex environment with multiple users: consisting of laboratory managers, storeroom managers, technicians, academic staff, and students. These users together are responsible for equipment booking, resource management, and maintenance. Current procedures rely heavily on manual logging, emails, and spreadsheets, resulting in inefficiencies, errors, and limited traceability.

Through contextual observation and stakeholder engagement, key requirements were identified, including:

- Real-time monitoring of equipment and user activity,
- Centralised data management and automation of administrative tasks,
- Human-centric interfaces for interaction and feedback,
- Safety enforcement and resource accountability.

These needs informed a set of functional requirements, such as resource booking, component management, safety compliance, and project tracking, alongside non-functional requirements related to efficiency, security, maintainability, and scalability[5].

The proposed DT system will provide a centralised, modular platform capable of integrating human, equipment, and data flows, thereby improving visibility, coordination, and adaptability within the laboratory's operations while still aligning with I5.0's principles: collaboration, resilience, and sustainability[4].

Architecture development: The reference architecture (Figure 1) adopts the approach of Human et al.[6], employing DT instances and DT aggregates in a hierarchical structure that enhances adaptability and modifiability.

- Each DT instance manages its own model, data, and services corresponding to specific laboratory instances or operations.
- DT aggregates extract information from multiple instances to provide higher-level system insights, enabling simplified management, data flow control, and system health monitoring.

The architecture comprises of three main components:

1. **Aggregation Hierarchy:** Reflects the physical structure of the laboratory, handling data capture, system modelling, and diagnostics.
2. **Services Network:** Implements microservices or service-orientated design to provide reusable

[a] 25438204@sun.ac.za, [b] nctaylor@sun.ac.za

services for data integration and manipulation, including external sources such as production or financial data.

3. **Management Services:** Coordinate operations across the hierarchy, supporting real-time decision-making and user interaction.

This modular design ensures that each DT component can operate independently or collaboratively, supporting scalable growth, rapid reconfiguration, and improved fault isolation. By mirroring both human and machine activities, the architecture delivers adaptive data orchestration and ensures that each stakeholder receives context-appropriate information and control at the right time.

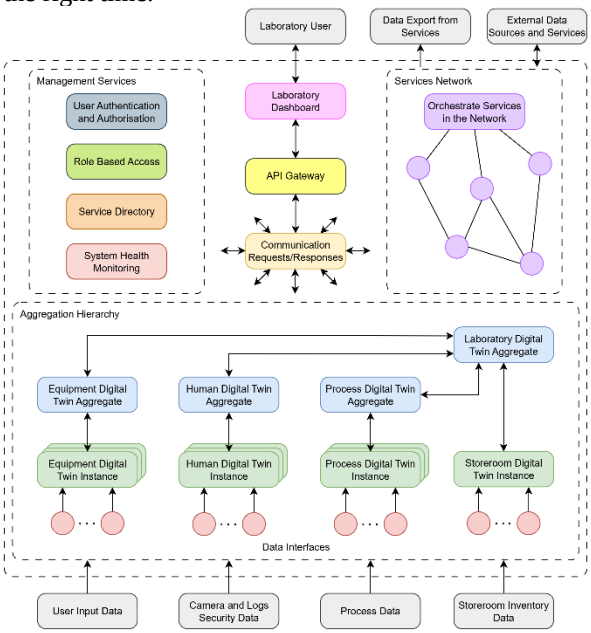

Figure 1: Laboratory Digital Twin reference architecture

MVP implementation: The MVP aims to demonstrate the feasibility of the modular DT system using a software to simulate the SALF Lab's operations to validate system functionality prior to physical deployment. The simulation models the laboratory's layout, workflows, and user interactions to produce three primary data streams:

1. **Camera Data:** Used to detect and track users and observable equipment states.
2. **Process Data:** Collected from live feeds of laboratory processes and equipment systems.
3. **User Interaction Data:** Derived from booking, equipment usage, and component tracking through the laboratory dashboard.

A typical workflow begins when a student books specific equipment or services using the dashboard. Upon collection, the student scans their student card, automatically linking their user profile to the transaction. The storeroom manager verifies and checks out the booked items by scanning the item's barcodes. After use, the student returns the items following the same identification and scanning procedure, allowing the system to update item availability and usage history in real time.

This workflow demonstrates the DT system's improvements over existing manual procedures: automated tracking replaces manual logs, system integration eliminates duplication, and real-time synchronisation enhances resource visibility and operational efficiency. The MVP thus validates not only technical feasibility but also usability, scalability, and potential for human-centered interaction.

Expected outcomes and implications: The MVP is expected to validate the feasibility of a modular, human-centric DT architecture for smart automation and learning factory environments. It will demonstrate real-time synchronisation between virtual and physical representations, automated tracking of user interactions and equipment states, improved coordination of resources and scalability for future extensions.

Beyond technical validation, the study contributes a reusable DT framework for educational and industrial laboratories, advancing I5.0 principles of collaboration, resilience, and sustainability. The approach supports laboratories, such as the SALF Lab, in streamlining operations, automating resource tracking and enabling data-driven management and training.

References:

1. Taylor, N., Human, C., Kruger, K., Bekker, A. & Basson, A. 2019. Comparison of Digital Twin Development in Manufacturing and Maritime Domains, in. *International Workshop on Service Orientation in Holonic and Multi-Agent Manufacturing*. 158-170.
2. Merkel, L., Berger, C., Schultz, C., Braunreuther, S. & Reinhart, G. 2017. Application-specific design of assistance systems for manual work in production. In. *IEEE International Conference on Industrial Engineering and Engineering Management.* 1189-1193.
3. Guide to the Systems Engineering Body of Knowledge (SEBoK). *The Trustees of the Stevens Institute of Technology*: Hoboken, NJ, 2024.
4. Leng, J., Sha, W., Wang, B., Zheng, P., Zhuang, C., Liu, Q., Wuest, T., Mourtzis, D. & Wang, L. 2022. Industry 5.0: Prospect and retrospect. *Journal of Manufacturing Systems*, 65:279-295.
5. ISO/IEC 25010:2011. Systems and software engineering—Systems and software quality requirements and evaluation (SQuaRE). ISO, Geneva.
6. Human, C., Basson, A.H. & Kruger, K. 2023. A design framework for aggregation in a system of digital twins. *Computers in Industry*, 144:103796.

SELF-ADAPTIVE PARAMETER SELECTION IN DIGITAL IMAGE CORRELATION

Raymond Miga[a], Melody Neaves[b] & Gerhard Venter[b]

[a] Department of Mechanical and Mechatronic Engineering, Stellenbosch University, Stellenbosch, South Africa

Abstract: Digital Image Correlation (DIC) is a non-contact photogrammetric technique, which captures full-field surface shape and deformation of specimens. Existing subset-based DIC algorithms require the user to select correlation parameters like the subset size and the order of the shape function in the correlation process. The selection of these correlation parameters strongly influence the accuracy of the results in local deformation measurements. To accurately and precisely capture the full-field deformation measurement, optimal subset sizes and appropriate shape functions need to be selected to obtain a balance in systematic and random errors. This research proposes the development of an algorithm that self-adaptively selects optimal DIC parameters that will minimize displacement and strain measurement errors. The algorithm will adaptively select optimal subset sizes based on local speckle pattern quality and deformation characteristics, while leveraging error estimation metrics to adaptively match the appropriate shape functions to each subset without user input.

Introduction: Digital Image Correlation (DIC) is a non-contact photogrammetric technique proposed by Peters and Ranson[1], which captures full-field surface shape and deformation of specimens. This technique involves segmenting the image into small subsets and correlating each subset of the reference image with a subset of the deformed image[2]. It is simple to use, cost effective and more accurate for a wide range of measurements when compared to other techniques such as speckle interferometry. Despite its advantages over other techniques, the accuracy of DIC heavily depends on the selection of correlation parameters. The correlation parameters are the set of variables that govern how the algorithm matches and tracks the deformation in images. The main parameters are subset size and shape functions. Traditional DIC methods rely on manual parameter selection, which introduces user-dependent variability and artificial uncertainty, often requiring iterative trial-and-error to achieve reliable results[3]. This inefficiency is particularly pronounced in complex deformation scenarios, where uniform parameter settings may fail to capture variations in speckle quality or strain gradients. To address these challenges, self-adaptive DIC algorithms are needed to optimize and select parameters based on image characteristics and deformation states.

Aim and objectives: The aim of this research is to develop a self-adaptive algorithm that selects the optimal subset size and shape function to minimise displacement and strain measurement errors. The objectives are to investigate methods of adaptively selecting the optimal subset size at each measurement point based on local speckle pattern quality and local deformation characteristics, and to investigate methods of adaptively selecting the appropriate shape function for each subset based on the local deformation gradient.

Errors in DIC measurement: There are several sources of error that affect the accuracy of the measurement results. These include errors from the image acquisition process and the analysis algorithm errors caused by the chosen shape functions, correlation criteria, interpolation schemes, and size of subsets[2]. In this work, only random and systematic errors due to subset size and shape function selection are discussed. To achieve optimal measurements, the subset size selected for each measurement point should be large enough to comprise sufficient intensity variations to suppress the random error caused by image noise, and the shape function chosen should precisely depict the underlying deformation in each subset. In general, larger subsets supress noise-induced random errors. However, when the local deformation within large subsets is complex or non-uniform, the commonly applied first order shape function cannot capture it accurately, leading to significant systematic errors in displacement measurements[3]. In such cases, a second order shape function should be applied to minimise the systematic error from undermatching the shape function. In overmatched cases, the random errors generated by the second order shape function are twice that of the first order shape function[3]. Therefore, an optimal subset size and shape function should be adaptively selected for each calculation point to achieve a balance between under-matched systematic errors and random errors in measured displacements.

Error estimation metrics: Generally, to evaluate the accuracy and robustness of a DIC algorithm error metrics such as Root Mean Square Error (RMSE) or Standard Deviation (SD) are used. Additionally, error criteria such as the Mean Absolute Error[3] (MAE) and the Sum of Squared Forward and Backward Displacements[4] (SFBD) have been explored as metrics for evaluating DIC accuracy. These two metrics will be used as objective functions of the adaptive algorithm to effectively select the optimal shape function that minimises their values.

Speckle quality metrics: The quality of a speckle pattern, within a subset, refers to the degree to which its characteristics are favourable for a DIC analysis

[a] 24329746@sun.ac.za

thereby dictating the accuracy and precision of the DIC displacement measurements[5]. To determine the optimal subset sizes, speckle quality metrics like the Sum of Square of Subset Intensity Gradients (SSSIG)[3], Sum of Subset Intensity Variation (SSIV)[6] and Intensity Variation Ratio (IVR)[7] will be used in the self-adaptive algorithm. These quality metrics were chosen as they are shown through either theoretical derivation or empirical observation to be related to the resulting displacement error of a DIC analysis.

Subset size selection using speckle quality metrics: A general flow chart of how the speckle quality metrics are used to obtain subset size is shown in Figure 1. For every subset in the reference image the speckle quality is evaluated using one the metrics and is compared to a predetermined threshold from literature. If the quality in the subset is insufficient the subset size is increased by two until the threshold is reached or a maximum subset size value is reached. A subset size of 9 is used as the initial value as this is the minimum size recommend by Hassan[7] to contain enough information for DIC analysis. These metrics are added to a regular DIC, SUN-DIC[8], to make it self-adaptive.

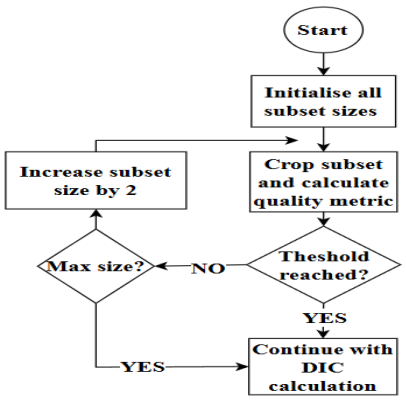

Figure 1: General subsets size selection using speckle quality metrics

Experiments and results: To evaluate the performance of the subset size selection using each of the above speckle quality metrics, a validation test was performed on a numerical dataset from the DIC challenge 1.0 (Sample14)[9]. The RMSE, which can be regarded as a total error of undermatched systematic error and random error, was used to evaluate the accuracy and precision of the self-adaptive algorithms and the regular DIC. A first order shape function was used for all the experiments. The test for the regular DIC was done with constant sizes of 9 and 71 throughout the region of interest. The subset sizes obtained from using the metrics and RMSE values of the x displacement are shown in Table 1. The SSSIG and IVR algorithms with varying subset sizes throughout the image dataset are found to perform better on this dataset than the regular DIC with a constant small or large subset size. A contour plot of the subset sizes selected by the SSSIG based algorithm is shown in Figure 2.

Table 1: Subset size range and RMSE results

	Subset size range	RMSE
Regular DIC	9	0.0329
Regular DIC	71	0.0213
IVR	9-53	0.0063
SSIV	39-41	0.0077
SSSIG	15-49	0.0065

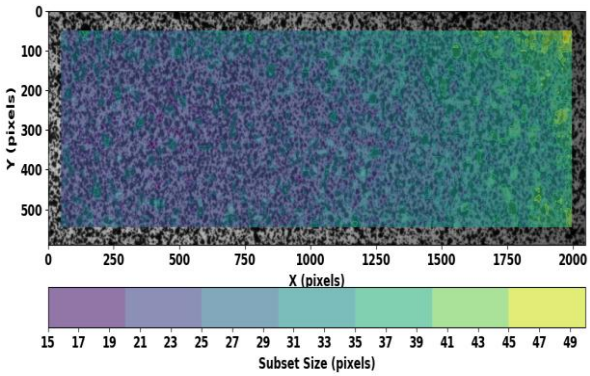

Figure 2: Subset size contour plot for SSSIG based self-adaptive DIC

Conclusion: The accuracy of DIC is dependent on many different parameters like the subset size and shape functions. Experimental tests demonstrated that using speckle quality metrics to adaptively select optimal subset sizes outperforms constant small or large subset sizes in DIC analysis.

References:

1. Peters, W. H., & Ranson, W. F. Digital imaging techniques in experimental stress analysis. *Optical Engineering*, 21(3), 1982 pp. 427–431.
2. Zhao, J., Sang, Y., & Fuhai, D. The state of the art of two-dimensional digital image correlation computational method. *Engineering Reports*, 1(1), 2019, e12028.
3. Zhao, J., & Pan, B. Smart DIC. *Mechanical Systems and Signal Processing*, 222, 2025.
4. Tu, P., & Liu, X. An error criterion in digital image correlation for unknown deformation fields. *Experimental Mechanics*, 57(5), 2017, pp. 783–799.
5. Dong, Y., & Pan, B. *Experimental Mechanics*, 57(7), 2017, pp. 1161–1181.
6. Zhang, W., Zhou, R., & Zou, Y. Self-adaptive and bidirectional dynamic subset selection algorithm for digital image correlation. *Journal of Information Processing Systems*, 13(2), 2017, pp. 305.
7. Hassan, G. MacNish, C., Dyskin, A., & Shufrin, I. Digital image correlation with dynamic subset selection. *Optics and Lasers in Engineering*, 84, 2016, pp. 23–33.
8. Venter, G., 2024. SUN-DIC: Digital image correlation. https://github.com/gventer/SUN-DIC.
9. Ahmad, W., Helm, J., Bossuyt, S. *et al.* Stereo-DIC challenge 1.0 – Rigid body motion of a complex shape. *Experimental Mechanics* 64, 2024, pp. 1073–1106.

VISCOELASTIC MATERIAL CHARACTERIZATION OF VIBRATION DAMPING MOUNTS

Elijah M. Stockhall[a] & Martin P. Venter[b] & Gerhard Venter[b]

[a,b] Department of Mechanical Engineering, Stellenbosch University, Stellenbosch, South Africa

Abstract: This research makes use of novel methods to characterize as-built rubber vibration damping mounts where standard testing and characterization methods are unavailable. The characterized model is then used to create a 1-D non-linear bushing element which can be used in a large-scale rigid-body simulation.

Introduction: Rubber is a class of materials made of randomly oriented long molecular chains that cross-link to form a network configuration[1]. Rubbers' behaviour displays both an elastic, and a time-dependent viscous component. Due to these behaviours, they are a common choice for vibration damping mounts[2]. The aim of this work is to characterize the hyperelastic and viscoelastic behaviour of an as-built rubber vibration damping mount and generate a material model. The material model will then be used to create a 1-D non-linear bushing element to represent the as-built parts behaviour in a large simulation.

As the specimen takes the form of an as-built part, standard characterization procedures are not viable. Instead, an approach that can accommodate the as-built part geometry is required.

Hyperelastic Characterization: In order to characterize the hyperelastic behaviour of the rubber mount, the Hyperplane Method was used[3]. As the specimen geometry is different from that used by Van Tonder (2024)[3], the method was adapted to suit this research. This research first characterizes the hyperelastic behaviour of Smooth-Sil 950, the same material characterized by Van Tonder (2024)[3] and others at Stellenbosch University[4,5,6]. A direct comparison of the results obtained in this research with those obtained by Van Tonder (2024)[3] and others validated the adapted method.

The Hyperplane Method can be broken down into two main components, the experiment and numerical pipeline. The numerical pipeline uses an inverse FE method to fit the hyperelastic model to the experimental data. A constrained optimization algorithm minimized the error between the deformed surface of the FE model and the deformed surface of the experimental data, while using equality constraints to minimize the error between the experimental force/displacement curve and the FE model force/displacement curve. The main advantage of the Hyperplane Method is that it avoids the problem of non-unique solutions that are found when using inverse update methods.

The experiment involves placing a specimen, which has been marked with a DIC speckle pattern, in-between two polished compression platens. The surface of the platens is coated with a thin PTFE based lubricant to reduce the effects of friction. The specimen is compressed and a stereo DIC system is used to capture the surface deformation of the specimen. The DIC data, along with the force-displacement data are then inputted into the numerical pipeline. The result of which is a set of fitted Mooney-Rivlin coefficients.

Viscoelastic Characterization: The viscoelastic behavior was characterized through Prony series coefficients, which describe time-dependent stress relaxation. This research develops and validates an inverse update method for determining Prony coefficients for complex geometries where classical analytical solutions are not feasible. Combining the Prony series with hyperelastic material models yields a hyper-viscoelastic model that is used in the creation of the 1-D non-linear bushing.

The inverse update method replicates the relaxation experiment virtually using FEA. Both the simulated and experimental force decay curves are normalized to reduce the influence of hyperelastic parameters on viscoelastic characterization. An optimization algorithm compares the normalized curves and adjusts the Prony series coefficients until the simulation matches the experimental data.

To validate this inverse update method, four different geometries were manufactured from Smooth Sil 950: dogbone specimens, compression pucks, tension rings, and a replicate as-built part. The dogbone geometry serves as the validation case due to its simple uniaxial stress state, which permits classical analytical determination of Prony coefficients. By comparing the analytical results against the inverse method output for dogbones, the pipeline's accuracy could be verified before applying it to geometries with more complex stress states.

However, the pipeline results for the dogbone specimens did not match the experimental data well. It was also observed that the classically obtained Prony series coefficients, when entered into the FE simulation, showed a large difference in the force decay curve compared to the experimental data which is shown in Figure 2. Further investigation into this is currently being done.

The experimental results for the different geometries can be seen in Figure 1. For each batch, a set of eight of the respective geometry and eight dogbones were cast. By comparing the results from the different geometries to that of the dogbones for each batch respectively, batch effect is negated. The batch effect is also captured by comparing the dogbones from

[a] 23648341@sun.ac.za

different batches. The results show a clear difference in the behaviour of the relaxation between geometries highlighting the need for the inverse update method.

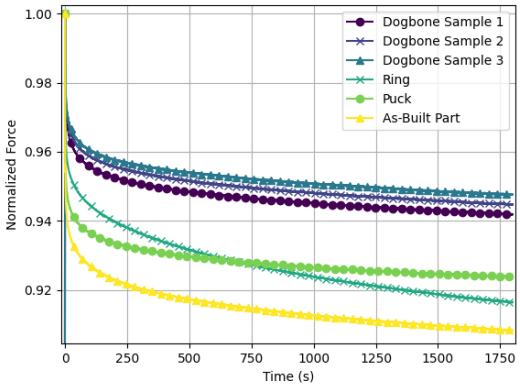

Figure 1: Comparison of the different viscoelastic geometries by using the normalized force. Samples from the same batch have the same symbol.

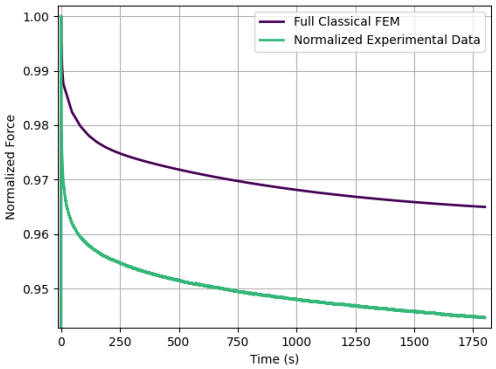

Figure 2: Normalized force decay curves for both the experimental data and the FE simulation using classically derived Prony series coefficients.

Results: This research is still a work in progress. The hyperelastic characterization of Smooth Sil 950 did not yield results that correlate with previous characterizations of the material. Further investigation and testing is being carried out to determine reasons for the differences. Figure 3 shows the differences between this research and prior research in uniaxial loading.

For the viscoelastic characterization, this research has noticed a large difference between the experimental data and virtual experiments done using material properties obtained through standard techniques. Further research is being conducted to understand these differences as well as fully validating the pipeline.

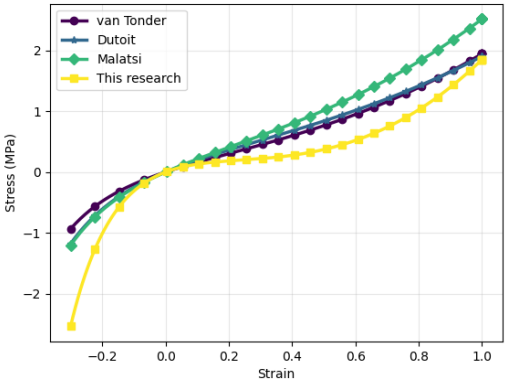

Figure 3: Comparison of uniaxial loading for this research vs literature.

References:

1. Khajehsaeid, H., Arghavani, J. and Naghdabadi, R. (2013). A hyperelastic constitutive model for rubber-like materials. European Journal of Mechanics - A/Solids, vol. 38, pp. 144–151. ISSN 0997-7538. Available at: https://www.sciencedirect.com/science/article/pii/S0997 53812001143

2. Ucar, H. and Basdogan, I. (2018). Dynamic characterization and modeling of rubber shock absorbers: A comprehensive case study. Journal of Low Frequency Noise, Vibration and Active Control, vol. 37, no. 3, pp. 509–518. Available at: https://journals.sagepub.com/doi/abs/10.1177/146134 84177 25954

3. Van Tonder, J.D. (2024). Using full field data to produce a single indentation test for fully characterising the mooney rivlin material model.

4. Du Toit, V. (2018). Characterising material models for silicone-rubber using an inverse finite element model updating method.

5. Ellis, D.R. (2020). Generative design procedure for embedding complex behaviour in pneumatic soft robots.

6. Malatsi, K.D. (2025). Hyperelastic and viscoelastic characterization and modelling of silicone rubber.

ASSESSING THE MACHINING PARAMETERS ON THE SURFACE ROUGHNESS OF EN19 SHAFTS

R. Kruger [a] ; P.A. le Roux [b]

[a, b] Independent Institute of Education, Emeris, Faculty of Science & Technology, Johannesburg South Africa

Abstract

Precision machining of alloy steels such as EN19 (AISI 4140) requires careful control of turning parameters to achieve optimal surface quality. This study evaluates how turning parameters influence the surface finish of EN19 shafts. Using cutting speeds ranging from 20 – 40 m/min and feed rates of 100, 200 or 300 mm/min as the variable parameters, the surface roughness was measured. Commonly measured surface roughness parameters aligned with theory showcasing an increase in measurements with an increased feed rate and decreased with cutting speed. Microscopy and hardness mapping of the test shafts revealed significant non-homogeneity in the material which likely contributed to the scatter in the surface roughness data. The results indicate that increasing the feed rate leads to higher surface roughness, while increasing the cutting speed produces a smoother finish. Variations in the microstructure and hardness across the test shafts introduced scatter into the data, partially obscuring the true effects of the cutting parameters.

Introduction:

The surface finish of any shafting component ensures sustained mechanical performance, prolonged component life and reduces financial and environmental impact of manufacturing. Surface roughness is a widely adopted measurement parameter to indicate the quality of a surface finish. As turning is the most common method of machining of metallic shafts, its machining parameters are one of the most influential factors in the performance in shaft performance.

EN19 is commonly used for shafting components in high-wear applications. EN19 has a high yield strength, shock resistance, and has a high wear resistance [1], making it suitable for applications where high cyclic stresses and wear are required. The machining parameters of turning and their impact the surface finish of a component is well documented for most materials, however, EN19 has a significant gap in the literature, especially in surface performance.

This study assesses how the machining parameters in the manufacturing of EN19 shafts by turning, altered the surface roughness of the shafts.

The aim of this experimental investigation is to determine the influence of single point machining parameters, specifically the cutting speed and feed rate, on the surface characteristics of EN19 test shafts.

Methodology:

The test shafts were machined with the ISO 1143 standard [2] in mind so that they could later be used for fatigue testing.

Machining was performed using a triangular ISCAR TNMG16404-TF cutting tool with a nose radius of 0.4mm. The cutting tool is a carbide tool and is graded M200, designed and rated for use on steel, stainless steel, hard materials and super alloys. The recommended turning parameters are feed rate 0.12-0.3mm/rev, maximum depth of cut 3mm.

The cutting parameters, presented in Table 1, were selected for this study based on other turning parameters of previous literature [1], [3], [4], [5], taking the cutting tool and available lathe parameters into consideration. A depth of cut of 0.15 mm and conventional flood cooling were implemented and kept constant for this study.

Table 1: Turning Parameters

Cutting Speed (m/min)	Feed Rate (mm/min)
20	100
30	200
40	300

Three cutting speeds, three feed rates, and four specimens per combination were manufactured. A total of 36 test shafts were machined and tested.

Results:

In **Figure *1*** below, the final machined test shaft is shown.

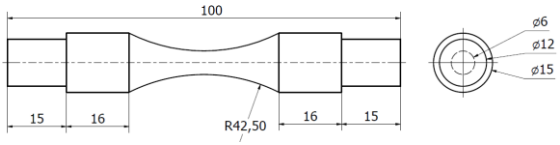

Figure 1: Machined Test Shaft

Surface Roughness:

The surface roughness measurements were taken along the hourglass test section of the test shafts. Four readings per test shaft were taken for all 36 test shafts. The surface roughness measurements recorded are as follows: Average Surface Roughness, Average maximum peak height, Root Mean Squared Surface Roughness, Skewness, and Kurtosis.

Figure *2*, shows the collated and refined data of the Average Surface Roughness. The trends for the average surface roughness, the average maximum peak height, and the root mean squared surface roughness all show that as the feed rate increases, so does the surface roughness. And as the cutting speed increases, the surface roughness decreases.

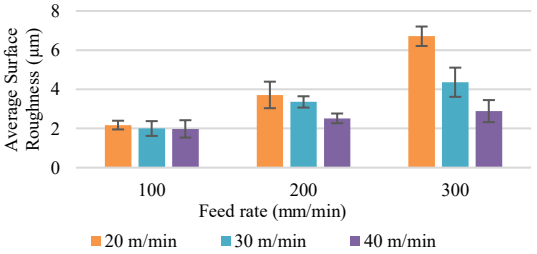

Figure 2: Average Surface Roughness Measurements

[a] Corresponding Author: R. Kruger; Email address: rkruger@iie.ac.za

The skewness results, **Figure *3***, were inconclusive as those of the other four surface roughness parameters, which resulted in the standard deviation often being larger than the mean value. The two test parameters which had the biggest standard deviation were both at a feed rate of 300mm/min and at cutting speeds of 20 and 40m/min.

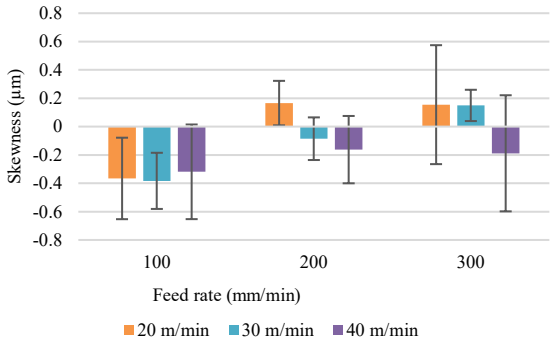

Figure 3: Skewness of Surface Roughness Measurements

The kurtosis surface roughness data, **Figure *4***, shows a near constant distribution at a feed rate of 200 m/min, with the other two feed rates, 100 and 300m/min showing much larger variation due to cutting speed when compared to the data from the 200m/min test shafts.

Comparing the impact on a constant cutting speed, the test shafts at a cutting speed of 30m/min show little variation in value, whereas the cutting speeds of 20 and 40m/min have larger variations when compared.

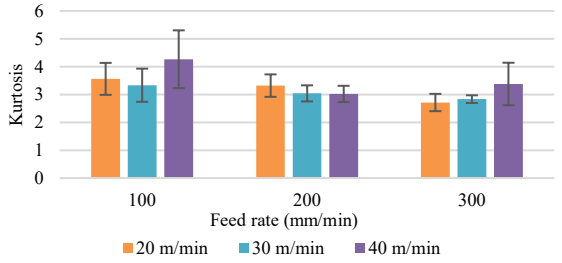

Figure 4: Kurtosis of Surface Roughness Measurements

Microscopy:

The test shafts chosen for microscopic analysis were the shafts which had the closest surface roughness values to the mean surface roughness of the 4 test shafts at the same speed and feed. **Figure 5** shows the image of the test shaft A4. These images revealed that the material sheared quite significantly during the cutting process, which was not expected for the EN19.

Figure 5: Microscopic Image of Test Shaft A4

Three uncut test shafts were polished, etched and then placed under the microscope for analysis.

Figure *6*, below shows one of the many defects in the surfaces of these test shafts. Along with the defects, it was also noted that the micro-structural phases of the steel were not consistent across the three samples. One sample had more significant pearlite sections than the other two, whereas one of the other test shafts showed much greater areas of ferrite. This led to the conclusion that this as-rolled, forged EN19 steel was not homogeneous throughout.

Figure 6: Microscopic Image of a Defect on the Surface of the Etched Test Shaft

Hardness Tests:

Due to the non-homogeneity of the EN19 steel, hardness tests were conducted on the opposite side of the uncut test shafts. The expected hardness in Rockwell C, according to literature is between 33.1 and 40.4 HRC. Across the three test shafts, a range of 30.8 to 40.9 HRC. This is a significant variation considering that the steel came from the same supplier in the same batch. The mean across all three test shafts is 34.2 HRC.

Conclusion:

In conclusion, the machining of EN19 test shafts under the chosen test ranges confirmed the dominant, opposing effects of the feed rate, increasing the surface roughness, and the cutting speed, which decreases the surface roughness. However, the available material had large variability in microstructure and hardness, which introduces additional scatter and can mask the effect the cutting parameters may have on the surface finish. Further study would be to anneal each sample before cutting to ensure a more homogeneous microstructure, and more likely to show the effects of the cutting parameters on the surface finish in greater detail.

References:

[1] P. Paengchit and C. Saikaew, "Effects of Cutting Speed and Feed Rate on Surface Roughness in Hard Turning of AISI 4140 with Mixed Ceramic Cutting Tool," *Key Engineering Materials,* vol. 779, pp. 153-158, 2018.

[2] ISO, *Metallic Materials- Rotating Bar Bending Fatigue Testing,* Geneva, Switzerland: International Standard, 2010.

[3] A. Javidi, U. Rieger and W. Eichlseder, "The effect of machining on the surface integrity and fatigue life," *International Journal of Fatigue,* vol. 30, no. 10-11, pp. 2050-2055, 2008.

[4] N. Qehaja, K. Jakupi, A. Bunjaku, M. Bruci and H. Osmani, "Effect of Machining Parameters and Machining Time on Surface Roughness in Dry Turning Process," *Procedia Engineering,* vol. 100, pp. 135-140, 2014.

[5] O. Zurita, V. Di-Graci and M. Capace, "Effect of cutting parameters on surface roughness in turning of annealed AISI-1020 steel," *Revista Facultad de Ingeniería,* vol. 27, no. 47, pp. 109-116, 2018.

Comparative Evaluation of Model Predictive and Adaptive Model Predictive Control for Demand-Side Optimization in Active Distribution Networks

Moteane Melamu [a] & Efe Orumwense[b]

Department of Electrical, Electronic and Computer Engineering, Cape Peninsula University of Technology, Cape Town 7535, South Africa
[b] Department of Mechanical and Mechatronics Engineering, Cape Peninsula University of Technology, Cape Town 7535

Introduction

The proliferation of RES, such as photovoltaic (PV) panels, electric vehicles (EVs), fuel cells, and wind turbines, can enhance energy security and reliability. However, due to the dynamic and intermittent nature of RES introduces several instabilities, thereby necessitating robust and precise control to achieve optimal control and functioning[1]. The attainment of optimal and functioning of the microgrid is based on three main control objectives: (1) load sharing among several distributed generators (DG) , (2) voltage and frequency regulation and stabilisation, and (3)economic benefit maximisation [2]–[4]. The two objectives can be attained by the regulation of power electronics, whereas the third one is to decide on energy dispatch, minimise power loss, and the operational cost[5]. This is what is known as an Energy Management System (EMS), and it varies from heuristic approaches to complex optimization algorithms. In the quest to reduce operational cost, energy losses, and fuel usage, the EMS will maximize the employment of RES[6], [7]. PID controllers are the most frequently employed in microgrid optimization; however, they struggle with fixed tuning, lack predictive ability, and handle nonlinearities poorly. They are sensitive to noise and not well-suited for multi-objective or large-scale systems. More advanced control methods are often preferred for better adaptability and performance. Model Predictive Control (MPC) optimises system performance by predicting future behavior and handling multiple variables with constraints[8].

MPC Concept

The MPC is a set of several control approaches that utilize information to predict the system output along the horizon that follows specific restrictions.. The computations in MPC are based on the current measurements and estimates of future output results. In order to properly estimate the outputs, a particular order of control actions must be followed for precise predictions that follow the reference point, depicted in Figure 1 below [9], [10].

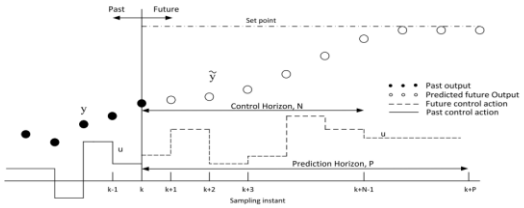

Figure 1: Basic concept of MPC

Traditional MPC has a limitation in adapting to dynamic grid conditions, too. To resolve this, the Adaptive Model Predictive Control (AMPC) framework combines offline reinforcement learning for parameter tuning with online MPC using soft constraints. It adapts to disturbances in real-time, ensuring safe and efficient operation. MPC's flexibility and optimization-based approach improve cost-effectiveness and system stability. Furthermore, AMPC also increases implementation complexity and demands more intricate tuning to ensure stability and convergence[8], [11].

Objective approach

The objective is to analyse AMPC and MPC to determine which is more effective in maximising the use of renewable energy sources (RES) to reduce operational costs and minimize power imports from the grid through disturbances of load variation and intermittency of RES.

Dispatch Strategy

Under Time-of-Use (TOU) tariffs, EV and battery charging and discharging are managed across peak, standard, and off-peak to optimize cost and grid interaction. During peak periods, EVs and battery discharge energy to support the load while ensuring power balance. EVs and batteries are charged when there is surplus generation from wind and PV from 11:00 to 15:00, depicted in Figure 2 below, when electricity prices are lowest. During peak periods, when electricity prices are high, EVs and energy storage participate in energy dispatch to export power to the grid to generate revenue depicted in Figure 3.

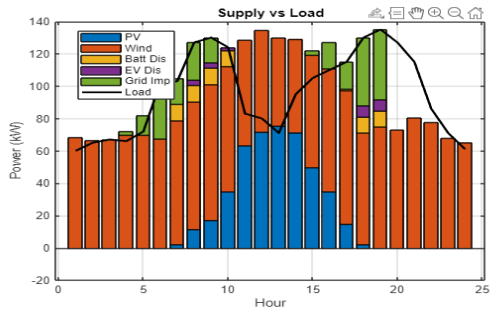

Figure 2: Load demand and power output from RES

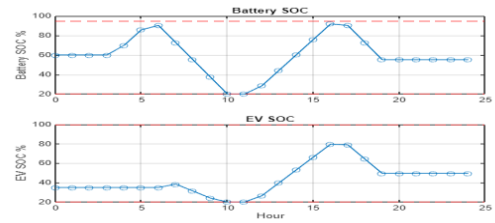

Figure 3: Battery and EV charging and discharging

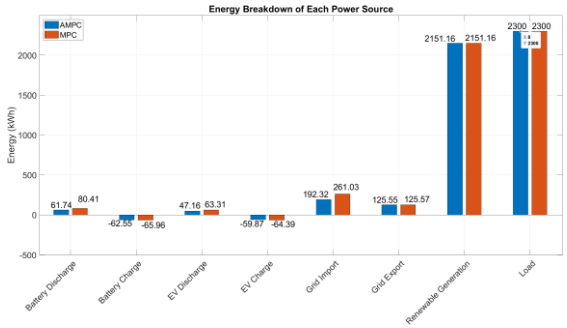

Figure 4: AMPC -MPC Comparison

Conclusion

MPC performs well under stable conditions, and AMPC adapts effectively to the system uncertainties. AMPC demonstrated superior cost reduction and improved energy dispatch. It maximised RES, EVs, and energy storage utilization and reduced dependency on fossil fuels. Overall, AMPC provides a more flexible and efficient control for modern microgrids. Future research should explore hybrid and intelligent optimization techniques to further improve AMPC performance.

Reference

[1] Mazzola.;S.;Vergara.;C.;Astolfi.;M.;Li.;V.; Perez-Arriaga.;I.;and Macchi.;E., Assessing the value of forecast-based dispatch in the operation of off-grid rural microgrids, Renew. Energy, vol. 108, pp. 116–125, 2017, doi: 10.1016/j.renene.2017.02.040.

[2] Shan.;Y.;Hu.;J.;and Liu.;H., A Holistic Power Management Strategy of Microgrids Based on Model Predictive Control and Particle Swarm Optimization, IEEE Trans. Ind. Informatics, vol. 18, no. 8, pp. 5115–5126, 2022, doi: 10.1109/TII.2021.3123532.

[3] IEEE Std 2030.7-2017, Standard for the Specification of Microgrid Controllers,. 2018.

[4] Hu.;J.;Guerrero.;J.;and Islam.;S., Model Predictive Control for Microgrids: From power electronic converters to energy management, Inst. Eng. Technol., p. 260, 2021, [Online]. Available: https://vbn.aau.dk/en/publications/model-predictive-control-for-microgrids-from-power-electronic-con

[5] Hu.;J.;Shan.;Y.;Guerrero.;J. M.;Ioinovici.;A.;Chan.;K. W.;and Rodriguez.;J., Model predictive control of microgrids – An overview, Renew. Sustain. Energy Rev., vol. 136, no. October 2020, p. 110422, 2021, doi: 10.1016/j.rser.2020.110422.

[6] Mariam.;L.;Basu.;M.;and Conlon.;M. F., Microgrid: Architecture, policy and future trends, Renew. Sustain. Energy Rev., vol. 64, pp. 477–489, 2016, doi: 10.1016/j.rser.2016.06.037.

[7] Molderink.;A.;Bakker.;V.;Bosman.;M. G. C.;Hurink.;J. L.;and Smit.;G. J. M., Management and control of domestic smart grid technology, IEEE Trans. Smart Grid, vol. 1, no. 2, pp. 109–119, Sep. 2010, doi: 10.1109/TSG.2010.2055904.

[8] Liu.;Y.;Chau.;T. K.;Wei.;Z.;Hu.;Y.;Zhang.;X.;and Manandhar.;U., A Novel Adaptive Model Predictive Control Strategy of Solid Oxide Fuel Cell in DC Microgrids, IEEE Trans. Ind. Appl., vol. 58, no. 5, p. 16, 2022.

[9] Joshal.;K. S. and Gupta.;N., Microgrids with Model Predictive Control: A Critical Review, Energies, vol. 16, no. 13, p. 4851, 2023, doi: 10.3390/en16134851.

[10] Schwenzer.;M.;Ay.;M.;Bergs.;T.;and Abel.;D., Review on model predictive control: an engineering perspective, Int. J. Adv. Manuf. Technol., vol. 117, no. 5–6, pp. 1327–1349, 2021, doi: 10.1007/s00170-021-07682-3.

[11] Yameen, Muhammad Zubair Lu.;Z.;El-Sousy.;F. F. M.;Younis.;W.;Zardari.;B. A.;and Junejo.;A. K., Improving frequency stability in grid-forming inverters with adaptive model predictive control and novel COA-jDE optimized reinforcement learning, Sci. Reports, 2025, doi: 10.1038/s41598-025-00896-5.

Propulsion Rig: A multirotor performance measurement test platform

G Hasewinkel[a] & A Pretorius[a]

[a] MechatronicSystems.Group, Department of Mechanical Engineering, University of Cape Town, Cape Town, South Africa

Off-the-shelf multirotor propulsion system components can produce uncertain static and dynamic performance. Commercially, solutions exist to characterise the inexact performance of a propulsion system, yet they can be prohibitively expensive. To that end, the Propulsion Rig, a low-cost and open-source multirotor test platform, is developed and used to measure the principal performance characteristics of multirotor propulsion systems. The data gathered can be used to generate static and dynamic models of the propulsion system of interest, thereby reducing the uncertainty in the drivetrain performance. The models can be used to validate conceptual multirotor designs, and, additionally, incorporated into simulation models to aid the control design process. By accounting for the propulsion system dynamics, the control scheme performance can potentially be improved. Static propeller characterisation results obtained from the Propulsion Rig are shown to closely match data provided in reputable online databases.

Unmanned Aerial Vehicles (UAVs) have become ubiquitous in their application and have seen a significant increase in research into the technology. Multirotor Aerial Vehicles (MRAVs), commonly known as drones, are being used in an ever-increasing variety of tasks in the real world. However, the constituent components of the multirotor drivetrain generally stem from off-the-shelf parts. Brushless DC motors, propellers, and electronic speed controllers, in various combinations, produce wide ranging and, at times, uncertain static and dynamic performance, which makes conceptual design non-trivial. To account for this, the propulsion system operating conditions can be emulated in an environment of sensors that capture the fundamental performance characteristics, such as thrust, motor current draw, rotor angular velocity, and PWM commands.

There have been numerous systems built within the commercial, research and hobbyist domains for the purpose of characterising a propulsion system. Generally, hobbyist solutions are cost-effective, but only measure thrust, while commercial solutions are usually expensive but measure torque too; research solutions fall somewhere between. There are two prominent commercially available solutions, that being from Tyto Robotics and Wing Flying Tech. The most affordable products offered by the two companies, and most applicable for small to medium scale MRAVs, cost $1075 (R19,957) and $2669 (R48,575), respectively[1,2]. This is often an infeasible cost point for research institutes with limited funding.

Due to the lack of low-cost solutions, the aim of this project is to develop an open-source measurement system with similar functional performance characteristics to that of the commercially available solutions. Through an examination of the reported approaches, a set of realistic and permissible attributes for the designed rig are generated as part of a user needs analysis. Constrained by the stipulated user needs analysis, the platform underwent numerous design iterations, with the latest, and version that is open-sourced, shown in Figure 1. The build cost of the open-sourced measurement rig amounts to under R1207.

Figure 1: Fabricated measurement rig

The Propulsion Rig's design principle is simple; it uses a straight beam load cell in cantilever configuration, where one end is fixed, and on the other end, the thrust load is applied. When the propeller generates thrust, a moment is induced on the straight bar beam load cell. The load cell is in full Wheatstone configuration, thus negating any strain that would otherwise be detected from the generated drag torque by the propellers. The bending moment results in elastic deformation, which in turn is captured by the resistors within the Wheatstone bridge of the load cell.

The Propulsion Rig's primary components are manufactured through additive manufacturing, namely, 3D printing. 3D printing was chosen due to the degree of shape complexity it allows for, the minimal manufacturing cost, low production time, and barrier to entry.

The embedded system architecture is designed and implemented to sense and acquire the generated thrust, motor current draw, rotor angular velocity, and PWM commands. On a top level, the measurement rig embedded system architecture is structured as shown in Figure 2. The measurement rig utilises an infra-red transmitter and receiver sensor to measure the propeller angular velocity. The current transducer is the AC758 hall effect sensor, and the thrust is measured using the

[a] HSWGUY001@myuct.ac.za

parallel beam TAL220B load cell and then discretised using the HX711; a low-cost COTS dual channel load cell amplifier with a 24-bit ADC. The embedded system code base is implemented on two microcontrollers, and one local PC machine. The testing routine is automated using a python script, whereby communication is routed through the respective serial ports of the microcontrollers.

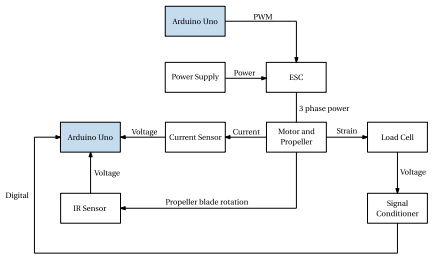

Figure 2: Measurement rig embedded system architecture.

To evaluate a motor and propeller combination, there are two types of tests: static and dynamic. Statically testing the propulsion systems yield several useful parametric studies. A small subset of the relevant and useful parametric studies is detailed in Table 1.

Table 1: Useful static performance parametric studies with purpose indicated.

Static parametric study	Purpose
Thrust versus angular velocity squared	Used to determine the propeller's coefficient of thrust and generate theoretical models
Thrust versus PWM duty cycle	Used to validate propulsion system performance and generate theoretical models
Motor current draw versus thrust	Used to indicate required battery specifications and generate theoretical models

To illustrate the validity of acquired data from the measurement rig, an example comparative test is performed, yielding satisfactory error analysis outcomes. In Figure 3, publicly available data from the propeller manufacturer, APC propellers, is evaluated against acquired data by the measurement rig. The results indicate a marginal systematic underestimation with the mean percentage error being -9.13%, and the mean absolute error and root mean square error being less than 8.64 g and 9.60 g, respectively. The marginal underestimation can be attributed to several factors, such as a degraded propeller, inaccurate taring and scaling of the load cell, drag effects from the measurement rig platform, and ground effect.

The motor exhibits varying dynamic responses depending on the step thrust input initial value and final value. This is due to the non-linear relationship between the commanded PWM duty cycle and thrust, among other factors. To account for this, several dynamic response tests can be conducted at varying PWM step inputs. The models generated from the tests can be stitched together to capture the entire permissible dynamic response range for the propulsion system. To illustrate the validity of acquired data from the measurement rig, the dynamic response of a propulsion system is characterised and modelled using an arbitrary step-up and step-down input, as shown in Figure 4. An error analysis of the generated second-order models produced a fit to estimation data of 97.9% and 94.4% and an RMSE of 3.04 g and 7.96 g, respectively, for the step-up and step-down input.

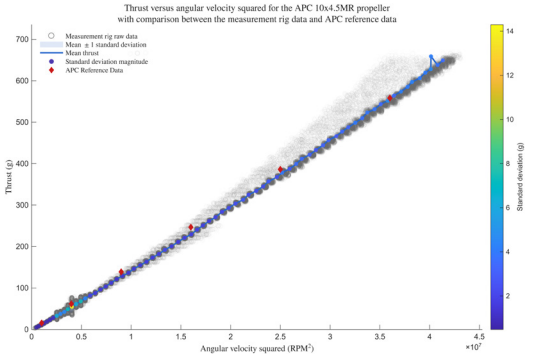

Figure 3: Example comparison of the measured thrust and the square of the rotational velocity from the measurement rig and APC propeller manufacturers

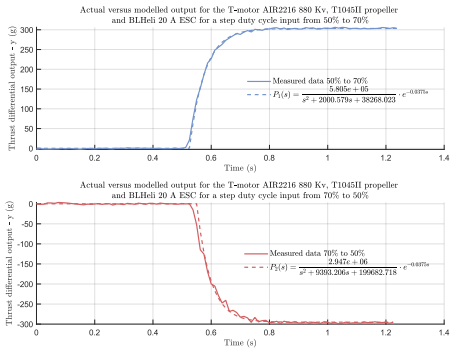

Figure 4: Dynamic response tests for an example step-up and step-down input on the Holybro X500 propulsion system.

The Propulsion Rig is a low-cost and open-source platform capable of measuring performance data of small- to medium-sized multirotor propulsion systems. The data can be used to inform and generate fundamental models of the multirotor propulsion system. Through experimentation and error analysis, static performance data acquired from the rig is proven to be comparable to reputable data. All aspects of this project are publicly available on GitHub[3].

References:

1. Tyto Robotics, Series 1585 Thrust Stand (2025). URL: https://www.tytorobotics.com/pages/1580.
2. Foxtech, LY-10KGF Thrust Stand (2025). URL: https://store.foxtech.com/ly-10kgf-thrust-stand.
3. GitHub, Propulsion-Rig (2025). URL: https://github.com/Propulsion-Rig.

Articulating Drop Foot Orthosis Testing Device

K Zapke[a] & MP Venter[a]

[a] Department of Mechanical and Mechatronic Engineering, Stellenbosch University, Stellenbosch, South Africa

Abstract: Drop foot weakens the upward tilt of the foot, leading to an altered gait often which is treated with ankle-foot orthoses (AFOs). This study evaluates an AFO testing device design's ability to replicate a normal and drop foot gait and load transfer accuracy for cyclic and static testing using multibody dynamic simulations (Hexagon Adams Modeler). The results yielded normal and drop foot tilt profiles with root mean square errors of 5.36° and 3.61. Load transfer yielded root mean square errors of 18.3 N and 32.2 N. These results demonstrate the device's capability to replicate gaits and meet relevant requirements. Future work includes manufacturing and control system design.

Background and Motivation: Drop foot weakens the upward tilt of the foot, leading to an altered walking style (gait) with a vertical foot tilt profile ranging from 15° to -18°[1], which is treated with Ankle-Foot Orthoses (AFOs)[3]. A normal gait's angle ranges from 17.4° to -17.9° [2]. Ankle-foot devices are evaluated using ISO 22675[4], assessing strength under static testing of 4.5 kN for heel and toe loading with the foot's sole creating an angle with the surface of 15° (heel) and 20° (toe). Figures 1 and 2 display the profiles for the load and the same angle as before for cyclic testing.

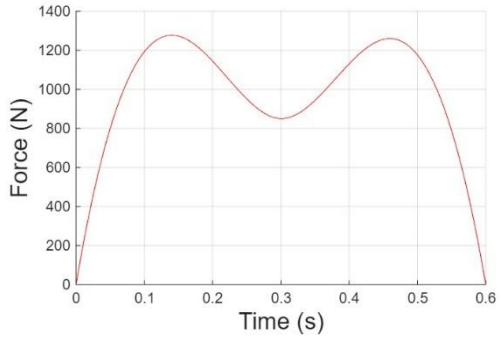

Figure 1: Required input force for cyclic testing (adapted from ISO 22675:2016)

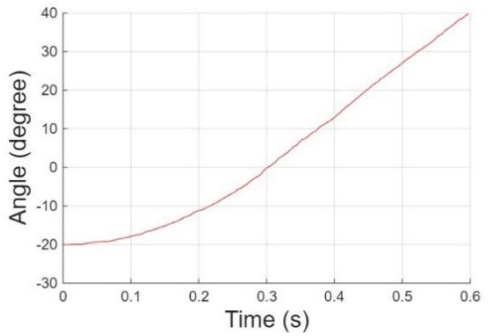

Figure 2: Required angle between foot sole and surface for cyclic testing (adapted from ISO:22675)

[a] 23671866@sun.ac.za

ISO 22675 does not address the testing of articulating AFOs, presenting a gap in standardized evaluation methods for articulating AFOs. A new testing device capable of evaluating articulating AFOs needs to designed and evaluated.

Objectives and Scope: This study evaluates an articulating AFO testing device design using simulations. The objectives are to evaluate the device's ability to replicate a normal and drop foot gait and the transfer of cyclic and static load profiles specified by ISO 22675 within the device. This study is limited to virtual analyses.

Methodology: The testing device was designed by using MBD simulations to adapt and improve the design without the need of manufacturing prototypes, reducing design time and costs. The CAD model of the testing device design can be seen in Figure 3 below.

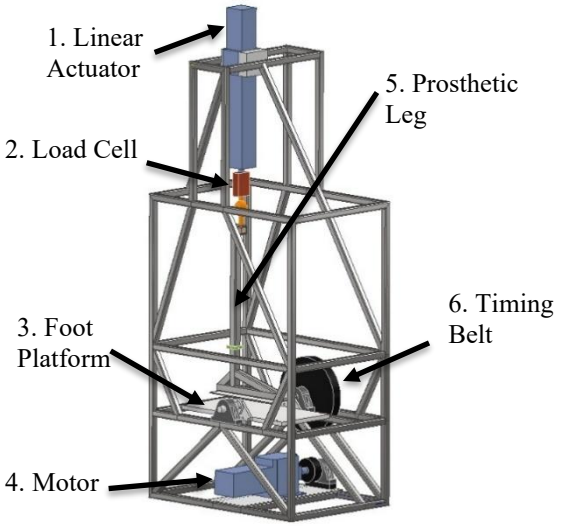

Figure 3: Testing Device CAD Model with a linear actuator (1), load cell (2), foot platform (3), motor (4), prosthetic leg (5) and a timing belt (6)

Results and Discussion: This section focuses on the results obtained from the MBD simulations using Hexagon Adams Modeler 2023.2. Figure 4 displays the comparison of the normal gait vertical foot tilt profile of the testing device and that determined by Brockett and Chapman (2016), with an RMSE of 5.36° (~13% of data range) and a maximum deviation of 4.5°, which is likely due to input parameter overestimation. Despite this, the simulations were able to replicate a normal gait vertical foot tilt.

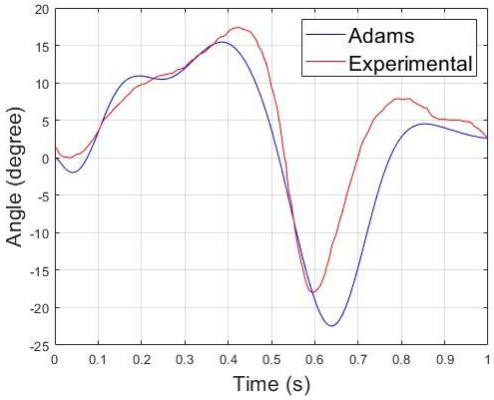

Figure 4: Testing Device vertical foot tilt profile for a normal gait compared to an experimental profile from literature[1].

Figure 5 compares the testing device vertical foot tilt for a drop foot gait with that of Shin et al. (2023), yielding an RMSE of 3.61° and a maximum deviation of 2.4°, demonstrating the simulation's ability to replicate a drop foot gait vertical foot tilt profile.

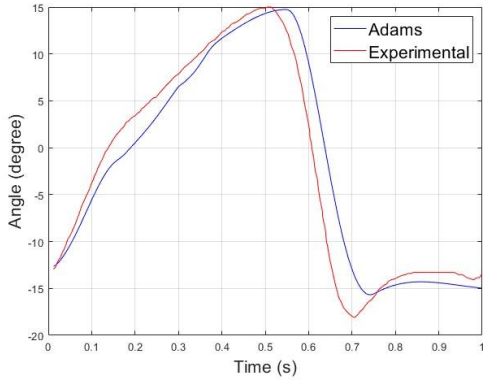

Figure 5: Testing device vertical foot tilt profile for a drop foot gait compared to an experimental profile from literature[2].

The comparison of ISO 22675's cyclic and static load profiles inputs showed RMSEs of 18.3 N and 32.7 N compared to the loads obtained using simulations, with a maximum deviation of 46.8 N, indicating load transfer between components with minimum deviation[4]. Figures 6 and 7 display these comparisons.

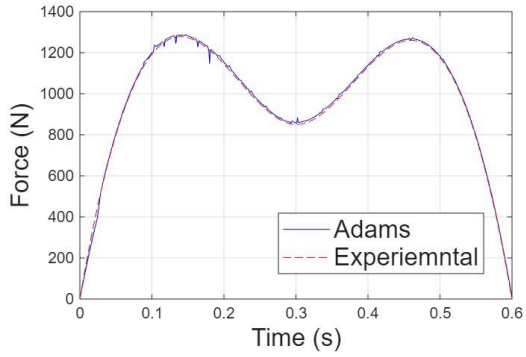

Figure 6: ISO 22675's cyclic load input profile compared to the load measured by the load cell[4].

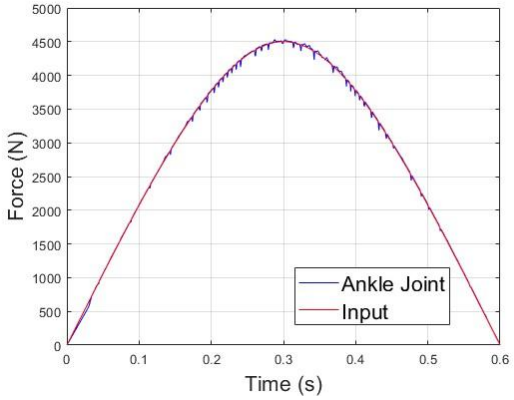

Figure 7: ISO 22675's Static load input profile compared to the load measured by the load cell[4].

Conclusion: This study evaluated a testing device for AFO testing via simulations. The device replicated normal and drop foot vertical tilt profiles with root mean square errors of 5.36° and 3.61°, and maximum deviation of 4.5°. Load transfer accuracy was confirmed with root mean square errors of 18.3 N and 32.2 N, and a maximum deviation of 46.8 N. These results demonstrate the device's capability to replicate gaits and meet relevant requirements. Future work includes manufacturing of the testing device and the control system design

References:

1. Shin, W., et al. (2023). "Ankle dorsiflexion assistance of patients with foot drop using a powered ankle-foot orthosis to improve the gait asymmetry." J Neuroeng Rehabil **20**(1): 140.

2. Brockett, C. L. and G. J. Chapman (2016). "Biomechanics of the ankle." Orthop Trauma 30(3): 232–238.

3. Alam, M., et al. (2014). "Mechanism and Design Analysis of Articulated Ankle Foot Orthoses for Drop-Foot." The Scientific World Journal **2014**: 1–14.

4. BS EN ISO 22675, (2016) Prosthetics – Testing of ankle-foot devices and foot units – Requirements and test methods, London: British Standards Institution.

AN EXPERIMENTAL INVESTIGATION OF MACHINGING PARAMETERS ON SURFACE CHARACTERISITICS AND PERFORMACE OF Ti-6Al-4V ELI SHAFTS

L van der Walt[a], RF Laubscher[b] & PA le Roux[c]

[a, b] Department of Mechanical Engineering Science, University of Johannesburg, Johannesburg, South Africa
[c] Independent Institute of Education, Emeris, Faculty of Science & Technology

This study investigates the effects of cutting parameters on the fatigue life of Ti-6Al-4V ELI. Using cutting speeds of 40, 70, and 100 m/min and cutting feeds of 0,1, 0,15, and 0,2 mm/rev as the dependent variables. The surface roughness, residual stresses and cyclic fatigue were measured and analysed. Increased residual stresses were measured as a function of the cutting parameters and showed little effect on fatigue life at higher feed rates.

Titanium alloys are widely used in industries such as aerospace, power generation, automotive, and medical sciences [1]. This is due to titanium's excellent strength-to-weight ratio, corrosion resistance, creep resistance, high temperature strength, low thermal coefficient of expansion and relative abundance [2]. These favourable qualities have long outweighed the high cost associated with the extraction, forming and manufacturing processes [2]. Another concern in the widespread use of titanium is its difficulty to machine. Machining titanium leads to high temperatures at the cutting interface, resulting in high tool wear due to localised plastic deformation of the bulk workpiece [3].

In recent years, more research has focused on improving the machinability of titanium alloys and the link between machining and fatigue life. There is a close link between surface integrity and fatigue life. Improved surface roughness has been shown to improve fatigue life in titanium alloys [4]. Increased residual stress has also been shown to affect the fatigue life [4]. Furthermore, there is a link between surface integrity and residual stress when altering the machining strategies by altering cutting speeds, feed rate, or cutting tools [4], [5].

The aim is to investigate the effect of different cutting parameters on the surface integrity and performance characteristics when machining Ti-6Al-4V ELI specimens. This will be accomplished by altering the cutting speed, and feed rate to establish well-defined machined surface characteristics. Residual stress analyses will be implemented to characterise the machining-induced residual stress field. Specimens will further be subjected to cyclic fatigue testing to establish performance characteristics.

The quantitative research study will be completed in three phases. In phase 1, the workpieces will be prepared through machining at three different cutting speeds and feeds. In phase 2, the surface characteristics and residual stress of the workpieces will be measured and documented. Lastly, the fatigue life of the workpieces will be measured, documented, and compared.

Workpieces were prepared using a CNC lathe. The pieces underwent a roughing process. The cutting tool was then replaced to avoid any discrepancies due to tool wear and underwent finishing passes as per the parameters in the table below.

Table 1: Finishing cut parameters

	Value	Unit
Depth of cut	0,1	mm
Tool nose radius	1,2	mm
Cutting speed	40 70 100	m/min
Cutting feed	0,1 0,15 0,2	mm/rev

Workpieces were prepared to the geometry shown in figure 1, below. 27 specimens were prepared to account for the 3×3 combination of cutting speed and cutting feed and allow for repeatability.

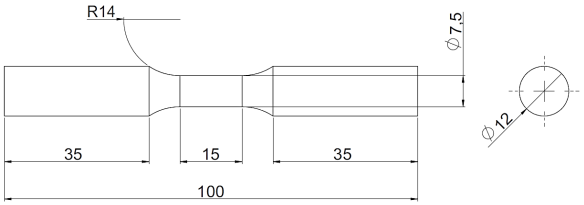

Figure 1: Workpiece geometry

A surface roughness analysis was completed on 3 sides of each specimen and eccentricity was measured. From this data, Ra, Rq, Rsk, and Rku was recorded.

Surface residual stress tests were completed on selected representative specimens. From this data, the principle residual stresses were calculated and compared.

Lastly, the workpieces underwent cyclic fatigue testing. The workpieces were loaded with $30\ kg$ in a simply supported load cell and the number of cycles before failure was recorded and compared. The results of all these testing phases are outlined below.

As previously discussed, the surface roughness testing

218011783@student.uj.ac.za

yielded Ra, Rq, Rsk, and Rku data for all 27 workpieces. For the purposes of this paper, only Ra values will be discussed. The results are outlined in figure 2.

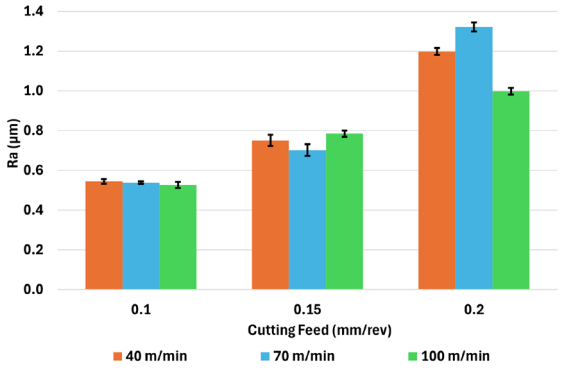

Figure 2: Ra results from surface roughness testing

From figure 2, Ra tends to increase as cutting feed increases. Cutting speeds of 70 m/min yielded the largest standard deviation in all cases, this trend is seen throughout all testing phases.

The results from the residual stress analysis were then used to calculate the principal stresses and θ. See the results in figure 3, 4, and 5.

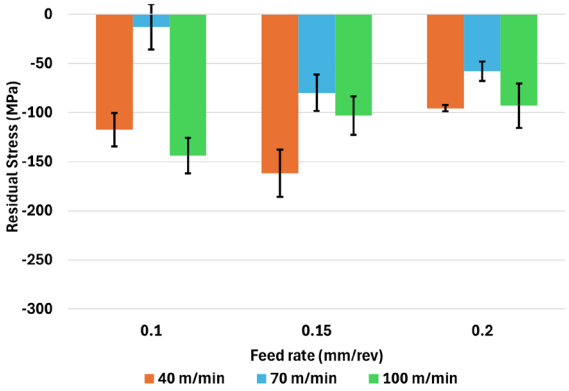

Figure 3: Principal stress 1 (σ_1) calculation results

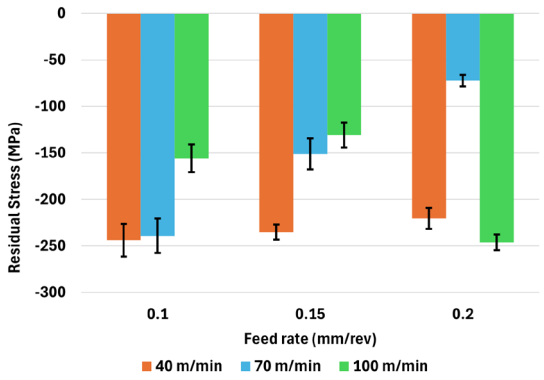

Figure 4: Principal stress 2 (σ_2) calculation results

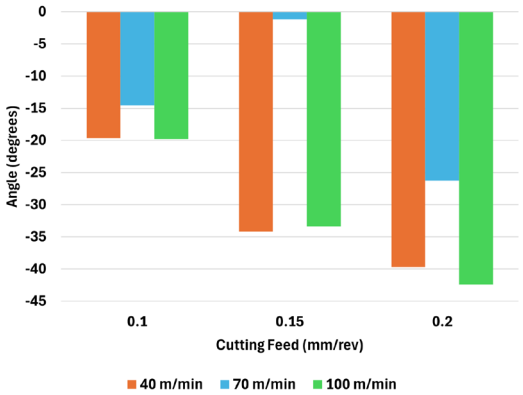

Figure 5: Theta calculation results

Lower cutting speeds are less-influenced in terms of residual stresses due to the low thermal conductivity of Ti-6Al-4V ELI. σ_2, orientated along the cutting direction, indicates that the influence of thermomechanical loading becomes more influential as a function of cutting feed rate. Thus, influencing the compressive residual stress state and the fatigue performance.

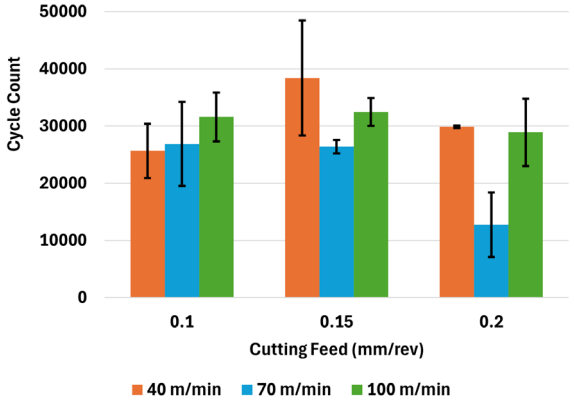

Figure 6: Cyclic fatigue results

Cyclic fatigue decreases significantly for 70m/min as the feed rate increased. It remained consistent for both 40m/min and 100m/min. The discrepancies in 70m/min throughout the research project indicates that there is an anomaly at that cutting speed. Further research would be required on the effects of the thermomechanical properties of Ti-6Al-4V ELI in the range of 70m/min. It is theorised that 70m/min is in the thermomechanical transition zone.

[1] M. J. Jackson and W. Ahmed, Eds., Surface Engineered Surgical Tools and Medical Devices. Boston, MA: Springer US, 2007. doi: 10.1007/978-0-387-27028-9.

[2] I. Chattoraj, "Stress corrosion cracking (SCC) and hydrogen-assisted cracking in titanium alloys," in Stress Corrosion Cracking, Elsevier, 2011, pp. 381–408. doi: 10.1533/9780857093769.3.381.

[3] A. Polishetty and G. Littlefair, "Advances in conventional machining processes for machinability enhancement of difficult-to-machine materials," in Advanced Machining and Finishing, Elsevier, 2021, pp. 3–44. doi: 10.1016/B978-0-12-817452-4.00007-5.

[4] P. A. Le Roux, R. F. Laubscher, and A. Schubert, "Machining for an increased fatigue life for a Ti-6Al-4V ELI component," in Procedia CIRP, Elsevier B.V., 2020, pp. 462–468. doi: 10.1016/j.procir.2020.02.103.

[5] S. Rinaldi, G. Rotella, D. Umbrello, and L. Filice, "A physically based model of Ti6Al4V turning process to predict surface integrity improvements," Procedia CIRP, vol. 87, pp. 497–502, 2020, doi: 10.1016/j.procir.2020.02.017.

218011783@student.uj.ac.za

EVALUATING EMOTIONAL ENGAGEMENT IN VIRTUAL REALITY-BASED ENGINEERING EDUCATION

A. Rawoot[a], A.R. Ingle, B.M. Nickerson, P.G.G. Durandt & C.A. Steed

Department of Mechanical and Mechatronic Engineering, Stellenbosch University, Stellenbosch, South Africa

This study evaluates the application of virtual reality (VR) to enhance emotional engagement and design comprehension in undergraduate engineering education. The study group consists of third-year mechanical engineering students tasked to design a gearbox and enclosure for a small wind turbine. Subsequent to design generation, students engaged in a VR-based peer review activity, evaluating each other's designs within an immersive environment. The Positive and Negative Affect Schedule (PANAS) framework was employed to quantify students' emotional responses. The results indicated high positive affect and moderate negative affect, reflecting strong engagement and minimal discomfort. Qualitative feedback further identified improvements in spatial awareness and collaborative reflection. The study concludes that integrating VR into design review processes supports both cognitive and affective learning, while also reporting an increased interest in emerging technologies like digital twins and Industry 4.0.

Introduction: The rapid advancement and decreasing cost of VR hardware have established immersive technologies as effective tools for enhancing engineering education[1]. VR allows students to interact with three-dimensional representations of complex systems, thereby bridging the gap between theoretical knowledge and practical design experience. In large or resource-constrained educational settings, VR provides a scalable and interactive alternative to physical prototyping[4,5] and site visits[6], enabling students to visualise, manipulate, and evaluate engineering designs within a shared virtual environment.

In addition to technical advantages, VR demonstrates potential to enhance emotional engagement, a frequently underemphasised aspect of learning that affects motivation, retention, and creativity. The use of emotional assessment frameworks such as the PANAS[2] offers a systematic approach to quantifying students' affective responses, thereby providing insights into the influence of immersive technologies on the learning experience[7].

This study investigates the capacity of VR to enhance emotional engagement and design comprehension in undergraduate engineering education. Specifically, it analyses the affective responses of third-year students during VR-based peer assessment of design projects, thereby connecting affective learning with collaborative design evaluation.

Background: In modern engineering curricula, active learning and collaborative design are central to developing critical competencies aligned with Industry 4.0, graduate attributes and sustainable development goals[3,8]. Traditional project-based learning environments, however, are often limited by physical resources and time constraints. VR overcomes some of these challenges by allowing students to explore, critique, and evaluate designs in realistic yet safe virtual environments[1].

Prior research indicates that the inclusion of VR in engineering education improves understanding of spatial and mechanical relationships[1] and elevates interest in science, technology, engineering, and mathematics (STEM) disciplines. Emotional engagement is also a critical factor in engineering education, influencing curiosity, persistence in problem-solving, and receptiveness to technology. This study applies the PANAS framework to measure these affective dimensions during a VR-based design review activity.

Objectives: The primary objectives of this study are to:

1. Evaluate the emotional responses of third-year mechanical engineering students when exposed to VR learning environments using the PANAS framework.
2. Determine the effectiveness of utilising VR as a tool to enhance learning and design consideration in engineering education.

Research methodology: The study involved a single cohort of third-year mechanical engineering students at Stellenbosch University. As part of a design project, students developed a gearbox and enclosure for a small wind turbine. Each team created a three-dimensional computer-aided design (CAD) model and an accompanying design rationale. After completing their design concepts, students participated in a VR-based peer review exercise, assessing other groups' designs in a virtual environment. This activity simulated an industrial design review process and provided students with immersive, interactive peer feedback.

After the VR session, participants completed the PANAS questionnaire, which included 15 emotional descriptors: 10 positive and 5 negative. Each descriptor was rated on a 5-point Likert scale from 1 (very slightly or not at all) to 5 (extremely). Positive Affect (PA) and Negative Affect (NA) scores were calculated for each respondent. Higher PA values indicate greater enthusiasm and engagement, while higher NA values reflect discomfort or stress[2]. Mean PA and NA values for the class were computed to assess the overall affective response to the VR experience. A positive PANAS outcome is defined as

[a] 24908479@sun.ac.za

PA greater than 3.5 and NA less than 1.5.

The VR environment was developed using Unity and deployed on freestanding headsets. Students navigated virtual models, inspected internal components, and assessed the manufacturability and functionality of peer designs. The beginning of the VR activity began with an introduction to the headsets, briefly explaining headset operation and user interface controls to ensure a smooth transition into using the technology.

Results: Participation in the VR session was mandatory, requiring all students to evaluate their peers' designs against specified criteria. The voluntary post-activity PANAS questionnaire was distributed via an online survey, yielding 32 responses from a total class size of 120 students.

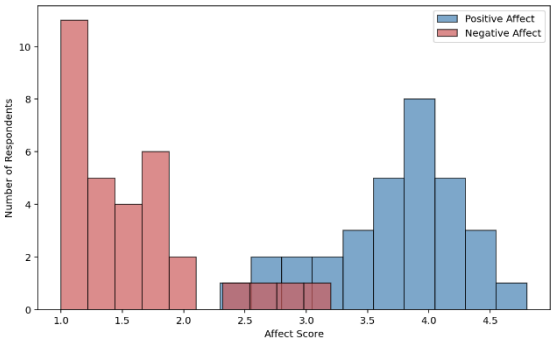

Figure 1: Histogram of PA and NA scores

The PANAS evaluation indicated a strong positive affective response to the VR design review activity. The survey recorded high PA and moderately low NA responses with average scores of 3.7 and 1.6 respectively. This indicates a generally positive emotional state experienced by the students. The clear separation between the two distributions in Figure 1 suggests low distress and a predominantly positive mood among the respondents. The slightly elevated NA score can be attributed to challenges encountered during the VR activity, including difficulty manipulating controls and minor motion discomfort.

Qualitative feedback was obtained from the learners through direct engagement during the VR session and through the first four questions of the survey. It indicated that the immersive environment improved spatial understanding, facilitated enhanced comparison between designs, and promoted collaborative discussion. Students reported experiencing excitement, curiosity, and inspiration when exploring peers' designs. It was also suggested that the VR activity be included in other design-based modules to improve design evaluation and understanding.

Conclusion: This study demonstrates the value of integrating VR into undergraduate engineering design education, particularly for enhancing emotional engagement and collaborative evaluation. The application of the PANAS framework provided quantifiable insights into students' affective responses, confirming that VR-based peer review activities can generate high positive affect and moderate negative affect among participants.

Incorporating emotional response assessment into immersive learning activities enables educators to better understand student interactions with technology, adapt content for diverse learners, and implement continuous improvement strategies. These findings underscore the potential of VR to foster both cognitive and affective learning, equipping future engineers to navigate complex, technology-driven environments with creativity, confidence, and emotional awareness.

Acknowledgements: This work is based on the research supported in part by the National Research Foundation of South Africa (Ref. Number TTK240319209840).

References:

[1] Ghazali, A.K., Ab. Aziz, N.A., Ab. Aziz, K., Tse Kian, N. 2024. The usage of virtual reality in engineering education. *Cogent Education*, 11(1). https://doi.org/10.1080/2331186X.2024.231944

[2] Tran, V. 2020. Positive affect negative affect scale (PANAS). *Encyclopaedia of Behavioural Medicine*. New York: Springer. https://doi.org/10.1007/978-1-4419-1005-9_978

[3] Castaño, C., Caballero, R., Noguera, J.C., Austin, M.C., Bernal, B., Jaén-Ortega, A.A., Ortega-Del-Rosario, M.D.L.A. 2025. Developing Sustainability Competencies Through Active Learning Strategies Across School and University Settings. *Sustainability*, 17, 8886. https://doi.org/10.3390/su17198886

[4] Heppell, R., Sendzul, A. D., Van Der Merwe, A. F., Steed, C. A. & Mangaroo-Pillay, M. 2025. Simulating Wearable Sensors in Virtual Reality: A Comparison of Physical and Virtual Sensor Movement Identification in a Learning Factory Setting. In L. Louw, V. Hummel, I. De Kock, & K. Von Leipzig (Eds.), Advancing Learning Factories: Enabling Future-Ready Skills (Vol. 1546, pp. 209–216). Springer Nature Switzerland. https://doi.org/10.1007/978-3-031-98883-7_25

[5] Van Dyk, M., Steed, C. A. & Mangaroo-Pillay, M. 2026. Scaling Industrial Robotics Education: A Serious Game Approach for Resource-Limited Regions. In L. Louw, V. Hummel, I. De Kock, & K. Von Leipzig (Eds.), Advancing Learning Factories: Enabling Future-Ready Skills (Vol. 1545, pp. 21–28). Springer Nature Switzerland. https://doi.org/10.1007/978-3-031-98880-6_3

[6] Steed, C. A., Mangaroo-Pillay, M. & Wolff, K. 2025. Scalable VR Solutions for Engineering Education: A Continuous Improvement Framework. Proceedings on IRPBL2025. International research symposium on PBL.

[7] Steed, C. A., Wolff, K. & Mangaroo-Pillay, M. 2026. A Framework for Virtual Reality Adoption in Engineering Education: Measuring Emotional Engagement and Long-Term Effects. In L. Louw, V. Hummel, I. De Kock, & K. Von Leipzig (Eds.), Advancing Learning Factories: Enabling Future-Ready Skills (Vol. 1545, pp. 12–20). Springer Nature Switzerland. https://doi.org/10.1007/978-3-031-98880-6_2

[8] Wolff, K. & van Breda, L. 2023. The complexity of graduate attributes in engineering for Industry 4.0 contexts. In 2023 World Engineering Education Forum-Global Engineering Deans Council (WEEF-GEDC) (pp. 1-8). IEEE.

EVALUATION OF A LIGHTWEIGHT VISUAL–INERTIAL STATE ESTIMATOR FOR GPS-DENIED ENVIRONMENTS

A Ramwell[a], A Pretorius[a] & N Botha[b]

[a] MechatronicSystems.Group, Department of Mechanical Engineering, University of Cape Town, South Africa
[b] Centre for Robotics and Future Production, Council for Scientific and Industrial Research, South Africa.

Unmanned aerial vehicles present an academically-interesting and practically promising solution for automating tasks in inaccessible environments. An appealing minimal sensor suite for localisation (the first challenge in automation) is the combination of monocular camera and inertial measurement unit. Although visual localisation is a well-developed field, fiducial marker-less methods remain computationally expensive. In this study, a simple, lightweight visual–inertial state estimator is evaluated in simulation and physical experiments, achieving a mean positional and angular error of within 15 cm and 5°, respectively. The proposed system shows promise as a skills development tool and a practical solution to the localisation problem.

Introduction: Their manoeuvrability and untethered nature make unmanned aerial vehicles (UAVs) well-suited to autonomous operations in complex environments. Multirotors, in particular, are able to traverse freely between multiple floor levels and through tunnels or corridors (e.g., for chemical plant inspections, search-and-rescue, etc.). This high degree of freedom also makes the design and control of UAVs a challenging and instructive research problem. There is therefore a growing interest in autonomous UAV systems for both industrial and research environments. Project Aerial Robotics Capability (ARC) aims to foster the growth of aerial robotics at the University of Cape Town. As a contributor to this initiative, this paper reports on the development and evaluation of a visual–inertial state estimation algorithm for onboard implementation on a low-cost quadcopter, with an emphasis on first-principles understanding, clarity of implementation, and computational simplicity.

Literature Review: To navigate autonomously, robots must be able to "localise", i.e. accurately track their own position in the environment. While there is growing interest in simultaneous localisation and mapping (SLAM), this approach is computationally intensive and there are many scenarios where robotic agents operate in relatively static environments. There is therefore a strong argument to be made for pure localisation paradigms, using known landmarks in pre-mapped areas.

Pure localisation is a well-studied topic, and a range of commercial and research solutions exist. While most off-the-shelf autonomous UAV systems rely on external architectures such as GPS-connectivity or motion capture systems for localisation and trajectory generation, these are sensitive to being obscured or disrupted in sheltered or complex environments. To capitalise on the manoeuvrability advantage of UAVs, various alternative on-board sensor combinations have been proposed.

The visual–inertial sensor suite, combining one or more cameras and an inertial measurement unit (IMU), is particularly appealing due to the relatively low cost and versatility. Visual data is highly information dense and can serve a dual purpose: localisation, and input to higher-level decision makers. However, low-cost cameras have a correspondingly low update rate, making inertial data a useful supplement for tracking high-speed manoeuvres. Many visual–inertial odometry paradigms exist, with the greatest distinction lying in the visual pose estimation and sensor fusion techniques.

The most lightweight visual pose estimators rely on fiducial markers, exploiting their planarity to simplify the mathematics [1]. In general, this requires the camera to have a relatively close and complete view of the marker. In large environments, this may require hundreds of markers and/or very large markers, which is not always convenient (such as in the case of filming). Typically, visual pose estimators intend to solve the "perspective-n-point" (PnP) problem by using n (non-planar) feature correspondences.

Of these, Kneip's [2] analytical solution to the P3P problem is widely applied for rapid, relatively computationally-low-cost pose estimation, often as a first step for outlier rejection prior to running more demanding pose solvers.

Of the many existing sensor fusion algorithms, the extended Kalman filter (EKF) is one of the simpler techniques that has been proven effective for UAVs, which exhibit highly non-linear dynamics away from hover conditions. EKFs are highly robust and scalable, having even been applied to relatively small-scale SLAM. For visual–inertial fusion, the inertial navigation system (INS) formulation [3] is common. In this configuration, the state vector tracks the position, orientation (represented as a quaternion), and velocity of the quadcopter. IMU data (acceleration and angular velocity) are treated as inputs to the EKF and propagated through a dynamics model to predict the quadcopter state at the next timestep. When visual pose estimates become available, these are incorporated as corrections, in the usual EKF formulation.

Methodology: The proposed visual–inertial state estimator is intended to be executed entirely onboard the UAV. However, for the early evaluations reported on in this study, the sensor fusion and image processing

[a] rmwaly001@myuct.ac.za

algorithms are implemented offboard in MATLAB and Simulink. A Pixhawk 6C flight controller using the uXRCE-DDS client publishes IMU data in a ROS2-compatible format, which is transmitted via 900 MHz telemetry to the uXRCE-DDS agent on the host computer, which publishes it to a ROS2 topic. The imaging system comprises an ESP32-camera using WiFi to stream video to the imaging thread, which estimates the camera pose using P3P and publishes the results to a ROS2 topic. A sensor fusion thread runs in parallel with the imaging thread, updating the state estimate in a loop, and incorporating visual pose data when available.

The accuracy of the state estimator is evaluated in simulation (Unreal Engine) and with hardware (above components on a Holyvbro X500 flight kit flying tracked using an Optitrack motion capture system) with several arbitrary reference trajectories (physical trajectories generated by hand). Although the system aims for marker-less state estimation, the evaluations reported in this study are based on point correspondences obtained by feature matching using an in-scene checkerboard and MATLAB's built-in detector based on that of Geiger et al. [4].

Results: Figure 1 shows an example of a tracked trajectory in simulation. The results of physical tests are summarised in Table 1. All state estimators exhibited similar performance, with mean orientation errors varying by less than 5%. Tracking the bias term in the EKF appears to have degraded the pose estimate in all cases. Similarly, trapezoidal integration either made very little difference or degraded the estimate. This may suggest that the additional computational complexity associated with higher order integrations and states is not justified by performance enhancement. However, it is also likely that these estimates have been negatively affected by slow data rates from the ROS2-based IMU telemetry (~16 Hz). For low update rates, trapezoidal integration causes the effective measurements to be even more out of date than they may already be, thus degrading the state update.

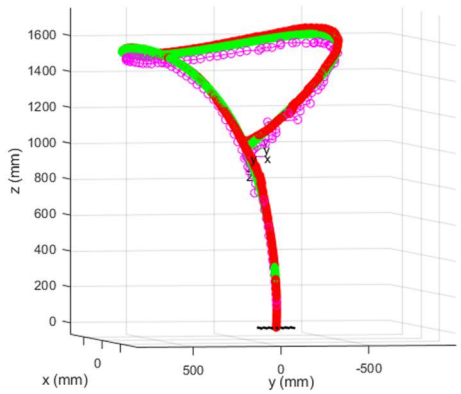

Figure 1: Position tracking result of 16-element EKF using trapezoidal integration with ideal IMU and camera data. EKF estimate in red, visual state estimate in pink, and true position in green.

Table 1: State estimator pose error in physical tests

	Orientation error (°) μ, σ	Position error (m) μ, σ
10-element EKF (rectangular integ.)	2.563, 1.628	0.129, 0.142
10-element EKF (trapezoidal integ.)	2.563, 1.628	0.129, 0.142
16-element EKF (rectangular integ.)	3.095, 2.048	0.136, 0.151
16-element EKF (trapezoidal integ.)	3.147, 2.102	0.138, 0.152

Conclusion: A computationally lightweight visual–inertial state estimator is developed for practical application and as a learning tool. The proposed system's pedagogical values stems from its reliance on fundamental algorithms from the computer vision and state estimation fields. The system achieves mean positional and orientation tracking errors of less than 15 cm and 5°, respectively, in simulation and physical experiments, without relying on planar constraints. However, there are some limitations: evaluations in the current work are based on a checkerboard target and a very slow measurement update rates. Future work will focus on onboard deployment and refinement of the estimation scheme to allow for marker-less pose estimation.

References:

1. E. Olson, 'AprilTag: A robust and flexible visual fiducial system', in 2011 IEEE International Conference on Robotics and Automation, May 2011, pp. 3400–3407. doi: 10.1109/ICRA.2011.5979561.

2. L. Kneip, D. Scaramuzza, and R. Siegwart, 'A novel parametrization of the perspective-three-point problem for a direct computation of absolute camera position and orientation', in CVPR 2011, Colorado Springs, CO, USA: IEEE, Jun. 2011, pp. 2969–2976. doi: 10.1109/CVPR.2011.5995464.

3. S. M. Weiss, 'Vision based navigation for micro helicopters', Doctoral Thesis, ETH Zurich, 2012. doi: 10.3929/ethz-a-007344020.

4. A. Geiger, F. Moosmann, O. Car, and B. Schuster, 'Automatic camera and range sensor calibration using a single shot', in 2012 IEEE International Conference on Robotics and Automation, St Paul, MN, USA: IEEE, May 2012, pp. 3936–3943. doi: 10.1109/ICRA.2012.6224570.

ACHIEVING TIME-OPTIMAL FLIGHT: A CONTROL SYSTEMS APPROACH FOR HIGH-PERFORMANCE QUADCOPTERS

T. Mwangi[a], A. Pretorius[a] & E. Boje[a]

[a] Department of Mechanical Engineering, University of Cape Town, Cape Town, South Africa

This extended abstract presents the initial phase of an ongoing project aimed at developing a quadcopter control system capable of high-agility, time-optimal flight. The work focuses on designing and simulating a Model Predictive Control attitude controller using a simplified three-degree-of-freedom linear model representing roll, pitch, and yaw dynamics. The controller enforces input and rate constraints to reflect actuator limitations and is tuned for stable, accurate attitude tracking. Closed-loop simulation results demonstrate smooth transient behaviour, minimal steady-state error, and well-damped responses within defined limits, confirming the feasibility of implementing the design on a real platform. These findings establish a foundation for subsequent development of a nonlinear Model Predictive Control scheme that incorporates dynamic coupling and real-time implementation. The project contributes to an embedded control architecture for agile quadcopter flight with applications in autonomous drone racing and time-critical quadcopter unmanned aerial vehicle missions.

Introduction: Unmanned aerial vehicles (UAVs), particularly quadcopters, have become integral to modern research and industry owing to their vertical take-off and landing capabilities, manoeuvrability, and compact design[1]. Among the most demanding applications is autonomous drone racing, which challenges control algorithms to achieve high-speed flight through cluttered environments using onboard sensing and computation. Similar requirements arise in time-critical missions such as search and rescue, surveillance, and disaster response, where rapid and precise trajectory tracking is essential[2]. These contexts underscore the need for control systems that enable high-performance flight under environmental constraints.

This research focuses on developing a control system for a quadcopter to follow a planned trajectory as quickly and accurately as possible while maintaining dynamic stability. The work addresses the interrelated challenges of time-optimal trajectory generation, agility, accurate tracking, and real-time implementation within the limits of onboard hardware systems. The project involves designing, simulating, and implementing the time-optimal controller on a pre-built quadcopter platform, validated through indoor flight experiments using motion capture data. Some of the limitations include computational and physical constraints of the hardware, limited indoor flight volume, and a two-year project duration.

Literature Review: Quadcopters are widely studied UAVs valued for their manoeuvrability and simplicity, yet their nonlinear and underactuated dynamics make control challenging, especially for agile and time-optimal flight. Recent research emphasizes advanced control methods that combine robustness, accuracy, and computational efficiency, ranging from classical PID and LQR controllers to nonlinear, adaptive, and predictive schemes[2,3]. Model Predictive Control (MPC) and its nonlinear variant (NMPC) have emerged as leading approaches, providing superior tracking precision and constraint handling compared to traditional methods. Cascaded MPC architectures further improve computational efficiency, addressing real-time challenges. Hybrid and adaptive frameworks, including backstepping and fuzzy logic integrations, further enhance robustness, while developments such as fault-tolerant architectures enable reliable and agile flight under dynamic and uncertain conditions.

The reviewed literature shows a clear evolution toward control strategies that balance real-time feasibility with the agility required for highly-dynamic quadcopter manoeuvres[4,5,6]. Several studies employ full nonlinear models based on the Newton–Euler framework and incorporate aerodynamic effects[7,8]. Despite notable advances, high computational cost and hardware constraints remain key challenges, which this research seeks to addresses in the control system design and implementation.

Methodology: This study adopts a mixed-methods approach that integrates theoretical modelling, computational simulation, and experimental validation to design and implement a high-performance quadcopter control system. The control problem is formulated to achieve time-optimal trajectory tracking through predefined waypoints while satisfying dynamic and actuator constraints. A nonlinear dynamic model is to be developed using the Newton–Euler formulation and quaternion-based orientation representation to ensure stability during agile manoeuvres. MPC is chosen for its ability to handle multivariable systems with constraints[9], with both linear and nonlinear variants to be evaluated through simulations in MATLAB/Simulink and Python. Following simulation-based refinement, the controller will then be implemented on a Kakute H7 flight controller, with offboard computation used if necessary. Experimental validation will be conducted in an indoor motion capture environment to assess trajectory accuracy, agility, and robustness through an iterative design–simulation–testing process.

[a] MWNTON001@myuct.ac.za

The initial attitude controller design employs a linear MPC scheme based on a simplified three-degree-of-freedom linearized quadcopter model, representing roll, pitch, and yaw dynamics. Each rotational channel is decoupled, and linear state-space models are derived from small-angle approximations. The MPC is tuned with suitable prediction and control horizons, weighting the roll, pitch and yaw angles more heavily than their rates to achieve stable tracking performance within actuator constraints, using the MATLAB MPC Toolbox.

Results: The significant results of the project so far include an extensive review of the literature on MPC and its variants, followed by initial modelling of the quadcopter's attitude dynamics and the design of a linear MPC controller. The controller is implemented using the linearized 3DOF state-space model developed for roll, pitch, and yaw channels, with constraints imposed on both the control inputs and their rate of change to reflect actuator limitations.

Closed-loop simulation results demonstrate that the MPC controller accurately tracks step commands for roll, pitch, and yaw angles, exhibiting smooth transient behaviour and minimal steady-state error, as shown in Figure 1. The control inputs remain well within the defined constraints of [0, 10] $(rad/s)^2$, ensuring feasibility of implementation on a real system, as shown in Figure 2. The responses show well-damped dynamics with no excessive overshoots.

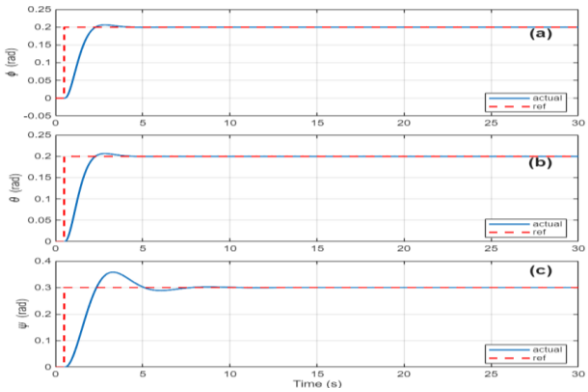

Figure 1: Closed-loop attitude tracking response of the (a) roll, (b) pitch, and (c) yaw angles

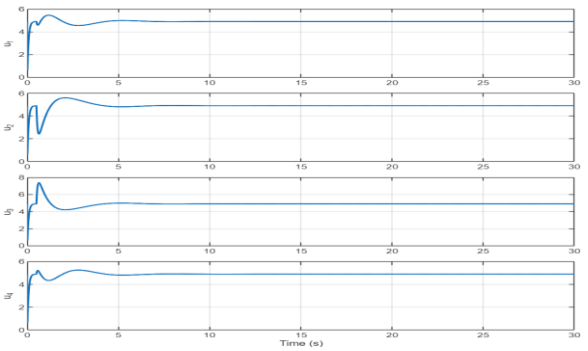

Figure 2: Control inputs (squares of the motor angular velocities)

Conclusion: These results validate the initial feasibility of the MPC design and confirm its capability to stabilize and command the quadcopter's attitude effectively. However, these are preliminary results, as the project is ongoing. Further work will focus on incorporating nonlinear dynamics, cross-coupling effects, and hardware-in-the-loop validation to assess the controller's robustness under realistic operating conditions.

References:

1. M. Okasha, J. Kralev, and M. Islam, 'Design and Experimental Comparison of PID, LQR and MPC Stabilizing Controllers for Parrot Mambo Mini-Drone', *Aerospace*, vol. 9, no. 6, Art. no. 6, June 2022, doi: 10.3390/aerospace9060298.
2. M. Okulski and M. Ławryńczuk, 'How Much Energy Do We Need to Fly with Greater Agility? Energy Consumption and Performance of an Attitude Stabilization Controller in a Quadcopter Drone: A Modified MPC vs. PID', *Energies*, vol. 15, no. 4, Art. no. 4, Jan. 2022, doi: 10.3390/en15041380.
3. J. Tang and M. W. Mueller, 'PairTilt: Design and Control of an Active Tilt-Rotor Quadcopter for Improved Efficiency and Agility', *Adv. Intell. Syst.*, vol. n/a, no. n/a, p. 2400494, doi: 10.1002/aisy.202400494.
4. T. Zanatta, 'Design of a small quadrotor UAV and modeling of an MPC-based simulator', laurea, Politecnico di Torino, 2021. Accessed: July 22, 2025. [Online]. Available: https://webthesis.biblio.polito.it/20944/
5. S. R. Sahoo and P. V. Manivannan, 'Hybrid high-level controller (H2LC) using LQR and MRAC for enhanced quadcopter trajectory tracking performance', *J. Control Decis.*, vol. 0, no. 0, pp. 1–22, doi: 10.1080/23307706.2025.2469887.
6. A. Abougarair, M. Almograbi, and A. Alaktiw, 'Model Predictive Control for Stabilizing Quadcopter Flight and Following Trajectories', *Int. J. Eng. Inf. Technol. IJEIT*, vol. 13, no. 2, pp. 14–25, Apr. 2025, doi: 10.36602/ijeit.v13i2.562.
7. F. Nan, S. Sun, P. Foehn, and D. Scaramuzza, 'Nonlinear MPC for Quadrotor Fault-Tolerant Control', *IEEE Robot. Autom. Lett.*, vol. 7, no. 2, pp. 5047–5054, Apr. 2022, doi: 10.1109/LRA.2022.3154033.
8. M. A. Sadi, A. Jamali, and A. M. N. Abang Kamaruddin, 'Optimizing UAV performance in turbulent environments using cascaded model predictive control algorithm and Pixhawk hardware', *J. Braz. Soc. Mech. Sci. Eng.*, vol. 47, no. 8, p. 396, June 2025, doi: 10.1007/s40430-025-05693-9.
9. F. Santoso, M. A. Garratt, S. G. Anavatti, and I. Petersen, 'Robust Hybrid Nonlinear Control Systems for the Dynamics of a Quadcopter Drone', *IEEE Trans. Syst. Man Cybern. Syst.*, vol. 50, no. 8, pp. 3059–3071, Aug. 2020, doi: 10.1109/TSMC.2018.2836922.

A NUMERICAL INVESTIGATION INTO CRYOGENIC FUEL STORAGE TANKS UNDER VIOLENT SLOSHING EXCITATION

M. Bischof[a] & A.G. Malan[b]

[a] InCFD Research Group, University of Cape Town, Cape Town, South Africa
[b] Department of Mechanical Engineering, University of Cape Town, Cape Town, South Africa

The management of sloshing liquid hydrogen is a key challenge for future fuel systems. This numerical investigation validates the in-house CFD code Elemental® against two experiments: isothermal water slosh and non-isothermal cryogenic slosh. Results show the hydrodynamic model accurately captures forces, while the cryogenic case reveals a strong sensitivity of pressure predictions to the turbulence model calibrations, directing future model refinement.

Introduction: Liquid hydrogen (LH_2) has become a key candidate for future fuel systems, with significant time and resources devoted to developing cryogenic propellant technologies. A major challenge is the management of fuel when the tank is subject to external excitation. Any movement of the tank induces movement of the fluids within the tank, known as sloshing.

Understanding the thermodynamic behaviour of sloshing LH_2 is crucial for advancing green combustion technologies. However, conducting experiments with cryogenic fluids is prohibitively expensive, making the development of Computational Fluid Dynamics (CFD) models a practical alternative. This study utilizes the in-house CFD code, Elemental®[1], developed by Elemental Numerics (Pty) Ltd.

To assess its predictive capabilities for cryogenic sloshing, we perform validation against two key experiments. The first is a simple isothermal slosh test conducted by researchers at the Universidad Politecnica de Madrid (UPM). This experiment serves as a baseline for validating the hydrodynamic response of the CFD solver. The second, is a non-isothermal cryogenic slosh experiment conducted at the NASA K-site facility. This case introduces additional thermodynamic effects and serves as a more realistic test for modelling the cryogenic conditions in which we are interested.

The following sections describe these test cases in further detail, the numerical setup used to simulate them, the current simulation results, and the work still required.

UPM Isothermal Slosh: Industry requires an understanding of sloshing-induced forces on cryogenic tanks. However, modelling the full thermodynamic behaviour of the fluids is complex. To address this, we first isolate the hydrodynamic response using a simplified isothermal model.

As part of project HASTA (Hydrogen Aircraft Sloshing Tank Advancement)[2], UPM has set up a number of isothermal slosh benchmark cases to be used in the validation of LH_2 computational tools. The test being focused on is the lateral excitation, along the axial plane of a horizontal cylindrical tank.

For this initial benchmark testing, water has been used as the fluid, with the forces and moments exerted on the tank observed and reported.

NASA Violent Slosh: In contrast to the isothermal case, the second validation case involves a non-isothermal cryogenic slosh experiment performed by Moran et al.[3] in 1994. Conducted at the NASA K-site facility, multiple tests were performed using a 62 cubic feet spherical tank, investigating how certain parameters (excitation frequency and amplitude, pressurant type, and fill level) affect tank pressure and fluid/wall temperatures during slosh.

The test tank is mounted inside a 25 foot diameter vacuum chamber and sealed off. The pressure is then ramped to a desired point with either gaseous hydrogen or helium pressurant, followed by a hold phase of constant pressure, and finally shaking is initiated. Figure 2 shows the pressure response for one of the tests conducted (RDG #870). This case is the best documented in the report from Moran et al.[3] and includes sufficient data to initialise a simulation.

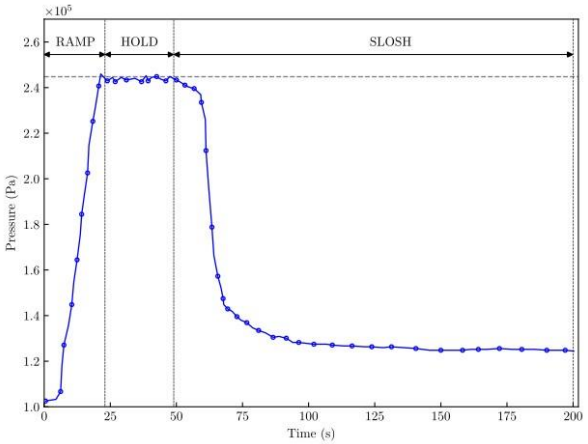

Figure 1: Pressure time history for test case RDG #870, showing the ramp, hold and sloshing phases.

[a] Corresponding author: bscmax001@myuct.ac.za

Numerical Implementation: The simulations employ the weakly-compressible volume-of-fluid (VoF) model in Elemental®, coupled with a calibrated Large Eddy Simulation (LES) turbulence model. The LES model provides an upper-cap of the turbulent viscosity based on cryogenic slosh experimental data. This approach accounts for enhanced thermal mixing at the liquid-gas interface.
Each of the simulations for the described experiments require a 3D computational mesh to capture all of the dynamics taking place and will solely focus on the sloshing phase of each experiment.

Current Results: For the isothermal case, results show a strong correlation with the experimental axial forces (see Figure 2), as indicated by the high Pearson correlation coefficient in Figure 3. Although certain peaks are being missed by the simulation.

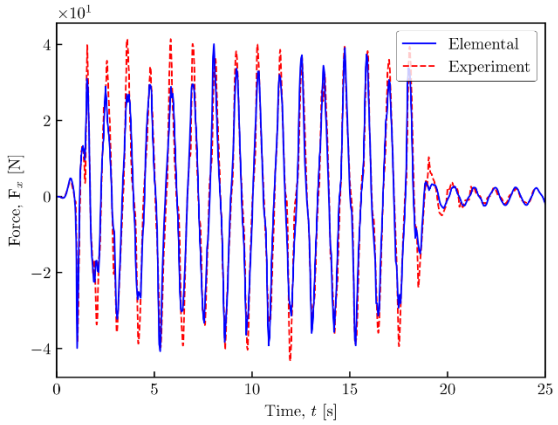

Figure 2: Axial force time history compared to the experiment.

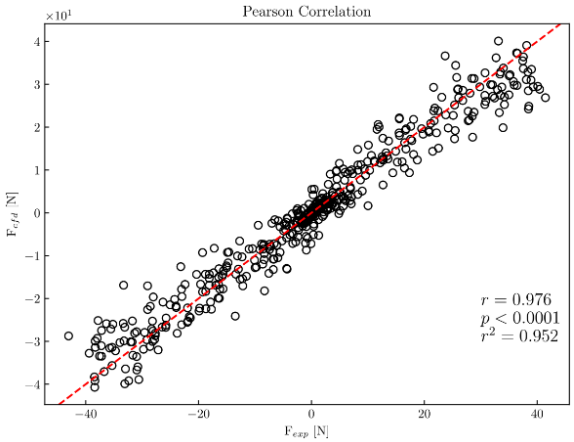

Figure 3: Pearson plot indicating a good correlation with the experimental data.

For the non-isothermal case, two LES model calibrations were tested: First, a more aggressive cap on the turbulent viscosity (C1), and second a less aggressive cap (C2). Shown in Figure 4, C1 provides a good fit on the pressure curve initially but diverges after ~12s, whereas C2 correlates poorly initially but provides a better fit later in the simulation.

[a] Corresponding author: bscmax001@myuct.ac.za

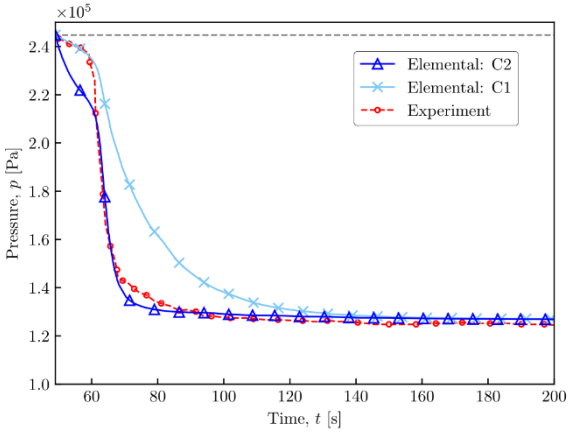

Figure 4: Pressure comparison against the sloshing pressure profile presented by Moran et al.[3] The performance of two turbulence model calibrations (C1 and C2) is shown.

Conclusion: The aim of the research is to validate Elemental® for cryogenic slosh using both isothermal and non-isothermal experiments. Currently two experiments have been considered, the isothermal case conducted by UPM and a non-isothermal case completed by Moran et al.[3]
The hydrodynamic model effectively captured the axial forces reported in the UPM experiment. The results for the non-isothermal case provide a clear path for future work, namely, identifying the optimal LES calibration.
This work successfully demonstrates an initial validation of the Elemental® solver and highlights the challenges in modelling thermodynamic behaviour in tanks at cryogenic conditions.

Future Work: Although the results are promising for both experiments, there are key areas to be improved:

- Certain peak forces are missed by the simulation in the isothermal case, suggesting an increase in the write-out frequency of the results or further mesh refinement.
- Another isothermal slosh test should be considered for further validation.
- Resolve the turbulent viscosity cap issue in the non-isothermal case and test it on an additional experiment.

References:

1. Elemental Numerics (Pty) Ltd. (2025) Elemental® Computational Fluid Dynamics Software. [Online]. Available: https://elementalnumerics.com/
2. HASTA. (2024) Hydrogen aircraft sloshing tank advancement. [Online]. Available: https://hasta-project.eu/
3. M.E. Moran, N.B. McNelis, M.T. Kudlac, M.S. Haberbusch, G.A. Satornino, "Experimental Results of Hydrogen Slosh in a 62 Cubic Foot (1750 Liter) Tank", *NASA Technical Memorandum 106625*, AIAA Paper 94-3259, presented at the 30th Joint Propulsion Conference, Indianapolis, IN, June 27-29, 1994.

DESIGN, COMMISSIONING AND MODELLING OF A LABORATORY-SCALE WATER DISTRIBUTION NETWORK

A Mohamed[a], P.G Rousseau[b] & A.H Basson[c]

Department of Mechanical & Mechatronic Engineering, University of Stellenbosch, Stellenbosch, South Africa

Introduction: Water is a valuable resource used daily on a global scale. Despite its frequent use, less than 2.5% of the water available on Earth is freshwater[1]. The effective and efficient use of water is therefore crucial.

To ensure that water distribution networks (WDN) function as intended and provide a reliable supply of water to end users, thermofluid simulation models are used[2]. These models are utilised within two stages of the WDN lifecycle: the design stage and the operation stage. During the design stage, a WDN is conceptualised, designed and modelled to ensure that it meets performance and demand requirements. During the operation phase, condition monitoring on the WDN is performed. Condition monitoring utilises the results of the hydraulic model developed in the design phase and compares it to the measured data recorded from the physical WDN. Any discrepancies between the two datasets indicate a potential fault within the physical network. However, before the hydraulic model can be used for condition monitoring applications, it should be calibrated to ensure that its outputs accurately match the physical system.

This paper discusses the design and commissioning of a laboratory-scale WDN test facility as well as the development of an accompanying Flownex thermofluid model. Results of initial measurements during commissioning to verify mass balances are presented and compared with preliminary results obtained with the uncalibrated Flownex model. In future, both the test facility and hydraulic model will be utilised in the development and demonstration of a model calibration methodology.

Design and construction of laboratory-scale WDN test facility: The test facility layout was conceptually designed to reflect the structure of a typical gravity-driven industrial scale WDN based on the following high-level system requirements: (i) It shall accommodate both gravity-driven and pumped flow test configurations. (ii) It shall mimic both branched and looped WDN layouts. (iii) It shall allow repeatable test conditions by employing digitally controlled rather than manual valves. (iv) It shall provide direct digital measurements and data collection. (v) The flow velocities shall not exceed 2 m/s.

The layout of the test facility is shown schematically in Figure 1. It consists of a water supply tank 0.5 m above ground level that represents the industrial water purification and storage plant, a pump line feeding elevated storage tanks, and a distribution network terminating at the proportional control valves, which emulate end-users. Both gravity-driven and pumped flow configurations combined with either branched or looped WDN flows can be emulated by manually opening and closing different valves. Various bleed lines and valves were additionally installed to remove trapped air from the system, but are not shown to avoid ambiguity.

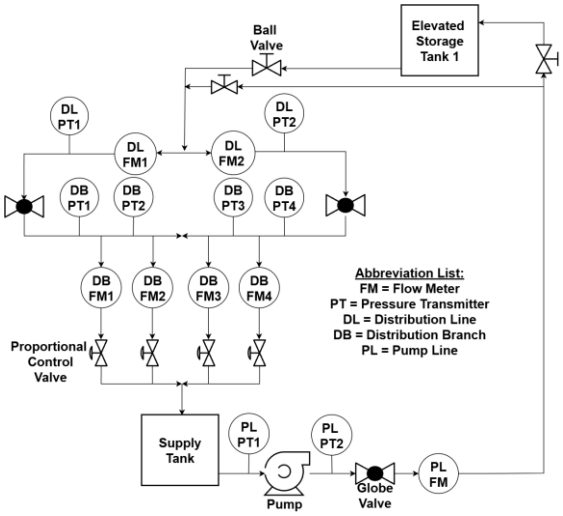

Figure 1: High-level schematic of the laboratory-scaled WDN.

The gravity-driven SR was achieved by placing the elevated storage tanks at a height of 5 m above ground level, but the distribution system can also be fed directly from the pump. Repeatable testing was ensured through the selection of proportional control valves (PCVs) installed within the distribution branches. The flow velocity requirement was met via appropriate pipe sizing and pump selection.

The design of the laboratory-scale WDN encompassed multiple engineering processes in parallel, including materials selection, pump sizing, valve sizing and selection, pipe sizing and sensor selection. Budget constraints were the primary limitation and significantly impacted component selection.

Flow meter selection, pipe sizing and pump selection were performed iteratively by employing the thermofluid model. The final configuration includes inline vortex flow meters, pressure transducers, 15 mm pipe used around the control valves and flow meters to accommodate their process connections and 32mm pipe used throughout the remainder of the system. A 0.75 kW pump with a 3 bar maximum head, selected to match the system curve near its best efficiency point,

[a] 22618929@sun.ac.za
[b] prousseau@sun.ac.za
[c] ahb@sun.ac.za

was installed. Upon achieving all requirements, the laboratory-scaled WDN was constructed and commissioned. Commissioning involved air purging via bleed lines and verifying mass balance across multiple flow configurations.

Modelling of the laboratory-scale water distribution network: A steady-state hydraulic model of the laboratory-scaled WDN was developed in Flownex SE to simulate flow and pressure distributions within the system.

The model was developed with the following assumptions: (i) Flow rates and pressures remained constant over time representing steady state operating conditions. (ii) The flow is fully developed. (iii) The fluid is incompressible. (iv) The flow is isothermal.

The modelling approach used when developing the hydraulic model of the system was as follows: Mirror the laboratory-scale WDN by utilising the available hydraulic components within Flownex, model the flow meters as an empirical general relationship component, and incorporate nodal elevations and input parameters. Minor losses not added through components were either grouped into a secondary loss factor or omitted if negligible.

Mass balance of flow measurements: Figures 2 and 3 show the verification, and consequently the reliability, of the flow rates within the network through mass balances of the distribution loop and branch paths. Configuration 1 involved two PCVs fully opened while configuration 2 operated with all PCVs set to 50%.

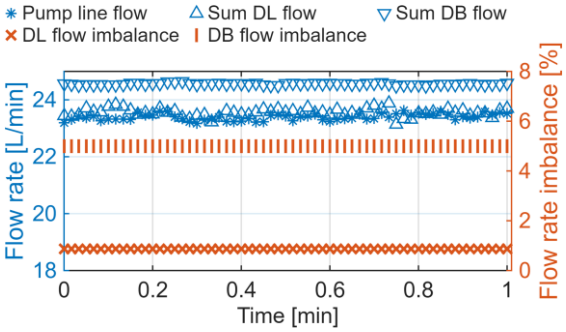

Figure 2: Measured flow rates and flow imbalances for configuration 1

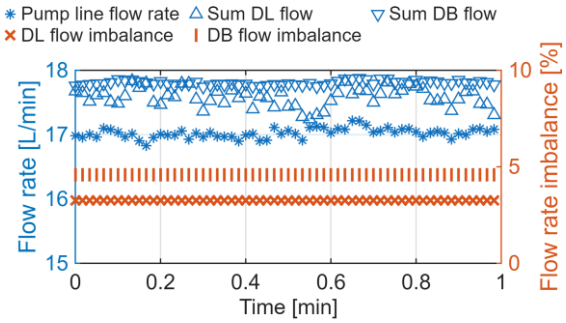

Figure 3: Measured flow rates and flow imbalances for configuration 2

Since the test facility has yet to be calibrated, flow imbalances were observed to be 0.68% and 5.0% as shown in Figure 2 and 3.3% and 4.5% as shown in Figure 3. Calibration will be performed on the test facility using the verified pump flow meter to assess flow meter discrepancies with one PCV open at varying flow rates.

Simulated vs measured flow measurements: Figures 4 and 5 show that across both configurations, the absolute relative error between the measured and simulated data remained within +/- 9%, indicating a strong preliminary agreement. Although based on uncalibrated flow measurements and an uncalibrated model these findings offer initial validation of the modelling approach.

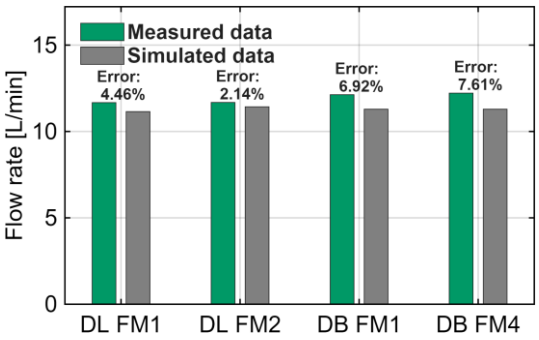

Figure 4: Measured distribution line and branch flow rates for configuration 1

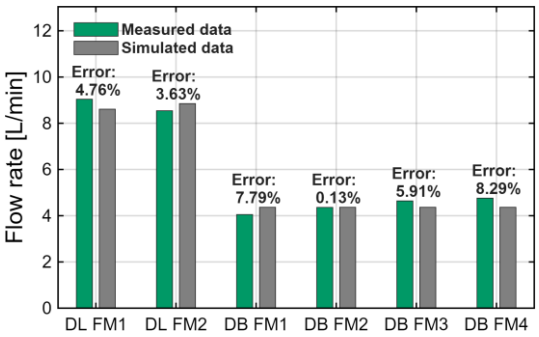

Figure 5: Measured distribution line and branch flow rates for configuration 2

Conclusion: This paper presented the design and commissioning as well as a model of a laboratory-scaled WDN test facility. It considered key design factors and system requirements. While based on fundamental assumptions and uncalibrated data, the preliminary results show strong alignment between the model and initial measurements providing confidence in the modelling approach.

References:

1. Uitto, J. Global freshwater Resources. Kluwer Academic Publishers, 2001.

2. Bello, O., Abu-Mahfouz, A.M., Hamam, Y., Page, P.R., Adedeji, K.B. & Piller, O. 2019. *Solving Management Problems in Water Distribution Networks: A survey of Approaches and Mathematical Models*. Water, Vol. 11, No. 562, 2019.

EXPLORING THE IMPACT OF ADDITIVE MANUFACTURING TECHNIQUES ON THE MICROSTRUCTURE AND MECHANICAL PROPERTIES OF Ti-6Al-4V

Kelvin Shiridzinomwa[a] & Thorsten Becker[a,b,c]

[a] Centre for Materials Engineering, University of Cape Town, Cape Town, South Africa
[b] Department of Mechanical and Mechatronics Engineering, Stellenbosch University, Cape Town, South Africa
[c] eNtsa, Nelson Mandela University, South Africa

Additive manufacturing of Ti-6Al-4V using laser powder bed fusion (LPBF), wire arc additive manufacturing (WAAM), and laser powder directed energy deposition (LP DED) techniques results in different microstructures that govern the mechanical performance of the prints. The mechanical properties of Ti-6Al-4V are sensitive to microstructural variations, and this study investigates the three AM techniques (LPBF, WAAM, and LP DED) to explore the relationship between the inherent microstructure and mechanical properties.

Introduction: Ti-6Al-4V, a titanium alloy composed of 6% aluminium and 4% vanadium, is widely utilised due to its high strength-to-weight ratio, excellent fatigue resistance, and notable corrosion resistance, especially in hostile environments [1]. These properties make it the most used titanium alloy across various industries, including aerospace applications such as compressor blades, casings, and fasteners.

Traditional manufacturing methods like forging, wrought processes, and machining often result in substantial material waste, with buy-to-fly (BTF) ratios ranging from 6:1 to 25:1. In contrast, additive manufacturing (AM) techniques—such as LP DED, WAAM, and LPBF—enable near-net shape fabrication, improving BTF ratios to approximately 2:1. These advanced methods enhance material efficiency and allow for the production of complex geometries challenging to achieve through conventional processes [2].

However, adopting AM for load-bearing components is challenging due to an incomplete understanding of the relationships between process parameters, resulting microstructures, and mechanical properties. Therefore, tailoring and establishing these correlations are essential for manufacturing critical components such as engine parts, airframes, and landing gears [3][4].

In AM technologies, Ti-6Al-4V typically exhibits columnar β grains with a (001) texture. At room temperature, it possesses a dual phase $\alpha + \beta$ microstructure; heating above the β transus, approximately 975 °C, induces a transformation into the β phase [4][5]. Upon cooling, the resultant microstructure is influenced by the cooling rate: High cooling rates above 410 °C/s, as observed in LPBF, lead to a metastable martensitic (α') microstructure. Cooling rates between 20 and 410 °C/s, typical in LP DED, result in a combination of the partial α' phase and massive α (α_m) phase. WAAM, with cooling rates below 20 °C/s, facilitates the nucleation and gro1`th of lamellar α structures, the Widmanstätten structure [6].

The microstructural characteristics of Ti-6Al-4V produced via LPBF, LP DED, and WAAM significantly influence its tensile properties, with each AM technique imparting distinct microstructures that affect mechanical performance. This study aims to elucidate the microstructural details and their impact on design parameters such as yield strength (YS), ultimate tensile strength (UTS), elongation to failure (EF), and Young's modulus (E).

Methodology: Ti-6Al-4V plates were fabricated using LPBF, LP DED, and WAAM within an inert argon environment, followed by a stress-relief heat treatment at 600 °C for 3 hours to mitigate residual stresses. ASTM E8-compliant sub-sized dog bone specimens with a gauge length of 25 mm were machined from these plates and speckled to enable strain measurement using Digital Image Correlation (DIC) via MatchID software. Tensile tests were performed on a Zwick 1480 machine. For microstructural characterisation, samples were sectioned, mounted in epoxy, polished, and etched with Kroll's reagent following ASTM E112 standards prior to optical microscopy analysis.

Results: Expected prior β grain boundaries along the build direction were observed in all AM techniques. The LPBF specimens displayed microstructural images of fine α' needles within elongated primary β-phase grains, accompanied by finely dispersed lamellar α-phase. The acicular morphology due to intrinsic heat treatment subjected to lower layers was recognised from the needle α' phase in LPBF samples (see Figure 1). The differences in cooling rates in the AM techniques result in distinct microstructures, mainly governed by lath size. The lath sizes and thickness increase from fine α' needles in LPBF to α colonies and an $\alpha + \beta$ Widmanstätten microstructure in WAAM (see Figure 3), and a coarse basketweave $\alpha + \beta$ microstructure in LP DED (see Figure 2).

[a] SHRKEL005@myuct.ac.za

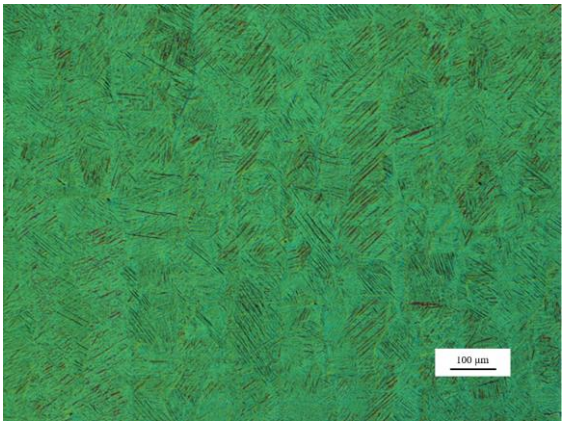

Figure 1: ZX micrograph of LPBF Ti-6Al-4V at X30 AS 3.

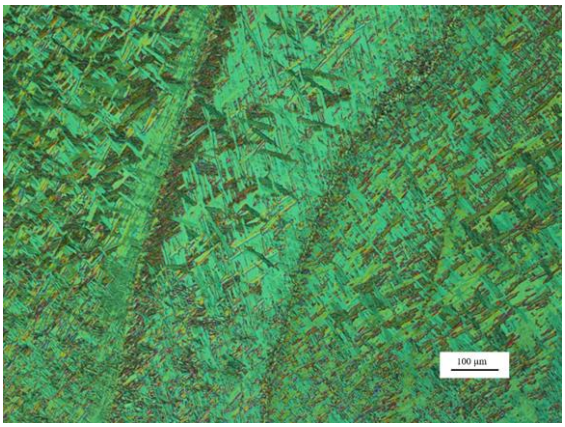

Figure 2: ZX micrograph of LP DED Ti-6Al-4V at X30 AS 3.

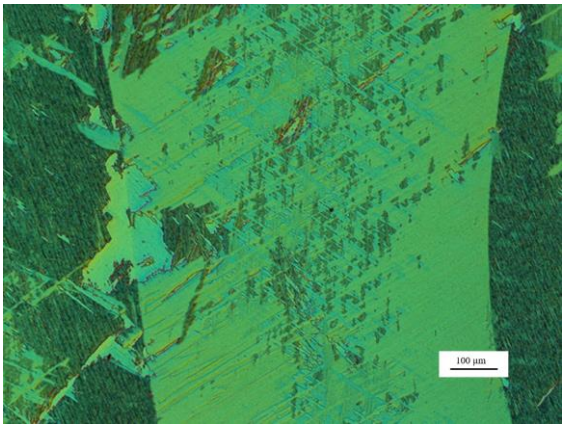

Figure 3: ZX micrograph of WAAM Ti-6Al-4V at X30 AS 3.

The LP-DED, WAAM, and LPBF tested dog-bone specimens exhibited a variation in tensile properties. All AM techniques exhibited an average consistent E of ~117 GPa due to similar crystal properties. The stress relief heat treatment homogenised the anisotropic strains in the lattice; however, anisotropy due to microstructural features such as grain orientation and texture persisted. An expected high YS and UTS (1127.6 ± 7.6 and 1195.1 ± 1.4 MPa) were exhibited from LPBF, exposing the reported high strength and low ductility of the α' martensite phase. WAAM-produced samples showed lower YS and UTS (966.2 ± 29.3 and 914.6 ± 16.2 MPa) than LPBF. The LP DED samples exhibited the lowest YS and UTS (837.4 ± 41.4 and 904.5 ± 9.1 MPa). The specimens showed higher strength in tensile loading perpendicular to the build direction than parallel due to inherent flaws between layers. LPBF exhibited a stable EF (10.5 ± 2 %), conventionally low, and expected from the martensitic microstructure. The EF in the DED processes was random and highly fluctuated due to flaws such as gas entrapment and lack of fusion, (7.5 ± 5 %) in WAAM, and (11 ± 5.5 %) in LP DED.

Conclusion: The established sensitivity of the mechanical properties of Ti-6Al-4V to its microstructural characteristics is evident across different AM techniques. Variations in phase composition, α lath morphology, β grain geometry, and manufacturing-induced defects significantly influence tensile performance. Following the Hall-Petch theory, the strength is inversely related to the α lath sizes from thin needles in LPBF, to colonies in WAAM, and coarse basketweave morphology in LP DED.

References:

1. S. Liu and Y. C. Shin, "Additive manufacturing of Ti6Al4V alloy: A review," Mater Des, vol. 164, Feb. 2019, doi: 10.1016/j.matdes.2018.107552.
2. H. Birmingham et al., "Manufacture of Complex Titanium Parts using Wire+Arc Additive Manufacture."
3. T. Zhang and C. T. Liu, "Design of titanium alloys by additive manufacturing: A critical review," Jan. 01, 2022, KeAi Communications Co. doi: 10.1016/j.apmate.2021.11.001.
4. T. H. Becker, P. Kumar, and U. Ramamurty, "Fracture and fatigue in additively manufactured metals," Oct. 15, 2021, Acta Materialia Inc. doi: 10.1016/j.actamat.2021.117240.
5. S. Zhou et al., "Microstructure evolution and fracture behavior of Ti–6Al–4V fabricated by WAAM-LDM additive manufacturing," Journal of Materials Research and Technology, vol. 28, pp. 347–362, Jan. 2024, doi: 10.1016/j.jmrt.2023.11.255.
6. A. M. Beese and B. E. Carroll, "Review of Mechanical Properties of Ti-6Al-4V Made by Laser-Based Additive Manufacturing Using Powder Feedstock," Jom, vol. 68, no. 3, pp. 724–734, 2016, doi: 10.1007/s11837-015-1759-z.
7. H. D. Nguyen et al., "A critical review on additive manufacturing of Ti-6Al-4V alloy: Microstructure and mechanical properties," May 01, 2022, Elsevier Editora Ltda. doi: 10.1016/j.jmrt.2022.04.055.

FRACTURE PREDICTION OF REALISTIC INTERMETALLIC PARTICLES IN A PLASTICITY MODEL OF WROUGHT ALUMINIUM

Abdul Gafeeth Benjamin[abc] & Ernesto Bram Ismail[abc]

[a] Centre for Research in Computational and Applied Mechanics, University of Cape Town, Cape Town, South Africa
[b] Centre for Materials Engineering, University of Cape Town, Cape Town, South Africa
[c] Department of Mechanical Engineering, University of Cape Town, Cape Town, South Africa

In 2015, South Africa transitioned to the production of fully aluminium beverage cans, which have since become the dominant type manufactured in the country. Two aluminium alloys are used for the production of beverage cans: AA3104 (for the body) and AA5182 (for the ends). AA3104 and AA5182 sheets undergo a series of production processes in which the processing parameters must be carefully controlled to ensure the desired final product quality. During casting of these two alloys, intermetallic particles (IMPs) form as a result of the limited solubility of certain alloying elements in the aluminium matrix[1]. At some point in the production process, the ingots of both alloys get hot rolled to reduce the thickness and break down IMPs[2]. This research aims to model the breakup of the IMPs, during hot rolling, by coupling a finite strain elastoplasticity model (for the matrix) and a small strain brittle fracture model (for the particle).

All modelling was done with the C++ open-source finite element library, deal.II[3]. The library includes parallel computing and built-in adaptive mesh refinement capabilities to improve computational efficiency.

Elastoplasticity model: The continuum elastoplasticity model by PRISMS-Plasticity[4] was used and edited to model the aluminium alloy matrix. The key features of this model are that it can model large strain responses (this is needed because during hot rolling the ingot experiences strains of up to 123.5%[5]) and it incorporates linear isotropic hardening, which captures the work hardening experienced during hot rolling. The model uses a quadratic logarithmic[6] hyperelastic law and a von Mises yield criterion. Some of the drawbacks of the model are that it is incapable of modelling the metal matrix as individual grains. Additionally, it is strain rate independent. During hot rolling, the metal ingot temperature is above one-third of its glass transition temperature and at these elevated temperatures it becomes strain rate sensitive. The governing equations are solved incrementally over pseudo-time steps to simulate the material's nonlinear evolution.

Fracture model: The fracture model which was used to model the breaking of the IMPs was developed by W. Munshi[7] and it forms part of the deal.II code gallery. The model implements the phase-field method (PFM) for simulating crack propagation because it addresses the difficulty of modelling a lower-dimensional surface (a crack) that cuts through a higher-dimensional material. The PFM treats cracks as smeared volumetric zones, rather than discrete surfaces by using a continuous scalar field, often termed the *damage field*. An outline of the model by Ambati et al.[8] which was implemented by W. Munshi is provided below. PFMs model crack propagation via the interplay between elastic deformation and the damage field. The damage field represents the weakening of the elastic material. We assume that the body is elastic. The *length scale parameter* l is used to diffuse a sharp crack.

Modelling procedure: We follow the approach of N. Moulin[5] where we start by modelling of 2D *representative* particles embedded in an elastoplastic matrix (see Figure 1). The elastoplasticity model is applied to the matrix domain and the fracture model is applied to the particle domain. We apply plane strain compression on the computational cell to mimic rolling; that is, compression in the normal direction (ND), free in the rolling direction (RD), and constrained in the transverse direction (TD).

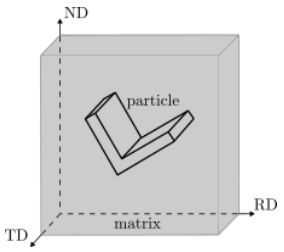

Figure 1: Computational cell used in FE models (adapted from [5]).

We assumed perfect contact at the matrix-particle interface. A Dirichlet-Dirichlet (DD) coupling was used to couple the two models. This coupling method works by applying the same Dirichlet constraint **on** the interface $\boldsymbol{u}^k_{\Gamma_D}$ of the two domains at some coupling iteration k and solving the two models for each load step. After solving, the interface tractions were extracted at every node on the interface using Cauchy's Law. Traction continuity requires that

$$\boldsymbol{t}^{\text{matrix}} = -\boldsymbol{t}^{\text{particle}},$$

therefore, we compute the iteration residual vector as

$$\boldsymbol{r}^k = \boldsymbol{t}^k_{\text{matrix}} + \boldsymbol{t}^k_{\text{particle}}.$$

We then compute the Euclidean norm of $\boldsymbol{r}^k$ and

[a] bnjabd005@myuct.ac.za

checked whether it fell below some tolerance. If yes, then the DD coupling for that load step has converged, and we carry the converged solution over to the next load step and use it as the initial guess for the first coupling iteration of the that load step. If the DD coupling has not yet converged, we then relax the interface displacement with

$$\boldsymbol{u}_{\Gamma}^{k+1} = \boldsymbol{u}_{\Gamma}^{k} \vdash \omega\rho\boldsymbol{r}^{k},$$

where ω is the relaxation parameter ($0 < \omega < 1$) and ρ is used to normalize the traction residual vector into a displacement increment vector. We then use $\boldsymbol{u}_{\Gamma}^{k+1}$ and follow the same procedure for the next coupling iteration $k + 1$.

Meshing: All the meshing was done primarily using an open-source FE mesh generator called Gmsh[10]. The 2D simple particle meshes were generated by specifying the geometric positions in a geometry file. The 3D complex particle meshing process involved using photogrammetry to reconstruct the IMP surface with multiple 2D scanning electron microscope images of the same particle at different camera orientations. After reconstruction, the surface was postprocessed to ensure that it was suitable for meshing. It was then meshed using Gmsh. Earlier versions of deal.II only works with purely hexahedral (3D) and quadrilateral (2D) elements therefore, all the meshes had to meet this constraint. The entire meshing process was automated in Python using shell scripts.

Results: Below are the results for a cell that experienced 20% strain, in the y-direction, with a V-shaped particle. Figure 2 shows the displacement magnitude and Figure 3 shows the von Mises stress of the cell.

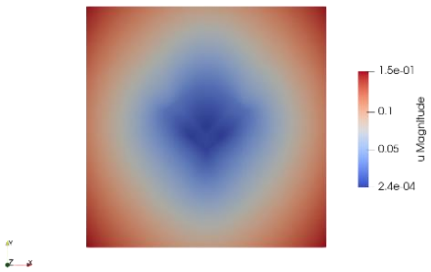

Figure 2: Displacement magnitude with a V-shaped particle.

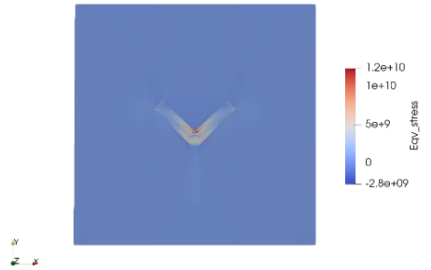

Figure 3: Von Mises stress with a V-shaped particle.

Figure 4 shows the damage distribution in the V-shaped particle.

Figure 4: Damage in the V-shaped particle.

References:

1. W. S. Ebhota and T.-C. Jen, "Intermetallics Formation and Their Effect on Mechanical Properties of Al-Si-X Alloys," in *Intermetallic Compounds - Formation and Applications*, InTech, 2018. doi: 10.5772/intechopen.73188.
2. J. Hirsch, K. F. Karhausen, and O. Engler, "Property Control in Production of Aluminum Sheet by Use of Simulation," in *Continuum Scale Simulation of Engineering Materials*, Wiley, 2004, pp. 705–725. doi: 10.1002/3527603786.ch38.
3. D. Arndt *et al.*, "The DEAL.II finite element library: Design, features, and insights," *Computers and Mathematics with Applications*, vol. 81, pp. 407–422, Jan. 2021, doi: 10.1016/j.camwa.2020.02.022.
4. M. Yaghoobi *et al.*, "PRISMS-Plasticity: An open-source crystal plasticity finite element software," *Comput Mater Sci*, vol. 169, Nov. 2019, doi: 10.1016/j.commatsci.2019.109078.
5. N. Moulin, D. Jeulin, and H. Klöcker, "Stress concentrations in non-convex elastic particles embedded in a ductile matrix," *Int J Eng Sci*, vol. 47, no. 2, pp. 170–191, 2009, doi: 10.1016/j.ijengsci.2008.08.012.
6. J. C. Simo, "Algorithms for static and dynamic multiplicative plasticity that preserve the classical return mapping schemes of the infinitesimal theory," 1992.
7. W. N. Munshi, M. Fehling, W. Bangerth, and C. Annavarapu, "An open-source implementation of the hybrid phase field method for 3D fracture modeling based on deal.II," Jan. 2025, [Online]. Available: https://ssrn.com/abstract=5088136.
8. M. Ambati, T. Gerasimov, and L. De Lorenzis, "A review on phase-field models of brittle fracture and a new fast hybrid formulation," *Comput Mech*, vol. 55, no. 2, pp. 383–405, Feb. 2015, doi: 10.1007/s00466-014-1109-y.
9. C. Miehe, F. Welschinger, and M. Hofacker, "Thermodynamically consistent phase-field models of fracture: Variational principles and multi-field FE implementations," *Int J Numer Methods Eng*, vol. 83, no. 10, pp. 1273–1311, Sep. 2010, doi: 10.1002/nme.2861.
10. C. Geuzaine and J. F. Remacle, "Gmsh: A 3-D finite element mesh generator with built-in pre- and post-processing facilities," *Int J Numer Methods Eng*, vol. 79, no. 11, pp. 1309–1331, Sep. 2009, doi: 10.1002/nme.2579.

Control Design of a Coaxial Tiltrotor Quadcopter for Mixed Flight Regimes

Mpilonhle Nxasana [a] & Arnold Pretorius [b]

Department of Mechanical Engineering, University of Cape Town, Cape Town, South Africa

Unmanned Aerial Vehicles (UAVs) are being increasingly deployed for military, industrial, and civilian applications, yet conventional quadcopters remain limited by their underactuated dynamics, which hinder precise navigation. This becomes problematic in confined spaces or tasks that demand high accuracy, such as search-and-rescue missions. To address this limitation, this research proposes the design and implementation of a control system for a coaxial tiltrotor quadcopter; an overactuated configuration that enables independent control of translational and rotational motion, allowing for precise path tracking. The project begins with the derivation of a nonlinear dynamic model using quaternions to avoid singularities, followed by the development of a cascaded Linear Quadratic Regulator (LQR) control scheme for full position and attitude control. The pose of the vehicle will be estimated through the fusion of IMU and GPS measurements to provide accurate real-time feedback. The proposed control strategy will be validated through simulations in MATLAB/Simulink under various disturbances and model uncertainties, before being implemented on a PX4-based flight controller. Hardware-in-the-loop and flight tests will be conducted on a physical prototype to evaluate real-world performance. The expected contributions include demonstrating precise and robust flight across multiple regimes and highlighting the performance advantages of the tiltrotor configuration when compared to conventional quadcopters.

Introduction: UAVs, particularly quadcopters, are playing an increasingly important role in the military and commercial sectors due to their versatility, simplicity, and vertical-takeoff-and-landing capabilities. However, one fundamental limitation remains that conventional quadcopters are underactuated, as they cannot move horizontally without pitching or tilting in that direction first. Hence, quadcopters cannot track arbitrary trajectories, which poses a significant challenge in certain applications, such as disaster relief, where precise path tracking is crucial. To address this limitation, tiltrotor quadcopters, which feature rotor arms capable of tilting, have been proposed[1]. This results in a vehicle that is overactuated, allowing for independent control of translational and rotational motion, thereby improving vehicle manoeuvrability. Nevertheless, the addition of tilting mechanisms introduces a strong coupling between the control inputs, giving rise to a highly nonlinear system. The aim of this project is to develop an optimal control algorithm that can handle the nonlinearities present in the tiltrotor, allowing it to fly stably under different flight regimes such as takeoff, landing, and hover.

[a] NXSPI001@myuct.ac.za
[b] arnold.pretorius@uct.ac.za

Methodology: Each major component of the project will be developed in three key phases:

1. Control system design for a standard quadrotor configuration.
2. Extension of the control strategy to the coaxial tiltrotor configuration.
3. Development and integration of the state estimation algorithm.

This phased approach allows each subsystem to be validated and fine-tuned individually before combining them to construct the full system.

1. System Modelling: A nonlinear state-space model is derived to capture the dynamics of the tiltrotor system. Since the tiltrotor will operate at low speed, all drag-like effects will be neglected. To avoid Gimbal Lock, the model will make use of quaternions to represent orientation.

2. Control Design: Several control schemes have been applied to tiltrotors in the literature, however, this project will employ LQR. LQR is a linear full-state feedback control method that computes the optimal control input by minimising a quadratic cost function of the state error and the control effort. Because the tiltrotor system is overactuated, several combinations of control inputs can produce the same trajectory. However, being an optimal control method, LQR naturally handles this control redundancy. Furthermore, its use of full-state feedback makes it well-suited for controlling platforms with multiple degrees of freedom. This is demonstrated by Kumar et al.[2], who achieve full attitude control with a single LQR controller. To enable full position and attitude control, a cascaded LQR architecture will be used, as shown in Figure 1.

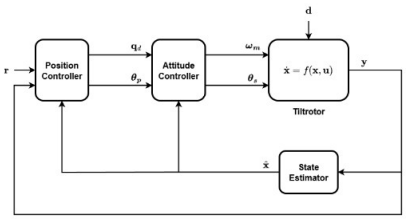

Figure 1: Block diagram of control scheme

The control scheme consists of an outer-loop LQR controller with integral action for tracking position setpoints, $\boldsymbol{r}$, which generates orientation and tilt commands, q_d and θ_p, and an inner-loop LQR controller for attitude control, which outputs motor and servo commands, ω_m and θ_s. The integral action in the

outer loop improves the disturbance rejection of the controller whilst also allowing it to deal with model uncertainty. Although LQR is a linear control method, the tiltrotor will remain mostly upright during operation, allowing the nonlinear state-space model to be linearised about the hover condition for the control design.

3. Validation: The controller will be implemented in MATLAB/Simulink and tested under a range of simulated flight regimes, including take-off, landing, and hover. The controller will be evaluated based on its setpoint tracking under wind disturbances and model uncertainty.

4. Implementation: To control the onboard electronics, a flight controller with sufficient computing power to run the control loop in real time and a compatible eight-channel motor controller will be selected. The PX4 autopilot software stack will be used to integrate the sensors, actuators, and the control algorithm.

5. Testing: Hardware-in-the-Loop testing will be used to verify that the controller runs in real-time. The system's performance will be evaluated by deploying it on a physical prototype and conducting real-world flight tests. Environmental disturbances such as wind gusts will be simulated using a large fan.

Preliminary Results and Discussion: The control strategy for the coaxial quadrotor configuration has been developed and validated in simulation as described in the previous section, marking significant progress in Phase 1 of the project. The controller was tested under different test scenarios, but one in particular is highlighted here: The control system and quadcopter were simulated for 15 seconds with a position setpoint of $\boldsymbol{r} = [1, -2, 3]^{\mathrm{T}}\, m$ and a wind disturbance with a wind velocity of $\boldsymbol{v}_{wind} = [1, 4, 0]^{\mathrm{T}}\, m/s$. The orientation commands of the inner loop, along with the orientation and position of the quadcopter, are shown in Figures 2 and 3, respectively.

At near-hover conditions, the second and third components of the quaternion, q_1 and q_2, are proportional to roll and pitch, respectively. From Figure 2, the attitude controller tracks the pitch commands generated from the position controller with a Root Mean Square Error (RMSE) of 0.0002, which allows the quadcopter's x position to settle on the setpoint as shown in Figure 3. Figure 2 also demonstrates the benefit of integral action, as the quadcopter experiences a tailwind in the x direction. This causes the quadcopter to overshoot the setpoint by 2.8%, but as the error accumulates in the integrator, the pitch command settles on a value that perfectly counteracts the wind disturbance, allowing the quadcopter to maintain its position in x. The same is not true for the y position, as the quadcopter is subjected to a much larger headwind in that direction.

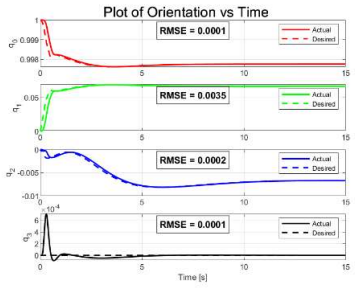

Figure 2: Graph of orientation against time

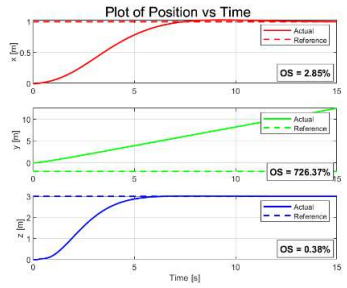

Figure 3: Graph of position against time

Because the orientation commands are constrained to keep the quadcopter near upright, the roll command saturates, as shown in Figure 2. This prevents the quadcopter from generating enough thrust to counteract the wind disturbance, resulting in the quadcopter being pushed off course in the y direction, as shown in Figure 3. The planned integration of the tiltrotor mechanism could mitigate this issue by enabling the controller to command the rotors to tilt toward the wind's direction, thereby enhancing the controller's disturbance rejection.

Conclusion: From the results presented above, the successful development of the proposed control strategy for the tiltrotor is expected to advance the design of UAVs that are more robust to external disturbances and capable of precise, efficient flight. These improvements will enhance the reliability of UAVs in critical missions such as disaster relief and search and rescue, while also offering the commercial sector a more stable platform for tasks such as factory inspections. These safer and more reliable autonomous aerial systems will foster greater public trust and acceptance of UAV technologies.

References:

1. M. Ryll, H. H. B¨ulthoff, and P. R. Giordano, "First flight tests for a quadrotor uav with tilting propellers," in *2013 IEEE International Conference on Robotics and Automation*, IEEE, 2013, pp. 295–302.

2. R. Kumar, M. Bhargavapuri, A. M. Deshpande, et al., "Quaternion feedback based autonomous control of a quadcopter uav with thrust vectoring rotors," in *2020 american control conference (acc)*, IEEE, 2020, pp. 3828–3833.

Structural optimisation of a lower limb exoskeleton for human locomotion assistance

[a] Nicla Kabila & [b] Micheal Petersen

[ab] Department of Mechanical Engineering, Cape Peninsula University of Technology, Cape Town, South Africa

A human locomotion assistance Lower Limb Exoskeleton (LLE) is a wearable robotic device that assists individuals with lower-limb paralysis in walking. LLEs are relatively heavy and, as a result, are inefficient and not easy to transport. This paper aims to determine if and how the weight of an LLE can be reduced to improve performance and portability. Focus is on structural optimisation to reduce weight while maintaining strength. Two methods are employed for weight reduction, namely, material selection and topology optimisation. This is done through 3D model FEA simulations.

Introduction: The South African province of Gauteng has one of the highest rates of trauma-induced spinal cord injuries due to assault[1]. In 2009, the Quadriplegia Association of South Africa (QASA) represented approximately 50,000 individuals who suffered mobility disorders[2]. Locomotive LLE devices give such patients the opportunity to walk again. The physical exercise that comes with regular use of an LLE can improve blood circulation, bowel and bladder function, and prevent secondary health conditions, such as muscle atrophy. The benefits are also psychological and social, including improved self-image and reduced depression. The disadvantages include weight, inefficiency and the high cost associated with designing, testing and manufacturing an LLE. Therefore, only a few LLEs have been commercialised, and wheelchairs remain the most efficient and affordable form of locomotion[3].

***Problem Statement*:** LLEs are considered to be relatively heavy.[4] The average weight of modern commercialised locomotive LLEs is 31kg, with some LLEs reaching 80kg.[3] Consequently, it requires much power to drive the structures, which are mostly made of standard aluminium alloy profiles. This has a significant impact on the functional performance.[34]

***Aim*:** To reduce the weight of a previously designed LLE structure through material selection and topology optimisation, while maintaining structural integrity.

***Research Objectives*:** Establishing the most suitable material and profile/shape for the structure through 3D model FEA simulations. Measuring weight reduction, maximum stresses, maximum strain, and factor of safety.

Current Design and Inputs: To design and evaluate an LLE structure, one must understand the forces acting on that structure. This is done by analysing human gait and the forces at work during the stance and swing phases. These inputs are used for the FEA simulations.

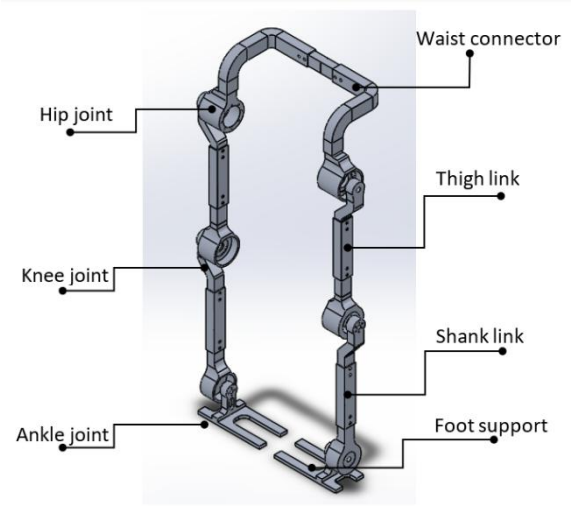

Figure 1: Current Exoskeleton Design

In Figure 1, the structure can be subdivided into four categories: a waist bracket, two shank links, two thigh links and two feet supports. The foot support, power source and actuation system of the LLE will not be optimised. The optimisation focuses on the three heaviest components of the structure, the waist bracket, thigh link and shank link. The specs for this structure are shown in Table 1.

Table 1: Current Exoskeleton Specs

	Current Design Weight (kg)	Material
Waist connector	2.81	Al7075
Thigh link	1.55	Al7075
Shank Link	1.35	Al7075
Total	**8.61**	

***Material Selection*:** Sixteen candidate alloys with high specific strength across five groups were considered. Namely, Aluminium, Titanium, Magnesium, polymers, and composites. The material selection process was done through comparing performance index. The performance index is calculated based on the material properties. For the LLE structure, which undergoes compression, bending, and cyclic loading, the considered properties were compressive strength, bending strength/stiffness, and fatigue strength. Because the aim of this material selection is weight

[a] niclakabila@gmail.com

reduction, these material properties were looked at in terms of "density ratios". In Equation 1, M_1 is the strength ratio, M_2 the stiffness ratio and M_3 the fatigue strength ratio. Z is the performance index.

$$Z = 3M_1 + 2M_2 + 1M_3$$

Equation 1: Performance Index Formula

Alloys/grades with the highest performance indices of the three best performing groups are listed in Table 2. Abaqus FEA simulations were run on the three components (waist bracket, thigh link and shank links) using these materials. The analysis was conducted using calculated human gait force inputs.

Table 2: Top Performing Materials

Material Property	Aluminium AA 7068	Titanium Ti-6Al-4V	Carbon Fibre Composite (CFRC)
Density kg/m^3	2850	4430	1550
Young's Modulus GPa	73	110	150
Poisson's Ratio	0.33	0.34	0.28

***Topology Optimisation*:** Abaqus topology optimisation feature was used to optimise the shape, size, and 2nd moment of inertia of the three components. The algorithm works by removing volume where not needed while maintaining strain energy. Models of the three components were simulated in selected materials AA7068, Ti-6Al-4V and CFRC. The axial joint holes on all three components were frozen, and the rest of the model was set for optimisation. Three iterations were run to reduce the volume of each model by 50%, 60% and lasty 70%.

Results: Results of material FEA and weight reduction are presented below in Table 3 for Aluminium AA7068, and Table 4 for Titanium Ti-6Al-4V

Table 3: Aluminium AA7068 FEA Results

AA7068	Max Von Misses	Max Strain	FOS	New Weight
Waist	69.06Mpa	7.46µm	7	2.80kg
Thigh	21.12MPa	0.80µm	23	0.63kg
Shank	19.46Mpa	0.80µm	24	0.68kg

Table 4:Titanium Ti-6Al-4V FEA Results

Ti-6Al-4V	Max Von Misses	Max Strain	FOS	New Weight
Waist	69.06Mpa	0.53µm	13	4.36kg
Thigh	21.12MPa	0.53µm	42	0.73kg
Shank	19.46Mpa	0.53µm	46	0.85kg

Figure 2 show the topology optimised models of the thigh, shank and waist.

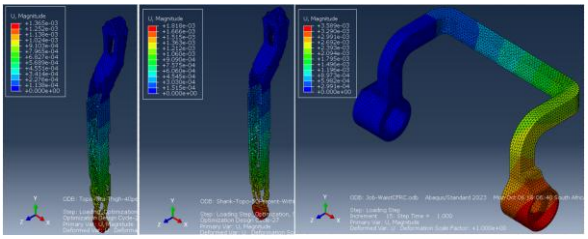

Figure 2: FEA of thigh, shank and waist models

***Discussion**:* Based on the simulation results in Table 3 and 4, the new total weight for a AA7068 and Ti-6Al-4V. structure is 5,42kg, and 7.52kg respectively. The better candidate being AA7068. Although more volume could be reduced with Ti-6Al-4V, its higher density resulted in heavier components. Its higher cost also makes it less favourable. Both materials present FOS above 5, and low maximum strain values. This indicates potential for further weight reductions. The topology optimisation resulted in organic, and more complex shaped thigh and shank links. The waist bracket models in all three materials were unsuccessful due to simulation complexities. CFRC though had a high material performance index could not be simulated either. Being an anisotropic material, design and simulation are too complex as models have to be built layer by layer and material properties are highly influenced by manufacturing technique. Prototyping and rigours post manufacturing testing are crucial for design feedback loop.

Conclusion: Weight reduction was achieved through material selection and topology optimisation. The recommended material is AA7068. High FOS indicate potential for further weight reductions, particularly for Ti-6Al-4V. Future research is needed in simulating CFRC.

1. M.A., Pilusa, S. & Mashola, M.K., 2023. The prevalence and profile of spinal cord injury in public healthcare rehabilitation units in Gauteng, South Africa. *The international Spinal Cord Society*, pp.9-15.
2. Joseph, C., Scriba, E. & Wilson, V., 2017. People with Spinal Cord Inury in Repubilic of South Africa. *Ameriacan Journal of Physical Medicine & Rehabilitation*, 96(2), pp.S109 - S111.
3. Rodriguez-Fernandez, A., Lobo-Prat, J. & Font-LLagunes, J.M., 2021. Systematic review on wearable lower-limb exoskeletons for gait training in neuromuscular impairments. Journal of NeuroEngineering and Rehabilitation, (18), p.22.
4. Rupal, B.S., Rafique, S. & Singla, A., 2017. Lower-limb exoskeletons: Research trends and regulatory guidelines in medical and non-medical applications. International Journal of Advanced Robotic Systems, (November - December).

[a] niclakabila@gmail.com

FEA simulation of combined loads to establish the impact of inclusions in steel on fatigue life

Wilhelm C. Augustyn[a] & Graeme J. Oliver[b]

[a] Department of Mechanical Engineering, Cape Peninsula University of Technology, Cape Town, South Africa
[b] Department of Mechanical Engineering, Cape Peninsula University of Technology, Cape Town, South Africa

This paper investigates the accuracy to which fatigue life can be predicted in a specimen, with and without non-metallic welded inclusions in a butt-welded joint using finite element analyses.

Aim. Can a *pragmatic*, ANSYS-only workflow predict the fatigue life of butt-welded carbon-steel test specimens with and without porosity to a level of accuracy useful in practice? This work quantifies that accuracy by explicitly modelling the weld metal, graded heat-affected zone (HAZ) and welding-induced residual stress field, validated against high-cycle tests on an Instron 8801 system.[1,2,6]

Introduction. Fatigue failure in welded joints is driven by structural stress concentration at the weld toe/root and by microstructural non-uniformity and residual stresses. Recent studies on welded steels emphasise surface-initiated cracking, HAZ softening/mismatch, and the utility of structural-stress approaches for consistent life correlation.[3,4,5] In low-carbon steels, measured longitudinal residual stress often exhibits an "M-shaped" profile peaking in the tempered HAZ, which motivates explicit HAZ zoning in the FE model.[1]

Methodology. Test specimens are cut from BS 1501-151-430A plate (6 mm) with a full-penetration butt weld. Root wire ER70S-6 and fill E7018-1 are applied under controlled procedures to produce a defect-free baseline and, separately, specimens with calibrated porosity mapped by NDT for model input. FE modelling uses ANSYS with a moving Goldak double-ellipsoid heat source to capture transient thermal fields, temperature-dependent properties and deposition sequencing.[2] The HAZ is represented by graded sub-zones (CGHAZ, FGHAZ, ICHAZ, tempered HAZ) consistent with where residual stresses localise.[1]

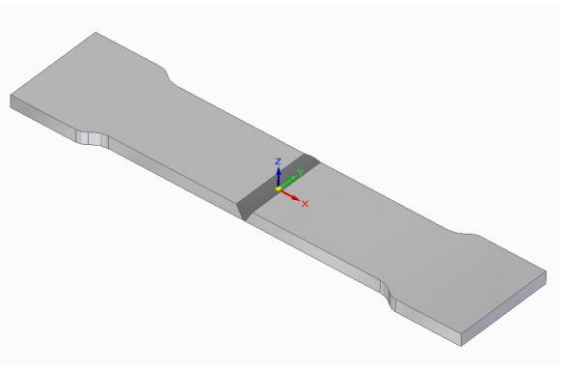

Fig 1. Physical representation of test specimen

The computed residual-stress field is carried into fatigue assessment. Fatigue is evaluated using a traction structural stress hot-spot method on the weld line, with comparison to BS 7608 classes for conservatism.[4,5] Tests on an Instron 8801 run in load-control at R≈0.1, 20 Hz, with failure at 2×10^6 cycles or crack-growth criteria, enabling FE-to-test life correlation and pore-size/location sensitivity.[5,6]

Results and discussion. The workflow reproduces the M-shaped residual-stress signature with a local maximum in the tempered HAZ, consistent with measurements in literature.[1,2] The structural-stress hot-spot from ANSYS is expected to co-locate with observed crack nucleation, enabling consistent life correlation without over-fitting to a single S–N family.[5]

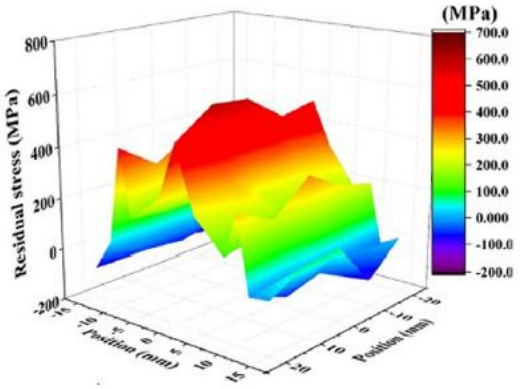

Fig. 2. Representative longitudinal welding residual stress with M-shaped profile (adapted from Lai and Wu, 2020).[1]

Porosity is introduced parametrically to quantify the reduction in fatigue strength and the shift in controlling hot spot versus pore size, location and cluster morphology, reflecting evidence that pores under tensile residual stress accelerate initiation and growth.[3,7] *Where simulation and test diverge, the root causes are traced to HAZ softening, residual-stress relaxation or mesh-to-feature resolution; these findings prioritise model-fidelity improvements for practice.*[2] Porosity and inclusions focus. Why emphasise *porosity*? In welded carbon steel, gas pores and non-metallic inclusions create local stress raisers that, when superposed with tensile residual stress, promote early crack nucleation and shorten endurance under high-cycle loading.[3,1] Under structural-stress control at the weld toe or root, pore size, shape, depth below the surface, and clustering govern the effective

notch severity and lifetime reduction.[3],[7] In this study, porosity fields will be characterised by NDT and mapped into ANSYS so that dominant pores are explicitly meshed at their measured locations; sensitivity cases examine proximity to the weld toe and root, single versus clustered defects, and volumetric fraction. The fatigue assessment then samples the traction structural stress at the controlling hot spot to obtain life estimates with and without the measured pores, revealing a quantitative decrement in fatigue strength versus pore metrics.[3] Where pores sit within the tempered HAZ under tensile residual stress, the life penalty is expected to be most severe; where pores lie deeper in compressive zones, the penalty reduces.[1],[2],[3],[7] The practical value is a defensible link between inspection data and life prediction, enabling acceptance criteria and weld-repair decisions to be framed on measured porosity rather than generic workmanship limits.[3],[7]

Conclusions. We present a validated, engineer-ready ANSYS workflow that couples weld thermal simulation, HAZ-aware material modelling and structural-stress-based fatigue assessment for butt welds with and without porosity. The outcome is an evidenced margin of accuracy for decision-making in fabrication, and guidance on when HAZ detail and residual stresses are non-negotiable for credible fatigue-life prediction.[1],[2],[5]

References

1. Lai, H.H. and Wu, W. (2020) ‘Practical examination of the welding residual stress in view of low-carbon steel welds’, Journal of Materials Research and Technology, 9(3), pp. 2717–2726.
2. Knoedel, P., Gkatzogiannis, S. and Ummenhofer, T. (2017) ‘Practical aspects of welding residual stress simulation’, Journal of Constructional Steel Research, 132, pp. 83–96.
3. Shen, F., Zhao, B., Li, L., Chua, C.K. and Zhou, K. (2017) ‘Fatigue damage evolution and lifetime prediction of welded joints with the consideration of residual stresses and porosity’, International Journal of Fatigue, 103, pp. 272–279.
4. Guan, X., Guo, H., Li, G., Yang, D. and Pan, Y. (2024) ‘Fatigue behaviour of welded joints of Q690D high strength steel’, Journal of Constructional Steel Research, 223, 109037.
5. Wang, C., Zhu, T., Yang, B., Xiao, S. and Yang, G. (2024) ‘Fatigue crack evaluation of butt weld joints in full-scale aluminium alloy joints: Experimental and numerical study of traction structural stress’, International Journal of Fatigue, 187, 108478.
6. Instron (2024) ‘8801 Servohydraulic Fatigue Testing System’, Product datasheet, 8801_ SHFatigueTestingSystems _V9.
7. Ren, Z., Chang, H., Yue, Q. and Liu, X. (2025) ‘Fatigue analysis and performance evaluation of stainless-steel cruciform joint with welding pore defect’, Journal of Constructional Steel Research, 235, 109814.

Design And Development of a Quadrotor-Integrated Tracked Robotic Subsea Exploration Crawler

M.O Ojumu, A.K Raji and E.F Orumwense

Faculty of Engineering and Built Environment,
Department of Mechanical Engineering Mechatronics Engineering, Cape Peninsula University of Technology,
PO Box 1906, Bellville, 7535, Cape Town, South Africa

1. Abstract

Exploring and excavating complex seabed terrains requires robust mobility and stability that conventional subsea crawlers often lack. This study presents a hybrid crawler combining a tracked platform with quadrotor-inspired vectored thrusters to enhance manoeuvrability, stability, and energy efficiency. Structural optimization, dynamic modelling, and control co-design ensure balanced traction and thrust, while a hierarchical control system coordinates tracks and thrusters in real time. Motion studies demonstrate superior performance on soft and inclined seabed's, establishing a versatile platform for next generation remotely operated underwater excavation vehicles.

2. Introduction / Background

Subsea mining and excavation are essential for resource recovery and seabed development, demanding compact, robust systems capable of stable motion on uneven terrains under strong currents. While traditional tracked crawlers provide good traction and load capacity, they often experience slippage, mobility loss, and instability on soft or dynamic seabed's as discussed by Ojumu [1]. In contrast, free-swimming vehicles offer agility but lack the stability and anchoring required for effective heavy-tool operations.

This research presents a hybrid subsea crawler that integrates tracked traction with quadrotor-inspired thrusters, enhancing dexterity, mobility, and energy efficiency for safer, longer, and more cost-effective operations. Despite increasing interest in subsea exploration, effective Navigability solutions for heavy, tool-equipped crawlers on complex seabed's remain limited. Mohd and Mike [2]; [3].

Earlier efforts, such as those by Ducourneau [4], Previous studies emphasized crawler mechanics and seabed interaction but neglected hydrodynamics and tool stability. Thruster-assisted hybrid designs remain underexplored, limiting performance. This study introduces a hybrid subsea crawler with quadrotor-inspired vectored thrusters and hierarchical control, enabling coordinated track-and-thrust operation. The platform enhances stability, and precision, allowing smaller crawlers to perform complex excavation tasks efficiently and adaptively in diverse underwater environments.

3. Aim of the Study

To design a hybrid subsea crawler integrating tracked locomotion with vectored thrusters to improve mobility, tool-point stability, and energy efficiency in challenging seabed environments.

4. Objectives

1. Design a compact hybrid subsea crawler integrating tracked mobility with vectored-thrust assistance.
2. Develop a coupled dynamic model capturing crawler mechanics, hydrodynamic effects, and seabed interaction.
3. Implement a hierarchical control system for real-time coordination of tracks and thrusters.
4. Enhance tool-point precision, minimize track slip, and ensure robust attitude control under currents.
5. Evaluate system performance through simulations and benchmarking with existing platforms.

5. Research Methodology

The development of the hybrid subsea crawler followed a systematic six-phase approach: Conceptualization → Structural Modelling → Motion Simulation → Performance Evaluation → Control Implementation → Comparative Validation.

This structured methodology guided the progression from initial design concepts to full system validation. Structural modelling enhanced overall rigidity and stability, while the integration of the tracked–thruster propulsion system significantly improved

[a] mikeoluwaseunojumu@gmail.com

manoeuvrability—showing an estimated 25–30% improvement in future design adaptability. Furthermore, optimization of thruster placement is projected to reduce power consumption by approximately 15%, ensuring efficient energy utilization and consistent seabed traction under varying operational conditions.

6. Results / Findings

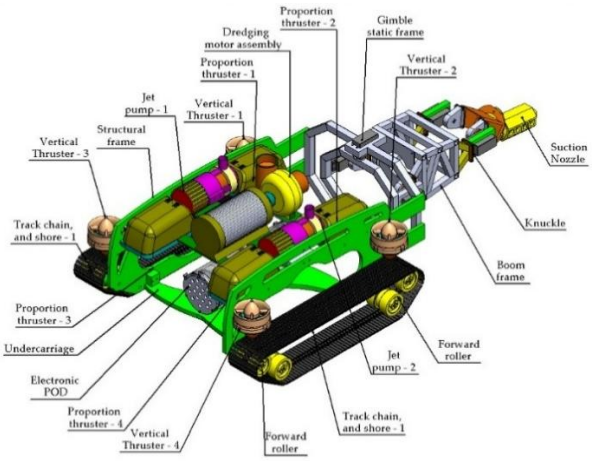

Figure 1: Quadrotor-Integrated Tracked Robotic Subsea Exploration Crawler

The hybrid subsea crawler system, as illustrated in Figure 2, was successfully conceptualized, modelled, and partially validated through simulation and prototype-level analysis in comparison with the MK1 ROST [5]. The design combines dual tracks with four vectored thrusters for six-degree mobility and dredging via a boom-mounted nozzle. SolidWorks modelling ensured balanced structure and hydrodynamic alignment, while simulations confirmed stable motion and efficient thrust–track coordination. The control logic maintained pitch–roll stability, achieving 25–30% higher mobility and improved stability over traditional tracked crawlers, outperforming the configurations presented by crawler M [6].

7. Discussion

The hybrid subsea crawler integrates tracked locomotion with quadrotor-inspired vectored thrusters, enhancing underwater mobility, robustness, and adaptability. Design motion study shows that its distributed thrust system improves manoeuvrability and stability under variable currents, achieving 25–30% higher mobility and energy efficiency than conventional crawlers, while bridging seabed traversal and mid-water manoeuvring.

These gains are achieved through a well design structural plant form with a cascaded PID–MPC control architecture with adaptive force allocation, fused sensor data, and SLAM-based localization for precise positioning. An adaptive disturbance observer ensures robust operation under dynamic subsea conditions. Its modular, scalable design suits deep-sea mining, infrastructure inspection, and underwater archaeology, with future work targeting autonomous operation and field deployment using the Quadrotor-Integrated system.

Keywords:

subsea crawler design, motion study, subsea mining, tracked locomotion, and quadrotor assistance.

References

i. Ojumu MO, Raji AK. Structural frame analysis of an electrically powered robotic subsea dredging crawler under static loading conditions. J South African Inst Min Metall. 2023;123(10):491–9.
ii. Mohd Aras MS, Kamarudin MN, Che Rusli MH Bin, Mohd Zainal MI. Small scale unmanned underwater remotely operated crawler (ROC). Indones J Electr Eng Comput Sci. 2016;3(3):481–8.
iii. Mike Oluwaseun Ojumu. The development of an electric-powered subsea robotic crawler for dredging . by [Internet]. 2022. Available from: https://etd.cput.ac.za/bitstream/20.500.11838/3728/1/Ojumu_Mike_Oluwaseun__217269680.pdf
iv. Ducourneau T. Development of an underwater gravimeter. 2012;2012.
v. Trans Hex Group. Trans Hex Group [Internet]. 2023 [cited 2021 Jul 28]. p. 1–3. Available from: https://www.imdhgroup.com/team.php
vi. Crawler M, seascape BV. Seascape developed a small electrical mini-crawler for subsea survey, inspection and cleaning. 2017 [cited 2021 Aug 25];1. Available from: https://www.seascapesubsea.com/downloads/Seascape-Mini-crawler-R1.1.pdf
vii. Keisner A, Raffo J, Wunsch-Vincent S. Robotics: Binnovation, intellectual property. Foresight STI Gov. 2016;10(2):7–27.

[a] mikeoluwaseunojumu@gmail.com

OPEN-SOURCE STEREO DIGITAL IMAGE CORRELATION SYSTEM IN PYTHON

H.A.J. Lombard* & G. Venter & M. Neaves

Department of Mechanical and Mechatronic Engineering, Stellenbosch University, Corner of Banghoek and Joubert Street, Stellenbosch 7599, Western Cape, South Africa

Digital image correlation (DIC) is a non-contact method used for measuring the full-field surface deformation and/or motion of an object[1]. These measurements are obtained by tracking the deformation, or "warping", of image sub-regions across a sequence of images using digital image registration techniques (i.e., template matching). A random pattern is typically applied to the surface of the object to ensure unique pixel intensity values per sub-region, as required for image registration.

Stereo-DIC is a form of three dimensional (3D) DIC, which makes use of stereo images to compute full-field 3D displacement and strain. Stereo-DIC is required for experiments involving significant out-of-plane deformation or non-planar geometries. Conventional planar (2D) DIC is prone to significant measurement errors[2].

Two primary formulations exist for modelling the displacement fields within a region-of-interest (ROI): local and global DIC. Local DIC tracks each sub-region independently by finding the parameters of a shape function that warps the sub-region in the reference image to the same shape and translation of the corresponding sub-region in the target/deformed image. In contrast, global DIC models the entire ROI as a Finite Element mesh, from which a piece-wise continuous displacement field is computed globally. This project employs the local method, which was selected for its superior accuracy and computational speed[3].

The SUN-DIC[4] software is an open-source Python library developed at Stellenbosch University that currently supports local planar DIC analysis. It makes use of the AKAZE algorithm for feature detection and description, the Brute-Force algorithm for feature matching, and the RANSAC algorithm for eliminating incorrect matches, which is used to estimate the initial parameters for the optimisation algorithm. It supports the inverse-compositional Gauss-Newton (IC-GN) and inverse-compositional Levenberg-Marquardt optimisation algorithms, using the zero-mean normalized sum of squared differences correlation criterion as the cost function to find the optimal shape function parameters.

The first objective of this project is to extend the SUN-DIC library to enable local stereo-DIC analysis by implementing stereo matching and 3D reconstruction of the sub-regions to calculate their 3D displacement and strain values.

An initial implementation of stereo matching and 3D reconstruction has been completed. The stereo matching makes use of AKAZE and IC-GN and the 3D reconstruction uses the least-squares triangulation method. The plot in Figure 1 shows the computed 3D sub-region displacements for the StereoSample5 tensile test from the Stereo-DIC Challenge 1.0 dataset[5].

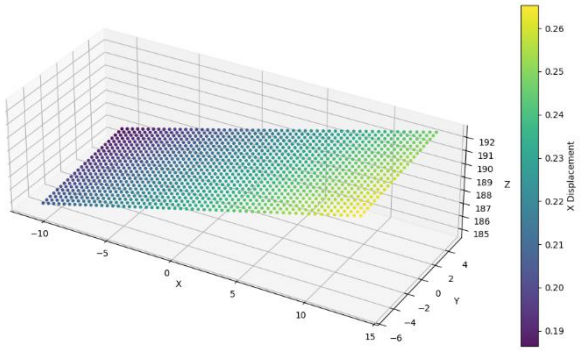

Figure 1: Scatter plot of reconstructed 3D sub-region coordinates coloured by their displacement magnitude in the X-direction.

The setup used to capture the images for stereo-DIC analysis is typically referred to as a stereo-rig. It consists of two cameras mounted horizontally from each other, both aimed towards a ROI at a specific angle known as the stereo-angle. Various choices, such as the stereo-rig layout[6], camera, lens, stereo angle and lighting selection are crucial for obtaining accurate measurements. The selection of the stereo-angle is an important trade-off between out-of-plane and in-plane measurement accuracy. The camera and lens selection is determined by the required field-of-view to ensure the ROI stays within the frame, the depth-of-field to ensure the ROI remains in focus after out-of-plane displacement, the pixel size for measurement resolution and frame rate for high-speed measurements. The images captured from the cameras must be synchronous and triggered by external hardware such as a tensile tester data acquisition (DAQ) device. Adequate lighting is essential for

* Corresponding author's email address: 24743496@sun.ac.za

achieving high image contrast and low noise, which directly impacts measurement quality[7].

The second objective is to design and build a low-cost stereo-rig. The motivation for this is to increase Stellenbosch University's capabilities for performing stereo-DIC measurements without the need to rely on expensive commercial systems. It is also to be used as a testbed for future DIC related research. The system will make use of a Raspberry Pi 5 for receiving the external trigger, synchronising the cameras, controlling the lights, obtaining the images and interfacing with DAQ devices.

Before stereo-DIC analysis, stereo camera calibration must be performed to obtain the required pinhole camera model intrinsic (focal lengths, skew) extrinsic (translation, rotation) and distortion parameters for accurate 3D reconstruction of the sub-regions. Although important, implementing accurate stereo camera calibration is outside the scope of this project. An existing solution within Stellenbosch University will be used obtain the calibration parameters after the stereo calibration images are captured using the stereo-rig.

There are two forms of sub-region matching employed in stereo-DIC. The first is temporal matching, which is the process planar-DIC uses to track the movement of sub-regions through a sequence of images. The second is stereo matching, which involves finding the locations of corresponding sub-regions in one image (e.g., the left image) within the other image (e.g., the right image) of a stereo pair.

The complete workflow for a stereo-DIC analysis is shown in Figure 2.

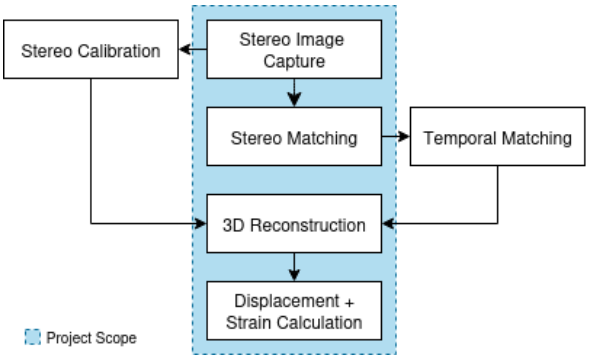

Figure 2: Flowchart showing the steps required to perform stereo-DIC analysis.

The analysis begins after the stereo images and calibration parameters are obtained. The first step is to define the sub-regions in the reference stereo image pair. The sub-regions for the reference left image are created in a grid layout within the ROI, based on the specified sub-region size and step distance. The corresponding locations for these sub-regions are then found in the reference right image using stereo matching, which typically employs a second order shape function to account for the perspective distortion between the image pair. Once the sub-regions for the reference image pair are defined, temporal matching is applied to track the movement of the left image sub-regions and right image sub-regions independently, in their respective image sets. After completion of the temporal matching, the sub-regions for each stereo image pair are 3D reconstructed. Finally, the 3D displacements are calculated as the difference between the deformed and reference 3D sub-region locations.

The final objective of this project is to integrate the stereo-DIC software implementation with the stereo-rig to create a low-cost and open-source stereo-DIC system. This system will be tested and compared to existing commercial systems within Stellenbosch University.

References:

1. Schreier, H., Orteu, J.-J. and Sutton, M.A. (2009) *Image correlation for shape, motion and deformation measurements: basic concepts, theory and applications*. Boston, MA: Springer US. Available at: https://doi.org/10.1007/978-0-387-78747-3.
2. Sutton, M.A. *et al.* (2008) 'The effect of out-of-plane motion on 2D and 3D digital image correlation measurements', *Optics and Lasers in Engineering*, 46(10), pp. 746–757. Available at: https://doi.org/10.1016/j.optlaseng.2008.05.005.
3. Wang, B. and Pan, B. (2016) 'Subset-based local vs. finite element-based global digital image correlation: a comparison study', *Theoretical and Applied Mechanics Letters*, 6(5), pp. 200–208. Available at: https://doi.org/10.1016/j.taml.2016.08.003.
4. Gerhard Venter (2025) 'SUN-DIC: Stellenbosch University Digital Image Correlation Code'. Available at: https://github.com/gventer/SUN-DIC (Accessed: 17 September 2025).
5. Ahmad, W. *et al.* (2024) 'Stereo-DIC challenge 1.0 – rigid body motion of a complex shape', *Experimental Mechanics*, 64(7), pp. 1073–1106. Available at: https://doi.org/10.1007/s11340-024-01077-7.
6. Reu, P. (2012) 'Stereo-rig design: creating the stereo-rig layout - part 1', *Experimental Techniques*, 36(5), pp. 3–4. Available at: https://doi.org/10.1111/j.1747-1567.2012.00871.x.
7. Reu, P. (2013) 'Stereo-rig design: lighting-part 5', *Experimental Techniques*, 37(3), pp. 1–2. Available at: https://doi.org/10.1111/ext.12020.

COMPARATIVE ANALYSIS OF FRICTION STIR ADDITIVE MANUFACTURED ALUMINIUM WITH CONVENTIONAL ALLOYS: MECHANICAL PROPERTIES

A. Magudu[a], V. Msomi[b], S. Mabuwa[c]

[a]Mechanical and Mechatronic Engineering Department, Faculty of Engineering and the Built Environment, Cape Peninsula University of Technology, Cape Town, South Africa.
[bc] Mechanical, Bioresources, and Biomedical Engineering, School of Engineering and the Built Environment,

Introduction

Recent advances in manufacturing technologies have intensified the demand for lightweight and high-performance structural materials in modern engineering applications, particularly in aerospace and automotive industries[1]. Conventional wrought aluminium alloys, such as AA1050-H14 and AA6082-T6, remain widely used due to their excellent strength-to-weight ratio, formability, and corrosion resistance[2]. Several state-of-the-art additive manufacturing (AM) processes, including Laser Metal Deposition (LMD), Electron Beam Additive Manufacturing (EBAM), and Wire Arc Additive Manufacturing (WAAM), have demonstrated significant potential for producing complex geometries with high material efficiency. Despite their advantages, these fusion-based AM methods often face challenges such as residual stresses, porosity formation, anisotropic mechanical properties, and the need for post-processing treatments to achieve desired performance levels[3]. In contrast, Friction Stir Additive Manufacturing (FSAM), a solid-state technique offers a promising alternative by mitigating fusion-related defects while enhancing metallurgical bonding and mechanical integrity[4]. This study investigates and compares the mechanical properties of FSAM-fabricated aluminium with conventional AA1050-H14 and AA6082-T6 alloys. The FSAM process involved multilayer using an aluminium 1050 base, with controlled variations in tool rotational and traverse speeds to optimize heat input and bonding quality[5], (refer to Figure 1). Tensile tests were performed to assess the ultimate tensile strength (UTS), fracture distance, and elongation of the FSAM-fabricated samples in comparison with the conventionally processed alloys.

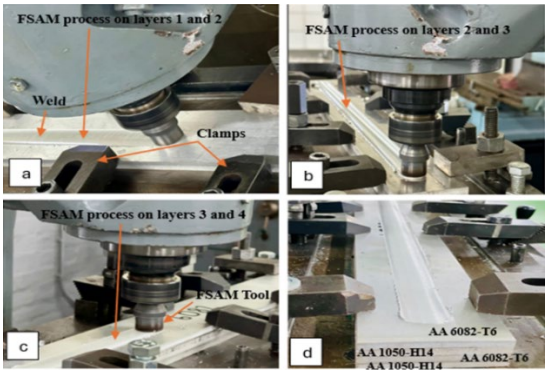

Figure1: FSAM process

2. Results

Figure 2 illustrates the stress-strain response of the FSAM-fabricated aluminium AA-FSAM compared to the conventionally processed AA1050-H14 and AA6082-T6 alloys. The FSAM specimen exhibits a distinct curve characterised by a moderate yield strength and an extended plastic deformation region, signifying improved ductility. The UTS of 95 MPa corresponds to the peak of the green curve, which occurs at a higher strain value 0.25, indicating that the material can sustain substantial plastic deformation before failure. In contrast, the AA6082-T6 sample shows a steep stress increase followed by an abrupt fracture at a strain of 0.23, consistent with its high UTS 313 MPa but limited ductility 24%. The AA1050-H14 alloy lies between these two behaviours, displaying a balanced combination of strength and ductility, with a UTS of 105 MPa and elongation of 30%[6]. The gradual slope of the FSAM curve in the elastic region suggests a lower Young's modulus relative to the heat-treated AA6082-T6, reflecting the reduced stiffness typically observed in solid-state processed aluminium. Overall, the mechanical response presented in Figure 2 demonstrates that FSAM produces components with lower stiffness and strength but superior ductility and structural integrity compared to conventional fusion-based alloys. The absence of fusion-related defects such as porosity or hot cracking, coupled with stable interlayer diffusion, validates FSAM's potential as a reliable solid-state manufacturing route for lightweight aluminium structures.

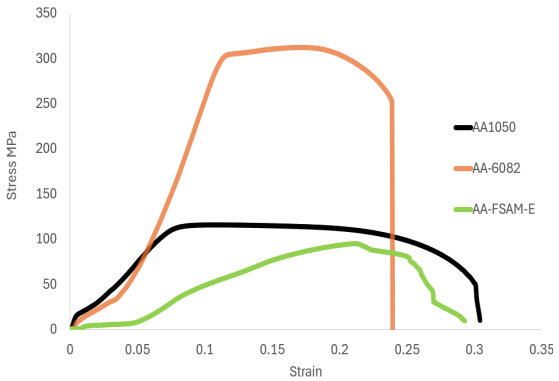

Figure 3: Stress vs strain graph

magudua@cput.ac.za

3.Conclusion

Overall, the findings confirm that FSAM can fabricate aluminium components with mechanical properties comparable to conventional wrought alloys while offering significant reductions in material wastage and production costs. This study contributes valuable insights into process optimisation for industrial-scale implementation, positioning FSAM as a promising approach for manufacturing high-integrity aluminium structures in the aerospace, transportation, and energy sectors.

4.References

1. Mishra, RS & Ma, ZY. Friction stir welding and processing. Materials Science and Engineering: R: Reports, Vol. 50, No. 1–2, 2005, pp. 1–78.
2. Zhang, D., Du, D., Xue, S., Qi, J., Pu, Z., Lu, Y. & Tang, Y., 2024. Residual stress and deformation in wire-feed electron beam additive manufactured aluminum components. The International Journal of Advanced Manufacturing Technology, 131, pp.1665–1676.
3. Mahoney, MW & Rhodes, CG. Friction Stir Welding of Aluminium Alloys. ASM International, Materials Park, OH, 2014.
4. Pal, S, Ghosh, A & Kumar, S. A review on friction stir additive manufacturing: process, properties, and prospects. Journal of Materials Research and Technology, Vol. 12, 2021, pp. 1641–1660.
5. Zhu, XK & Chao, YJ. Numerical simulation of transient temperature and residual stresses in friction stir welding of 304L stainless steel. Journal of Materials Processing Technology, Vol. 146, No. 2, 2004, pp. 263–272.
6. Zhang, H, Wu, A & Wang, G. Influence of process parameters on mechanical and microstructural properties of friction stir additive manufactured aluminium alloys. Materials Science Forum, Vol. 1004, 2020, pp. 149–156.

DEVELOPMENT OF A DATA MODEL FOR HOSPITAL WASTE STREAMS

R. Liebenberg[a], C.A. Steed[a] & A.H. Basson[a]

[a] Department of Mechanical and Mechatronic Engineering, University of Stellenbosch, Stellenbosch, South Africa

Background

Hospitals play a critical role in improving the quality of life by providing essential medical care to the public. The significance of hospitals extends beyond healthcare services. They are major consumers of resources, leading to a significant environmental impact. The health care sector is a large contributor to carbon emissions [1], waste generation [2], and resource consumption. Healthcare waste management is critical regarding sustainability, as hospitals generate millions of tons of medical waste worldwide. Hospital waste management is a complex system due to the various types of waste produced and the disposal requirements that follow. Hazardous waste consists of infectious waste, pathological waste, chemical waste, and radioactive waste, which can be harmful, toxic, and carcinogenic.

Improper waste management can cause a small amount of hazardous waste to mix with general waste. This will render all the general waste potentially hazardous or infectious [3]. Hazardous waste disposal is higher in cost because it needs to be treated carefully due to its toxicity [4]. This project aims to develop a data model of hospital waste flows to inform decision-making. The proposed model focuses on visualizing and analyzing a hospital's waste cycle. Figure 1 shows that the cycle ranges from procurement to final disposal to identify key cost drivers and assess the impact of interventions before implementation. Simulating hospital waste generation enables proactive decision-making to reduce costs and improve sustainability.

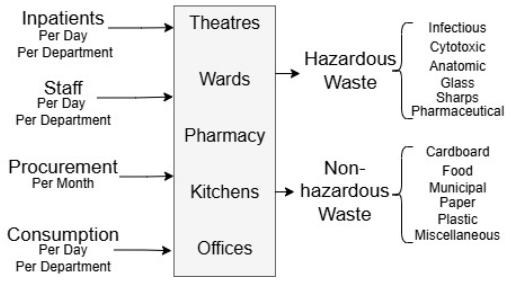

Figure 1: Hospital Inputs and Outputs

Methodology

The methodology for developing the proposed model, seen in Figure 2, is based on Cross-Industry Standard Process for Data Mining (CRISP-DM), modified to include the development of a Minimum Viable Product (MVP). CRISP-DM provides an iterative and structured approach for model refinement. There are six key phases of CRISP-DM: business understanding, data understanding, data preparation, modelling, evaluation, and deployment.

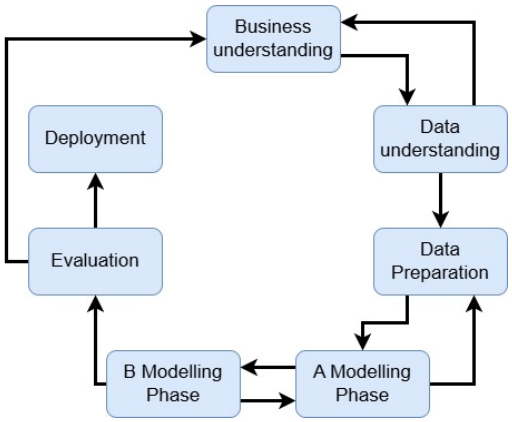

Figure 2: Adapted CRISP-DM methodology

Business understanding placed Mediclinic in an operational context to understand the various flows and operations throughout a hospital. Data understanding and preparation includes the collection and cleaning of hospital data. The dataset can be explained from Figure 1. The various inputs and their time scales focusing on data per day where possible, and the outputs which can be categorized per waste stream.

The research is currently in the modelling phase, where simulation techniques are being developed and tested. The modelling phase is split into two phases. Modelling phase A is a data-based step that will reveal correlation and causation between hospital inputs and outputs. Modelling phase B is a simulation base model that is formed from the causation and correlation relationships in phase A. The modelling phase B utilizes system dynamics (SD) integrated with discrete event simulation (DES), with the potential of introducing agent-based modelling (ABM). SD simulates time-based behavior and time-dependent relationships with the use of feedback loops. DES is used to simulate specific operational processes such as waste collection and transport, as these processes are not continuous but rather happen at certain times throughout the day. Procedures are discrete events as they happen at certain times and for certain periods, whereas the number of patients and staff is a continuous factor. This example is to show the need for DES as well as SD. The relationship between hospital operations and waste generation is a complex system with many different time-based and event-based relationships. The model structure includes unidirectional, causal loop, and stock flow diagrams.

This phase includes the development of an MVP. An MVP helps identify potential implications of the model design, helps reduce the risk of large-scale complications, and provides an estimate of the time required to complete the final model development.

The evaluation phase is planned as a future stage and will determine the accuracy and usability of the MVP, as well as guide the final model development. The evaluation will be done through a case study at a local hospital. The deployment stage, although part of the CRISP-DM methodology, will not be implemented in this project.

Implementation

The implementation of the model will make use of AnyLogic simulation software, which is capable of combining SD, DES, and ABM. An initial grey box model was developed to identify all the inputs and outputs coming in and out of the system. This model can be seen in Figure 3. Procurement is represented as a single input for the entire hospital, as procurement data is only available at the hospital level and not disaggregated by department. We can get staff, patient, and consumable data per department. The high-impact departments responsible for significant waste generation are identified and modelled. This is a core objective of the research as these areas are closely associated with key cost drivers within the hospital system.

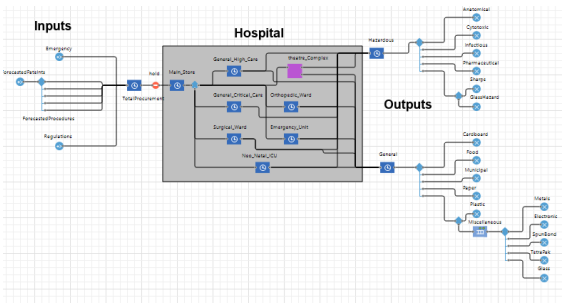

Figure 3: Grey Box Model

The idea is to track procurement through the hospital, link procurement to consumption, and be able to determine waste generation per department based on a range of factors and assumptions.

The data received requires extensive processing and analysis. This will be carried out in *Python* to clean the datasets, perform regression analysis, and identify causation and correlation relationships between hospital operations and waste generation. These analyses will help inform the structure of the causal/correlation simulation model, and ensure relationships are data driven. The development of the MVP will form the foundation for validating the model. It is expected that early results will highlight the correlation between hospital operations and waste generation. The MVP will be validated using historical data of the hospital's operations and waste generation to assess its accuracy and reliability

Outcomes

The expected outcome of this research is to develop a validated decision-support tool for waste management in a hospital. Evaluating interventions before implementation provides a practical tool for hospitals to explore various sustainability scenarios. The findings will demonstrate the use of hybrid modelling approaches in waste management and offer healthcare providers a structured and data-driven approach to sustainable operations.

References

[1] P. P. Pichler, I. S. Jaccard, U. Weisz, and H. Weisz, "International comparison of health care carbon footprints," *Environmental Research Letters,* Article vol. 14, no. 6, 2019, Art no. 064004, doi: 10.1088/1748-9326/ab19e1.

[2] T. Sanyal, I. Rakshit, and P. Bhattacharjee, "Green healthcare: initiatives and adaptations for sustainable future," *Environment, Development and Sustainability,* Review 2024, doi: 10.1007/s10668-024-04957-z.

[3] I. A. Al-Khatib, D. Eleyan, and J. Garfield, "A system dynamics approach for hospital waste management in a city in a developing country: the case of Nablus, Palestine," *Environmental Monitoring and Assessment,* Article vol. 188, no. 9, 2016, Art no. 503, doi: 10.1007/s10661-016-5487-9.

[4] E. S. Windfeld and M. S. L. Brooks, "Medical waste management - A review," *Journal of Environmental Management,* Review vol. 163, pp. 98-108, 2015, doi: 10.1016/j.jenvman.2015.08.013.

VEHICLE-MOUNTED SMALL WIND TURBINE: AERODYNAMIC FLOW ANALYSIS, VIBRATION EFFECTS, AND PERFORMANCE EVALUATION

YUN Mbekela, GJ Oliver, HT Fawkes

Department of Mechanical Engineering, Cape Peninsula University of Technology, Bellville, 7535, South Africa

Abstract: This study investigates the impact of test conditions on a vehicle-mounted small wind turbine through a combination of on-road experimental testing and computational fluid dynamics (CFD) simulation.
The work responds to gaps identified by authors in [1], who highlighted the need for vehicle-based testing methods and aerodynamic flow analysis for small turbines.
The vehicle testing method provides a flexible and cost-effective approach to evaluating turbine performance under realistic, dynamic wind conditions. However, uncertainty around the impact of turbine vibration due to uneven road surface, and the impact of vehicle shape on the flow of air through the turbine, prompted this investigation. Aerodynamic flow around the vehicle and turbine was analysed using ANSYS workbench 2025 R2 Fluent to assess flow uniformity and potential flow interactions between the vehicle and turbine. Results of on-road testing show the relationship between vehicle speed, wind speed, turbine power output, and turbine vibration.

Introduction: Traditional wind tunnel testing methods for small scale wind turbines present several challenges including blockage effects, limited scalability, and cost. Wall interference can distort global aerodynamic coefficients, such as lift and drag, leading to inaccurate performance assessments. Corrections are essential to ensure results reflect undisturbed flow conditions [2].

Alternative testing methods have therefore gained attention, with vehicle-based testing to simulate dynamic wind conditions [1]. Other studies have also noted the limitations of closed-section wind tunnels and proposed slotted test sections to reduce blockage effects [3]. This study builds on these insights by integrating vehicle-mounted experimental testing, vibration analysis, and CFD simulations to better understand the impact of uneven road surface and the aerodynamic interference of the fluid flowing over the vehicle body during the test.

Methodology: The methodology for testing the wind turbine involved mounting the turbine on a vehicle and measuring its performance under real-world motion conditions. Key parameters such as wind speed, current voltage, and vibrations were recorded while the vehicle was driven at controlled speeds for six trial runs

Experimental Setup: The experimental setup consisted of a small horizontal-axis wind turbine mounted on a pickup vehicle. The turbine was installed 2.6 m above the vehicle roofline to avoid aerodynamic interference. Measurements were taken using a custom-built anemometer with a LM393 sensor for wind speed, where current was logged through the ACS712 current sensor and voltage scaled down through a voltage divider for Arduino processing.
Vibration was logged through an ADXL345 accelerometer. Tests were conducted on a straight, open road segment at various speeds to simulate different wind and road conditions.

Figure 1: Vehicle-mounted wind turbine setup

Data Acquisition: Wind speed, electrical current, voltage, and accelerometer data were logged simultaneously during trial runs. The data was recorded at a fixed sampling rate and later analysed to determine the correlation between, wind speed, turbine power, and vibration levels.

[a] Corresponding author: mbekelaY@cput.ac.za

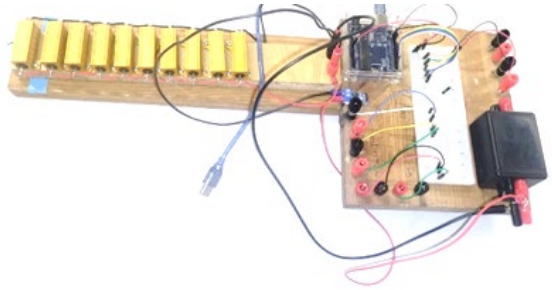

Figure 2: Data acquisition system showing the resistor bank, Arduino Uno R3, voltage divider, and connection terminals for the accelerometer and anemometer.

Aerodynamic Simulation: A computational fluid dynamics (CFD) simulation was conducted using ANSYS Fluent to analyse airflow around the vehicle and turbine. A steady inlet velocity of 15 m/s was applied, using the turbulence model k–ε with standard wall functions and boundary conditions set to reflect realistic road-testing conditions. The turbine was positioned at a height 2.6 m above vehicle roof to minimise wake interference from the vehicle cab.

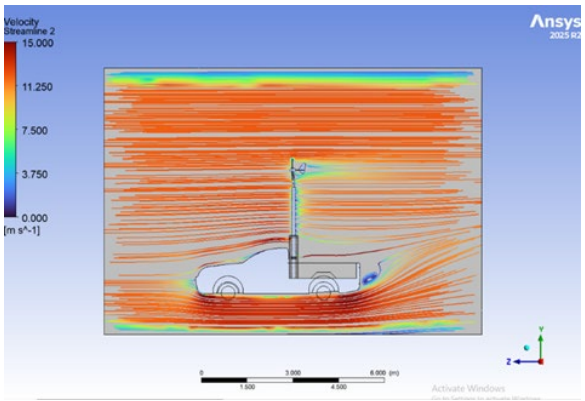

Figure 1: Velocity streamline plot from CFD simulation

Results and Discussion: The experimental results shown in figure 4 highlighted two distinct vibration events recorded during the test, Z-axis spike at 25.5 s, associated with the vehicle passing over a speed bump, and an X-axis spike at 31.5 s, caused by contact with a sandbag. These events coincided with short-term fluctuations and a drop in turbine power output. The CFD results confirmed that turbine placement 2.6 m above the roofline positioned the rotor in a region of uniform high-velocity flow, minimizing aerodynamic interference

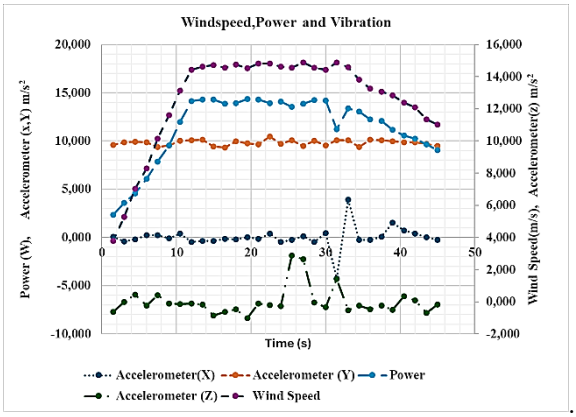

Figure 2: A graph showing correlation between windspeed, power and vibration

Conclusion: The numerical flow analysis revealed high-pressure stagnation zones over the vehicle cab and a wake region of low kinetic energy immediately behind the roofline. These areas are unsuitable for rotor placement, as they cause uneven inflow and reduce turbine efficiency. In contrast, regions above 2.5 m from the vehicle roofline showed smoother velocity contours, indicating more stable airflow and greater potential for consistent power generation.
The experimental results demonstrated that road-induced vibration had a measurable impact on turbine stability and power output. Short-term power drops corresponded with vertical and lateral vibration events, confirming the system's sensitivity to structural motion.

Recommendations: Based on the combined experimental and computational findings, it is recommended that future designs of vehicle-mounted wind turbines incorporate improved vibration isolation and structural damping within the tower assembly to reduce the effects of road-induced shocks on turbine alignment and power output. The turbine should remain positioned above regions of aerodynamic interference identified in the flow simulation, preferably beyond the vehicle's wake boundary where velocity distribution is more uniform.

References:

1. Q. Song and W. D. Lubitz, "Design and Testing of a New Small Wind Turbine Blade," J Sol Energy Eng, vol. 136, no. 3, pp. 85–95, 2014, doi: 10.1115/1.4026464.
2. M. BURGHIU, "Evaluation of wind tunnel wall interference using homogeneous and measured boundary conditions," INCAS BULLETIN, vol. 15, no. 4, 2023, doi: 10.13111/2066-8201.2023.15.4.5.
3. M. Mokry, "Wall interference correction to drag measurements in automotive wind tunnels," Journal of Wind Engineering and Industrial Aerodynamics, 1995, doi: 10.1016/0167-6105(94)00119-X.

Author Index